Lightwave Electronics Based on Nanoantenna Networks

By

Matthew Yeung

B.Sc., University of Southern California (2016)
S.M., Massachusetts Institute of Technology (2022)

Submitted to the Department of Electrical Engineering and Computer Science
in Partial Fulfillment of the Requirements for the Degree of

Doctor of Philosophy

at the

MASSACHUSETTS INSTITUTE OF TECHNOLOGY

May 2024

Authored by:	Matthew Yeung Department of Electrical Engineering and Computer Science May 16, 2024
Certified by:	Phillip D. Keathley Principal Research Scientist Thesis Supervisor
Certified by:	Karl K. Berggren Joseph F. and Nancy P. Keithley Professor of Electrical Engineering and Computer Science Thesis Supervisor
Accepted by:	Leslie A. Kolodziejski Professor of Electrical Engineering and Computer Science Chair, Department Committee on Graduate Students

Lightwave Electronics Based on Nanoantenna Networks

by

Matthew Yeung

Submitted to the Department of Electrical Engineering and Computer Science
on May 16, 2024, in partial fulfillment of the
requirements for the degree of
Doctor of Philosophy

Abstract

The evolution of commercial lasers has played a pivotal role in advancing our comprehension of the natural world. Emitting coherent, high-intensity light, lasers offer unparalleled capabilities, reaching peak intensities of terawatts per centimeter squared at frequencies exceeding a million times per second. Such immense peak intensities facilitate electric field amplitudes at the focus that scale to the V/nm range, rivaling the electric field strengths within atoms and molecules responsible for atomic-scale electron dynamics. Through the realm of ultrafast nonlinear optics, the manipulation of optical waveforms has paved the way for controlling electrons at optical frequencies [1]–[7]. This breakthrough has led to a deeper understanding of electron dynamics, particularly in the context of light field-driven phenomena in solids, a field commonly referred to as lightwave electronics.

As traditional semiconductor electronics approach their saturation limits in terms of speed and size, researchers are turning to light as a means of encoding information, ushering in the era of integrated photonics. Light, with its minimal absorption and high data propagation rates coupled with low power dissipation, offers an ideal medium for transmitting information. While integrated photonics encodes information within the time-averaged intensity and polarization of light, the harnessing of ultrafast electric field oscillations in light, analogous to the behavior of modern-day high-speed electronics, presents an opportunity to encode information in the sub-cycle field oscillations.

In pursuit of electronics operating at optical frequencies, various methods have been explored to realize practical lightwave electronic circuit elements analogous to those in traditional electronics. Pioneering experiments have showcased that optical waveforms can initiate attosecond electron currents across various interfaces, encompassing metal-vacuum [8]–[17], dielectric [18]–[20], and air interfaces [21], [22]. However, a significant hurdle arises from the difference between the characteristic frequencies of optical (PHz) and electronic systems (GHz-THz), making it difficult to integrate optical systems with electronic ones.

This thesis underscores the pivotal role of metallic nanoantennas as a scalable platform for lightwave electronics. It demonstrates how metallic nanoantennas en-

able control over light field-driven responses through rectification, resonance control (leading to lower peak fields required to operate), and polarization control. A comprehensive framework is introduced, serving as the backbone for subsequent chapters. The thesis showcases three nanoantenna variants: one facilitating shot-to-shot measurements of PHz optical phase on a chip, yielding over 2000 optical phase-sensitive electrons, ideal for compact optical waveform synthesis and interferometry-free frequency combs. When leveraging rectification, the thesis further illustrates harmonic frequency mixing with bandwidth surpassing that of the input light, enabling the direct detection of PHz frequencies using multi-cycle light from commercial laser systems. This practical demonstration facilitates frequency mixing, positioning the device as a compact detector for optical oscilloscope-like measurements. Finally, an architecture is presented to enable polarization-sensitive rectification, highlighting the flexibility of the nanoantenna platform for PHz-driven electrons.

As is exhibited through the work in this thesis, nanoantennas possess the potential to emerge as a comprehensive solution for lightwave-driven electronics, enabling a new era of high-speed, low-power electronic systems driven by oscillations of light.

Acknowledgments

I first want to thank my friends, relatives, and most importantly, my mother. Thank you for your endless support. Although my family and friends I have met over the years will probably never read this, I would not be where I am today without my time with them. I would also like to thank Prof. Rehan Kapadia as he has provided me with tons of support ever since I joined his lab in 2015. My time in his group allowed me to develop my core beliefs in education and scientific research. Special thanks to Prof. Jayakanth Ravichandran, Prof. Nate Hohman, and Dr. Debarghya Sarkar for their continued support in my scientific journey and for being a phone call or message away.

At MIT, I would like to begin by acknowledging Donnie and Karl's continued support and flexibility in research direction and our administrators, Dorothy Fleischer and Rinske Wijtmans. A very special thanks to Leslie, Kathy, Janet, Alicia, and Meredith from the Electrical Engineering and Computer Science graduate office. They were always there to help me with everything ranging from administrative details to personal issues. To Prof. Peter Hagelstein, thank you for being an great lecturer and friend to converse with, your wisdom and advice helped me a lot during my first semester here. Thank you to Prof. Rajeev Ram for serving on my qualifying exam committee. Thank you to Prof. Sixian You for serving on my qualifying exam, and thesis committee, and serving as a recommender. Thank you Prof. Nuh Gedik for serving on my thesis committee and allowing me to work on applying such lightwave electronic devices for studying condensed matter systems in your group. Thank you Prof. Franz Kaertner for serving as a reference writer and allowing me to come to Deutsches Elektronen-Synchrotron through PIER Hamburg program.

I would like to thank the numerous people I have met during my time at MIT. Special thanks to those outside of my lab: Benson Chen, John Niroula, Qihang Zhang, Jixiang Yang, Zhengguang Lu, Patrick Chou, Deanna Montgomery, Alex von Hoegen, and Neetesh Singh. Whether it was chatting about life, helping on get things to work, or with life concerns, they were always there to help me through my problems or listen

to them.

To my labmates, those from the NanoStructures Lab, and MIT.nano staff, special thanks to Felix Ritzkowsky, Lu-Ting Chou, John Simonatis, Marco Turchetti, Marco Colangelo, Owen Meideros, Mark Mondol, Jim Daley, Gary Riggot, Eric Lim, and Kurt Broderick for their invaluable support in navigating technical intricacies, including fabrication, characterization, and explaining complex technical concepts. Whether it was helping with performing processes, developing processes, or teaching me about diagnosing the nanofabrication process, they were always a phone call or text away.

To those at Lincoln Laboratories, I thank Kyung-Han (Kyle) Hong for your help with our homebuilt laser and OPAs. I am also very grateful that Vlad Liberman published a paper on aluminum plasmonics as I was able to meet Kevin Ryu and Ilya Prigozhin because of that paper. I look forward to seeing where the ONR program will go.

Outside of MIT, I would also like to thank LightConversion and its support staff, especially Nick Evans, Andrey Serin, and Lucian Hand. Nick, thank you for teaching me the basics of OPA when I was first starting and for finding a non-homebuilt laser source that I could use to perform my research. Andrey, thank you for helping me get a demo unit. Lastly, thank you to Andrey and Lucian for providing a discount to allow us to get the Pharos into our price range. All of these things have allowed me to complete the work shown in this thesis.

Finally, I would also like to acknowledge my funding support from the Department of Electrical Engineering and Computer Science Hewlett-Packard Fund, the National Science Foundation (NSF) Graduate Research Fellow Program under grant number 1745302, the School of Engineering MathWorks Fellowship, and the EECS Communication Lab. The fellowship support from the Hewlett-Packard fund, NSF, and MathWorks has allowed me to work on the projects that interested me. The work presented in this thesis was supported by the Air Force Office of Scientific Research under award number FA9550-18-1-0436, the National Science Foundation CAREER under award number 2238575, the Department of Energy Office of Basic Energy Sci-

ences under award number DE-SC0022054, and Partnership for Innovation, Education and Research (PIER) Hamburg.

Preface

The goal of this thesis is to understand how the nanoantenna platform is a promising candidate for lightwave electronics. I begin by discussing the concepts that are required to understand the work in this thesis (Chapter 2). Chapter 3 is then used to establish the foundation to describe the important aspects of lightwave electronics in nanoantennas, highlighting two applications that are demonstrated in Chapters 4-7. Then in the final chapter, a conclusion on the work demonstrated and directions for future work are discussed.

Contents

List of Figures

List of Tables

Chapter 1

Introduction

The discovery of rectification

The evolution of electronics has been one of the most remarkable journeys in human history. It began with the development of vacuum tubes in the early 20th century which paved the way for the creation of the first electronic computers and radio receivers. The invention of the transistor in 1947 by Bardeen, Brattain, and Shockley marked a crucial turning point. The demonstration paved the way for modern electronics, replacing bulky and power-hungry vacuum tubes with smaller and more energy-efficient semiconductor devices.

Devices that only allow current to flow freely in one direction are known as diodes and can be described through the rectification effect. In 1874, this effect was first discovered by Braun [23] and was explained by Schottky later [24]. Three decades later in 1904, Fleming made the first practical electronic device which was described as a one-way "oscillation valve," known today as a diode. The diode revolutionized electronics by enabling the rectification of oscillating voltages into direct currents using nonlinear elements [25]. Rectification and conversion of high-frequency signals to non-zero currents are important because they allow one to measure the field information of very fast oscillating signals at realistic readout rates. Building upon this breakthrough, in 1962, Bass et al. achieved a groundbreaking milestone by demonstrating the optical rectification of light for the first time [26] using a ruby laser (0.432

PHz, 694 nm) with 0.1 μs pulses. Expanding on these achievements, Auston et al. showcased sub-cycle gating using short-lifetime photoconductive silicon in 1975 [27], followed by the realization of electro-optic sampling using the same photoconductive switches just five years later [28]. Two years later, Valdmanis et al. successfully demonstrated these techniques in bulk nonlinear elements [29]. These early demonstrations of converting high frequencies to a signal that could be practically used paved the way for the exploration of terahertz (THz) transients. However, as demands for higher bandwidth electronics grow and the desire to leverage light and light-matter interactions for technological advancements intensifies, the development of devices operating at optical (PHz) frequencies and a deep understanding of light-matter interactions become crucial as conventional electronics have reached the limits of their speed and efficiency.

Researchers are exploring radical new ways of controlling electrons at optical frequencies and one promising approach is based on optical field emission (also known as optical tunneling), which uses the oscillating electric field of light to tunnel-emit charge carriers faster than an optical period of light. This interest in optical field emission is driven by the demand for high-power and high-frequency devices, advances in materials and fabrication, and potential advantages in specific applications. Optical field emission can be realized in various ways, such as in gas [30], dielectrics [18], and at surfaces and interfaces [10], [14], [31], [32]. The Keldysh parameter, defined as the ratio of the tunneling time to half the optical cycle time, was theorized by Leonid Keldysh in 1965 and is a key parameter for predicting the onset of optical field emission [33].

In 2006, Hommelhoff et al. demonstrated optical field emission from a single tungsten tip [31], [34] after recognizing that sharp tips and laser sources have been previously combined in the context of time-resolved scanning tunneling microscopy. This demonstration provided the basis to allow one to conceive experiments and devices that exploit optical field emission. Since then, there have been numerous studies and experimental demonstrations ranging from single-tip emitters in free space [10], [11], [15], [35]–[40], and networks of nanoscale tips on a chip [41]–[45]. These demonstra-

tions of optical field emission have repeatedly shown its use in understanding ultrafast electron transport, strong-field physics, the characterization of ultrafast pulses, showing great potential for on-chip lightwave electronics. Such work is directly relevant to ultrafast sciences and future technologies.

Lightwave electronics

The development and application of ultrafast sciences have repeatedly shown its importance in basic science, applied science, and practical technologies such as, but not limited to allowing for new insights into the behavior of materials and chemical reactions, micromachining, biomedical imaging and surgery, and precision timing technologies. Ultrafast sciences have revolutionized many fields of science and technology and continue to be an area of active research and development.

One direction of great importance that could potentially revolutionize scientific and technological development is lightwave electronics. Lightwave electronics refers to an approach where intense light waves drive electronic processes in materials at speeds far exceeding the limits of traditional electronics. Unlike conventional light-matter interactions, where photons induce transitions between matter states, lightwave electronics harness the light fields to rapidly manipulate electronic states. This concept offers the potential to coherently control complex states in various materials, from semiconductors to individual molecules. However, integrating lightwave electronics faces significant challenges. The mismatch between the ultrafast oscillations of light and the slower clock cycles of electronic systems poses a fundamental obstacle. Current electronic technologies operate at much lower speeds, leading to a disparity of five orders of magnitude in clock rates. Overcoming these challenges is crucial for realizing the full potential of lightwave electronics and achieving seamless integration between optics and electronics.

While various methods have been explored to demonstrate functional lightwave electronics, including graphene-based devices [46], [47], thin-film dielectric currents [18]–[20], [22], [48], and nanoantennas [11], [14], [15], [32], [42]–[44], nanoantennas

have emerged as the most extensively studied platform. This preference is due to their scalability, drastically reduced pulse energy requirements, geometric control, which enables polarization and rectification control, and the subwavelength nature that removes the need for phase matching. The significance of these details will become increasingly evident through this thesis.

In this thesis, I will present work that highlights many of the great advantages of this nanoantenna platform for lightwave electronics. In Chapter 2, I discuss important fundamental principles, starting with the fundamental principles of modelocked lasers, linear pulse propagation, nonlinear pulse propagation, and ending with fundamental principles of strong-field electron emission. This introduction will be sufficient for understanding the subsequent chapters. Next, in Chapter 3, nonlinear processes for lightwave electronics are examined in detail, highlighting why nanoantennas are a flexible platform for lightwave electronics. Specifically, I will show that the nonlinear mechanism (e.g. multiphoton, optical field emission) and the input lightwave, in addition to the geometry of the antenna are crucial to enable precision rectification for control over the electronic frequency response of the devices. This will lay out the theoretical foundation for later sections in this thesis.

Expanding on the groundwork laid in Chapter 3, Chapter 4 focuses on showcasing the shot-to-shot measurement of the carrier-envelope phase employing a non-rectifying nanoantenna architecture. This endeavor was a collaborative effort with Prof. Franz Kärtner at Deutsches Elektronen-Synchrotron (DESY), leveraging a tailored mid-infrared laser source endowed with carrier-envelope phase stability. Just like in conventional electronics, detecting the carrier-envelope phase is crucial for maintaining phase stability in applications and technologies such as the frequency comb or combining waveforms (also known as waveform synthesis). This demonstration paves the way for new potential applications such as creating a compact optical waveform synthesizer over a broad wavelength range; active locking of the carrier-envelope phase of a laser system without the need for bulky setups based on f-2f interferometry or stereographic above-threshold ionization; and enables unthinkable experiments such as trying to use the carrier-envelope phase of a pulse as a medium for sensing or en-

coding information. I will also discuss the potential issues of scalability across various repetition rates.

In Chapters 5 and 6 I will present work that demonstrates that a half-wave rectification configuration results in an electronic harmonic mixer capable of operating at optical frequencies. In conventional electronics, a broadband mixer enables numerous applications such as frequency conversion, information and communication technologies, and signal processing. I will start by introducing the concept of harmonic frequency mixing and experimentally demonstrating such a broadband mixer through a proof of concept measurement of a higher-order harmonic using a lower-frequency optical waveform. I will also study the bandwidth of the optical field emission process through the generation and measurement of a supercontinuum based on soliton self-compression.

In Chapter 7, I will demonstrate an alternative architecture that leverages the inherent polarization sensitivity of the nanoantennas and provides the ability to measure things with polarization and phase sensitivity. Just like in conventional electronics, where polarization is important for signal transmission and reception, antennas and polarization sensitivity play a crucial role in wireless communication and signal quality.

Lastly, I will address some of the current challenges of this platform in the detection and operation at higher frequencies, then conclude with a summary and outlook of the work presented and progress toward scalable lightwave electronics. As the field of lightwave electronics becomes more important, it will be essential to have components analogous to RF components that can operate at optical frequencies.

Chapter 2

Fundamental principles

This chapter serves to bring the reader up to speed by providing the fundamental concepts necessary to understand the use of nonlinear optics and electron emission from metallic nanostructures that will be discussed throughout the remainder of this thesis. This chapter lays the groundwork for understanding laser beam propagation and light-matter interactions. Before beginning to describe linear and nonlinear optics, in the next sections, the following variables will be used:

E	Electric field
H	Magnetic field
D	Electric displacement
B	Magnetic flux density
J	Electric current density
P	Polarization (dipole moment) density
χ	Electric susceptibility
ρ	Electric charge density

Table 2.1: Table of variables and their corresponding symbol.

Laser radiation is treated as an electromagnetic field in a source-free dielectric medium which is described by Maxwell's equations as shown below.

$$\nabla \times \mathbf{E} = -\frac{\partial \mathbf{B}}{\partial t}$$
$$\nabla \times \mathbf{H} = \frac{\partial \mathbf{D}}{\partial t} + \mathbf{J}$$
$$\nabla \cdot \mathbf{D} = \rho$$
$$\nabla \cdot \mathbf{B} = 0$$

Table 2.2: Maxwell equations.

Further relations between the polarization and magnetization densities link the flux density and fields through the following table shown below.

$$\mathbf{D} = \epsilon_0 \mathbf{E} + \mathbf{P}$$
$$\mathbf{P} = \epsilon_0 \chi \mathbf{E}$$
$$\mathbf{B} = \mu_0 \mathbf{H} + \mu_0 M$$
$$\mathbf{J} = \sigma \mathbf{E}$$

Table 2.3: The constitutive relations for Maxwell equations.

where ϵ_0 is the free space electric permittivity and μ_0 is the free space magnetic permittivity, both of which are electromagnetic constants related to the speed of light in vacuum c by $c = 1/\sqrt{\epsilon_0 \mu_0}$.

2.1 Ultrafast Lasers

While there are two generalized classes of lasers, continuous wave or pulsed, the following chapters rely on ultrafast pulsed lasers. In such ultrafast pulsed lasers, a cavity is constructed such that a finite number of monochromatic waves are allowed to exist and propagate. Pulses can be generated through modelocking, where the phases of these traverse modes align to lock and constructively form a localized peak in time.

To illustrate this concept of modelocking, in Fig. 2-1a, three different sinusoidal waves of differing frequencies are shown. In the green trace in Fig. 2-1b, the three sinusoidal waves are summed together, demonstrating that when all the sinusoidal waves are in phase, the formation of a localized peak in time occurs which consists of the three frequencies. However, when these sinusoidal waves are not in phase, a peak occurs but with alternating signs and is not as high intensity.

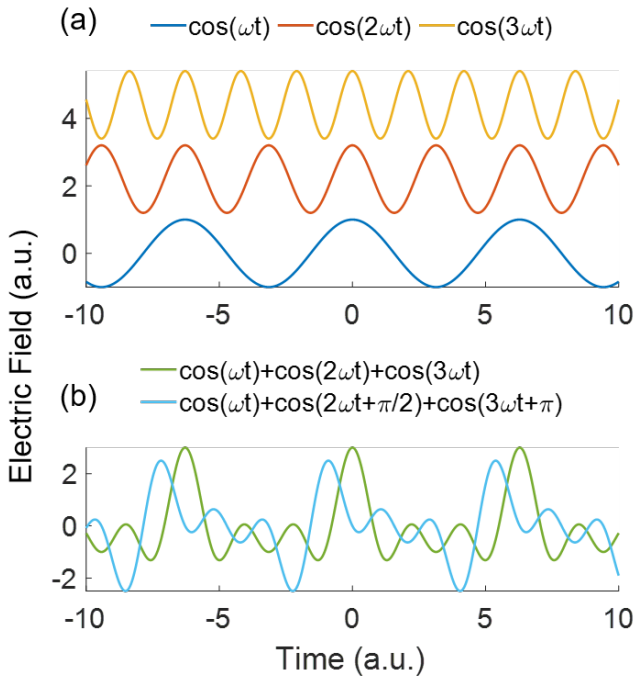

Figure 2-1: **Illustration of modelocking.** (a) Three different frequencies of integer harmonics. (b) Demonstration of what happens if the three frequencies are summed without any phase shifts (green) and with integer phase shifts. In essence, the condition of modelocking requires that the different frequencies add up constructively.

In modelocked lasers, shorter pulses can be made by adding additional frequency components that are in phase. The limitation to how short of a pulse can be described through the time-bandwidth product (TBP) and is also known as a Fourier-transform-limited pulse. TBP $= \Delta f \Delta t$. Depending on the shape of the pulse, the TBP itself can differ. In the real world, to lock different modes constructively, there are different types of mechanisms such as Kerr lens modelocking or additive pulse modelocking. Regardless of the modelocking mechanism, the control of dispersion is crucial to ultrafast pulse formation. Further details on modelocking can be found in [49].

2.1.1 Optical phase (Carrier-envelope offset phase)

An optical pulse can be conceptualized as a rapid sinusoidal oscillation (the electric field with a carrier frequency f as shown in Fig. 2-2a, solid lines), modulated by a gradually changing envelope function (Fig. 2-2a dashed envelope). Despite often

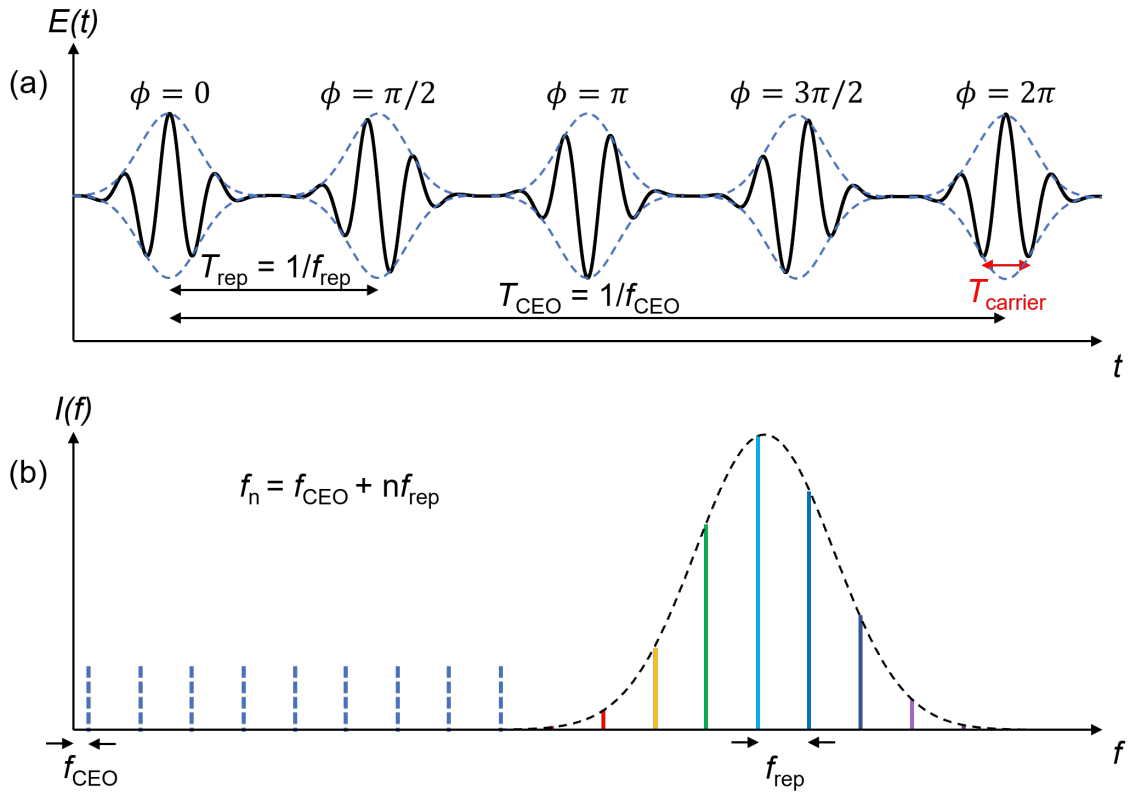

Figure 2-2: **Illustrative time-frequency picture for carrier-envelope phase.** (a) The time-domain depiction showing the varying carrier-envelope phase as a function of time. (b) A frequency-domain picture showing the carrier-envelope offset (CEO) frequency and how the repetition rate dictates the frequency spacing.

being ignored, there exists a relative phase shift between the peak of the envelope and the maximum of the carrier. This phase shift is known as the carrier-envelope phase, and it becomes increasingly important as the envelope approaches just a few optical cycles in duration. Discrete carrier-envelope phase shifts from $\phi_{\text{cep}} = 0$, $\pi/2$, π, $3\pi/2$, and 2π are shown in Fig. 2-2a. Also highlighted is the repetition rate f_{rep} which signifies the time between optical pulses and the carrier-envelope offset time (T_{CEO}) which signifies the time it takes for the carrier-envelope phase to cyclically repeat. This can be better visualized in the frequency domain where the repetition rate f_{rep} dictates frequency spacing of the frequencies contained in the pulse which is also referred to as the frequency comb (lines under the dashed envelope in Fig. 2-2b), whereas the f_{ceo} corresponds to the offset between DC and the first f_{rep} line. Typically, f_{ceo}, and thus the carrier envelop phase, shifts stochastically as a function

of time if not stabilized.

The stability of f_{ceo}, and by relation the stability of the carrier envelope phase, is important for realizing control over light waves. Active control over the f_{ceo} is crucial for spectroscopy applications (e.g. frequency combs), optical waveform synthesis, and ultrafast field-sensitive processes such as those used in lightwave electronics. In field-sensitive processes, the f_{ceo} is typically important when a pulse consists of a few optical periods as the phase shift is even more pronounced in the time domain.

2.2 Linear pulse propagation

To begin describing what happens when a pulse propagates, a monochromatic plane wave with the following electric field will be used $E(z,t) = E_0 e^{i(\Omega t - kz)}$.

In a vacuum, the wave will propagate with a phase velocity (v_p) c and has the wavenumber $k = \Omega/c$ where $\Omega = \omega + \omega_0$ (rewritten as $\omega = \Omega - \omega_0$). Once the wave passes through a dispersive material, the phase velocity becomes c/n where n is the refractive index, a ratio of the speed of light in a medium relative to its speed in a vacuum. The wavenumber in a dispersive medium becomes $\Omega n/c$.

Typically, dispersive media have a different refractive index as a function of frequency. It is easiest to illustrate what occurs in linear pulse propagation by utilizing linear system theory. First, the time-domain electric field $E(z,t)$ is transformed into the frequency domain and becomes $\tilde{E}(z,\omega)$ through Fourier transformation, then interacts with a system $\tilde{H}_{\text{sys}}(\omega)$ (directly related to the refractive index), and using the inverse Fourier transformation to obtain the time-domain fields. Here, the Fourier transform is defined as $\tilde{E}(z,\omega) \equiv \mathcal{F}[E(z,t)] = \int E(z,t) e^{(-i\omega t)} dt$ and $\tilde{H}_{\text{sys}}(\omega)$ will be referred to as the transfer function.

An optical pulse consists of a continuous superposition of monochromatic plane waves which are grouped around the center frequency ω_0. Each frequency component has its own phase velocity depending on the dispersive medium, which leads to phase shifts between adjacent frequency components. The phase in discussion is $k(\omega)$ multiplied by a certain thickness which will be denoted as z so $\varphi(\omega)$ can be defined.

Shown in Fig. 2-3 is an example of what happens to a pulse before and after it passes through some dispersive medium $n(\omega)$.

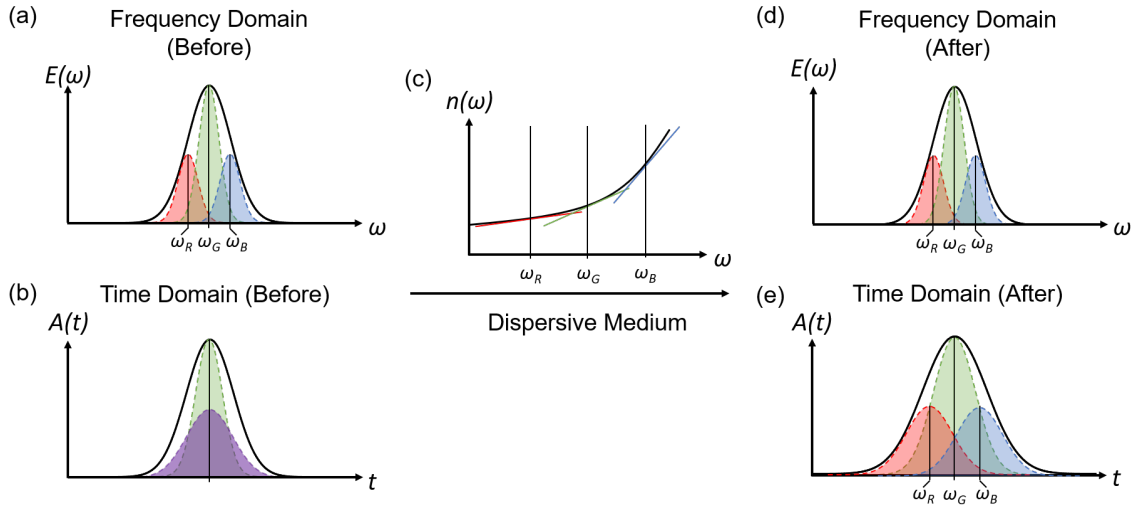

Figure 2-3: **Illustrative figure on linear pulse propagation.** (a) Corresponds to the pulse in frequency and (b) time before passing through a dispersive medium. In the frequency domain, the red, green, and blue sub-pulses correspond to the different frequencies contained within the pulse. In the time domain, the red and blue pulses overlap such that there is a green color sub-pulse and a purple sub-pulse. (c) An arbitrary dispersive medium with different slopes at the red, green, and blue frequencies highlighted. Then after passing the arbitrary dispersive medium, (d) the pulse in the frequency domain remains unchanged. (e) In the time domain, the three frequencies spread out in time due to the dispersion. Not to scale. Adapted from [50].

One can take $\varphi(\omega)$ and perform a Taylor expansion to gain an intuitive understanding of how the different type of phase plays a role in dispersion.

$$\varphi(\omega) = \varphi(\omega_0) + \underbrace{\left(\frac{\partial}{\partial\omega}\varphi(\omega)\Big|_{\omega_0}\right)}_{T_g(\omega_0)} \cdot\omega + \underbrace{\left(\frac{1}{2!}\frac{\partial^2}{\partial\omega^2}\varphi(\omega)\Big|_{\omega_0}\right)}_{D_2(\omega_0)} \cdot\omega^2 + \underbrace{\left(\frac{1}{3!}\frac{\partial^3}{\partial\omega^3}\varphi(\omega)\Big|_{\omega_0}\right)}_{D_3(\omega_0)} \cdot\omega^3 + \ldots \tag{2.1}$$

The first term $T_g(\omega_0)$ corresponds to group delay which provides a tremendous amount of insight into the dispersion induced by an optical element. It is the time delay experienced by a pulse and has the unit of fs. The second term $D_2(\omega_0)$ corresponds to the group delay dispersion (also known as second-order dispersion) and is responsible for how a medium affects the duration of an optical pulse as it can cause

frequencies within the pulse (sub-pulses) to change temporally (bandwidth, location in time) to the envelope. It has the unit of fs^2. Lastly, $D_3(\omega_0)$ corresponds to the third-order dispersion and results from the frequency dependence of the group delay dispersion, it quantitatively describes how the GDD changes depending on which frequencies are considered.

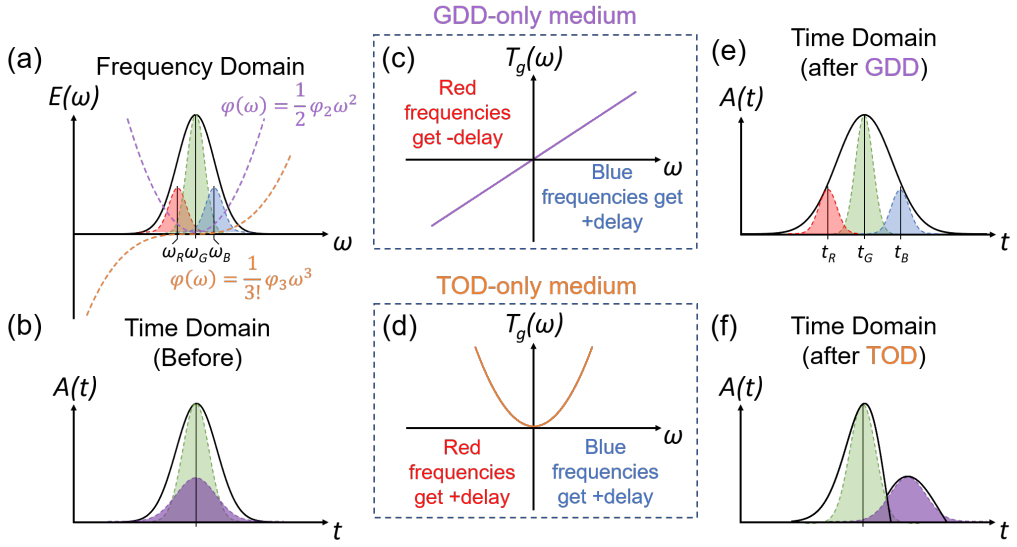

Figure 2-4: **Intuition on group delay.** Illustration of a pulse with its corresponding (a) frequency- and (b) time-domain representation. In (a) the frequency domain shows in the dashed lines a GDD-only phase (purple) and a TOD-only phase (orange). In the middle are two different media, one with the (c) GDD-only phase and the (d) TOD-only phase plotted as the corresponding group delay as a function of frequency. (e) After passing through the GDD-only material, the pulse in time is shown with the red, green, and blue frequencies shifting in time, ultimately broadening the pulse. (f) Whereas when passing through the TOD-only material, the red and blue frequencies shift in time resulting in a side lobe in time. Not to scale.

To build an intuition on how phase plays a role in an optical pulse, in Fig. 2-4 are pictorial examples where a pulse is introduced to $\varphi(\omega) = \frac{1}{2!}\varphi_2\omega^2$ and $\varphi(\omega) = \frac{1}{3!}\varphi_3\omega^3$. The group delay is used to provide insight into how the sub-pulses are changed through the phase. In Fig. 2-4a is a pulse in the frequency domain with the sub-pulses shaded in red, green, and blue. The dashed purple curve indicates second-order dispersion $\varphi(\omega) = \frac{1}{2!}\varphi_2\omega^2$ whereas the orange curve indicates third order dispersion $\varphi(\omega) = \frac{1}{3!}\varphi_3\omega^3$. In the time domain, the red and blue pulses overlap such that there is a green color sub-pulse and a purple sub-pulse in Fig. 2-4b. When $\varphi(\omega) = \frac{1}{2!}\varphi_2\omega^2$

is converted to group delay, the parabolic phase becomes linear group delay as shown in Fig. 2-4 c. In Fig. 2-4c, the y-axis line corresponds to the green frequencies which experience a group delay of 0, meaning the green sub-pulse does not change. However, the red frequencies left of the y-axis obtain a negative delay causing them to shift toward negative time whereas the blue frequencies to the right of the y-axis obtain a positive delay causing them to shift toward positive time (Fig. 2-4e).

In the other example where $\varphi(\omega) = \frac{1}{3!}\varphi_3\omega^3$ is converted to group delay (Fig. 2-4d), the corresponding curve becomes a parabola. Again, the green frequencies on the y-axis line experience a group delay of 0. In this case, both the blue and red frequencies experience a positive delay as the group delay is finite and positive due to the parabolic shape. This causes the sub-pulses to shift toward positive time as shown in Fig. 2-4f. Note: the sub-pulses in Figs 2-3, 2-4 are not 1:1 and are only supposed to provide insight into how the second and third-order phase influences the pulse in time.

While the example shown provides some intuition of linear pulse propagation, one may ask at what level of finite GDD, TOD, etc. starts to affect the pulse significantly? Typically, GDD becomes important when GDD $> \tau^2$ and TOD $> \tau^3$ where τ is the pulse duration in full-width at half maximum (FWHM). Such effects play a role in any light pulses but are crucial to ultrafast pulses in the ps- to fs- regime. For further details on linear pulse propagation, refer to [50]

Now that linear pulse propagation has been introduced, one naturally can wonder what is the impact of optical nonlinearities on pulse propagation?

2.3 Nonlinear Optics

Diving into the realm of nonlinear optics, a foundational question emerges: from when and where do these intriguing effects arise? Can everything be deemed nonlinear? The answer is a resounding yes, although, for some materials, the effects are negligibly small, warranting a linear approximation in most cases. Even a vacuum can exhibit nonlinearity [51], [52], but in practice, it is so small that for all intents and purposes,

it can be described as linear. Nonlinear effects in materials emerge due to their nonlinear polarization response, which can deviate from linearity under an applied field (polarization being the dipole field generated from separated charges in the material). This nonlinear material response has the potential to dynamically alter how the material interacts with the optical field, leading to phenomena known as nonlinear optics.

The origins of nonlinear optics can be traced to the generation of the second harmonic of a ruby laser pulse through a quartz crystal in 1961 by Franken and Bloembergen [53]. Today, nonlinear optics is the basis of ultrafast optics, which is an important platform for studying how light interacts with matter on relevant time scales. The fascinating aspect of nonlinear optics is the ability to generate and manipulate light spanning from angstrom to micron in wavelength with attosecond precision. This light can be used to excite or probe certain properties in matter, acting as a flash of light, similar to the length and timescale of the macroscopic property investigated, effectively frozen in time like a photographic camera taking an image of a moving object.

Nonlinear optics provides a formalism to describe and understand how incident light can interact with matter beyond a linear fashion. To begin the description of nonlinear optics, we begin with polarization P:

$$\begin{aligned} P &= \epsilon_0[\chi^{(1)}E + \chi^{(2)}E^2 + \chi^{(3)}E^3 + \dots] \\ &= \epsilon_0[P^{(1)} + P^{(2)} + P^{(3)} + \dots] \\ &= \epsilon_0[P_{\text{Linear}} + P_{\text{Nonlinear}}] \end{aligned} \tag{2.2}$$

where ϵ_0 is the free space permittivity, $\chi^{(n)}$ is the n-th order susceptibility of a medium, and E is the incident electric field. Various sources can contribute to nonlinearities in materials, including motions of bound electrons, field-induced vibrational or orientational movements, optically induced acoustic waves, thermal influences, and other interactions. These nonlinearities can also be conceptually understood through a phenomenological perspective using an anharmonic oscillator model. For example, in this model, the Coulomb force that binds the electron to the nucleus acts akin

to a spring, and the nonlinearity arises from alterations in the spring constant when the spring (i.e., the electron-nucleus separation) undergoes significant stretching or compression.

2.3.1 Second-order nonlinear polarization

To illustrate the concept of nonlinear polarization, consider the second-order nonlinear polarization that emerges when input fields at two distinct frequencies are applied. The input electric field is defined as

$$E(t) = \frac{1}{2}[\tilde{E}_1 e^{-i\omega_1 t} + \tilde{E}_2 e^{-i\omega_2 t} + c.c.] \tag{2.3}$$

The corresponding nonlinear polarization arising from the second-order nonlinear susceptibility can be written as

$$\begin{aligned} P^{(2)}(t) = \frac{\epsilon_0 \chi^{(2)} E^2(t)}{4} = \frac{\epsilon_0 \chi^{(2)}}{4}\big\{\text{SHG} + \text{SFG} + \text{DFG} + \text{OR} + \text{c.c.}\big\} = \\ \text{Second Harmonic Generation (SHG): } E_1^2 e^{-2i\omega_1 t} + E_2^2 e^{-2i\omega_2 t} \\ \text{Sum Frequency Generation (SFG): } 2E_1 E_2 e^{-i(\omega_1+\omega_2)t} \\ \text{Difference Frequency Generation (DFG): } 2E_1 E_2^* e^{-i(\omega_1-\omega_2)t} \\ \text{Optical Rectification (OR): } 2\left[E_1 E_1^* + E_2^* E_2\right] \end{aligned} \tag{2.4}$$

The second-order nonlinearity mixes the input fields resulting in second-harmonic generation, sum-frequency generation (ω_1 + ω_2), difference-frequency generation (ω_1 - ω_2), and optical rectification (zero frequency terms). In second harmonic generation, the two input fields are the same in frequency ($\omega_1 = \omega_2$) and is shown in the Jablonski diagram Fig. 2-5a where the y-axis corresponds to energy and the dashed line corresponds to a virtual state. In this diagram, $\omega_1 + \omega_1$ is excited into a virtual state that relaxes into a new third photon which corresponds to $\omega_3 = 2\omega_1$.

Sum-frequency generation is similar to second harmonic generation (Fig. 2-5b), except that ω_1 and ω_2 are not degenerate, resulting in some higher frequency photon that is not an integer harmonic. In difference-frequency generation (Fig. 2-5c), a

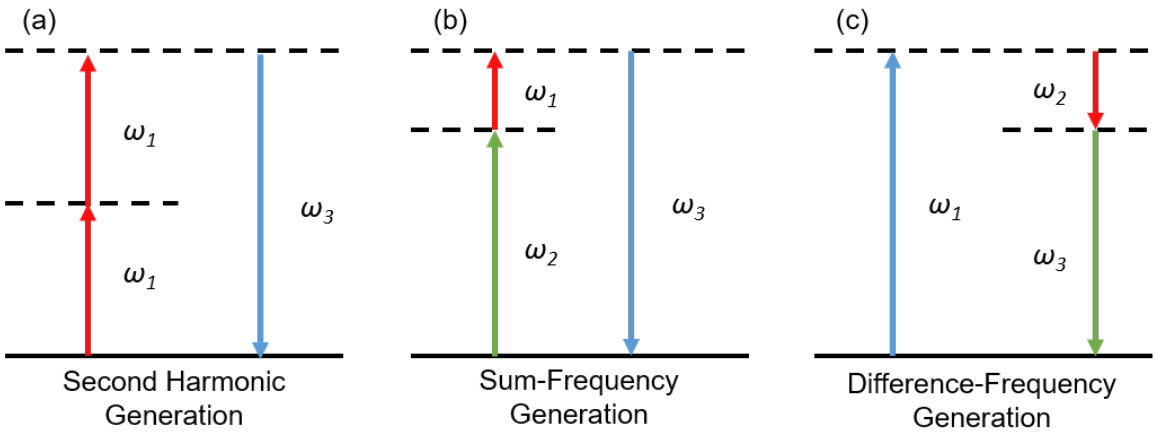

Figure 2-5: $\chi^{(2)}$ **processes.** (a) The Jablonski diagram of second harmonic generation where two ω_1 photons are absorbed to a virtual state (dashed line) and emitted at ω_3. (b) The corresponding Jablonski diagram for sum frequency generation where ω_1 and ω_2 combine to generate ω_3 through virtual states. (c) The corresponding Jablonski diagram for difference frequency generation (ω_3) is depicted as the difference ω_1 between ω_2.

photon is generated from the difference of a high energy photon ω_1 and lower energy photon ω_2, resulting in a new photon at ω_3. The diagram shown here is stimulated, however, spontaneous difference frequency generation, also known as spontaneous down conversion takes one high-energy photon and makes two low-energy photons. This is especially useful for making entangled photon pair sources.

An important concept in generated optically amplified pulses through the second-order non-linearities is called optical parametric amplification (OPA). The scheme for OPA is similar in that a high-energy photon and a lower-energy photon that one would like to amplify are mixed through second-order nonlinearities. This effectively transfers the high-energy photon into two non-degenerate lower-energy photons. Conventionally this is written as $\omega_{\text{pump}} = \omega_{\text{signal}} + \omega_{\text{idler}}$, where the pump is the high-energy photon that amplifies the lower-energy photon known as the signal, which results in the generation of the idler photon due to energy conservation.

Optical rectification can be viewed as difference frequency mixing of optical frequency components contained within a single excitation pulse and is typically used to generate a THz.

Such second-order nonlinear generation is typically done in noncentrosymmetric

crystals such, as a birefringent material, as phase matching is crucial to favorably mix frequencies to generate a new frequency. These processes require that inversion symmetry be broken, so it can be done at air-solid interfaces as well. Phase matching is crucial to the efficiency of the process and for sum-frequency generation is defined as the $k_3 = k_1 + k_2$ or $n_3\omega_3 = n_1\omega_1 + n_2\omega_2$. To maximize the efficiency of the nonlinear generation, the difference between the wavevector of the generated frequency (k_3) should match closely with the sum of the input wavevectors $k_1 + k_2$ in the case of sum-frequency generation, defined as Δk.

2.3.2 Third-order nonlinear polarization

As described above, second-order nonlinearities take two input fields to generate a new frequency and are described by three-wave mixing. With third-order nonlinearities, 3 waves are mixed to generate a fourth wave, hence the process is called four-wave mixing. Typically, all materials have odd-order nonlinearities and such nonlinearity is used heavily throughout this thesis. The third-order contribution to nonlinear polarization is given by $P^{(3)}(t) = \epsilon_0\chi^{(3)}E^3(t)$. The polarization has various frequency components where the simplest being third harmonic generation.

Given an input field $E(t) = [\tilde{E}e^{-i\omega_0 t} + \text{c.c.}]$, the nonlinear polarization is given by

$$P^{(3)}(t) = \epsilon_0\chi^{(3)}\left[(E^3e^{-i3\omega_0 t} + \text{c.c.}) + 3EE^*(E + E^*)e^{-i\omega_0 t}\right] \tag{2.5}$$

where the first term oscillating at 3ω gives the third harmonic contribution. In Eqn. 2.5, the second term oscillating at the input frequency ω_0 has the coefficient that depends on the intensity of the input. This contribution leads to a refractive index that depends on the intensity of the input which is given by $n = n_0 + n_2I$, which is known as the optical Kerr effect, and $n_0 = \sqrt{\chi^{(1)}}$ is the linear refractive index and n_2 is the nonlinear refractive index that is directly linked with the third-order nonlinear susceptibility.

$$n_2 = \frac{3\chi^{(3)}}{4\epsilon_0 c n_0^2} \tag{2.6}$$

To build an intuition on both second and third-order nonlinear polarization, the nonlinear Lorentz model can be used to visualize what is occurring (Fig. 2-6). The equation of motion $\ddot{x} + 2\gamma\dot{x} + \omega_0^2 x + ax^2 = -eE\tilde{(t)}/m$ where $E\tilde{(t)}$ is the applied field, the charge of the electron is -e, the damping force is $-2m\gamma\dot{x}$, and a restoring force $F_{\text{restoring}} = -m\omega_0^2 x - max^2$. With force, one can directly obtain the potential energy function for the noncentrosymmetric medium $U(x) = -\int F_{\text{restoring}}\, dx$, resulting in $\frac{1}{2}m\omega_0^2 x^2 + \frac{1}{3}max^3$. For a second-order nonlinear polarization, the first term corresponds to a harmonic potential whereas the second term corresponds to an anharmonic correction term (Fig. 2-6a). Whereas in a third-order nonlinear polarization, one can utilize the nonlinear Lorentz model with a quartic potential which takes the form $\frac{1}{2}m\omega_0^2 x^2 + \frac{1}{4}mbx^4$ (Fig. 2-6b). For further details of nonlinear polarization, refer to [54].

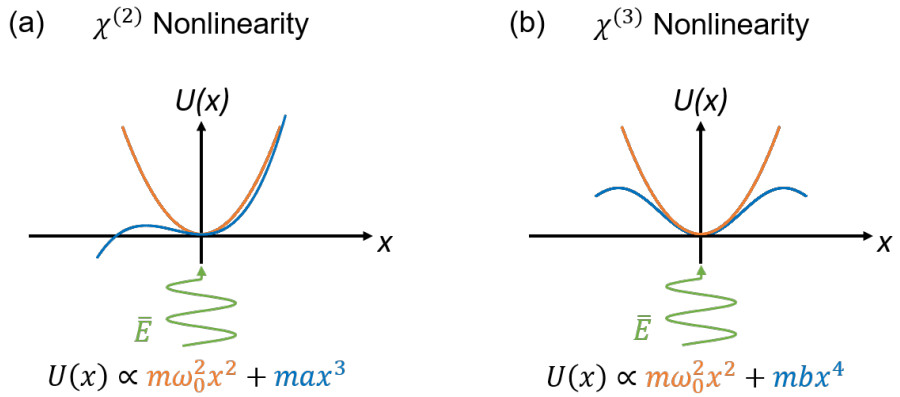

Figure 2-6: **Nonlinear oscillator model.** Visualization of the (a) second- and (b) third-order nonlinear polarization using the nonlinear Lorentz model.

Nonlinear pulse propagation with $\chi^{(3)}$

The Kerr effect results in a change in the refractive index through a high-intensity $I = \frac{1}{2}\epsilon_0 c n_0 |E^2|$ and can lead to self-induced spectral broadening, also known as self-phase modulation (SPM). In 1967, Shimizu reported the first experiment showing mainly SPM. At the time, there were various reports of frequency broadening which was typically attributed to stimulated Raman, Brillouin, and/or Rayleigh-wing scattering. In the experiment, they used a Q-switched ruby laser in different liquids, including

carbon disulfide, where no Raman emission was observed [55].

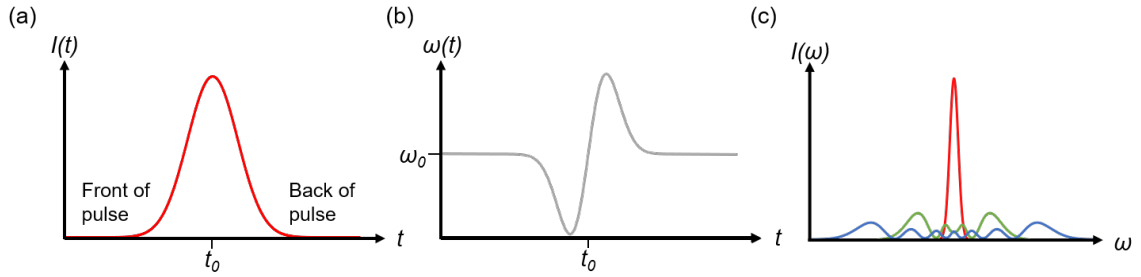

Figure 2-7: **Illustration of self-phase modulation (SPM).** (a) The intensity of a pulse in the time domain. The pulse is sufficiently intense and passes through a material with $\chi^{(3)}$, resulting in SPM. (b) In the time domain, new frequencies are generated where on the y-axis is the frequency. ω_0 corresponds to the initial pulse frequency and in time, new positive and negative frequencies are generated. (c) The frequency-dependent intensity is shown for arbitrary distance traveled in the $\chi^{(3)}$ medium.

When a pulsed laser is used, the changes in laser intensity over time cause SPM to occur temporally. Because the rate of change of the wave's phase over time is just the frequency of the wave, SPM also creates frequency modulation. This results in the output beam appearing with widened spectral characteristics. This nonlinear phase shift corresponds to:

$$\varphi(t) = \omega_0 t - \big[n_0 + n_2 I(t)\big] k_0 L \tag{2.7}$$

where ωt is the frequency of the input field and the second term $\big[n_0 + n_2 I(t)\big] k_0 L$ corresponds to a nonlinear phase shift that is dependent on the Kerr effect over a material length L. A time-dependent phase shift corresponds to frequency modulation. In other words, when the phase of a wave changes over time, it affects the frequency of the wave. By taking the derivative of the phase in time, one can obtain the instantaneous frequency expressed as

$$\omega(t) = \frac{d\varphi(t)}{dt} = \omega_0 - n_2 k_0 L \frac{dI(t)}{dt} \tag{2.8}$$

where the second term generates new frequencies as a function of time. This can be visualized in Fig. 2-7a where the intensity of the pulse as a function of time is shown. If one took the derivative at the front of the pulse, the corresponding change

in frequency would be negative (lower frequency) whereas the derivative of the back of the pulse would result in a positive (higher frequency) frequency change with respect to ω_0.

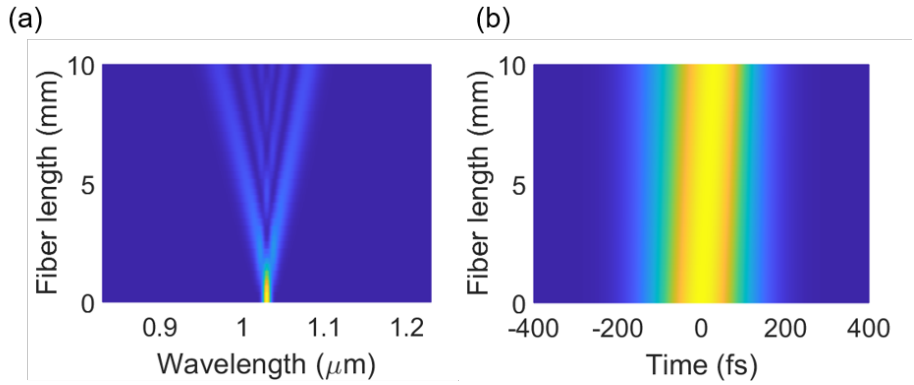

Figure 2-8: **Simulation of SPM in a photonic crystal fiber.** Using a transform-limited Gaussian pulse centered at 1030 nm (0.291 PHz) with a pulse duration of 220 fs, 10 nJ is launched into NKT 1050-ZERO-2, (a) pure SPM dominates as seen in the spectral evolution due to the normal dispersion in the range of the 1030 nm pulse. (b) In the time domain, the output of the fiber results in a pulse that does not change significantly. Although new frequencies are generated, they will need to be compressed externally since the newly generated frequencies lie in the normal dispersion as well.

With pure SPM, the spectral broadening should be symmetric such that in the frequency domain the red- and blue-shifted components are equal as shown in Fig. 2-7c and in Fig. 2-8a. Pure SPM can be achieved as long as the nonlinear index n_2 is large enough for a given wavelength. An example is shown in Fig. 2-8 through a numerical calculation using the nonlinear Schrödinger equation (NLSE). Various textbooks, such as Argawal [56], Boyd [54], or Keller [50] derive the NLSE and describe the equation in greater detail. A Gaussian pulse with a center wavelength of 1030 nm of 220 fs with 10 nJ is launched into NKT 1050-ZERO-2, a fiber with pure normal dispersion (GDD > 0) centered around 1050 nm.

As hinted above, dispersion can play a role in nonlinear generation. For the case of $n_2 > 0$, with no dispersion (GDD $= 0$), the input spectrum will be broadened. When there is $n_2 > 0$ with normal dispersion, the same will occur but the pulse will be stretched in time faster. However, when there is $n_2 > 0$ and anomalous dispersion

(GDD < 0), the chirp generated by SPM can be compensated for while propagating in a medium. If balanced properly, the SPM and anomalous dispersion can result in a situation where a pulse can propagate unchanged in the temporal and frequency domain, thus an optical soliton has formed.

Solitons are solitary waves that maintain their shape and speed while propagating with a constant velocity. The first observation of a soliton in water was in 1838, several decades later in 1895, the mathematical description of waves in shallow water (Korteweg–De Vries equation) was made. Almost a century later, the theoretical prediction of optical solitons from the NLSE was made and finally, in 1980 the experimental observation of optical solitons was made. In the 1990s, soliton control techniques were developed and throughout the 2000s, the role of solitons in supercontinuum generation (a process where laser light is converted into light with broad spectral bandwidth) was uncovered.

If the interplay between SPM and dispersion is right, an arbitrary pulse shape like a Gaussian can propagate and become a soliton that has the shape of a hyperbolic secant. This takes the form

$$A_{\text{soliton}}(z,t) = A_0 \,\text{sech}(t/\tau) e^{-i\varphi_0(z)} \tag{2.9}$$

The dynamics of optical solitons can be complicated as when a pulse undergoes self-compression, the pulse becomes shorter, contributing to higher peak intensity. As the intensity continues to increase, additional nonlinear effects such as self-steepening, stimulated Raman scattering, and higher-order dispersion (HOD) can perturb the pulse. This leads to the splitting of the main pulse into sub-pulses in a process called soliton fission. Depending on the nonlinear effects, many different frequencies can be generated due to Raman or wave-mixing, some of which can result in an incoherent output pulse.

Under certain circumstances, HOD can be used to one's advantage in soliton fission. The presence of HOD alters soliton fission in two main ways. Firstly, as a fundamental soliton moves to longer wavelengths due to the Raman effect, it encoun-

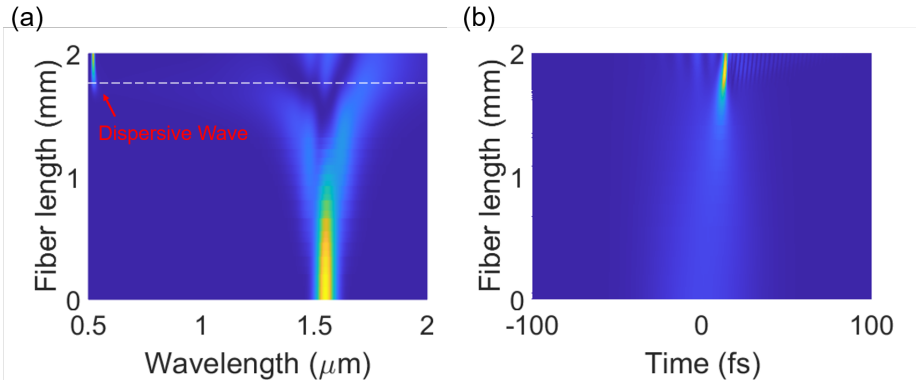

Figure 2-9: **Simulation of dispersive wave generation in a photonic crystal fiber.** Using a transform-limited Gaussian pulse centered at 1550 nm (0.193 PHz) with a pulse duration of 50 fs, 10 nJ is launched into NKT NL-3.2-945, (a) a soliton forms and fission occurs as the pulse propagates through the fiber. Eventually, a dispersive wave is generated at ≈1.7 mm, resulting in the optimal fiber length for the shortest output pulse of 3.75 fs (TFL = 3.25 fs). (b) As the fiber continues to propagate, after the 1.7 mm, interference occurs and more energy is transferred to the dispersive wave.

ters varying values of dispersion, causing its width and power to adjust to maintain soliton integrity. Secondly, HOD can transfer energy from the soliton to a narrow-band resonance in the normal dispersion regime, leading to the development of a low-amplitude temporal pedestal. This energy transfer from the soliton to a narrow-band resonance in the normal dispersion regime is also known as a dispersive wave (DW) and is also called Cherenkov radiation. The position and spectral bandwidth of the DW depend on phase matching between the phase of the soliton and HOD in the material. If done properly, one can generate a coherent supercontinuum consisting of the fundamental soliton, Raman-shifted soliton, and a dispersive wave to get an output with a very short pulse. Further details of these mechanisms are well described in [56], [57].

To demonstrate this, a simulation using the NLSE is shown in Fig. 2-9. In this simulation, 10 nJ of a transform-limited 50 fs 0.193 PHz (1550 nm) Gaussian pulse is launched into 2 mm of an NKT NL-3.2-945 photonic crystal fiber. As the pulse evolves when propagating, new frequencies are generated as shown in Fig. 2-9a. At ≈1.7 mm, a dispersive wave starts to form and results in an ultrashort pulse that is

predicted to be 3.75 fs at the output with a corresponding Fourier-transform limit of 3.25 fs (Fig. 2-9b).

Thus, to compress pulses based on $\chi^{(3)}$, it is crucial to simulate the proposed scheme to understand what is occurring and to properly design the apparatus. As these processes are highly nonlinear, it is far easier to use a high pulse energy, low repetition rate laser in a single-pass scheme to generate new frequencies by SPM and compress later. However, with higher repetition rates, the lack of large pulse energies makes it more difficult to directly generate SPM in a single-pass scheme. Recently, Okamoto et al demonstrated the compression of a Yb laser with 184 fs to 5.7 fs through the use of a single-pass multi-plate scheme [58]. However, in many cases, one can use a nonlinear fiber or a multipass scheme. The multipass scheme is highly attractive as the transmission efficiencies can be engineered to be relatively high depending on the amount of pulse energy available. For further details on multipass compression, one can refer to [59].

2.4 Electron Emission

Photoinduced electron emission is a well-studied phenomenon in optics, dating back over 120 years to its initial observation as the photoelectric effect by Lenard [60]. This effect was later elucidated by Einstein [61]. It was observed that when a high-energy photon strikes a metal surface, a measurable electric current can flow between the metal surface and a positively charged anode.

With the emergence and advancements in ultrafast lasers, research into nonlinear photo-induced electron emission has flourished, enabling breakthrough techniques such as the generation of attosecond pulses via high-harmonic generation in gases and time-resolved angle-resolved photoemission spectroscopy, which enables dynamical studies of atoms, molecules, and condensed matter [9], [62], [63].

Historically, cold field emission, a form of tunnel emission induced by strong direct current (DC) electric fields (i.e. a voltage bias), laid out the foundational work in electron emitter development [64].

In a metal, electrons occupy a range of states up to the Fermi level E_F, following the Fermi-Dirac distribution. When it comes to electron emission, the primary contribution arises from electrons near the Fermi level. There are two dominant mechanisms for DC cold field emitters, (1) Schottky, and (2) field emission where electrons can tunnel and emit.

As one introduces light, there exists traditional photoemission, the most straightforward mechanism, which occurs when the energy of a photon ($\hbar\omega$) surpasses the metal's workfunction (ϕ), allowing an electron from a bound state near the Fermi level to emit (Fig. 2-10a, blue line). The resulting energy of the emitted electron corresponds to$E = \hbar\omega_0 - \phi$. There is also thermal and photo-field emission where electrons are first excited from their original energy level to a higher energy-level state by absorbing thermal energy or photon(s) where they then face a much narrower tunneling barrier (Fig. 2-10b, red line).

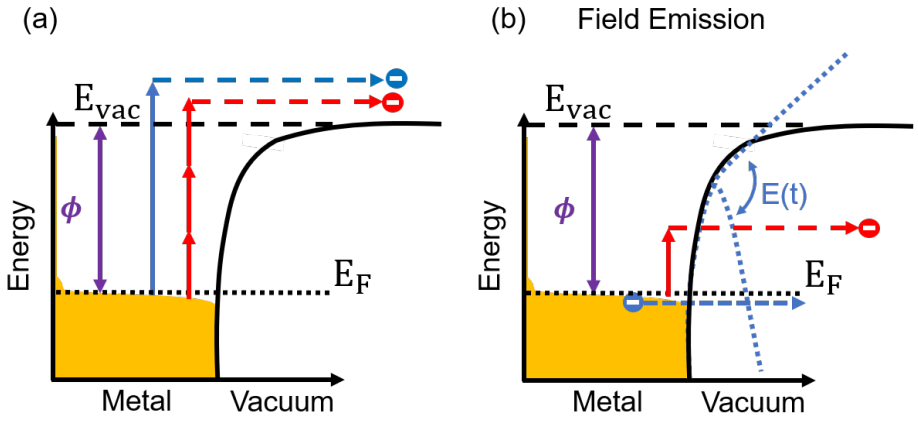

Figure 2-10: **Electron emission mechanisms.** (a) Illustration of two different types of photoemission. In the blue arrow, a single photon with an energy larger than the workfunction is absorbed, and an electron is emitted. In red, three photons are absorbed, resulting in multiphoton emission. (b) Illustration of two different types of field-driven emission. In blue is optical field emission where the optical field modulates the vacuum level. When the barrier is pulled down, the electron can directly emit. In red is photofield emission where a photon is absorbed and the vacuum level barrier is low enough to directly emit.

Upon excitation with an ultrafast optical pulse, a metal can absorb multiple photons at once to emit an electron through multiphoton photoemission. In the mul-

tiphoton photoemission regime (Fig. 2-10a, red line), the emitting surface absorbs a minimum number, n, of photons $\hbar\omega$ to overcome the workfunction. The resulting photocurrent follows a power law, I^n, where I represents the laser intensity and n indicates the number of photons absorbed. The time scale of multiphoton photoemission coincides with the width of the laser pulse.

Much faster electron emission can be achieved through optical field emission, which represents a form of strong-field photoemission where the intense optical fields are sufficient to induce a periodically varying surface vacuum level, as illustrated in the blue lines in Fig. 2-10b. Electrons can tunnel through a narrow barrier from states near the Fermi level during a fraction of the half-optical cycle, thereby enabling the generation of sub-optical-cycle duration electron pulses.

The transition from photon-driven photoemission to optical tunneling occurs with an increase in the optical field strength. The theoretical framework for understanding this transition was originally developed by Keldysh for strong-field ionization in gas-phase atoms and molecules [33]. Later, this framework was extended to strong-field photoemission from solid surfaces by Bunkin and Fedorov, specifically for the emission from metal surfaces [65]. They derived cycle-averaged ionization rates that scale from the multiphoton to the tunnel emission regime. A key outcome of their work is captured by the Keldysh parameter, denoted as $\gamma = \omega\frac{\sqrt{2m_e\phi}}{eE}$, which delineates the dominance of each pathway. Here, m_e represents the electron mass, e denotes the elementary charge, E signifies the electric field amplitude of the optical field, and ω denotes the frequency of the optical field.

Within the Keldysh framework, the parameter γ serves as a crucial discriminator between two fundamental regimes: multiphoton photoemission ($\gamma > 1$) and tunneling emission ($\gamma < 1$), commonly known as optical tunneling. To grasp this concept intuitively, γ can be interpreted as the square root of the ratio between the work function (ϕ) and twice the ponderomotive energy (U_p), where U_p is defined as $e^2E_0^2/(4m\omega^2)$. When the ponderomotive energy surpasses the work function, tunnel emission prevails; conversely, multiphoton photoemission dominates when the ponderomotive energy is smaller.

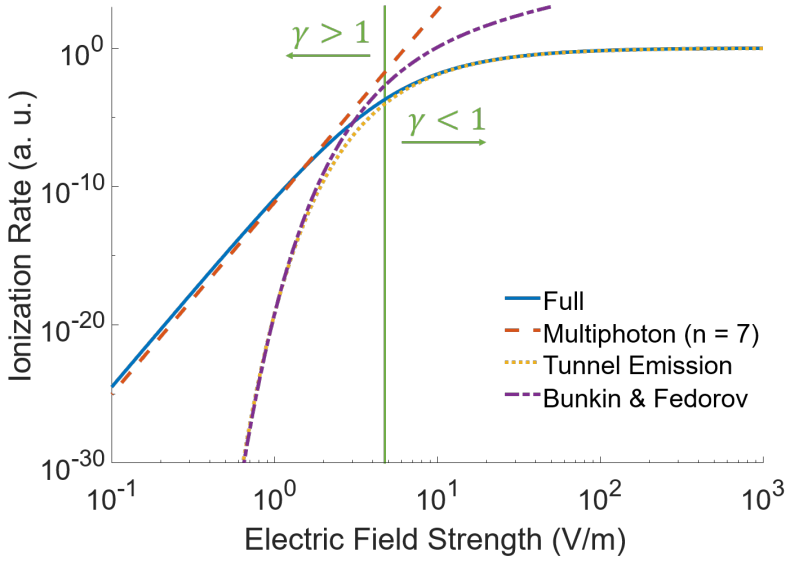

Figure 2-11: **Ionization rates.** Ionization rates versus electric field strength using f = 0.177 PHz and ϕ = 5.1 eV, illustrating the general case, as well as the limit cases of multiphoton and tunnel emission, along with the quasi-static Bunkin and Fedorov. The green line indicates when the Keldysh parameter is equal to 1.

The ionization rates $\Gamma(E)$ for atomic ionization cases for both high and low γ can be closely approximated by a single analytical model (denoted as the general case), which also encompasses the transitional regime when γ is approximately 1 [66].

$$\Gamma(\gamma) \propto \exp\left(-\frac{2\phi}{\hbar\omega}\left(\left(1+\frac{1}{2\gamma^2}\right)\operatorname{arcsinh}(\gamma)-\frac{\sqrt{1+\gamma^2}}{2\gamma}\right)\right). \tag{2.10}$$

This model, provides exponential precision and applies to both limit cases: The limit cases of small and large gamma will yield the known formulas for multiphoton and tunneling emission rates,

$$\Gamma(E) \propto E^{\frac{2\phi}{\hbar\omega}}, \qquad \text{for } \gamma \gg 1 \tag{2.11}$$

$$\Gamma(E) \propto \exp\left\{\left(-\frac{4\sqrt{2m_e}\phi^{3/2}}{3e\ \hbar E}\right)\right\}, \qquad \text{for } \gamma \ll 1. \tag{2.12}$$

For the case discussed in this thesis, we will now limit our case to values of $\gamma \leq 1$ and emission from a metal surface into a vacuum. In the case of nanophotonics dealing with near-infrared (NIR) few-cycle laser and field strength above $10\,\mathrm{V\,nm^{-1}}$,

it was experimentally found that the approximation of quasi-static tunneling emission, corresponding to $\gamma \ll 1$, describes the experimental data sufficiently well [11], [14], [15], [43]–[45], [48].

The quasi-static tunneling rates, initially described for a DC field by Fowler and Nordheim [64], and for AC fields by Bunkin and Fedorov [65], not only provide a robust depiction of the cycle-averaged rates but also allows for the calculation of sub-cycle dynamics. The current density, represented as $\Gamma(E)$ and dependent on the electric field strength E, is expressed as:

$$\Gamma(E) = \frac{e^3}{16\pi^2\ \hbar\phi} E^2 \exp\left(-\frac{4}{3}\frac{\sqrt{2m_e}\phi^{3/2}}{\hbar e E}\right), \tag{2.13}$$

This expression, although similar to the previous approximation, incorporates a quadratic field component as a prefactor. With this equation, the ionization rate dynamically tracks the electric field, enabling the estimation of electron emission within a half-cycle of the electric field. As discussed previously, the highly nonlinear tunneling rate yields an electron pulse significantly shorter than half a cycle when considering an optical field emission. This observation underscores the complete influence of the electric field in shaping the temporal profile of electron emission.

2.5 Conclusion

In this chapter, we have delved into the fundamental principles governing ultrafast lasers, linear pulse propagation, and nonlinear optics. Ultrafast lasers serve as the primary source of lightwaves throughout this thesis. Understanding linear pulse propagation (Section 2.2) becomes essential when dealing with femto- or sub-femtosecond pulses, particularly in the context of dispersion. Section 2.3 provides insight into the nonlinear processes employed in this thesis, where ultrafast pulses are either utilized directly or nonlinearly converted into other frequencies. These lightwaves, ranging into the PHz range, are then harnessed to induce electron emission from nanoantennas, a topic that will be further explored in subsequent chapters.

Chapter 3

Nanoantenna-based Lightwave Electronics

The demand for faster and more efficient electronic devices is constantly increasing in today's interconnected world, where technology plays an ever-expanding role in our daily lives. The push to higher-frequency electronics, such as those operating in the PHz range, is crucial for meeting this demand and driving technological innovation forward.

One of the primary reasons we strive for high-frequency electronics is speed. Higher frequencies enable electronic devices to process information and perform tasks at unprecedented rates, leading to faster communication, data processing, and computation. For example, in telecommunications, higher-frequency electronics allow for faster data transfer rates, leading to quicker internet speeds and more responsive wireless communication networks.

High-frequency electronics open doors to new capabilities and applications that were previously unattainable or inconceivable, vital for pushing the boundaries of scientific exploration and discovery. They facilitate the development of sophisticated instruments for studying complex phenomena at the atomic and molecular levels, providing valuable insights into fundamental scientific questions and driving progress across various disciplines. Thus it is essential for powering the next generation of technological advancements, driving innovation, enabling new capabilities, and expanding

our understanding of the world around us. As we continue to push the limits of what is possible, the pursuit of higher frequencies in electronics will remain a cornerstone of technological progress and scientific discovery.

To develop an understanding of lightwave electronics, this chapter establishes a comprehensive framework that delves into pivotal concepts analogous to conventional electronics such as nonlinear elements, input frequency, rectification, and so on. While the framework discussed here focuses on the fundamental aspects of using optical tunneling in nanoantennas as the nonlinear medium, the significance of nonlinearity is also highlighted and discussed.

First, the examination of the fundamental symmetry inherent in nonlinear emission processes is examined in Section 3.2 through the description of rectification. This general framework is then further applied in the context of nanoantennas in Section 3.3 by describing how geometry dictates rectification and affects frequency bandwidth. Section 3.5 builds upon properties of geometry by describing a key advantage of nanoantennas, the tunability of the resonance in an antenna (i.e. the frequencies for which the antenna can respond). Having described the advantage of geometric control in nanoantennas, another key factor is described in Section 3.6.2, the impact of the lightwave. Following the exploration of rectification, geometric tunability of nanoantennas, as well as the impact of input lightwaves, two distinct applications of optical phase detection and field sampling are outlined briefly. These applications, focusing on no rectification and half-wave rectification, are experimentally investigated in Chapter 4 and Chapters 5-7, respectively.

3.1 Introduction

Lightwave electronics seek to integrate optics and electronics effectively, leveraging the ultrafast oscillations of light. However, a significant obstacle arises from the mismatch between the characteristic frequencies of optical (PHz) and electronic systems (GHz-THz). In pursuit of electronics operating at optical frequencies, various methods have been explored to achieve practical lightwave electronic circuit elements analogous to

those in conventional electronics. In this chapter, the nanoantenna platform will be modeled and forms the basis for the subsequent chapters.

At the core of lightwave electronics is a medium sensitive to light's electric field. One can control two crucial components in the real world: the light used and the interaction between the lightwave and electronic medium. For this reason, nanoantennas have emerged as an attractive option for numerous reasons such as their geometric tunability for control over the electron emission, CMOS compatibility for future scalability, and lateral design for rapid prototyping and testing. First, unlike nonlinear crystals, the nanoantennas have deep sub-wavelength geometries and a very well-defined point electron emission surface in space (*i.e.* one does not need to consider phase-matching). As a sub-wavelength nanoantenna, the shape and metal directly dictate what light can interact with the electrons in the metal. This in practice significantly reduces the energy required for field emission by optical pulses which can reach up to three orders of magnitude, lowering the energy requirement to picojoule levels [45]. They can also be connected in series in an network such that electronic pulses propagate in macroscopic striplines on a millimeter scale [42]. Second, the nonlinear medium is the detector as the light illuminated is converted directly into electrons. This removes the requirement for filtering and enables the investigation of optical pulses with nearly arbitrary spectral content. Third, it is straightforward to control the rectification properties by changing the geometry of the nanostructures.

Beyond the practical scalability and control through the nanoantenna platform, this chapter focuses on the maximum operating frequency achievable, providing insight into how fast lightwave electronics can operate. Like in conventional electronics, control over rectification is crucial when utilizing alternating currents (AC) and voltages. After using optical tunneling based on Fowler-Nordheim tunneling to visualize the importance of rectification, this maximum achievable bandwidth is generalized to n-photon processes. Afterward, the tunability of nanoantennas is highlighted

3.2 Role of Rectification and the Impact on Electronic Frequency Bandwidth

In this section, we delve into the concept of rectification in shaping the electronic frequency response from a theoretical standpoint as it is a crucial function in many electronic devices. In the context of lightwave electronics, rectification refers to the process of controlling which half-cycle oscillations of light contribute to finite emission. As the rectification properties dictate the frequency response, we will examine this step by step, and then apply this to optical tunneling. Additionally, we will generalize our discussion to consider rectification in scenarios involving n-photon processes, shedding light on the broader implications of rectification phenomena.

As an input pulse (also referred to as E_{gate}), generates some response in time and frequency, it is useful to develop an analytical treatment of the effects of emission rate nonlinearity and rectification. This can be done by separating the Fourier-transformed amplitude of the emission $\mathcal{F}(\Gamma(E_{\text{gate}}(t)))$ (referred to as the frequency response throughout the chapter) into two parts: (1) the emission rate Γ; and (2) a rectification function $R(E)$ which is dependent on the field amplitude.

$$\mathcal{F}(\Gamma(E_{\text{gate}})) = \mathcal{F}\{\Gamma_{\text{unrectified}}(E_{\text{gate}}(t)) \cdot R(E_{\text{gate}}(t))\}^* = \tilde{\Gamma}(\omega)^* * \tilde{R}(\omega)^* \tag{3.1}$$

A 3-cycle optical pulse at 0.193 PHz (1.55 μm) is used with a rectification function $R(E)$ (e.g. Heaviside or Signum function) as seen in Fig. 3-1a. This is done to separate the cycle-to-cycle emission rate from the effect of rectification more explicitly to clearly examine the two effects separately to understand how they individually contribute to the overall sampling response. In these examples, only the pure AC response of such geometries is considered (i.e. without any DC field).

Mathematically, the Heaviside function is defined for the field as shown

$$\theta(E) = \begin{cases} 1 & E > 0 \\ 0 & E \leq 0 \end{cases}$$

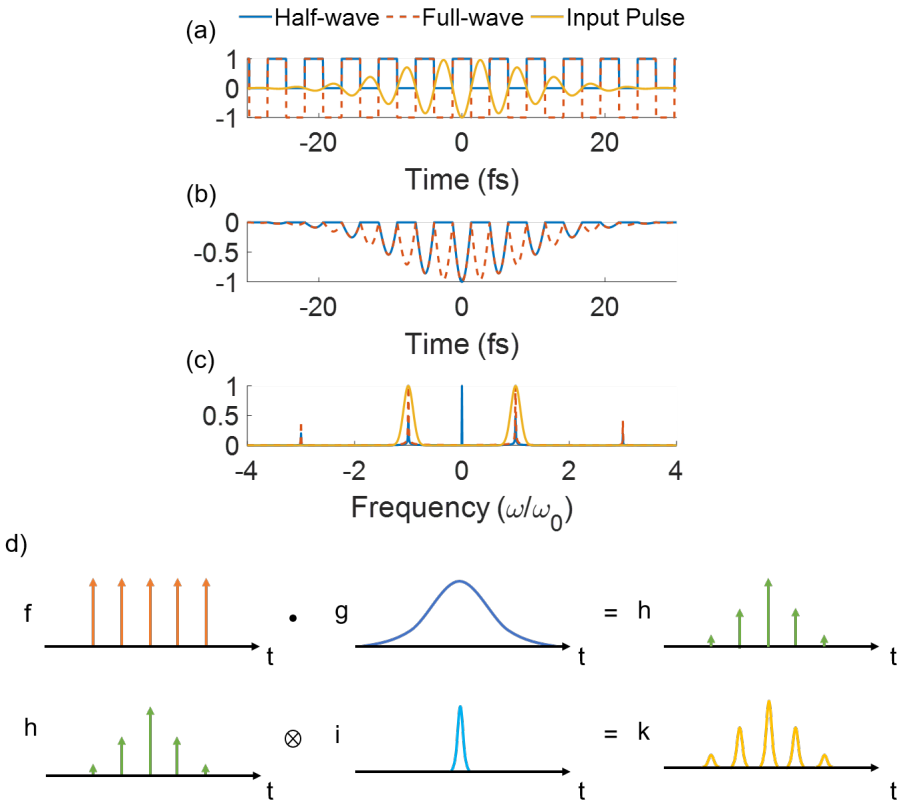

Figure 3-1: **Rectification function.** (a) The time domain representation of the half-wave rectification function (Heaviside function, blue line) and the full-wave rectification function (Signum function, orange dashed line) with a 3-cycle 0.193 PHz (1.55 μm) input pulse. (b) The rectified input pulse shows that the half-wave response has 0 field at every other half-period whereas in full-wave rectification, all half-periods are rectified. (c) The frequency-domain representation of the half-wave and full-wave rectification, including the input pulse. (d) Illustration on the electronic comb generation in time.

whereas the Signum function is defined for the field as shown

$$\text{Signum}(E) = \begin{cases} 1 & E \geq 0 \\ -1 & \text{otherwise} \end{cases}$$

Notably, in the half-wave rectification, there is 0 field at every other half-period whereas in full-wave rectification, all half-periods are rectified. This can be seen in Fig. 3-1c where at f = 0 is a peak, whereas in the full-wave rectification peaks only exist at odd integer harmonic frequencies. To get the full transfer function $H(\omega)$,

one needs to convolve the rectification function with the input pulse which will be discussed below.

The emission can be seen as the multiplication of a comb in time with the peaks separated depending on the device geometry. With an asymmetric design, the spacing is the optical period of the gate frequency. Mathematically, it can be described as the following:

$$\begin{aligned} h(t) &= f(t) \cdot g(t) \\ k(t) &= h(t) * i(t) \end{aligned} \tag{3.2}$$

In time, a comb (f) is generated and the amplitude of the comb follows an envelope function (g), resulting in h and is purely dependent on the gate-dependent localized electric fields at the tip. Then, h is convolved with the electron emission rate envelope with finite bandwidth (i) which is directly related to the optical period of E_{gate}.

To illustrate the importance of rectification, we utilize a single-cycle pulse (the dashed line shown is the Fourier-transformed amplitude of the single-cycle pulse) to illustrate the maximum achievable frequency bandwidth (Fig. 3-2). Schottky and Fowler-Nordheim tunneling is shown as two mechanisms for optical tunneling, in addition to generalizing to an n$^{\text{th}}$ order photon process.

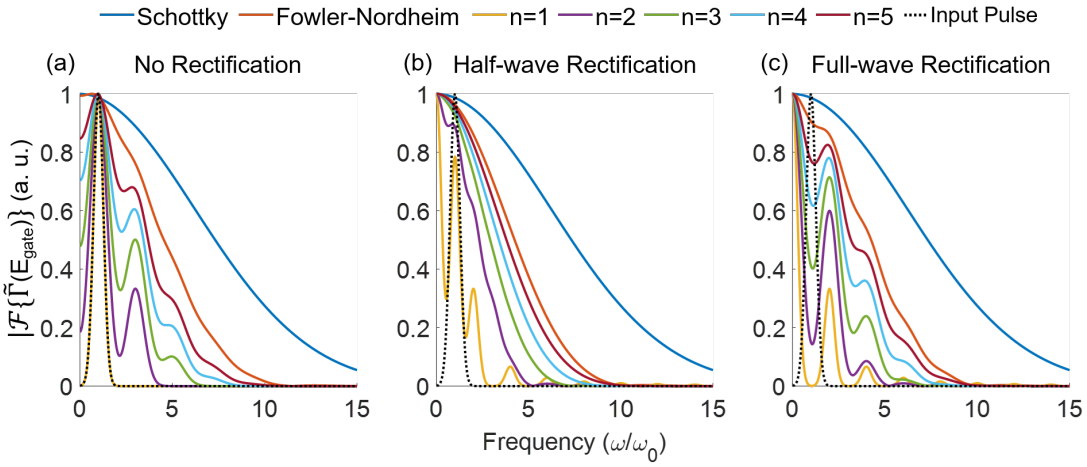

Figure 3-2: **A comparison of non-rectified and rectified Fourier-transformed amplitudes of the emission rate for optical tunneling and n$^{\text{th}}$ photon order processes as a function of frequency.** (a) No rectification (b) Half-wave rectification, and (c) Full-wave rectification

We begin with the $n = 1$ (yellow) case where in Fig. 3-2 we show what happens to the frequency bandwidth as we change $R(t)$. For the case of no rectification in Fig. 3-2a, the system response Γ that is linear with the field can be written as

$$\Gamma(F) = \alpha F, \tag{3.3}$$

where α is some constant and F some electric field.

Thus, for a linear detector response, one would only have access to the fundamental component of the signal.

Interestingly, as one adds in rectification (Fig. 3-2b, c), one can see the frequency bandwidth is extended, allowing us to gain information beyond our E_{gate}. This demonstrates that one can do small-signal cross-correlations in an $n = 1$ photon process with the assumption that the experiment measures intensity ($I = E^2$) rather than the field (e.g. a linear photodiode). This is because the rectification provides finite frequency for odd-order harmonics.

Physically, in the final frequency bandwidth, the odd harmonics are provided by the convolution of $\tilde{\Gamma}(\omega)$ and the central $\delta(\omega)$ component of $\tilde{R}(\omega)$ at 0. However, the odd-harmonic components of $\tilde{R}(\omega)$ introduce even harmonic passbands as the convolution of the E_{gate} pulse (yellow line in Fig. 3-3b convolves with each $\delta(\omega)$ component at the odd-harmonics (blue line in Fig. 3-3b). Such a pedagogical example demonstrates the importance of rectification.

3.3 Geometric Architecture Dictates Rectification in Nanoantennas

Optical field emission from nanoantennas depends not only on the local field strength but also when the optical field bends the surface potential downward. By designing the device geometry, which essentially allows one to control the symmetry, the electron emission contribution can be controlled to each half-cycle of the input light (*i.e.* the rectification response).

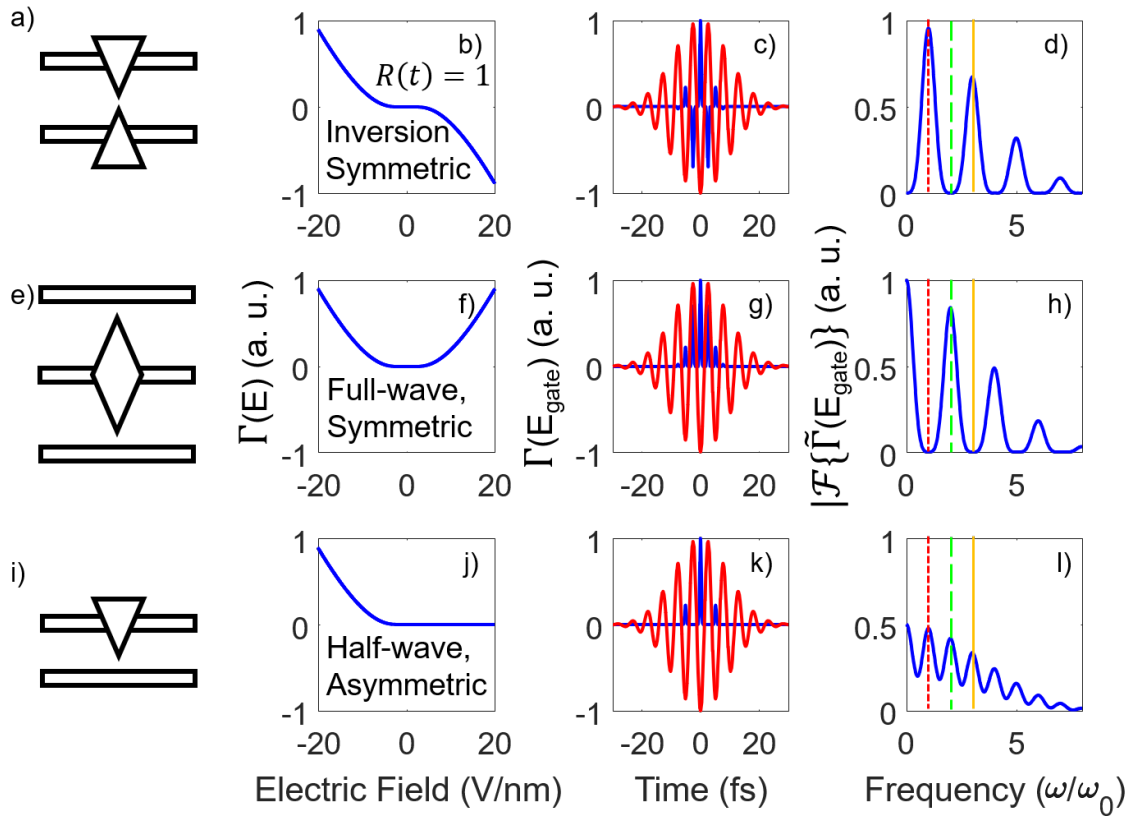

Figure 3-3: **Inversion symmetric device.** (a) Geometric depiction of the inversion symmetric device structure (b) The electron emission rate as a function of electric field strength showing an inversion symmetric response. (c) The electron emission (blue) from a 3-cycle electric field E_{gate} (red) where every half-optical cycle induces electron emission. (d) The corresponding Fourier-transformed electron emission demonstrates the frequency components in the electrons with sensitivity to only even orders due to the symmetric electron emission. The dense red dashed line corresponds to the first harmonic, the less dense dashed line in green corresponds to the second harmonic, and the yellow solid line corresponds to the third harmonic. **Symmetric device** (e) Geometric depiction of the symmetric device structure. (f)The corresponding electron emission rate shows a symmetric response across the origin (0 V/nm). (g) The electron emission (blue) from a 3-cycle electric field (red) where both the positive and negative amplitude electric fields result in finite electron emission of the same polarity. (h) The corresponding Fourier-transformed electron emission demonstrates that the electrons are only sensitive to odd-order harmonics. **Asymmetric device** (i) Geometric depiction of the asymmetric device structure. (j) The asymmetric electron emission rate as a function of electric field strength. (k) The electron emission (blue) from a 3-cycle electric field (red) where only the negative amplitude electric fields result in a finite electron emission rate. (l) The corresponding Fourier-transformed electron emission demonstrates that the electrons are sensitive to all harmonic orders.

Having explored how rectification is crucial to frequency response, it is now essential to consider how the geometric characteristics of an antenna further contribute to this phenomenon. While symmetry provides a fundamental framework for understanding rectification behavior, the specific shape and dimensions of an antenna introduce additional complexities. In this section, we delve into the intricate relationship between antenna geometry and rectification properties, shedding light on how subtle variations in shape and size can significantly impact the performance of rectifying devices. Γ is chosen to be optical field emission (Fowler-Nordeim) for the example shown in Fig. 3-3. Three different nanoantenna device geometries exhibit three possible symmetries of the emitted current response: an asymmetric emission response, symmetric, and inversion symmetric. These different geometries have practical applications in frequency mixing, detecting light, and phase detection.

The simplest case is when one inputs E_{gate} and every half-cycle oscillation contributes to electron emission (no rectification, $R = 1$). Geometrically this occurs with a bowtie antenna with two nanotriangles that are symmetrically oriented with respect to the midpoint of the two tip axes as shown in Fig. 3-3a. The electron emission as a function of the electric field is shown in 3-3b. Its response can be seen to be inversion symmetric about $E = 0$ meaning that negative electric field amplitudes, will result in a positive electron emission response, and conversely, a positive electric field amplitude will result in a negative electron emission response. Fig. 3-3c demonstrates the electron emission response (blue line) when E_{gate} (red line) is illuminated onto such a nanoantenna geometry. When the electric field amplitude is negative, the E_{vacuum} barrier of the top antenna is brought up, but the bottom antenna barrier is brought down such that optical field emission can occur and result in a positive burst of electrons (see blue line in Fig. 3-3c at $t = 0$). When the E_{vacuum} barrier of the bottom antenna is brought up, the top antenna barrier is brought down. In this half-cycle, the output would be a negative burst of electrons (see blue line in Fig. 3-3c at $\pm$ 2.5 fs). Taking the Fourier transform of the derivative of the electron emission rate reveals the frequency response of such sub-cycle electron bursts. For the inversion symmetric device, one can see the response in Fig. 3-3d. Highlighted in the densest

dashed line is the 1st harmonic of E_{gate}, in the less dense dashed line is the 2nd harmonic of E_{gate}, and the solid line is the third harmonic E_{gate}. In this device geometry, the device is only sensitive to even harmonic orders. However, when a DC field is applied, a net electric field is no longer symmetrically distributed around the central axis of the antenna, breaking the inherent mirror symmetry, and two-fold rotation symmetry since the direction of the electric field generated by the antenna depends on the direction of the DC field. This results in the appearance of odd harmonics in the frequency response.

Next, for a symmetric device geometry as shown in Fig. 3-3g, every half-cycle oscillation also contributes to electron emission, however, regardless of the sign of the electric field amplitude, the electron emission results in a positive burst of electrons. A unit cell of such a device consists of two triangles whose bases are attached and have wires near the tips to collect the electron bursts. To model this, one starts with an input that contributes to electron emission every half-cycle oscillation, then multiply the output by the Sign function applied to E_{gate}.

Shown in Fig. 3-3f is the electron emission as a function of the electric field, revealing the symmetric response. The electron emission response (blue), when illuminated by E_{gate} (red), is shown in Fig. 3-3g. Every half-cycle oscillation results in a positive electron emission rate. The Fourier transform of the electron emission results in the frequency response shown in Fig. 3-3h. The same dashed lines are used to represent the first three harmonics and reveal that the symmetric device geometry is only sensitive to odd harmonic orders. Likewise, in the symmetric device, a DC field will also break the mirror symmetry and two-fold rotation symmetry for the same reasons. The breaking of the symmetry results in the appearance of even harmonic orders.

Lastly, for a device that provides an asymmetric response as shown in Fig. 3-3i. Geometrically, an example of a unit cell of such a device is one nanoantenna with a collector wire. The electron emission is only expected for negative amplitude electric fields since that reduces the E_{vacuum} barrier and allows for optical field emission to occur. This can be observed in the electron emission response as a function of the

electric field in Fig. 3-3j. To model this, an input that contributes to electron emission every half-cycle oscillation is used, and then the output is multiplied by the Heaviside step function applied to E_{gate}.

The electron emission response (blue), when illuminated by E_{gate} (red), is shown in Fig. 3-3k. It can be seen that for the negative E_{gate} amplitudes, a positive electron emission rate is observed. Taking the Fourier transform reveals that such a device is sensitive to all harmonics with the first three shown. However, the strength of the response is much weaker than in the symmetric and inversion symmetric cases. From this point of view, the asymmetric device is the most enticing for use as a device since it naturally responds to all frequencies. Taking the integral of the three frequency responses reveals the response is constant since the area under the curves is the same.

3.4 Tunability of Nanoantennas

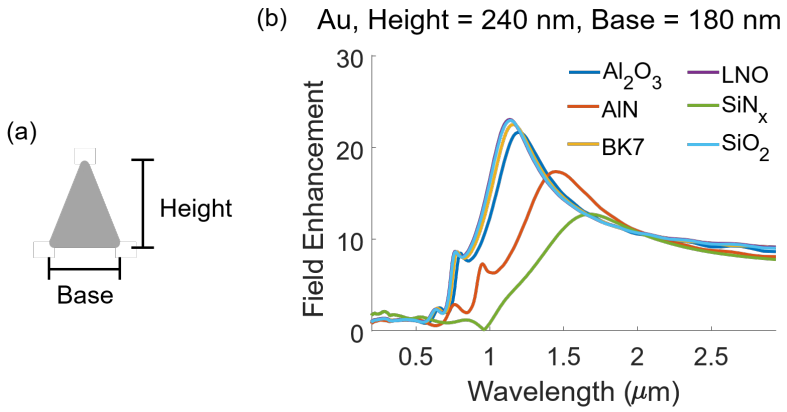

Figure 3-4: **Substrate effects.** (a) Diagram of a nanoantenna showing the definition of height and base used. (b) Electromagnetic simulations with a gold antenna with a height of 240 nm and a base of 180 nm. As the substrate changes, the resonance changes and can result in a lower peak field enhancement for a given geometry. Proper optimization is necessary to obtain the largest field enhancements when operating with minimal pulse energies.

Having explored how the geometric configuration of an antenna profoundly influences its rectification properties, another critical aspect is discussed: the impact of geometry on the peak resonance of the antenna. Just as the structural design of an

antenna determines its rectification efficiency, it also governs the frequency at which the antenna resonates most strongly. By examining how different geometric parameters shape the resonance characteristics, we can gain valuable insights into optimizing antenna performance for specific applications.

The benefit of this nanoantenna platform is the ability to control the resonance, allowing one to get large field enhancements, and ultimately allowing a device to respond to small signals. Finite difference time-domain simulations are performed (FDTD) to better understand how materials play a large role in PHz optical field sampling using a single triangle with a radius of curvature of 10 nm. First, substrate choice is discussed since this is directly related to field enhancement. A gold triangle with 20 nm in thickness, 240 nm in height, and 180 nm in the base for these simulations (See Fig. 3-4a for convention). Based on the local electric field at the interface (defined as the sum of the incident electric field and the reflected electric field), the larger index difference would mean a smaller local electric field. As seen in Fig. 3-4b when the substrate material is varied, it is found that substrates with a larger index of refraction result in a smaller local electric field, reducing the field enhancement. Although this provides some intuitive understanding of how the substrate plays a role in field enhancement, the substrate also can dampen the plasmon which is attributed to the reduction of 5 in field enhancement between silicon nitride (index, n, at 1 μm is 2.01) and aluminum nitride (index, n, at 1 μm is 2.15).

Then, to understand how the geometry of the nanoantennas plays a role in field enhancement, finite-difference-time-domain electromagnetic simulations were run using MEEP [69] (further details can be found in the appendix). It is well known that if the sample size is proportional to the wavelength, it is easier for the photon to scatter and interact. This means that it is very difficult to couple 1 THz ($\sim$ 300 μm) to a sample that is only on the order of 10s of μm. On the other extreme, if the wavelength of the photon is extremely short, the photon will scatter with everything. One would expect as the dimension of the nanoantenna gets smaller, the larger the field enhancement is at the shorter wavelengths. Conversely, as the dimensions become larger, the nanoantenna becomes more resonant with longer wavelengths, meaning that the reso-

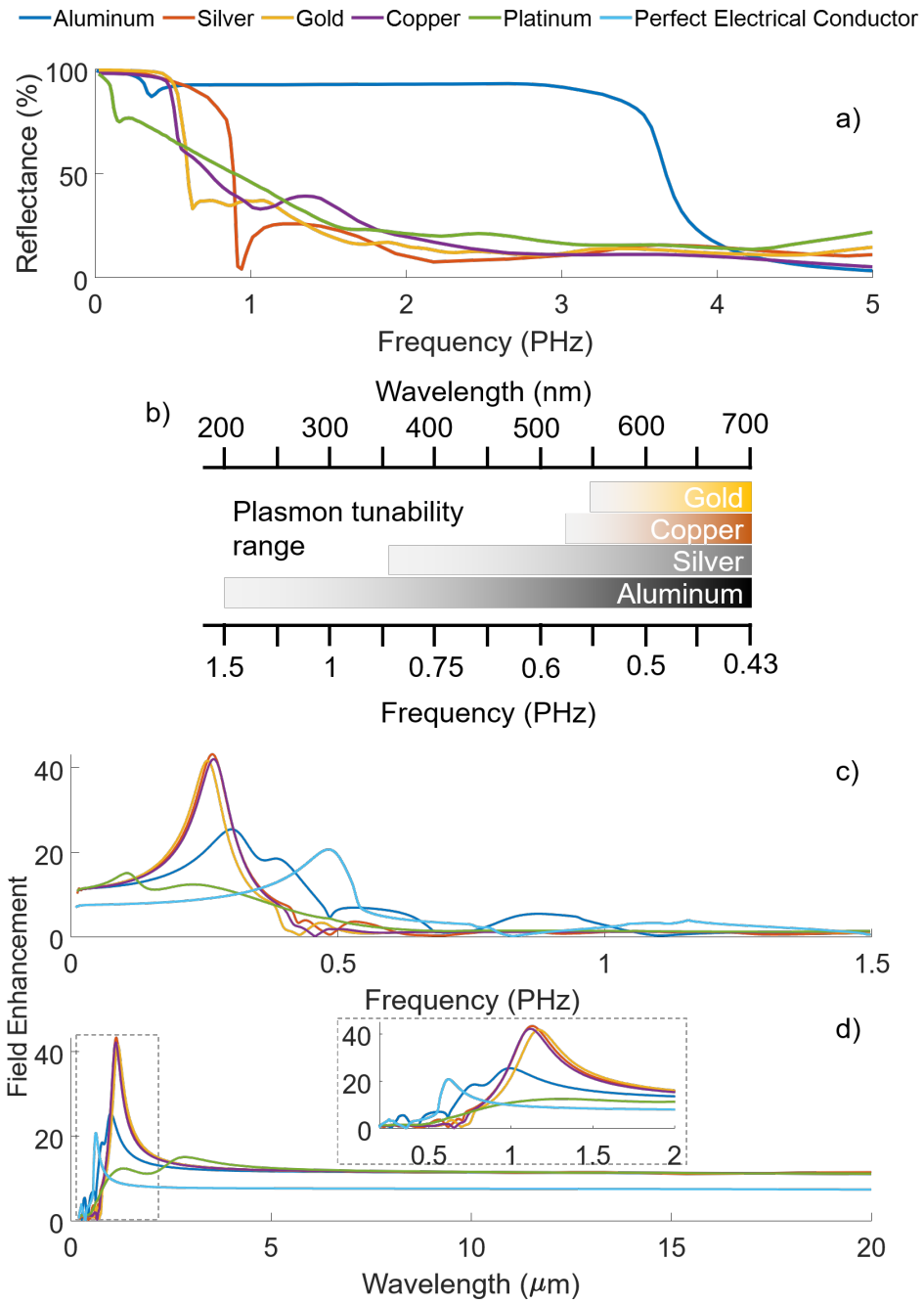

Figure 3-5: **Alternative materials.** (a) Reflectivity of plasmonic metals and platinum (refractory metal) from [67]. (b) The plasmon tunability range of a function of wavelength adapted from [68]. (c) Field enhancement electromagnetic simulations with various metals and a perfect electrical conductor as a function of frequency and (d) wavelength (inset is zoomed into the 0.2 μm to 2 μm range) using an antenna geometry with a base of 240 nm, height of 180 nm, and thickness of 20 nm.

nance shifts towards the longer wavelengths. In metals like plasmonic and refractory metals, such as gold, silver, and copper, resonance shifts towards longer wavelengths as the height increases. This trend is consistent across various metals. Furthermore, when a network of antennas is made, the larger the array, the more long-wavelength can be coupled.

Finally, the choice of antenna material plays a pivotal role in achieving significant field enhancements and realizing practical lightwave electronics. Field enhancement is particularly crucial, as even small pulse energies can lead to substantial intensity enhancements locally at the antenna tip, with enhancements of up to 30× translating to a remarkable 900× increase in intensity. To illustrate the electromagnetic response across various materials, Figure 3-5 presents data on the reflectance of plasmonic and noble metals, the tunability range of plasmonic metals, and electromagnetic simulations of nanoantennas employing these diverse metals, referenced against a perfect electrical conductor (all using the same geometry as shown in Fig. 3-4). In Figure 3-5a, the plot depicts reflectance versus frequency for different metals, sourced from [67]. It is evident that several common metals lack high reflectivity in the ultraviolet regime ($\geq$ 1 PHz), with aluminum being a notable exception, commonly employed for UV-enhanced optical mirrors.

The use of such plasmonic materials imposes a constraint on the achievable frequency range due to practical limitations in fabrication capabilities. Drawing inspiration from [68], Figure 3-5b illustrates the tunability range of plasmons for common plasmonic metals. This is also shown through electromagnetic simulations depicted in Figures 3-5c and 3-5d, showcasing the field enhancement as a function of frequency and wavelength, respectively. Notably, with both perfect electrical conductors and the various metals illustrated, all antennas exhibit responsiveness to low frequencies and long wavelengths. Consequently, it is generally more feasible to engineer lightwave electronics in the infrared spectrum compared to the visible spectrum. Moreover, achieving significant enhancements and responsiveness at higher frequencies poses challenges, as noble or plasmonic metals inherently exhibit limitations in their ability to respond to such high frequencies.

3.5 Impact of Driving Lightwave

Having established the critical role of geometric tunability in shaping antenna characteristics, the other key factor one can control is described: the input light waveform and its influence on the electronic frequency response. While geometric parameters determine the structural properties of an antenna, the shape of the driving waveform profoundly affects its response as well. By examining how variations in input driving waveform and its interaction with various geometric configurations, one can gain a comprehensive understanding of the intricate interplay between antenna design and operational performance.

3.5.1 Frequency

Up to this point, the input frequency for nonlinear emission has been fixed to a specific wavelength. However, the maximum achievable bandwidth is highly dependent on the input frequency. Here, two 5-cycle pulses with frequencies of 0.177 PHz (1690 nm) and 0.353 PHz (845 nm) are shown. Fowler-Nordheim is used as the optical field emission medium for these examples and will provide insight into the theoretical upper limit of the frequency bandwidth optical field emission can provide.

The corresponding Fowler-Nordheim electron emission rate for the two Gaussian pulses is shown in Fig. 3-6b. Since there are several cycles, there are several bursts of electrons that are generated. The inset displays the main burst at $t = 0$, which is modulated by the signal pulse, enabling small signal sampling. The current burst full-width at half maximum (FWHM) determines the time resolution and is 0.28 fs for $f_{\text{gate}} = 0.353$ PHz and 0.55 fs for $f_{gate} = 0.177$ PHz. Lastly, the frequency response given the 10-cycle f_{gate} is shown in Fig. 3-6c. Here, since a 5-cycle pulse is used, there are multiple electron bursts in time, reducing the frequency bandwidth response. If one were using a single-cycle gate pulse, the frequency domain response would result in the envelope without any frequency interference.

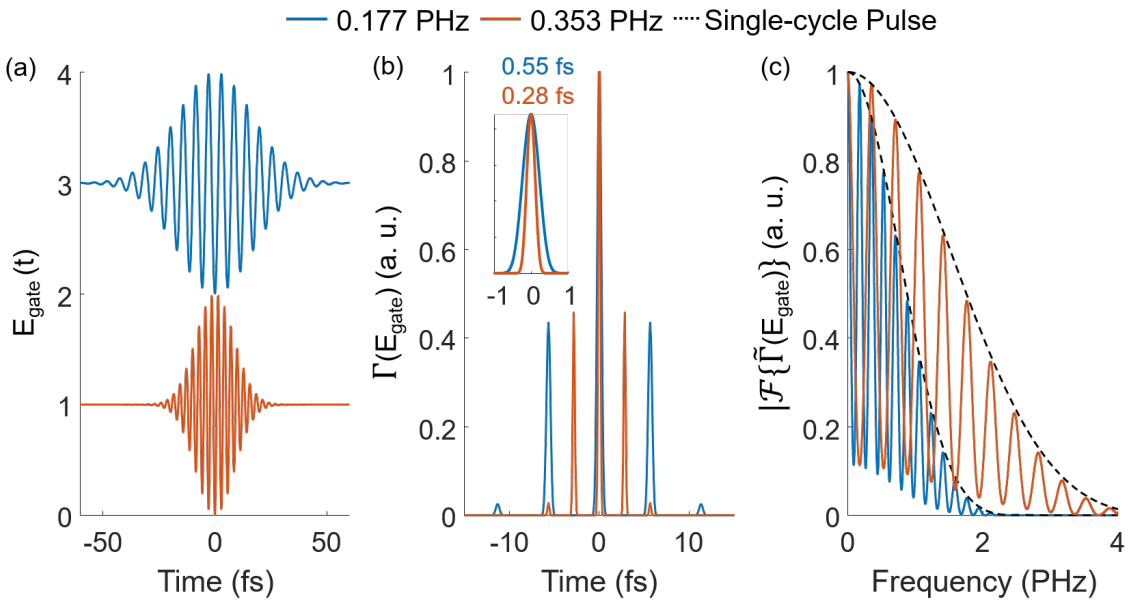

Figure 3-6: **Input frequency dependence of a 5-cycle pulse.** A 5-cycle Gaussian pulse input (a) with a carrier frequency of 0.353 PHz and 0.177 PHz to illustrate the frequency bandwidth dependence when the gate pulse changes. (b) The corresponding time domain emission for the two gate frequencies used. The inset shows the highest intensity time-domain emission which sets the theoretical time resolution. For 0.177 PHz, the FWHM corresponds to 0.55 fs in comparison to half of the optical period of 2.8 fs. For 0.353 PHz, the FWHM corresponds to 0.28 fs whereas the half-optical period corresponds to 1.4 fs. (c) The corresponding frequency response of the emission rate for the two gate frequencies used

3.5.2 Dispersion

In this section, the impact of dispersion in the input electric field E_{gate} on the frequency response $\mathcal{F}(\tilde{\Gamma}(E_{\text{gate}})$ is discussed by fixing the field strengths and changing the dispersion within the pulse. As typical ultrafast lasers do not typically emit transform-limited pulses, this section generalizes what happens when the input lightwave contains significant dispersion.

First, a single-cycle 0.193 PHz (1.55 μm) pulse with half-wave rectification is used with Fowler-Nordheim as the nonlinear emission mechanism, then second- (group delay dispersion, GDD) and third-order dispersion (TOD) are introduced. First-order dispersion (group delay, GD) is ignored as it causes a linear displacement corresponding to a linear phase factor. It should be noted that in these examples, the field is

normalized to 1 which is not realistic as typically when dispersion is added, the field amplitudes will be reduced.

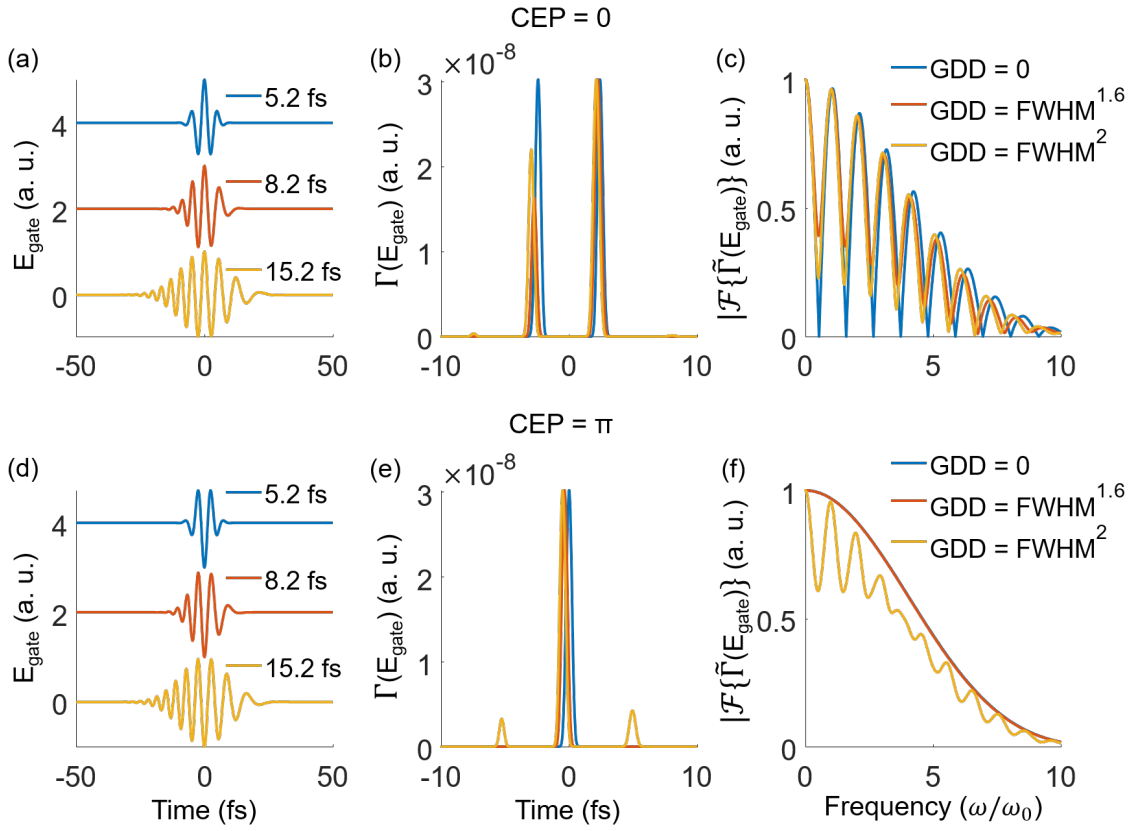

Figure 3-7: **Influence of GDD on nonlinear emission rates.** For CEP = 0, (a) shows the pulse that is used to nonlinearly generate electron emission. (b) The nonlinear emission and (c) the corresponding Fourier-transformed emission, comparing the frequency response as a function of 3 GDD conditions. For CEP = π (d) shows the pulse that is used to nonlinearly generate electron emission. (e) The nonlinear emission and (f) the corresponding Fourier-transformed emission, comparing the frequency response as a function of 3 GDD conditions.

To begin, a pulse with GDD = 0 fs^2, corresponding to a 5.2 fs pulse (Fig. 3-7a, d, blue line), is input into a half-wave rectified device where a negative amplitude electric field generates positive electron emission. The emission rate $\Gamma(E_{\text{gate}})$ is as expected for half-wave rectification (Fig. 3-7b, e, blue line). For the case of CEP = 0, there are two half-period oscillations with negative electric field amplitudes, resulting in the two positive electron emission peaks. In the case of CEP = π, there is only one negative electric field half-period oscillation, resulting in one positive electron

emission peak. The frequency response in both cases reaches up to the 10^{th} harmonic (Fig. 3-7c, f, blue line) but when the CEP = 0, there is finite frequency interference due to the two positive emission amplitudes in time. When +FWHM$^{1.6}$ fs^2 of GDD is added, the pulse stretches to 8.2 fs (Fig. 3-7a, d, orange line). In the case of CEP = 0, there is now an asymmetry in the electron emission rate intensity (54% difference) due to one of the half-period oscillations being 3% smaller in amplitude. Due to this asymmetry, the frequency response results in an increase in bandwidth near the nodes as previously using the transform-limited pulse, the nodes would result in 0 frequency response whereas now the nodes are non-zero. When +FWHM^2 fs^2 of GDD is added, the pulse stretches to 15.2 fs (Fig. 3-7a, c yellow line). When the CEP = 0, there is less of an asymmetry between the two main electron emission peaks centered around $t = 0$. The difference between the negative electric field amplitude is 0.6%, which corresponds to a change in the electron emission rate amplitude of nearly 27%. Whereas when the CEP = π, the electron emission rate now has additional peaks (Fig. 3-7e, yellow line) at -7.5 fs and 7.5 fs that were not observed for the previous two cases. The peak at -7.5 fs has a FWHM of 0.46 fs while the peak at 7.5 fs has a FWHM of 0.58 fs with an amplitude of 1.3× the -7.5 fs peak. In the frequency domain (Fig. 3-7c, f, yellow line), for the case of CEP = 0, the nodes change their position, not reaching 0 like in the case of the transform-limited pulse. With CEP = π, the asymmetry distorts the frequency response from the 2^{nd} to 5^{th} harmonic and the added group dispersion results in an oscillatory group delay smaller than 1 fs. This example highlights how CEP and GDD can change the emission rate and how that change translates to the frequency response.

Next, the impact of TOD on the electron emission rate will be illustrated. To begin, +FWHM^2 fs^3 of TOD is added as represented by the blue line in Fig. 3-8a, d. There is some asymmetry in E_{gate} due to the TOD and this asymmetry does not affect the electron emission rate (Fig. 3-8b, e blue line) in time or the frequency response (Fig. 3-8c, f, blue line) in both cases of CEP. This is because the nonlinearity is thresholded and only electric field amplitudes that are greater than the threshold can contribute to a finite emission rate, characteristic of nonlinear generation. As the

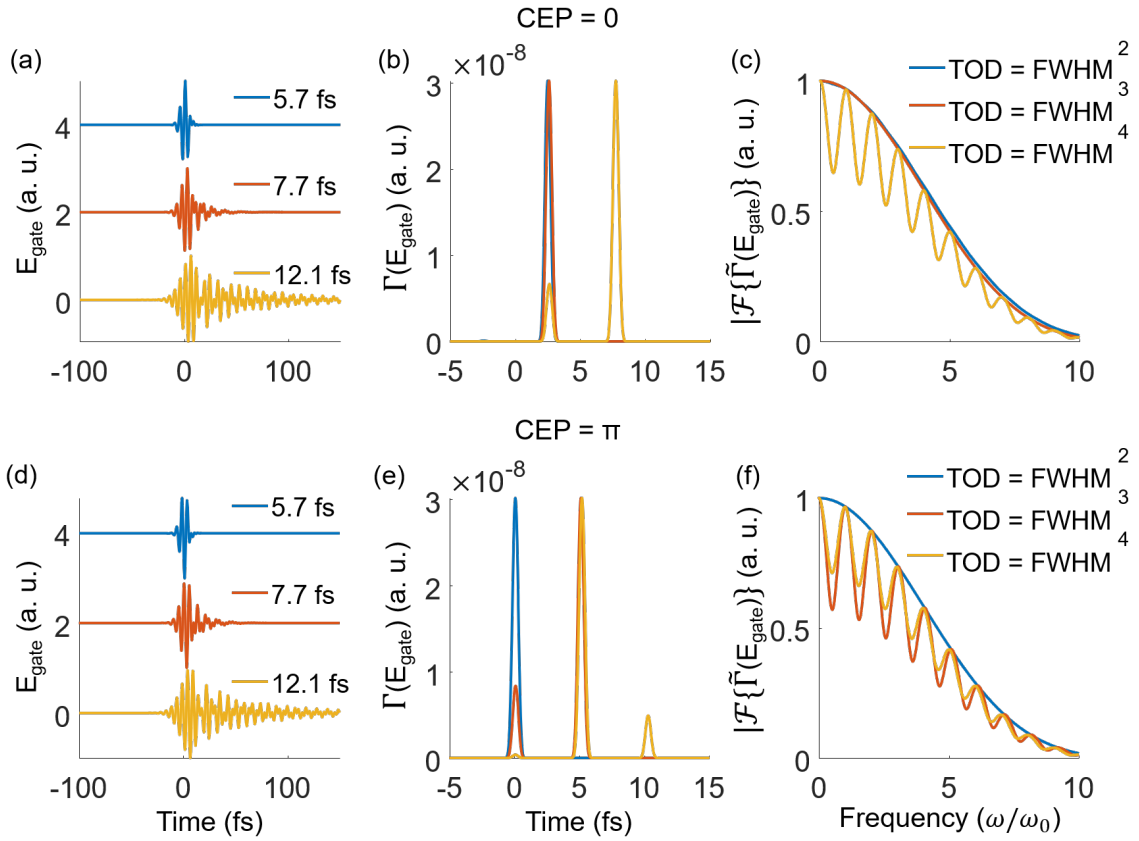

Figure 3-8: **Influence of TOD on nonlinear emission rates.** For CEP = 0, (a) shows the pulse that is used to nonlinearly generate electron emission. (b) The nonlinear emission and (c) the corresponding Fourier-transformed emission, comparing the frequency response as a function of 3 TOD conditions. For CEP = π (d) shows the pulse that is used to nonlinearly generate electron emission. (e) The nonlinear emission and (f) the corresponding Fourier-transformed emission, comparing the frequency response as a function of 3 TOD conditions.

TOD is set to +FWHM^3 fs^3, the pulse has small side lobes and for CEP = 0, this does not affect the electron emission rate or corresponding frequency response, but for CEP = π, an asymmetry appears in the electric field (Fig. 3-8de orange line). This results in two finite peaks in the emission rate (Fig. 3-8e, orange line) at $t = 0$ and 5 fs with the same FWHM but an amplitude difference of 72%. These two asymmetric peaks in time interfere in the frequency domain as seen in Fig. 3-8f, orange line. Lastly, TOD = +FWHM^4 fs^3 results in an electric field with many sudden side lobes in the time domain, characteristic of TOD. For the case of CEP = 0, asymmetric electron emission occurs (Fig. 3-8b, yellow line) similarly to the CEP = π case with

+FWHM^3 fs^3 (Fig. 3-8e, orange line) but this time with an amplitude difference of 78%. Whereas for the case of CEP = π and TOD = +FWHM^4 fs^3, it is observed that there are finite emission rate peaks at 0, 5, and 10 fs. The smallest peak at 5 fs is 80× smaller than the center peak at 5 fs whereas the peak at 10 fs is ≈ 6× smaller. 3-8e, orange line. Although there is some asymmetry the FWHM of the emission rate peaks are the same, and the frequency response stays periodic without any distortion as seen in Fig. 3-8f, yellow line. Although the pulse shape may change significantly due to TOD, the electron emission rate stays relatively unchanged when compared to the addition of GDD. However, it should be stressed that the peak field strengths would have to be identical to these examples of normalized peak field strengths.

3.6 Applications Based on Nanoantenna Architectures

Having examined the interplay between geometric tunability and input frequency in shaping frequency response, attention is now given to a compelling application of this versatile antenna platform. First is the application of nanoantennas with no rectification for carrier-envelope phase detection. The second is with and without rectification for small signal detection of optical fields. With the observation of broad frequency bandwidth based on the different architectures shown in Fig. 3-3 and oscillatory behavior in non-single-cycle or dispersed lightwaves in Sections 3.3 and 3.6.2, we can now discuss frequency mixing.

3.6.1 Carrier-envelope phase detection

By leveraging the insights gained from our analysis in previous sections of this chapter and drawing from radio-frequency (RF) electronics, we can discuss the importance of phase detection. Phase plays a crucial role in RF applications such as FM radio, phased-locked loops (PLLs), and radar systems. In FM radio, the phase of the carrier wave determines the instantaneous frequency of the transmitted signal, enabling

the modulation of audio signals for broadcasting. PLLs utilize phase synchronization to track and maintain a constant phase relationship between a reference signal and a voltage-controlled oscillator, essential for frequency synthesis, clock recovery, and demodulation tasks. Radar systems rely on phase coherence for accurate target detection, tracking, and imaging. These examples illustrate the significance of phase in RF communications, where precise phase control is vital for signal integrity, modulation, and demodulation processes. This emphasis on phase control seamlessly transitions to the realm of optics, where phase detection of optical waveforms is equally crucial for ultrafast science applications such as frequency comb generation and optical waveform synthesis.

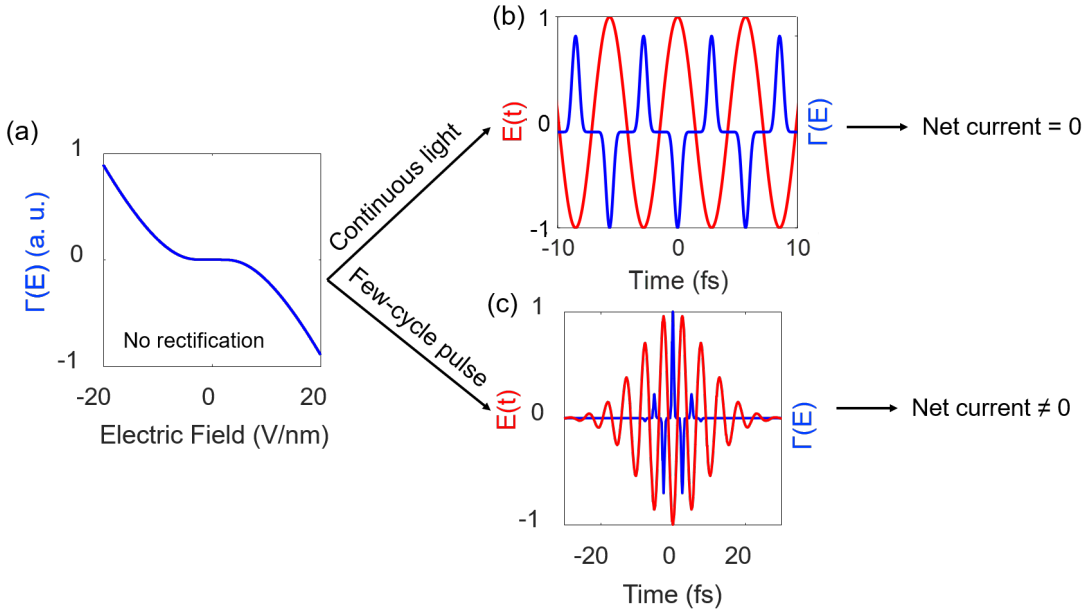

Figure 3-9: **Detection of optical phase using non-rectifying antennas.** (a) With continuous wave light, oscillations (red) lead to a finite electron emission rate (blue). When negative, it produces a burst of finite electron emission, and when positive, an opposite-signed burst occurs. Over time, when integrated, this results in a net current of 0. (b) In a pulsed laser, the varying electric field amplitude as a function of time results in varying electron emission rates which integrates to a finite measurable net current.

As seen in Section 3.5.2, the optical field emission mechanism has a dependence on the carrier-envelope phase. This combined with the key mechanism of non-rectifying antennas enables carrier-envelope phase detection through the emission response of

the antennas (Fig. 3-9a). If we use a continuous oscillating light wave without any rectification, every up-and-down cycle generates electrons (Fig. 3-9b). When the wave's amplitude is negative, it produces a positive electron emission, and vice versa. However, when using a pulsed laser, the electric field shape varies in amplitude during each pulse. As a result, the electron emission can become asymmetric, leading to a finite, nonzero current (Fig. 3-9c). The details will be further discussed in Chapter 4.

3.6.2 Perturbative optical field-resolved sampling

RF mixers play a pivotal role in modern communication systems by enabling the conversion of signals from one frequency to another. These devices are essential for tasks such as frequency upconversion, downconversion, modulation, and demodulation in various RF applications. By combining multiple input signals, RF mixers generate output signals containing frequency components that are the sum and difference of the input frequencies. This capability allows for efficient transmission, reception, and processing of RF signals across different frequency bands, facilitating tasks such as signal amplification, filtering, and signal synthesis. RF mixers serve as essential components in various RF systems, including radio receivers, transmitters, and frequency synthesizers, playing a critical role in the functionality and performance of modern wireless communication networks.

Similarly, the concept of frequency mixing is pivotal in optics. In Chapter 2, we discussed how nonlinear conversion exploits electrons in nonlinear crystals to generate different frequencies. However, these crystals have limitations such as bandwidth constraints and sensitivity to angle dependence. By leveraging the sub-wavelength nature of nanoantennas, we eliminate the need for phase matching. This advancement opens doors to exploring the potential of these antennas in revolutionizing ultrafast spectroscopy through optical field sampling and lightwave frequency mixing. This application serves as a central theme in the subsequent chapters of this thesis, where we delve deeper into the complexities of frequency mixing in the context of optical field sampling.

It was observed in Figs. 3-3, 3-6, 3-7 and 3-8 there are frequency oscillations at specific harmonic orders. These oscillations can be harnessed for frequency mixing, akin to nonlinear electronic frequency mixers fundamental in electronic systems. While conventional mixers operate within a limited frequency range, the extension to PHz would enable comprehensive optical signal analysis across multiple spectra octaves. In Chapters 5-7, PHz harmonic frequency mixing is demonstrated using nanoantennas through optical field sampling, showcasing its capability for complete, field-resolved detection of spectral content beyond conventional techniques. This advancement holds significance for applications requiring spectroscopic analysis or imaging of coherent femtosecond-scale dynamics across multiple harmonics.

It has been demonstrated in the THz and mid-infrared that optical field sampling (also known as time-domain spectroscopy) can provide insightful information such as the dynamics of the contracting or stretching of specific chemical bonds[35], [70]–[73]. This has led to the development and widespread adoption of commercial systems for time-domain THz spectroscopy systems. The importance of time-domain spectroscopy in the THz spectral region has spurred the more recent development of similar techniques for field-resolved detection in the visible to infrared spectral regions. Such measurement techniques are important for understanding dynamical light-matter interactions. Visualizing fields in the time domain rather than the intensity domain offers several direct advantages. Firstly, it allows for direct extraction of phase information from the signal. Additionally, it enables background-free measurements with a large dynamic range (dependent on E_{gate}), facilitates direct visualization of dynamics with relative field strengths, and enables measurement across a broadband frequency range.

Furthermore, field sampling also offers a key advantage over frequency-domain spectroscopy known as the Fellgett advantage or sometimes called the Multiplex advantage, which manifests as an improved signal-to-noise ratio (SNR) in spectra obtained in the frequency domain compared to those acquired in the time domain [74], [75]. This advantage was instrumental in driving the widespread adoption of Fourier-transform (FT) spectroscopy, especially in scenarios requiring precise mea-

surement of weak signals. The essence of the Fellgett advantage lies in the nature of FT spectroscopy as a multichannel method. In the case of Fourier-transform infrared (FTIR) spectrometers, by sweeping the moving mirror in the interferometer, FT spectrometers capture an interferogram that represents contributions from multiple wavelengths simultaneously, effectively measuring every wavelength or channel of the spectrum concurrently. In contrast, in a single-channel dispersive experiment, only one wavelength component's intensity is measured at a time. Consequently, FT spectrometers require significantly less time to acquire the same spectrum compared to dispersive methods. Furthermore, within a given measurement duration, FT spectrometers can average numerous spectra, resulting in an enhancement of the SNR.

The other advantage of field sampling is the throughput advantage, also known as Jacquinot's advantage [75], [76], which arises from the design differences between dispersive and Fourier-transform spectrometers. In a dispersive instrument, light passes through entrance and exit slits in the monochromator, which inherently limits the amount of light that can pass through. In contrast, FTIR spectrometers achieve their throughput advantage by relying solely on the diameter of the collimated beam from the source. While FTIR spectrometers do require an aperture to control the convergence of the collimated beam within the interferometer, this aperture, known as a Jacquinot stop, allows for more light transmission compared to slits used in dispersive instruments. Consequently, for a given resolution and wavelength, the circular aperture of the Jacquinot stop facilitates higher light throughput, resulting in an improved signal-to-noise ratio. These two advantages make field sampling a technique that provides both time- and frequency information.

Now that the importance of field sampling and the role of the input pulse (E_{gate}) in a nonlinear medium has been established, one can bring in a small signal to perturb the emission rate Γ using a measurement system as shown in Fig. 3-10. In the following we mathematically define this small signal field sampling, introducing the transfer function of the sampling response. These concepts will be utilized in Chapters 5-7.

To start, there is some input "probe" or "gate" pulse $\tilde{P}(\omega)$ that is fed into an interferometer with controllable delay τ in one arm. In the other arm, the input pulse is filtered through some system with response $\tilde{A}(\omega)$, such that at the output of the system one has a "signal" pulse of the form $\tilde{S}(\omega) = \tilde{A}(\omega)\tilde{P}(\omega)$. These are interfered together as a function of delay, and the output is recorded on a detector with frequency response $\Gamma(t)$. Note that we will be frequently switching between frequency-domain and time-domain signals and responses wherever convenient. To differentiate between the two, we will always indicate whether the field is a function of time or frequency, and use a tilde to represent a complex value. As an example, the probe in the frequency domain will be represented as $\tilde{P}(\omega)$, but in the time domain as $P(t)$.

Note that switching between frequency-domain and time-domain signals and responses will be done wherever convenient. To differentiate between the two, we will always indicate whether the field is a function of time or frequency, and use a tilde to represent a complex value. As an example, the probe in the frequency domain will be represented as $\tilde{E}_{gate}(\omega)$, but in the time domain as $E_{\text{gate}}(t)$.

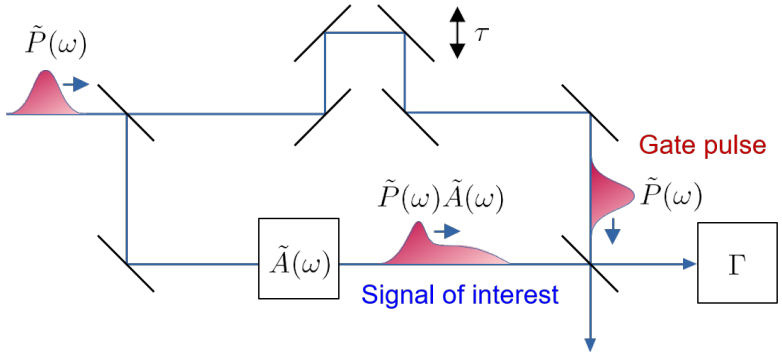

Figure 3-10: **Measurement schematic.** A pulse enters from the left and is split into two parts. One part passes through a delay stage which allows precise temporal control of the two pulses (top), while the bottom interacts with some medium denoted as $\tilde{A}(\omega)$. Afterward, the two pulses recombine on the nonlinear medium for perturbative sampling.

From the measurement system, the user will detect some integrated response I which is expressed as

$$I = \int_{-\infty}^{\infty} q\Gamma\big[P(t-\tau) + S(t)\big]dt. \tag{3.4}$$

While I is the complete response, for much of our analysis below we will examine the strong gate, a weak signal condition where we assume that the signal is weak enough that a first-order Taylor expansion of Γ is sufficient to express I as follows

$$\Gamma(F(t)) \approx \Gamma(P(t-\tau)) + \Gamma'(P(t-\tau))S(t). \tag{3.5}$$

Note that Γ' is the first derivative of Γ with respect to F. Now we can re-write our measured signal as

$$I(\tau) \approx I = \int_{-\infty}^{\infty} q\big[\Gamma(P(t-\tau)) + \Gamma'(P(t-\tau))S(t)\big]dt \tag{3.6}$$

It is useful for us to break equation 3.6 into two parts: the background offset I_{bg}, and the cross-correlation response I_{cc}. These are given as

$$I_{\mathrm{bg}} = \int_{-\infty}^{\infty} q\Gamma(P(t))dt, \tag{3.7}$$

and

$$I_{\mathrm{cc}}(\tau) = \int_{-\infty}^{\infty} q\Gamma'(P(t-\tau))S(t)dt. \tag{3.8}$$

For optical sampling, we are primarily interested in the cross-correlation signal $I_{\mathrm{cc}}(\tau)$ as that provides information about the signal electric field waveform of interest, $S(t)$. To see how, consider the Fourier transform of $I_{\mathrm{cc}}(\tau)$

$$\tilde{I}_{\mathrm{cc}}(\omega) = \mathcal{F}\{\Gamma'(P(t))\}^*\tilde{S}(\omega), \tag{3.9}$$

where the tilde notation represents the complex Fourier transform, and the asterisk represents the complex conjugate. Note that in Appendix A we provide a derivation of the Fourier transform of a correlation for those interested in how this expression was derived.

It is interesting that at this point, one can view the sampling device as an effectively linear device with inputs being the gate field, small-signal field, and delay τ,

having a transfer function given by

$$\tilde{H}(\omega) = \mathcal{F}\{\Gamma'(P(t))\}\big|_{-\omega}, \tag{3.10}$$

and current signal output $I(\tau)$. If the time duration of $\Gamma'(P(t))$ is short enough to be approximated as a delta function (*i.e.* the ideal sampling case), the signal output would simply be $I(\tau) = S(\tau)$.

3.7 Conclusion

In this chapter, the role of rectification was demonstrated and generalized for various nonlinear media. Analogous to traditional electronics, rectification in lightwave electronics is also crucial for the creation of practical lightwave electronic devices. Then, the geometric tunability is discussed, highlighting a key advantage of nanoantennas. In the following chapters, two of the three geometric architectures discussed are utilized, specifically, the non-rectified inversion symmetric devices (Chapter 4) and half-wave rectified asymmetric devices are studied for optical phase detection and frequency mixing in the context of optical field sampling, respectively (Chapters 5-7).

Chapter 4

Nanoantennas Without Rectification for Single-shot Optical Phase Readout

The work presented in this chapter is in collaboration with Dr. Felix Ritzkowsky at the Ultrafast Optics and X-Rays group led by Prof. Franz X. Kaertner at Deutsches Elektronen-Synchrotron DESY. This builds on the inversion symmetric antennas shown in Fig. 3-3a-d and is used for the application discussed in Section 3.6.1. My contributions include the discussions of experiment and design, the fabrication of the inversion symmetric sawtooth antennas, the initial setup of the measurement, and the writing of the manuscript. A portion of this chapter is taken from a submitted manuscript [77] with slight modifications to the writing. Code and data can be found in the following repository: https://github.com/qnngroup/manu-Large-Area-Optical-Frequency-Detectors-for-Single-Shot-Phase-Readout

Abstract

Attosecond science has demonstrated that electrons can be controlled on the sub-cycle time scale of an optical wave, paving the way toward optical frequency electronics [4]. Using controlled few-cycle optical waveforms with μJ of energy, the study of sub-cycle electron emission has enabled the generation of attosecond ultraviolet pulses and the control of attosecond currents inside solids. However, these experiments rely on

high-energy laser pulses and test systems not suitable for integration in microcircuit elements. To move towards integrated optical frequency electronics and their practical applications, a system suitable for integration into microcircuits capable of generating detectable signals with low pulse energies is needed. While current from plasmonic nanoantenna emitters can be driven at optical frequencies, low charge yields have been a significant limitation. In this work, we demonstrate that large-scale electrically connected plasmonic nanoantenna networks, when driven in concert, enable a much higher charge yield sufficient for shot-to-shot carrier-envelope phase detection, which is a hallmark of the underlying sub-cycle processes. We use a tailored sub-2-cycle mid-infrared waveform of only tens of nJ of energy to drive over 2000 carrier-envelope-phase-sensitive electrons from interconnected plasmonic nanoantenna networks that we detect on a single-shot basis using conventional readout electronics. Our work shows that electronically integrated plasmonic nanoantennas are a viable approach to integrated petahertz electronics. By using engineered nanoantenna networks, we show that previous fundamental limits in single-shot CEP detection techniques, such as the energy requirement of gas-based tunnel ionization schemes [78] or the lack of absolute phase sensitivity in f-2f-interferometry can be overcome [79]. This flexible approach to optical frequency electronics will further enable many other interesting applications, such as petahertz-bandwidth electric field sampling and the realization of logic gates operating at optical frequencies [45], [47].

4.1 Introduction

When John A. Fleming developed the first widely usable vacuum diode based on the thermionic emission of electrons from a tungsten filament and showed for the first time rectification of electronic AC signals, he laid the foundation for modern electronics [25]. Around one hundred years later, in the pursuit of ever faster electronics, a major advancement was made by utilizing carrier-envelope phase (CEP) controlled few-cycle pulses to rectify electric fields at hundreds of terahertz at sharp metal tips [8]. This not only demonstrated the generation of rectified, optical-frequency currents but also

demonstrated control over attosecond electron currents by controlling the optical pulse CEP. Subsequent investigations into these emission processes revealed complex attosecond-fast dynamics [9], [80].

To achieve electronics operating at the frequency of optical waves, many methods have been investigated for generating rectified femto- to attosecond currents directly in closed electric circuit elements. For example, by using sub-cycle interband transitions in dielectrics [18], [19], [46], [81], or metallic nanoantennas [11], [14]. These steps toward integrated circuits significantly reduced the experimental requirements from large and bulky vacuum equipment to low-energy ambient operation. Applications exploiting the sub-cycle nature of these currents have been demonstrated. Examples include attosecond-resolution electric field measurements, CEP detection of few-cycle pulses, and petahertz logic gates [11], [14], [18], [21], [22], [45]–[47], [82]–[84]. Specifically CEP detection presents a great testbed for petahertz electronics, as previous methods have been fundamentally limited, such as f-2f-interferometry lacking sensitivity for the absolute CEP or gas-ionization based methods, that do provide absolute CEP sensitivity, but require μJ-level pulses. Resonant nanoantennas have emerged as an attractive option, as they significantly reduce the energy required for field emission by optical pulses and present a physical reference for the absolute CEP [11], [14], [43]–[45], [48]. This reduction can reach up to three orders of magnitude, lowering the energy requirement to pJ levels, while confining electron emission to a well-defined hotspot at the sharp tip of the nanoantenna. Additionally, by exploiting the extreme spatial confinement of nanoantennas, attosecond time-scale charge transport across nanometer-sized junctions has been achieved [15].

While resonant nanoantennas offer several advantages, they also have limitations that impact their practicality. To the best of our knowledge, the electron yield from these nanoantennas has never exceeded one electron per shot in CEP-sensitive yield [8], [11], [14], [44], [45]. As a result, thousands of individual laser shots must be integrated to achieve a statistically significant signal, which means high-repetition-rate laser sources are required. Ideally, enough current would be generated per laser shot for CEP-sensitive readout without the need for averaging. Simply increasing

the peak intensity of the laser pulse cannot scale the signal level of these devices, as this would cause irreversible laser-induced damage. Additionally, scaling up the number of nanoantennas in a single network has been shown to present difficulties as fabrication variance couples to the detected CEP signal and reduces the overall signal strength [44]. Second, large variations of intensity across the network might exhibit CEP vanishing points, that either cause a vanishing CEP signal, when the local intensity hits a waveform-specific resonant intensity, or even causes a π phase shift for intensities above that resonance [43].

In this work, we overcome these issues and demonstrate single-shot detection of CEP-dependent electrons generated by optical tunneling in a fully on-chip nanoantenna device for shot-to-shot carrier-envelope phase detection. We achieve this through the simultaneous excitation of hundreds of interconnected off-resonant metallic nanoantennas [44]. This approach enables coherently-driven, attosecond-timescale electron emission across the entire detector area of $225\,\mu m^2$. Moreover, by employing a custom-developed mid-infrared (MIR) sub-2-cycle laser source [85] we obtain a more than tenfold increase in charge emission per individual antenna compared to previous results, with a CEP-sensitive charge emission as high as 3.3 electrons per shot per antenna [44]. Optical pulses with longer central wavelengths have a proportionally higher electron yield per individual half-cycle compared to their shorter-wavelength counterparts. Additionally, the longer wavelength driver excites the nanoantenna off-resonantly, which enables the full reproduction of the incident electric field at the nanoantenna tip. The off-resonant excitation is crucial, as the number of optical cycles dramatically influences the amount of CEP-sensitive charge produced [44]. Through this combination of short-pulse excitation and scaling of the emitter area, we achieve to the best of our knowledge the highest ever recorded CEP-sensitive charge yield from an integrated petahertz electronic detector and a single laser shot, achieving over 2300 e per laser shot at the full repetition rate of the laser system (50 kHz). The energy requirements of less than 100 nJ represent a reduction of 2 to 3 orders of magnitude compared to alternative gas-phase methods, while removing the need for vacuum conditions [78], [84]. Such devices enable compact, shot-to-shot

CEP detection for various attosecond experiments that require CEP diagnostics [3], [86], [87]. Our work more broadly demonstrates the viability of low-energy, chip-scale petahertz-electronics with single-shot readout.

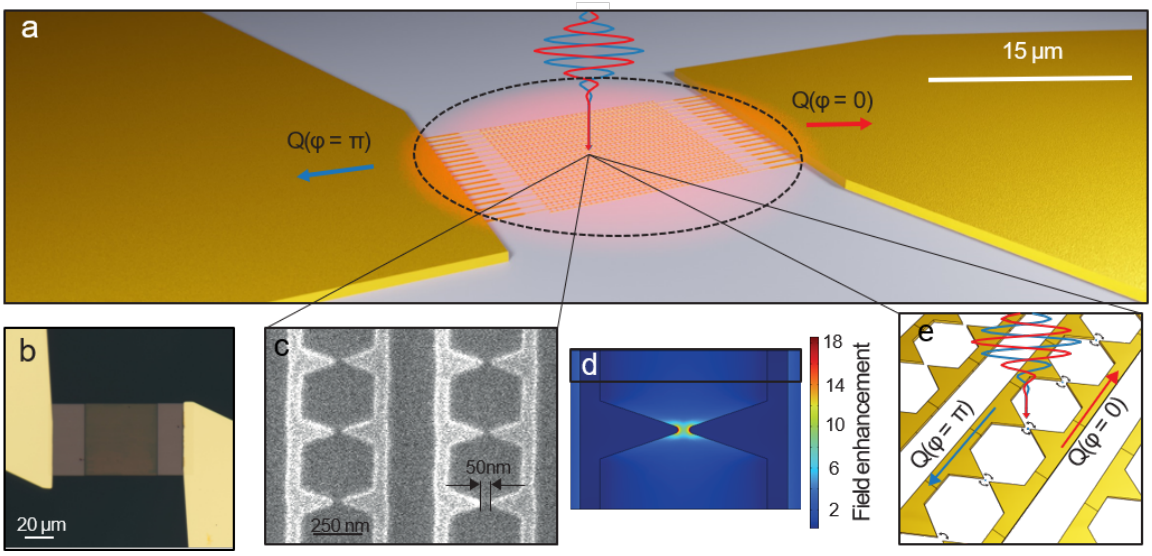

Figure 4-1: **CEP dependent charge generation in nanoantenna networks.** (a) Schematic of the charge generation process in the network showing two electric fields with a π CEP shift corresponding to the charge generated with positive $Q(\varphi = 0)$ or negative sign $Q(\varphi = \pi)$. (b) Optical microscope image of an integrated nanoantenna network contacted with gold leads. (c) Scanning electron microscope image of a metallic nanoantenna network. (d) Finite-element method simulation using COMSOL of the spatial field enhancement distribution of a single antenna pair. (e) Schematic of the nanoscopic emission process, showing the sub-cycle electron currents generated in the antenna-vacuum junction by the driving field.

4.2 Description of the Sub-cycle Field Emission Current

To gain a qualitative understanding of the sub-cycle dynamics of the field emission process, it is useful to simulate the probability of measuring an electron at a given point in time and space outside the metal in a vacuum state. To that end, Yalunin et al. showed that the numerical integration of the time-dependent Schrödinger equation

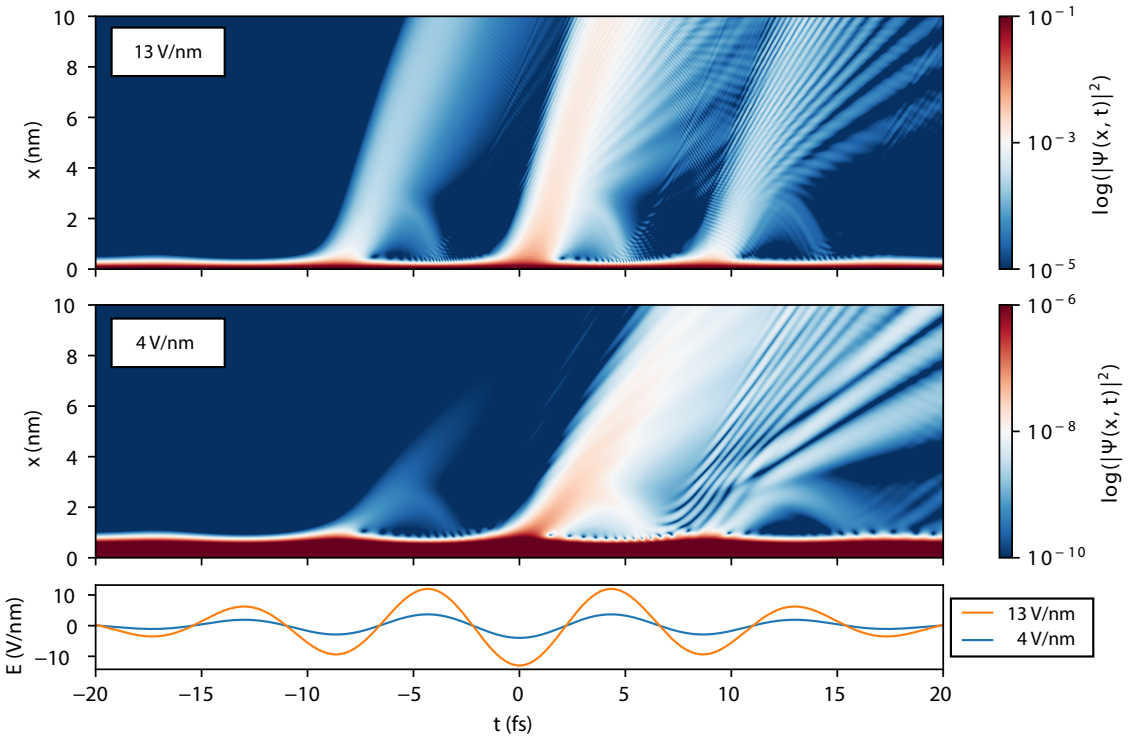

Figure 4-2: **Numerical solution to the time-dependent Schrödinger equation.** Integration of the time-dependent Schrödinger equation, by using the modified Crank-Nicolson scheme as described by [88]. The top two panels show the probability amplitudes for two cases assuming an 18 fs duration MIR pulse at a center wavelength of 2.7 µm with 4 V/nm and 13 V/nm field strength. The bottom panel shows the electric field waveform as a function of time for each case.

[88],

$$i\frac{\partial \Psi}{\partial t} = \left(-\frac{1}{2}\frac{\partial^2}{\partial x^2} + V\right)\Psi, \tag{4.1}$$

describing the interaction of a bound electron in a metal with a time-periodic field $F(t)$ is a valid approach. The potential V used is of the form,

$$V = -\begin{cases} xeF(t), & x \geq 0 \\ E_F + \phi, & x < 0, \end{cases} \tag{4.2}$$

were E_F is the Fermi energy and ϕ the workfunction. By using the modified Crank-Nicolson scheme as described in [88], we calculate the probability $|\Psi(x,t)|^2$ for a gold workfunction of $\phi = 5.1$ eV and an 18 fs duration MIR pulse at a center wavelength

of 2.7 µm. The used field strength is 4 V/nm and 13 V/nm.

The results of the integration, presented in Fig. 4-2, show the probability $|\Psi(x,t)|^2$ of measuring an electron at a given coordinate (x,t). At the low field strength of 4 V/nm the emission process is already highly sub-cycle. Driven by the peak of the electric field the electrons are ejected from the surface within a half-cycle. Strong scattering of electrons re-accelerated to the potential barrier occurs between 5 fs and 10 fs. For the case of 14 V/nm, we can see stronger emission probabilities with suppressed quiver motion and rescattering at the surface. Despite the fact that such numerical integration qualitatively and quantitatively describes the scaling laws of electron emission [88], we found difficulties adapting this scheme when accounting for our experimentThe differential readout scheme leaves only the CEP-dependent charge, which is on the order of 0.1 or less of the total emitted charge. We found in the end that the measured CEP dependent charge yield was better described by the quasi-static Fowler-Nordheim approximation [64].

4.3 Designing and Modelling

Our devices, as seen in Fig. 4-1 a, consist of 722 interconnected metallic (Au) bow-tie nanoantennas embedded in a 15 µm × 15 µm network. The device is integrated into an off-chip readout circuit using conventional electronics. The individual bow-tie nanoantennas, as shown in the scanning electron microscope image in Fig. 4-1 c, have designed dimensions of 530 nm in length, 142 nm in width and 20 nm in thickness, resulting in an antenna density of 3.2 μm^{-2}. Fig. 4-1 d shows the finite element electromagnetic simulation of the field distribution, showing a peak enhancement of up to ∼18-fold for 111 THz (2.7 µm wavelength) localized at the tips of the bow-tie structure. The sharp antenna tip creates a spatially confined hot spot for electron emission to occur. When the whole network is illuminated with a few-cycle infrared laser pulse with a peak electric field on the order of 1 V/nm, highly nonlinear tunnel ionization of electrons occurs at these hotspots at the tip of the bow-tie antennas. Additionally, the tunnel ionization is temporally confined to the peak regions of the

strongest half-cycles of the exciting field [9], [15], [33], [43], [45], [65], [80], [89].

In the case of sufficiently strong electric fields, with a Keldysh parameter $\gamma \ll 1$ the tunneling emission for a metal-vacuum boundary is described by the quasi-static Fowler-Nordheim tunneling current $\Gamma_{FN}(E) = \theta(E)\alpha E^2 \exp\left(-\frac{f_t}{|E|}\right)$ [33], [64], [65], [89], with $\theta(E)$ noting the Heaviside function, f_t =78.7 V/nm the characteristic tunneling field strength for gold and α a material and geometry dependent scaling factor. Since a single bow-tie is a symmetric system consisting of two metal surfaces facing each other with a 50 nm vacuum gap, we can approximate the total instantaneous currents at the junction with $\Gamma(E) = \Gamma_{FN}(E) - \Gamma_{FN}(-E)$, as experimentally shown in [11], [15], [44]. A CW laser would lead to fully symmetric charge injection and transport across the gap. In such a case, the time average of the residual charge in the network is zero. However, for the case of a few- to single-cycle pulse, the highly nonlinear dependence of the tunneling current with respect to the electric field amplitude does result in a residual net charge. The residual net charge is caused by the significant amplitude differences between the individual half-cycles of the pulse, effectively breaking the symmetry of emission and transport [11]. To understand the symmetry breaking, it is useful to look at the detailed instantaneous tunneling rates as a function of the electric fields for a metal-vacuum boundary.

The instantaneous current response of this nanoantenna configuration, shown in Fig. 4-3a, is equivalent to the response of two parallel diodes in opposing directions. The quantitative current response is adapted from [90], [91] and considers the frequency-resolved field enhancement, while also averaging over the antenna tip surface area of 628 nm^2, resulting in an effective field enhancement of 8.2 for the considered excitation field. When calculating the instantaneous currents of the nanoantenna, the local field at the tip of the nanoantenna is relevant. Therefore, we need to consider the antenna's complex transfer function [45]. The antenna is designed to have a resonance wavelength of 1500 nm and be off-resonant with the exciting field centered at 2.7 µm for two main reasons; the first is to transfer the full bandwidth of the optical pulse to the antenna tip, as a sharp resonance would increase the local pulse duration and reduce the CEP-dependent charge yield drastically. The second

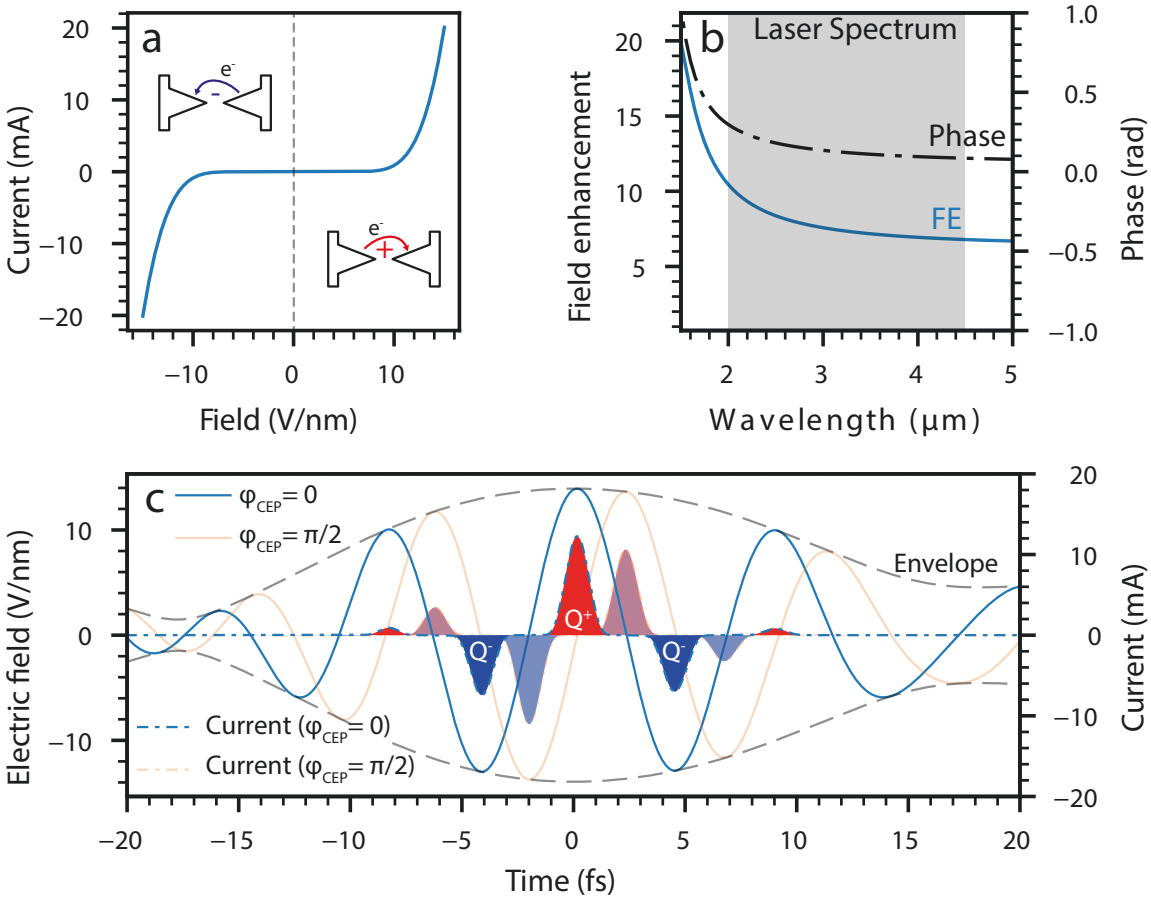

Figure 4-3: **Theoretical description of the antenna gap currents.** (a) Effective instantaneous tunneling rate for two opposing gold surfaces in the nanoantenna junction, assuming scaling parameters from [90] with an effective emission area of 628 nm^2. (b) The response function of the local electric field at the tip of the nanoantenna to an exciting electric field was simulated using a FEM electromagnetic solver. The simulation shows the wavelength-dependent field enhancement and phase. The effective field enhancement of the incident pulse is ~ 8.2. (c), The electric field as a function of time and the instantaneous current as a function of the electric field for a CEP of $\varphi = 0, \pi/2$. The electric field is the calculated local antenna field using the characterized optical pulse and the simulated antenna response. The solid lines note the electric field and the dashed lines the current. The shaded areas underneath the current curves show the total charge yield, with red areas contributing positively and blue areas contributing negatively.

reason is that the fabrication process is not fully uniform throughout the detector area, resulting in small spectral shifts of the antenna resonance [44]. When designed on-resonance, small variations will result in large phase differences between individ-

ual antennas, as the phase response has a steep slope at resonance. Considering the collective phase response of all antennas, variations in individual phases will reduce the collective CEP response of the detector [44]. Therefore, when the antennas are driven off-resonance, small variations in the fabrication will not translate into large phase changes of the optical field at the antenna tip. Additionally, a reduced variance of the device-induced phase shift is critical to improved precision in measuring the absolute CEP value. Any well-known phase offset induced by the antenna can simply be removed from the detected phase. The local field enhancement and the phase response of an off-resonance antenna for wavelengths above 2 µm is shown in Fig. 4-3 b. The local field at the antenna tip E_{loc} is therefore the frequency domain multiplication of the incident pulse $\tilde{E}(\omega)$ and the antennas complex frequency response $\tilde{H}(\omega)$, $E_{\mathrm{loc}}(t) = \mathcal{F}^{-1}\{\tilde{E}(\omega) \cdot \tilde{H}(\omega)\}$.

The effective instantaneous current response of the system to such a pulse with a peak field of ∼13 V/nm is shown in Fig. 4-3c. The employed optical pulse shape is the reconstructed optical pulse used in the experimental apparatus, combined with the simulated local field enhancement. The central half-cycle with the highest field amplitudes generates the largest peak current with up to 12 mA for a duration of 1.1 fs (FWHM). The neighboring half-cycles generate substantially smaller currents with the opposite sign. Since conventional electronics do not support the petahertz bandwidth currents, the device acts as an integrator, and the net charge deposited by the optical pulse resides in the circuit network, similar to a photodiode. The mathematical description of these charges Q as a function of the pulse CEP φ is simply the integral over the instantaneous currents;

$$Q(\varphi) = \int_{-\infty}^{\infty} \Gamma(A(t) \cdot \cos(\omega_0 t + \varphi))\ \mathrm{dt} \tag{4.3}$$

$$= \underbrace{\int_{-\infty}^{\infty} \Gamma_{FN}(A(t) \cdot \cos(\omega_0 t + \varphi))\ \mathrm{dt}}_{=\ Q^{+}(\varphi)} - \underbrace{\int_{-\infty}^{\infty} \Gamma_{FN}(-A(t) \cdot \cos(\omega_0 t + \varphi))\ \mathrm{dt}}_{=\ Q^{-}(\varphi)}. \tag{4.4}$$

$$= Q^{+}(\varphi) - Q^{-}(\varphi) \tag{4.5}$$

The CEP dependence of the charge now stems from the small difference of $Q^{+}(\varphi)$ and $Q^{-}(\varphi)$. For the case of a cosine pulse ($\varphi = 0$), the charge yield becomes maximal, and for the case of a sine pulse ($\varphi = \pi/2$), the charge components cancel out to zero. Based on the results shown in [44] with 0.1 e per antenna, one can anticipate CEP-dependent charge amplitudes of around 1.4 e per antenna for the optical pulses used in our experiments and a peak field of 1.7 V/nm. The resulting charge increase is due to a reduced number of cycles (from 2.5 to 2), and the use of a longer central wavelength [90]. With the known charge yield per antenna, one can extrapolate the charge yield of a network of interconnected antennas to a charge that is within the reach of reasonable detection limits.

4.4 Electromagnetic Simulation of the Nanoantenna

An electromagnetic simulation was performed to estimate the local field at the apex of the nanoantenna. A simulation procedure similar to the one described in [44] was used. A fully linear response of the device is assumed, which allows for the calculation of the response function in the frequency domain. A numerical solution of the Maxwell equations is obtained using the finite element method electromagnetic waves, frequency domain solver from the wave optics module of COMSOL Multiphysics. The system was modeled by a connected antenna bow-tie consisting of gold placed on a glass substrate. The dimensions of the antenna geometry were chosen to fit the fabrication design parameters. The n and k values of gold were taken

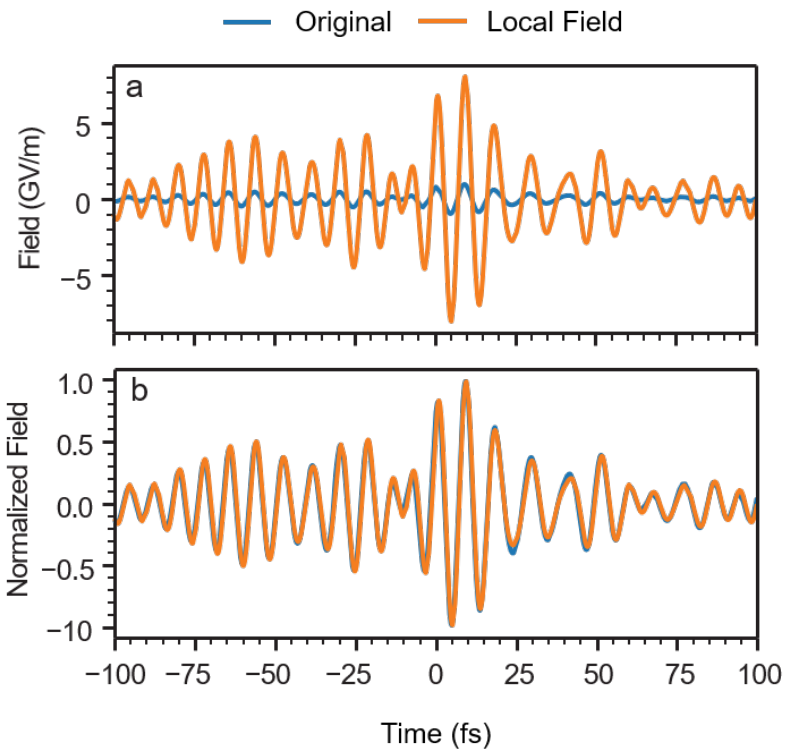

Figure 4-4: **Comparison of the original electric field versus the local field.** (a) The original incident electric field waveform and the calculated local field at the tip of the nanoantenna as a function of time. The original field has a peak amplitude of 1 V/nm and a local field of 8.2 V/nm. (b) The two field waveforms are normalized to their peak values for a qualitative comparison.

from [92] and a constant refractive index of 1.46 was assumed for the glass substrate. An incident plane wave with a propagation direction perpendicular to the antenna-substrate interface was added on top of the geometry. The incident light is linearly polarized with the electric field being orthogonal to the connecting wires. Periodic boundary conditions were added around the antenna boundary to model the network. The semi-infinite vacuum and substrate were modeled using perfectly matched layers on the top and bottom of the simulation domain. The linear response function was evaluated by comparing the results obtained with the results of an empty simulation domain with the same simulation settings. To calculate the spatial average of the antenna response, we integrated over the whole curvature of the nanoantenna tip, which is assumed to have a radius of curvature of 10 nm and a height of 20 nm.

With the simulated complex frequency response $\tilde{H}(\omega)$, see Fig. 2, and the incident field $E(t)$ the local field $E_{\mathrm{loc}}(t)$ averaged over the surface of the nanoantenna tip can be calculated,

$$\tilde{E}_{\mathrm{loc}}(t) = \mathcal{F}^{-1}\{\tilde{E}(\omega) \cdot \tilde{H}(\omega)\}. \tag{4.6}$$

The resulting normalized local field is shown in Fig. 4-4. The local field is only marginally different from the incident electric field. However, the effective field enhancement is 8.2, making the local field substantially stronger than the incident one. Compared to the field enhancements of around 20 in references [11], [14], [15], [44], [45], the antenna was designed to be off-resonant to preserve the incident electric field shape, while still having a sufficiently large field enhancement. Furthermore, the antenna design allows for a high antenna density of $\sim 3\,\mu\mathrm{m}^{-2}$, compared to an antenna design that is resonant with the MIR field, since these would require roughly double the antenna size.

4.4.1 Geometric design study

The antenna networks presented in the results were designed to enable high charge yield with low sensitivity to fabrication errors when fabricated using a robust lithography process flow. Further investigation of the design showed that the maximum value of the CEP-dependent current can be improved by up to a factor of two by increasing the the amount of antennas per unit area. The parameterized antenna unit-cell geometry is shown in Fig. 4-5 a. The increased density damps the resonant part of the response function but maintains a broadband off-resonant field enhancement with a factor of $\sim 6-7$. The gradual change of antenna density is shown in Fig. 4-5 b. Using the formulas of the quasi-static model, the increase in CEP-dependent current per unit area is estimated and corresponds to a factor of two improvements from the devices presented.

However, by not only optimizing the network density but also adjusting the resonance of the field enhancement while still ensuring off-resonant excitation, we can

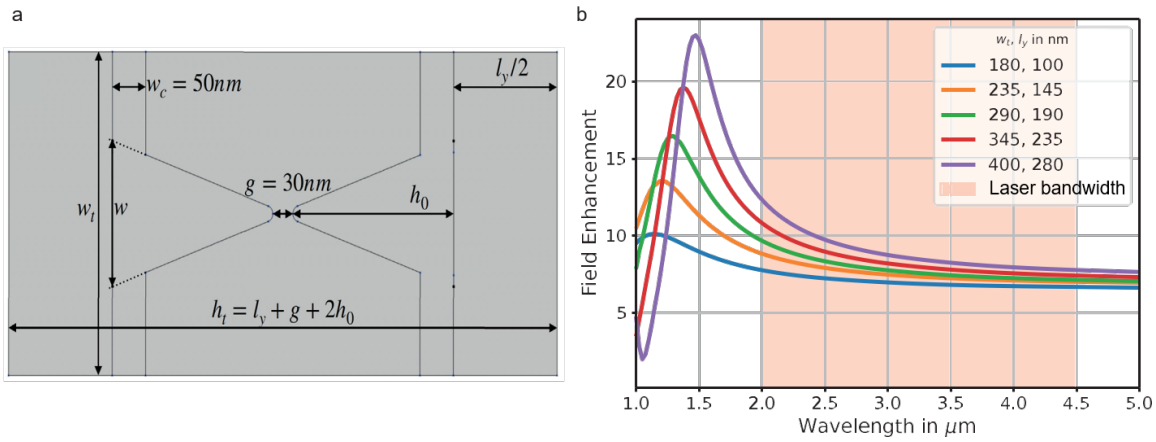

Figure 4-5: **Simulated field enhancement for different antenna densities.** (a) Parameterized antenna geometry. (b) The average field enhancement at the nanoantenna apex as a function of wavelength for different antenna densities. w_t denotes the distance between neighboring antennas and l_y is the closest distance between two stripline of antennas. The values $w_t = 400\,\text{nm}$ and $l_y = 280\,\text{nm}$ correspond to the small area network presented. The densest case with $w_t = 180\,\text{nm}$ and $l_y = 100\,\text{nm}$ has an approximately 2.9 times higher antenna density while maintaining a similar off-resonant field enhancement.

achieve further improvements in the generated CEP-dependent current. The results of this optimization are shown in Fig. 4-6.

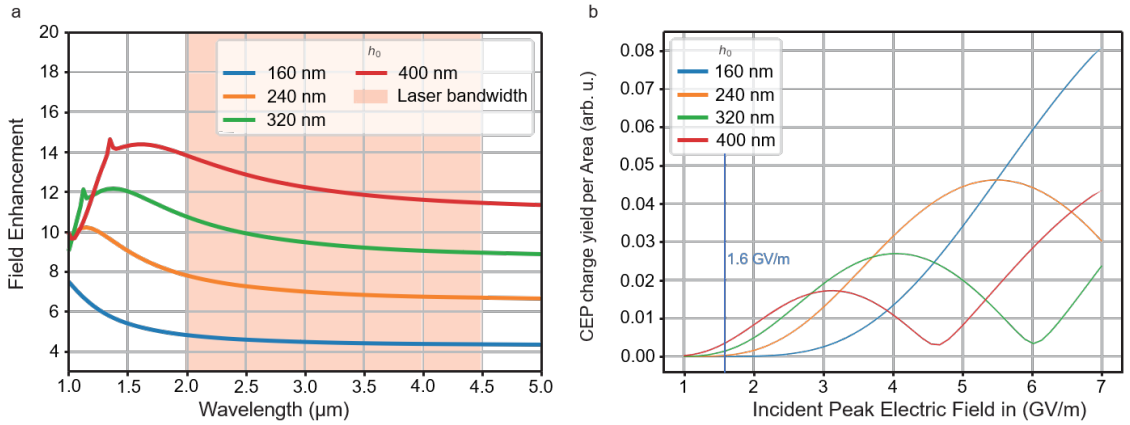

Figure 4-6: **Simulated field Enhancement for different antenna resonances with the optimum density.** (a) The average field enhancement at the nanoantenna apex as a function of wavelength for different antenna configurations, varying the antenna height h_0 with a fixed width at a ratio of $w = 3/4h_0$, while keeping the densest configuration of the network. (b) CEP-sensitive current normalized to the unit area for the different antenna variations in (a).

The idea of this study is to sweep the resonance of the antenna length at the most

dense network configuration. The resonance is mostly defined by the antenna height h_0, with a fixed width of the antenna base of $w = 3/4h_0$. The unit-cell dimension is chosen at $w_t = w$ an the horizontal antenna spacing at l_y =100 nm yielding a cell width of $h_t = l_y + g + 2h_0$, where g denotes the gap width of 30 nm. By calculating the CEP-dependent charge yield per individual antenna and normalizing it to the occupied area of the unit cell, we can define the normalized CEP sensitivity and effectively compare the different configurations. The normalized CEP sensitivity is plotted in Fig. 4-6. For a given operating point for the peak electric field of the excitation pulse, we can find the optimum configuration. At 1.6 V/nm, we find that an antenna height of 400 nm gives up to a 7-fold improvement in CEP sensitive current, compared to what was tested in the small area network. With this naive optimization process, we can already see that substantial improvements in antenna design can be found. Further study of the multidimensional parameter space, will certainly allow us to find the actual global maximum for the antenna design.

4.5 Experimental Setup

4.5.1 Laser source characterization

The laser source used to run the experiments is described in detail in reference [85]. But to reflect the state of the laser source used for the described experiment, we show here the characterization of the pulse duration within a 24 h time window to the experiment. The pulse duration is measured by an adapted version of two-dimensional spectral shearing interferometry (2DSI) [93], [94], where the ancillary pulses are derived from the pump laser at 1030 nm instead of directly from the mid-infrared pulse under test [85]. This allows for the use of broadly available and cost-effective spectrometers based on Si detector arrays, since in this implementation the up-converted spectrum will cover the NIR from 600 nm to 900 nm. The ancillary pulses are generated by fine-tuned narrowband line filters in a Michelson interferometer, resulting in a shear frequency of 1.35 THz. The resulting measurement is shown in Fig. 4-7

in logarithmic color coding. The retrieved group delay is shown on the right-hand y-axis. As can be seen, the group delay is reasonably flat and shows a sharp oscillation at 2.7 µm, which corresponds to known water absorption lines [95].

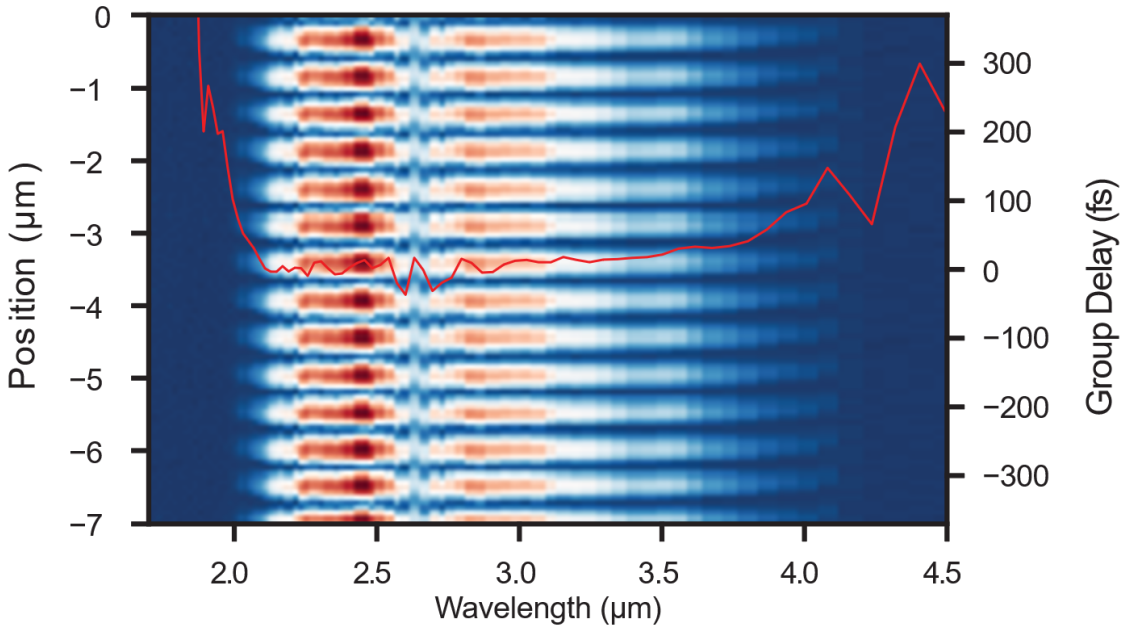

Figure 4-7: **Two-dimensional spectral shearing interferometry.** Measured 2DSI trace shown in logarithmic color coding. An overlay of the retrieved group delay is on the right-hand axis in red.

In Fig. 4-8 the raw mid-infrared spectrum is shown. The spectrum was measured on a PbSe grating-based spectrometer (Spectral Products). Using the measured mid-infrared spectrum and the retrieved group delay, the time domain of the pulse can be calculated up to an arbitrary CEP. The calculated time domain in intensity and electric field are shown in Fig. 4-9. The retrieved pulse FWHM duration is 18 fs at a center wavelength of 2.69 µm. This corresponds to two cycles of the carrier wave within the FWHM duration.

The passive CEP stability of the system was measured with f-2f interferometry to be lower than 190 rad RMS, with details found in Ref. [85]. The CEP was controlled by adjustment of the pump-seed delay of the adiabatic difference frequency generation stage. To move the CEP by 2π of the mid-infrared pulse, the pump is delayed by one wavelength λ =1030 nm. The delay is produced by a slip-stick piezo stage (SLC-2430,

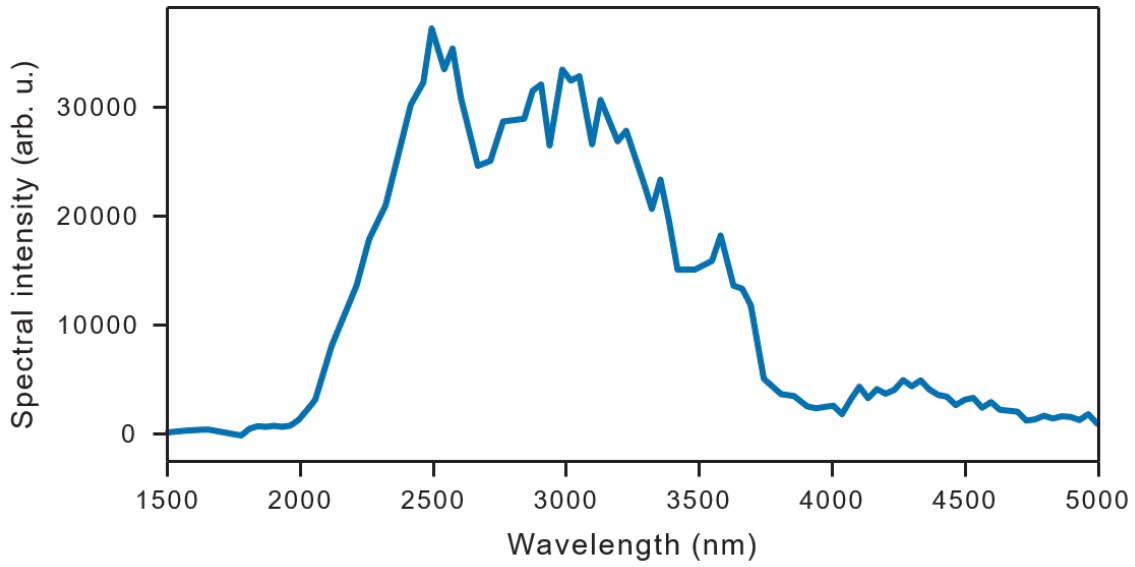

Figure 4-8: **Measured mid-infrared spectrum.** Raw mid-infrared spectrum measured on a PbSe grating-based spectrometer.

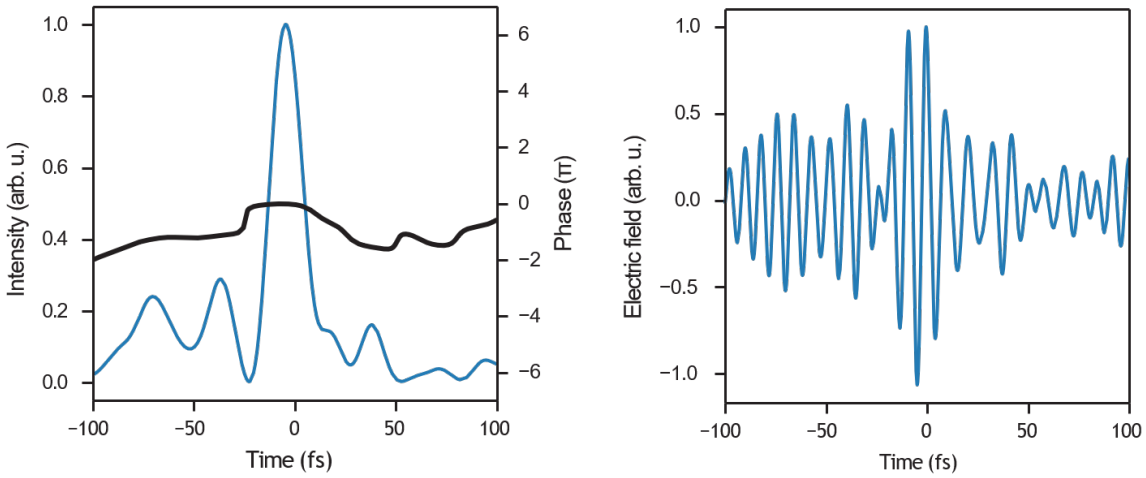

Figure 4-9: **Reconstructed time domain.** (Left) Reconstructed intensity distribution of the mid-infrared pulse (blue) and the retrieved phase (black). (Right) Electric field profile of the retrieved mid-infrared pulse set at an arbitrary CEP.)

Smaract GmbH) and a hollow roof mirror, which delays the pump.

4.5.2 Measurement of focal-spot size

To have an accurate estimation of the peak intensity in our experiment we used the knife-scan technique to measure the beam size of the MIR beam inside the focus. To realize a sharp edge, we used the lithographically defined leads of the chip itself and

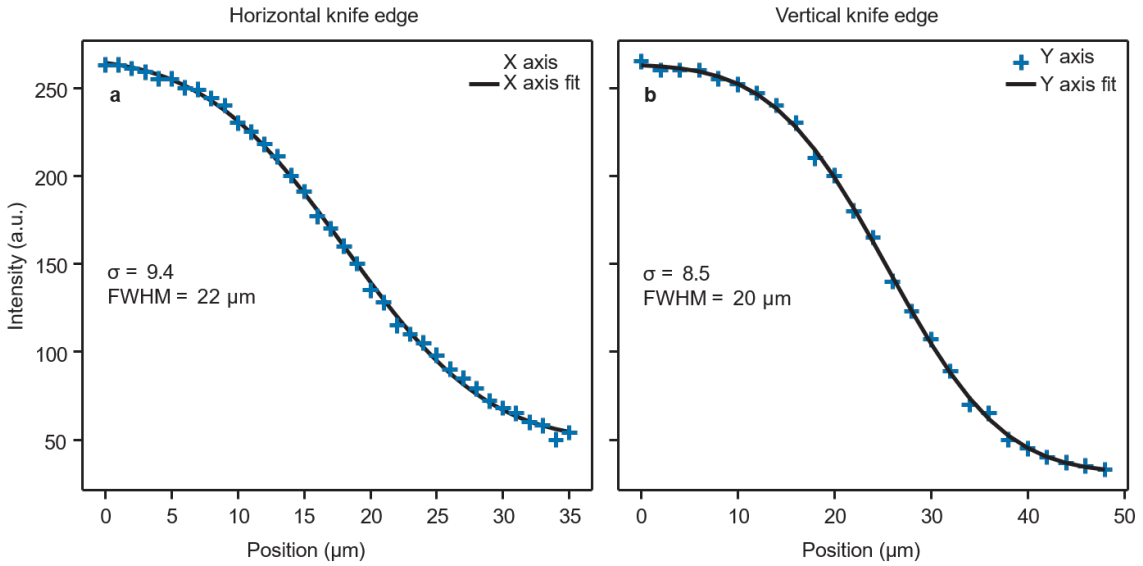

Figure 4-10: **Focal-size measurement.** (a) Horizontal knife-edge measurement with a resolution of 1 µm. The error-function fit results in a FWHM of 22 µm. (b) Vertical knife-edge measurement with a resolution of 2 µm. The error-function fit results in a FWHM of 20 µm.

scanned the edge through the focus for the horizontal and vertical dimension with 1 µm and 2 µm step-size, while measuring the transmitted intensity with a pyroelectric detector.

The measured intensity as a function of position is shown for the horizontal and vertical beam-axis in Fig. 4-10. To retrieve the FWHM of the beam axis, we used a fit with the error function erf(x),

$$P(x) = P_{\mathrm{Min}} + (P_{\mathrm{Max}}/2) * (\mathrm{erf}((x - x_0)/(\sigma \cdot \sqrt{2}))). \tag{4.7}$$

The fit parameters are the minimum intensity P_{Min}, the maximum intensity P_{Max}, the center position x_0, and the standard deviation σ. The resulting parameters are $\sigma_{\mathrm{Horiz.}} = 9.4$ and $\sigma_{\mathrm{Vert.}} = 8.5$, which correspond to the FWHM with FWHM $= 2\sqrt{2\log(2)} \cdot \sigma$. Giving for the horizontal axis a FWHM of 22 µm and for the vertical FWHM 20 µm. Qualitatively the focal-spot shape is well approximated by a Gaussian intensity distribution, as indicated by the fit of the error-function.

4.5.3 Charge generation and readout

The trigger signal falling slope was used as a reference to sort the individual shots with their respective time stamp. Before integrating over the AC coupled current signals, a baseline was introduced by averaging over the signal for 3 µs before every trigger and subtracting it locally for the respective time windows. To retrieve the charge contained within each current pulse, the current pulse was integrated over and the integrated signal was sampled at points t_1, t_2. The integrated charge is simply the difference of charges measured at the sampling points, $Q_{Shot} = Q(t_2) - Q(t_1)$. This technique is called correlated double sampling (CDS) and is commonly used in charged-coupled device readout circuitry [96]. The time-correlated differentiation significantly reduces uncorrelated low-frequency noise [97].

4.6 Experiment and Results

4.6.1 Small area network

The optical pulses used in this work were generated with a home-built laser source based on optical parametric amplification and difference frequency generation that delivers CEP stable pulses with a FWHM duration down to 16 fs at a center wavelength of 2.7 µm passively. The pulse energy was > 84 nJ at a repetition rate of 50 kHz . The CEP of the laser was controlled by adjusting the pump-seed delay in the difference frequency generation stage. The delay adjustment was implemented by controlling the pump beam path length via a retro-reflector mounted on a piezo-actuated linear stage.

To illuminate the nanoantenna network, we focused the incident pulse down to ~ 21 µm (FWHM) with an off-axis parabola of focal length 25.4 mm. The nanoantenna networks were placed in the center of the focus. To achieve single-shot charge readout, we used a custom transimpedance amplifier with a gain of 1 V/nm and a -3 dB-bandwidth of 50 kHz (WiredSense GmbH). The RMS noise floor of our detection was measured to be ~ 1100 e per shot. To overcome this noise, we illuminated a

network consisting of 722 antennas in a rectangular area of 15 µm × 15 µm to generate in excess of 1000 e per shot.

After interaction with the nanoantenna networks, pulse energies were measured by a pyroelectric photodetector with the same −3 dB-bandwidth of 50 kHz as the transimpedance amplifier. This arrangement allowed for the simultaneous recording of shot-to-shot pulse energy fluctuations. The pyroelectric detector uses an identical transimpedance amplifier to the one used for the nanoantenna read-out to ensure comparable statistics of the two signals.

In this experiment, each dataset consisted of the measured charge from the nanoantenna network and the corresponding pulse energy, recorded for around 50000 shots (1 s). In each dataset, the CEP of the laser was linearly ramped for 600 ms with a speed of 20 π rad s^{-1}, starting at ∼120 ms. For different datasets, the pulse energy was systematically varied by more than a factor of ten.

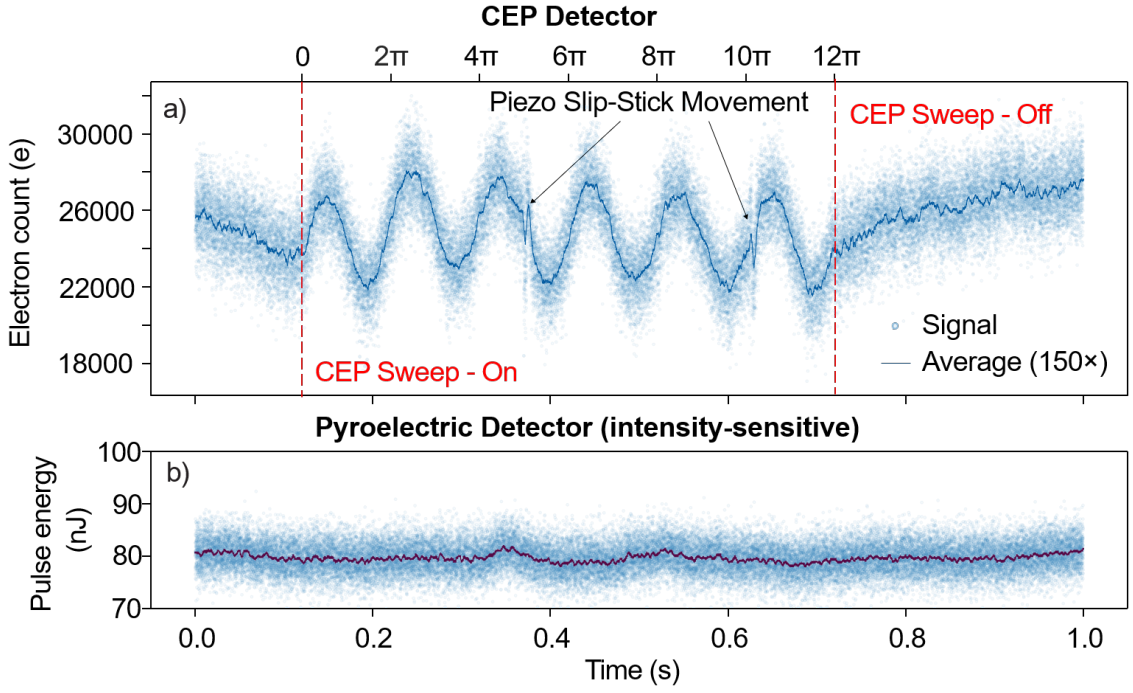

Figure 4-11: **Single-shot charge readout.** (a) Single dataset recording of 50000 laser shots for the charge yield of the nanoantenna detector and (b) the laser energy recorded by the pyroelectric detector. The peak field of the incident laser pulse on the network is 1.6 V/nm. From 120 ms to 720 ms the CEP was linearly ramped over 6 cycles. The instantaneous phase was interpolated with the scan speed of 2πs^{-1}.

A single dataset is presented in Fig. 4-11, including both the single-shot data and the moving average calculated over 150 shots (dark line). The upper panel shows the recorded charge produced by the nanoantenna network, with an average yield of 25000 e per shot. From 120 ms to 720 ms the CEP is linearly ramped over a 12π range. The data points show a clear sinusoidal CEP dependence with an amplitude of 2370 e and a signal-to-noise ratio (SNR) of 4.6, while the pulse energy does not show modulation. Additionally, we estimated the CEP noise of our measurement to be 0.75 rad rms). When considering the number of illuminated antennas, the individual CEP-sensitive yield per antenna and shot is 3.3 e, we estimated peak currents through the nanoantenna gap of up to a 95 e/fs, corresponding to ∼15 mA. Given the surface area of a single nanoantenna tip, $\sim 628\,\mathrm{nm}^2$, the estimated current density reaches a remarkable $2.4\,\mathrm{GA\,cm}^{-2}$. At $t = 370$ ms and 620 ms, sharp changes are visible in the charge yield of the detector element. These features, which are 250 ms apart, are caused by the specific movement pattern of the closed-loop slip-stick piezo stage used to control the CEP, that re-centers the piezo position every 1.3 µm.

To isolate the CEP-dependent signal from readout noise and pulse energy fluctuations, we Fourier transformed the dataset between t =120 ms and t = 620 ms and compared it to the frequency spectrum obtained without any optical input; see Fig. 4-12.

The spectrum of the antenna network shows a clear peak at 10 Hz corresponding to the $2\pi{\cdot}10$ Hz modulation of the CEP. This signal amplitude is around two orders of magnitude (40 dB) higher than the readout noise floor. The noise in the measured spectrum is dominated from DC to $\sim$ 250 Hz by $f^{-3/4}$ scaling, which is typical for field emission devices and is attributed to Brownian noise of the work function due to dynamical changes of adsorbates on the surface [44], [98]. At frequencies higher than 250 Hz the spectrum is limited by shot noise, with a substantial component originating from the detection noise of the transimpedance amplifier. The calculated shot noise of the signal is $\sim$ 160 e rms. We also want to note, that we did not observe noticeable degradation of the devices, in comparison to studies using oscillator-type laser sources with MHz-level repetition rates, where degradation was present on the

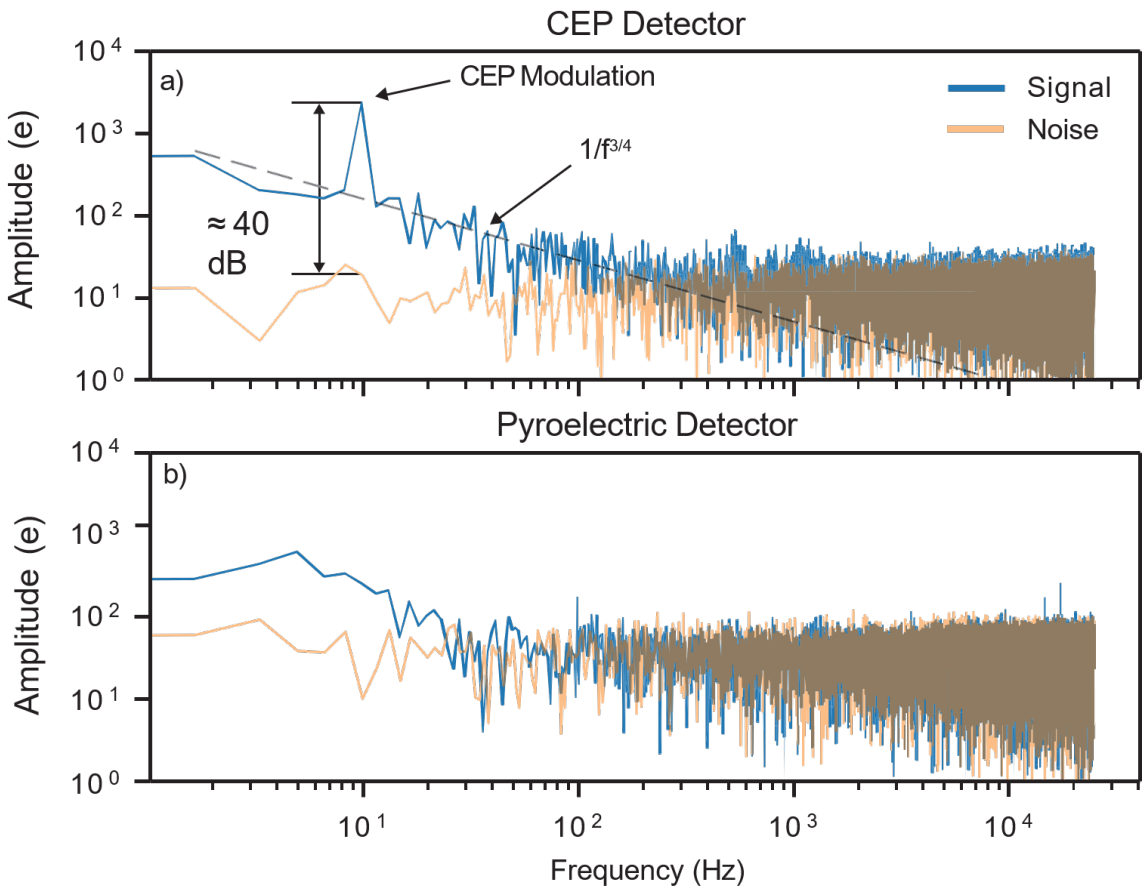

Figure 4-12: **Frequency domain of the single-shot data.** The respective data from Fig. 4-11 $t = 370\,\text{ms}$ to $t = 620\,\text{ms}$ is Fourier transformed and shown in charge amplitude as a function of frequency. For comparison, the electronic noise floor is shown in orange for both spectra. (a) The frequency-resolved signal of the nanoantenna network. The 10 Hz CEP modulation is separated by 40 dB from the noise floor. (b) The frequency-resolved pulse energy fluctuation is detected with the pyroelectric detector.

few-minute time scale[44]. However, detailed studies of durability and lifetime are certainly warranted, as has been carried out at DC field emission with comparable devices over 2500 hours [99]. When evaluating the recorded pulse energy fluctuations at the photodetector, no 10 Hz modulation is distinguishable from the background (see Fig. 4-12 b). Above 100 Hz the pulse energy spectrum is dominated by detector noise. Systematic investigation of signal strength as a function of peak electric field has shown that at $\sim 1\,\text{Hz}$ resolution bandwidth a signal distinguishable from noise can be observed down to 0.6 V/nm (corresponding to $\sim 10\,\text{nJ}$).

4.6.2 Complementary measurements

Field-dependent scaling of the CEP-sensitive charge yield

To elucidate the mechanism underlying the CEP-dependent electron emission, the amplitude of the CEP modulation is shown in Fig. 4-13 (blue triangles) as a function of the incident peak field of the laser pulse. In order to estimate the CEP-

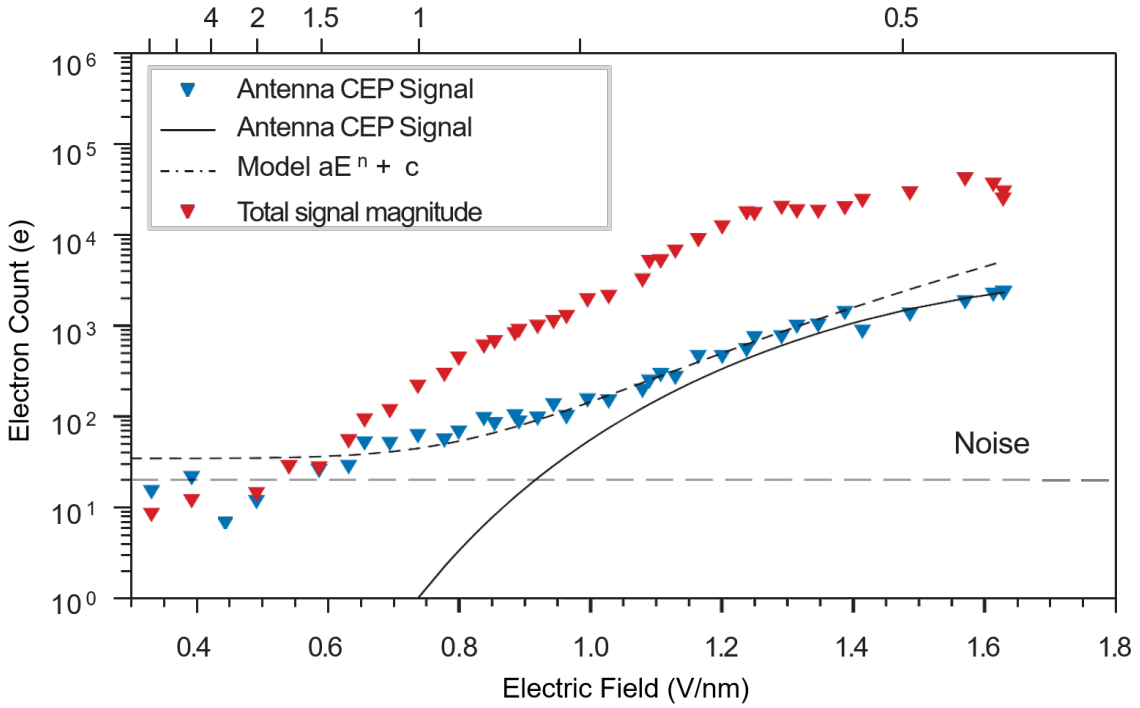

Figure 4-13: **Charge yield scaling.** The CEP modulation amplitude and the total magnitude (average of each measurement) of the electron counts are plotted as a function of the peak field (average of each measurement), estimated for CEP= 0, for the respective dataset. The CEP signal is taken from the amplitude of the 10 Hz frequency component of the measurement data. The Fowler-Nordheim model describing the tunneling current yields a field enhancement of $g = 7.41$. Furthermore, a power law fit, $aE^n + c$ to the first 30 values is shown.

dependent emission, we first calculated the field at the tip by convolving the applied field (as retrieved by optical pulse characterization) with the calculated impulse response function of the nanoantenna. For peak fields larger than 1.2 V/nm (estimated for CEP= 0), corresponding to a Keldysh parameter $\gamma \sim 0.6$, the CEP-dependent charge yield scales according to the quasi-static tunneling approximation. Here our

fit model, using a field-enhancement factor g and a pre-factor α results in a field-enhancement of $g = 7.41$, which is in good agreement with the calculated enhancement 8.2 given the design antenna geometry. Alpha results in $\alpha = 1517$. For values below 1.2 V/nm, the data follows a power law model $aE^n + c$, with $n = 7.85$, $a = 110$ and $c = 35$. This scaling behavior suggests a transition from nonadiabatic tunneling emission to the quasi-static tunneling regime [89], [100]. This scaling behavior was verified by repeating the experiment with a different nanoantenna network. The results of this second device are presented later in the section on the large-area network. The interaction of the optical pulse with our nanoantenna network generates not only CEP-dependent charges but also a pulse energy-dependent charge offset. The magnitude of the average charge yield of each trace (red triangles) is around one order of magnitude larger than the CEP-dependent yield and scales nonlinearly with the pulse energy. It should be noted that this current does not increase monotonically, but goes through a local minimum in the field range from 1.25 V/nm to 1.6 V/nm. This current scales differently from the CEP-dependent current, implying a different origin than the nanoantenna network. Additional investigation is required as we suspect parasitic field emission from the electrodes close to the nanoantenna network or thermal emission processes play a role. We believe that an improved electrode design would greatly suppress the charge offset. Similar behavior of the charge offset has been observed in a large area network as well.

Background charge signal

During the measurements across all tested devices, we observed an intensity-dependent charge background. To investigate the possible origin of this contribution, we tested two different hypotheses. First, the charge signal is generated by a multiphoton emission process, and second, it is generated by a field emission process based on Fowler-Nordheim tunneling. The results are shown in Fig. 4-14. The multiphoton fit is defined as,

$$Q(E, n, \alpha) = \alpha \cdot (E)^n + c, \tag{4.8}$$

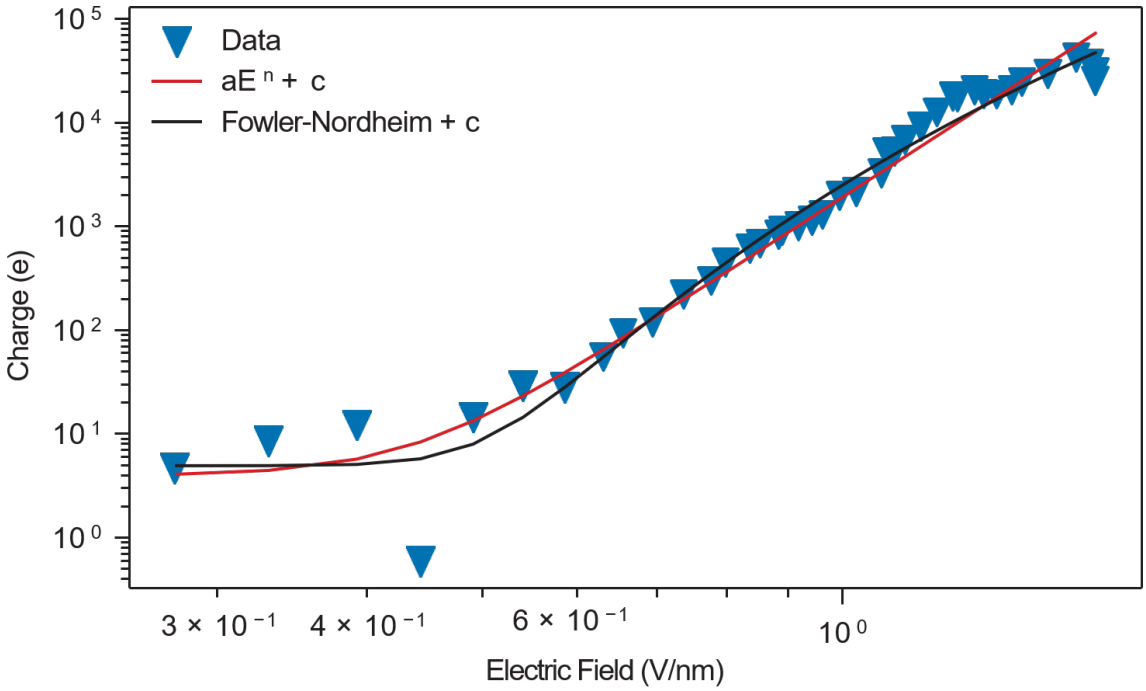

Figure 4-14: **Background charge yield.** The average charge yield as a function of the peak electric field. A multi-photon absorption and Fowler-Nordheim-based model are fitted to the data. For the multi-photon the function $Q(E, n, \alpha) = \alpha \cdot E^n + c$ is used, with fit results $\alpha = 1.9 \cdot 10^3$, $n = 7.4$ and $c = 3.9$. For the Fowler-Nordheim fit the function $\Gamma(E, g, \alpha) = \alpha(gE)^2 \exp\left\{\left(-\frac{78.7}{|gE|}\right)\right\} + c$, with the results $\alpha = 1705$, $g = 15.4$ and $c = 4.9$.

with the polynomial order n and a scaling prefactor α. $n = 7.4$, $\alpha = 1.9 \cdot 10^3$ and the offset $c = 3.9$. This hypothesis implies that a 3-4 photon process is causing electron emission, which is incompatible with the photon energy of the optical pulse spanning 0.3 eV to 0.6 eV and the work function of gold with 5.1 eV. This means that either another process is inducing a current other than electron emission from gold or that multiphoton is not the right explanation. The second tested hypothesis is that of a field emitter other than the nanoantenna network. To test this we used the Fowler-Nordheim fit function $\Gamma(E)$,

$$\Gamma(E, g, \alpha) = \alpha(gE)^2 \exp\left\{\left(-\frac{78.7}{|gE|}\right)\right\} + c, \tag{4.9}$$

with the prefactor α, the field enhancement g and critical field strength of 78.7 V/nm. The Fit results show a prefactor of $\alpha = 1705$, a field enhancement of 15.4, and the offset $c = 4.9$. This result implies that there is a different field emitter causing this charge yield, as the designed field enhancement of the nanoantenna is on the order of ~ 8. However, as this is merely quantitative speculation, further research is warranted to uncover the cause of this charge contribution. One test experiment could be to use an identical device but excluding the nanoantenna networks. With that, all contributions from the large gold leads, if also contributing, can be measured independently. Second, the change of polarization could be tested, as these nanoantennas are highly polarization sensitive [14]. However, continuous changing of polarization in the MIR is difficult due to a lack of suitable achromatic waveplates and cannot easily be implemented.

Estimation of the spatial charge-yield distribution

Given the measured field dependence in Sec. 4.6.2, we can estimate the spatial dependence of emitted charge across the whole network. The small area networks have a size of 15 µm × 15 µm or equivalently 19 by 38 devices that are illuminated with a beam FWHM larger than the network. However, this is only a rough estimation and a more quantitative approach is warranted to understand what fraction of the total network contributes to the measured charge. Based on the focal-spot measurement of 22 µm × 20 µm and combined with the extracted field strength dependence, we can calculate the spatial charge-dependence and normalize it by the number of antennas.

Estimation of phase-noise

The retrieved phase $\varphi(t)$ is shown in Fig. 4-15 with an additional linear fit. In the phase signal, we can see the linear phase shift induced in the experiment, closely matching the experimentally induced phase-scan speed of $62.8\,\mathrm{rad\,s^{-1}}$. By removing this linear phase movement we can estimate the rms phase noise in our experiment. For a more intuitive representation of our complex signal, we plot the phasor representation of the initial measurement data in Fig. 4-16 a. This polar plot shows the

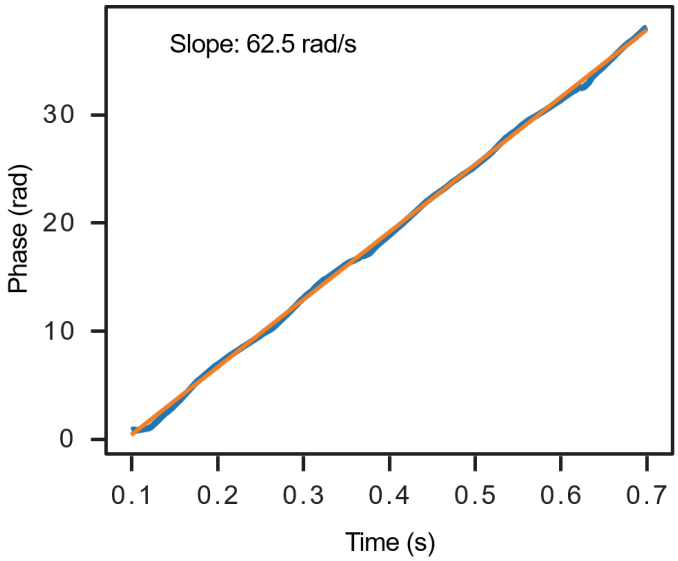

Figure 4-15: **Time series of the phase.** Phase as a function of time extracted from the measurement data (blue) and a linear fit (orange) with a slope of 62.5 rad s^{-1}.

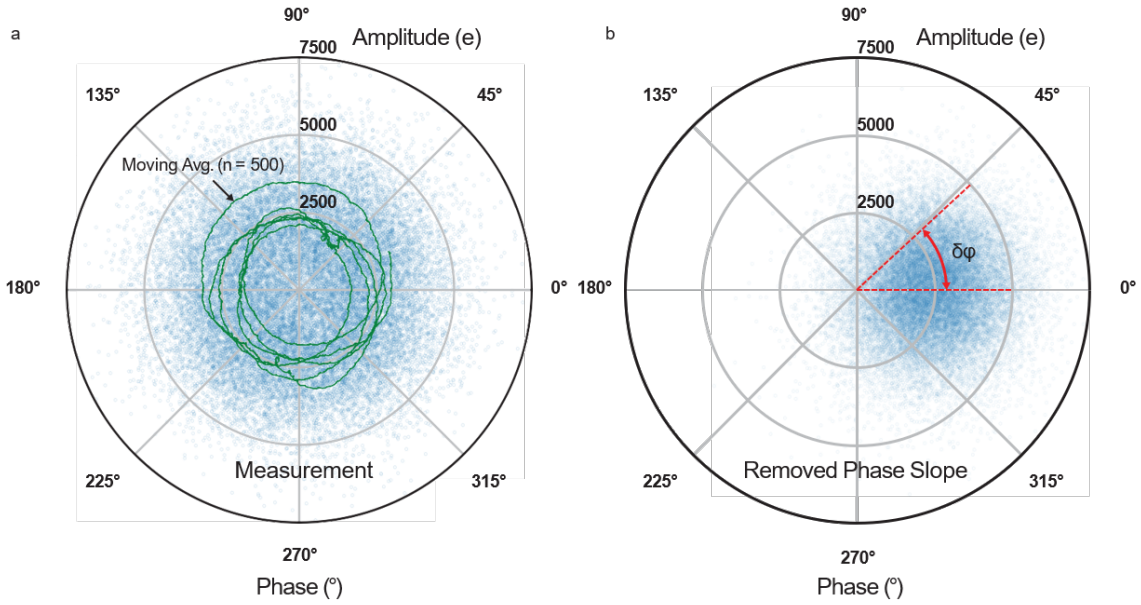

Figure 4-16: **Synthetic phasor diagram.** (a) Phasor representation of the Hilbert-transformed measurement data. The green line shows the data filtered by a moving average of n = 500 to visualize the underlying phase movement. (b) Phasor representation of the Hilbert-transformed measurement data with the removed phase slope.

amplitude and phase of the signal and forms for the original case of a donut distribution of the data points, as the phase of our signal rotates by 20π over 600 ms. To extract the rms phase noise we remove the linear phase movement, with the result

shown in Fig. 4-16 b. From the distribution of $\varphi(t)$ the standard deviation $\delta\varphi$ is retrieved and yields a rms noise of 0.75 rad.

To put this result into perspective we calculated the contribution of 1100 e rms noise to an artificial sinusoidal signal of 10 Hz with an amplitude of 2370 e. This helps to understand the contribution of electronic noise to the total signal noise of 750 mrad rms, that was measured. Assuming we are dealing with uncorrelated noise sources, the total noise is expressed as the square root over the sum of the individual contributions squared,

$$\delta\varphi_{\text{Total}} = \sqrt{\delta\varphi^2_{\text{Electr.}} + \delta\varphi^2_{\text{Shot}} + \delta\varphi^2_{\text{Laser}}}. \tag{4.10}$$

Considering that we have an estimate for the electronic noise contribution of 550 mrad rms, see Fig. 4-17 a, and a shot noise contribution of $\sqrt{2730} \approx 50$ e rms from the nanoantenna signal plus an additional charge background of 25000 e corresponding to shot noise of 160 e rms, we can estimate that the contribution of the laser is on the order of 480 mrad. This would include any contribution from the phase noise, which is on the order of 190 mrad rms measured at a bandwidth of 1 kHz. Further study will be necessary to establish a ground truth to the laser phase noise, as for example by using fast f-2f schemes as introduced by Guo et al. [79].

With this analysis, we can also establish how specific improvements in electronic noise or signal amplitude translate into an improved phase noise. Considering electronic detection noise at 100 e rms, as would be the limit of the amplifier used in this manuscript, we expect a phase noise contribution of 40 mrad rms (see Fig. 4-17b). Furthermore, when implementing improvements in the device design or by increasing the network area, a 10-fold improvement in amplitude will result in an electronic noise contribution corresponding to around 4 mrad (see Fig. 4-17c). However, in this regime, we would be predominantly shot-noise limited with 160 e rms, which would correspond to a phase noise of approximately 7 mrad. This analysis highlights the potential for using petahertz electronic devices to realize a phase detector that is highly

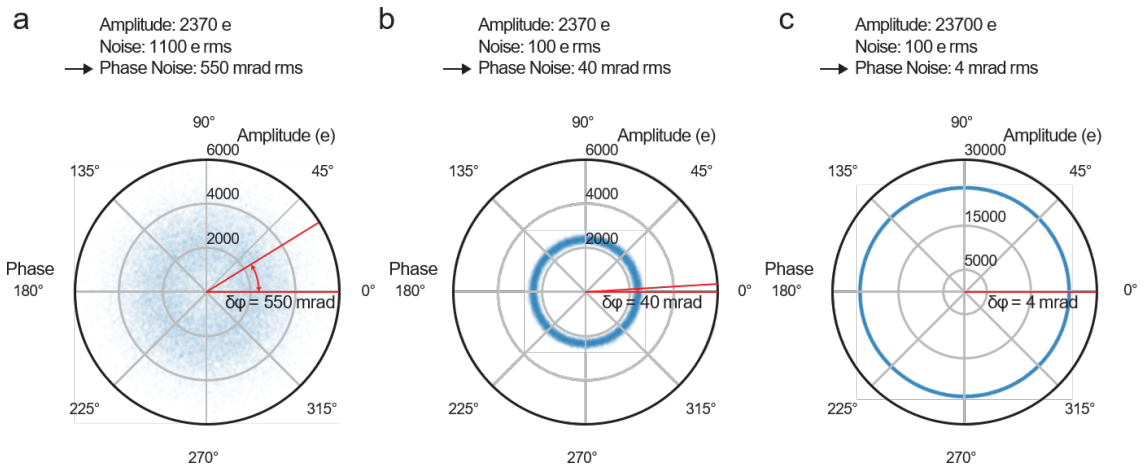

Figure 4-17: **Comparison of different phase noise levels.** (a) Electronic noise (1100 e rms) contribution to the phase noise for a 10 Hz sinusoidal signal of amplitude 2370 e. (b) Electronic noise (100 e rms) contribution to the phase noise for a 10 Hz sinusoidal signal of amplitude 2370 e. (c) Electronic noise (100 e rms) contribution to the phase noise for a 10 Hz sinusoidal signal of amplitude 23700 e.

sensitive, but is also extremely compact and allows for micrometer scale integration.

4.6.3 Large area network

To verify the results measured in the small area network we repeated the same measurements with an antenna network that measures 30 µm × 30 µm, which is substantially larger than the FWHM beam width of ∼ 21 µm. The other difference between these measurements is the use of a different detector for the single-shot pulse energy, which is, in this case, a commercial mercury cadmium telluride detector. This amounts to roughly 1000 antennas within the spatial FWHM contributing to the measured charge yield. A single-shot measurement is shown in Fig. 4-18. Identical to the small area network, a clear CEP modulation is present in the measured data. Furthermore, also the same signatures of the piezo slip-stick motion are present in the data. In addition, we see a 3x larger background charge signal compared to the other measurement.

As in the small area network, the same frequency analysis of the single-shot measurement is shown, which presents reproducible behavior. Aside from the clear CEP

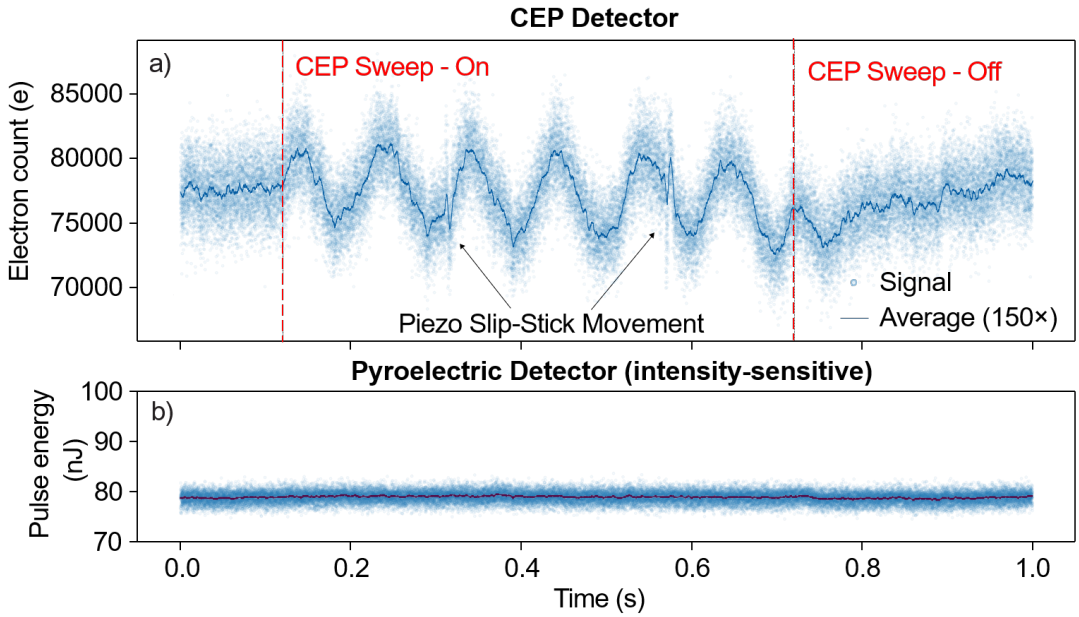

Figure 4-18: **Single-shot charge readout.** (a) A single dataset recording of 50000 laser shots for the charge yield of the nanoantenna detector and (b) the laser energy recorded by the pyroelectric detector. The peak field of the incident laser pulse on the network is 1.6 V/nm. From 120 ms to 720 ms the CE phase is linearly ramped over 6 cycles.

peak, we see in addition the same $1/f^{3/4}$ noise characteristic is present in the data. The narrow band noise peaks at ~ 17 kHz in the electron amplitude are clearly discernible from noise. In conjunction with the higher background charge signal, we can strengthen the argument that the noise peaks are driven by high-frequency laser intensity changes predominantly modulating the background charge signal.

Analyzing the scaling of the CEP peak as a function of the incident peak field (Fig. 4-20), we find in general similar behavior to Fig. 4-13. The Fowler-Nordheim fit results in a field enhancement $g = 8$, very close to the simulated field enhancement of 8.2. Furthermore, the prefactor $\alpha = 1647$ is almost identical to the one in Fig. 4-13 text with $\alpha' = 1517$, indicating that this network, despite the larger size, has a comparable amount of antennas contributing to the charge signal, as a is proportional to the number of antennas. Further measurements with different network sizes could map more precisely how many antennas are involved in the charge signal. The heuristic power law fit, $Q(E) = aE^n + c$, shows as well comparable behavior to the

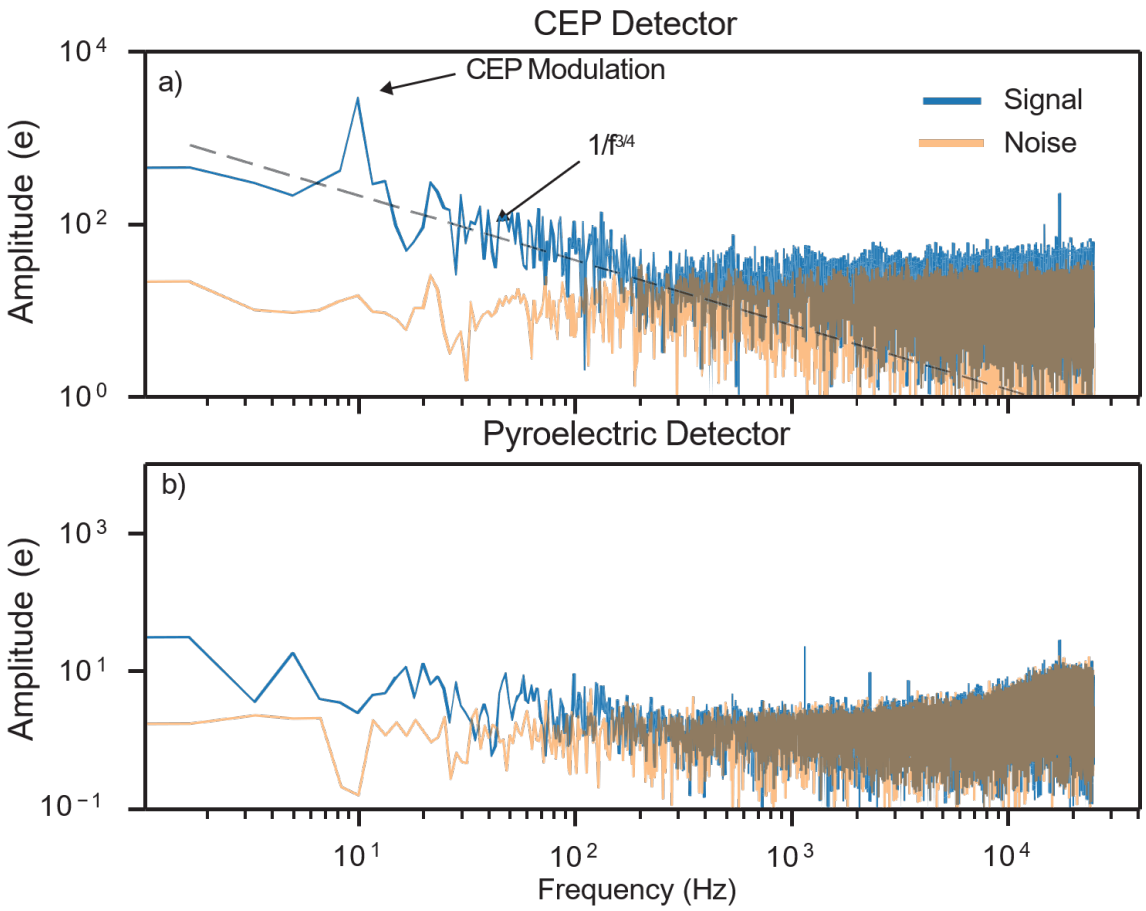

Figure 4-19: **Frequency domain of the single-shot data.** The respective data from Fig. 4-18 $t = 370\,\text{ms}$ to $t = 620\,\text{ms}$ is Fourier transformed and shown in charge amplitude as a function of frequency. For comparison, the electronic noise floor is shown in orange for both spectra. (a) The frequency-resolved signal of the nanoantenna network. (b) The frequency-resolved energy signal, as a function of pyroelectric charge yield.

network discussed in the small area network section. The fit results are $a = 147$, $n = 7.65$, and $c = 13$, which in particular with the power law order n agrees very well with the small area network where $n' = 7.85$ is measured. This shows that the measurements are in general of predictable behavior. Although the scaling law for low field strengths is not fully explained, models like the Yudin-Ivanov [89], could help to explain these scaling behaviors.

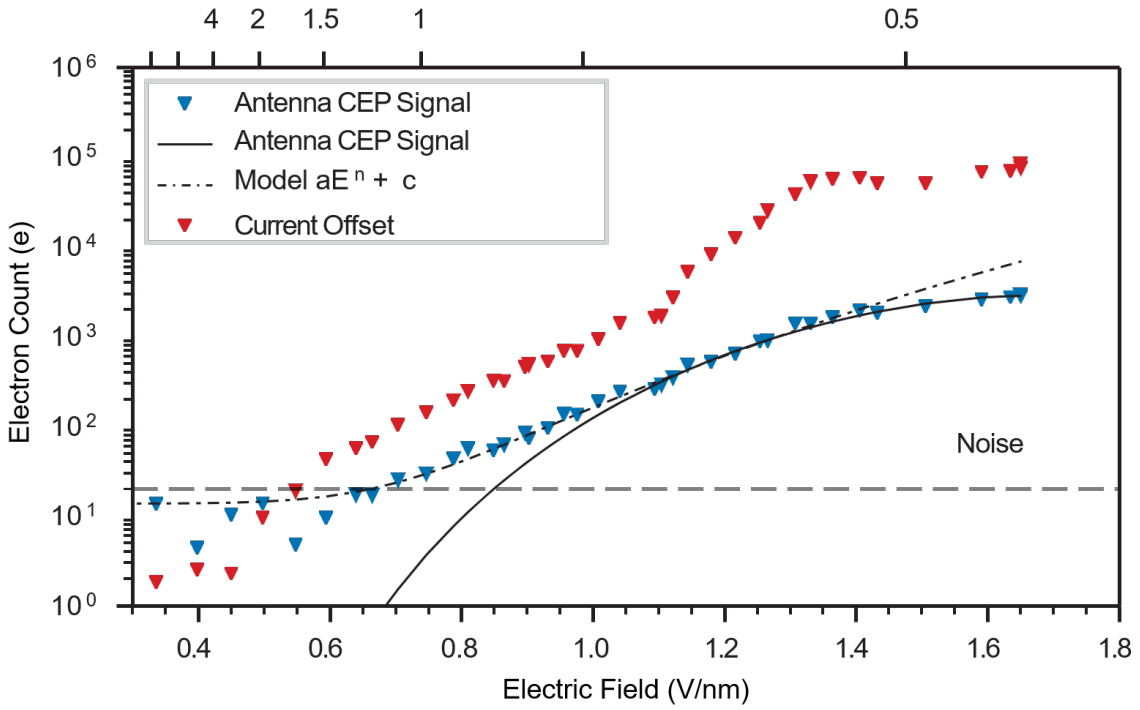

Figure 4-20: **Charge yield scaling.** The carrier-envelope phase modulation amplitude and the average charge yield are plotted as a function of the average peak field for the respective dataset. The CE phase signal is taken from the amplitude of the 10 Hz frequency component of the measurement data. Furthermore, a power law fit, $aE^n + c$ to the first 30 values is shown.

4.7 Concluding remarks and outlook

We have demonstrated single-shot readout of CEP-dependent charge signals at 50 kHz repetition rate, underlying sub-cycle current generation across a macroscopic device area of 225 µm^2 integrating more than 700 individual antenna pairs. This was made possible by improving the average CEP-dependent charge yield per single antenna by a factor of $\sim$ 30 [15], [44], now reaching 3.3 e per shot, and by illuminating hundreds of antennas simultaneously. The enhanced antenna yield implies a remarkable peak current density of up to 2.4 GA cm^{-2} [11], [15], [44]. With this result, we show that metallic nanoantenna networks, fabricated via state-of-the-art lithographic methods, are a flexible and scalable approach to optical-frequency electronics that allows the designing of individual circuit elements, similar to conventional microelectronics. Thanks to this advance, we demonstrated off-resonant antennas that are sensitive

to pulse energies two orders of magnitude lower than any other photoemission-based single-shot absolute CEP detection techniques [78], [84], [101] and comparable to or lower than f-2f interferometry [79], enabling absolute CEP detection of optical pulses with only tens of nJ of energy. Further optimization of the network density combined with a reduced number of optical cycles in the pulse would potentially increase the total yield by an additional two orders of magnitude [44], [90]. As the measurement is dominated by read-out noise, further noise reduction of electronics downstream of the detector element will have a significant impact on SNR with the potential for another 5- to 10-fold improvement [102]. With these improvements the measured phase noise of 0.75 rad will be lowered down to tens of milliradians and soon competitive with established techniques, but integrated fully on a chip and with a compact detector footprint.

Chapter 5

Harmonic Frequency Mixing using Asymmetric, Half-wave rectification Nanoantennas

The work presented in this chapter builds upon asymmetric half-wave rectifying antennas shown in Fig. 3-3i-l and is experimentally used for the application discussed in Section 3.6.2. It was done in collaboration with Drs. Lu-Ting Chou, Marco Turchetti, and Felix Ritzkowsky. They helped with the experimental setup, fabrication, and writing, respectively. Code and data can be found in the following repository: https://github.com/qnngroup/manu-HarmonicMixer

Abstract

Nonlinear electronic frequency mixers are fundamental building blocks of electronic systems. Harmonic frequency mixing in particular enables flexible and broadband electromagnetic signal analysis across octaves of spectrum using a fixed reference frequency (the local oscillator). However, conventional nonlinear frequency mixers do not operate beyond the hundreds of GHz to a few THz frequency range. If extended to the petahertz scale in a compact and scalable form, nonlinear electronic harmonic mixers would enable field-resolved optical signal analysis spanning octaves of spec-

tra in a monolithic device without the need for prior conversion nonlinear crystals. Here we demonstrate lightwave-electronic harmonic frequency mixing beyond 0.350 PHz using plasmonic nanoantennas with vacuum emission channels. We demonstrate that the mixing process enables complete, field-resolved detection of spectral content well outside that of the local oscillator, greatly extending the range of detectable frequencies compared to conventional heterodyning techniques. Our work has important implications for applications where optical signals of interest for spectroscopic analysis or imaging exhibit coherent femtosecond-scale dynamics spanning multiple harmonics.

5.1 Introduction

Lightwave electronics (also often called PHz electronics) seek to integrate optics and electronics effectively, leveraging sub-cycle information contained within the ultrafast oscillations of light fields [4], [42], [103]–[105]. In this pursuit of electronics operating at optical frequencies, a significant obstacle arises from the mismatch between the characteristic frequencies of optical (PHz regime) and conventional electronic systems for readout (GHz-THz). To solve similar issues in frequency mismatch in more conventional radio-frequency electronics, nonlinear frequency mixers are used, with myriad applications including radar, cellular phone service, and radio communications. Harmonic frequency mixers in particular enable the use of a single local oscillator to capture information from both the fundamental as well as higher-order harmonic frequency channels, bringing their information content down to lower, baseband frequencies for readout [106] (see Fig. 5-1c). Compact petahertz-electronic harmonic frequency mixers would enable field-resolved optical signal analysis spanning octaves of the optical spectrum within a single device. Here we demonstrate the use of plasmonic nanoantennas as lightwave electronic harmonic frequency mixers (see Fig. 5-1) for the field-resolved characterization of harmonic optical waveforms (PHz-scale).

To provide a more flexible, field-resolved readout of optical signals using electronic systems, early efforts in the 1970s aimed to extend electronic harmonic frequency mix-

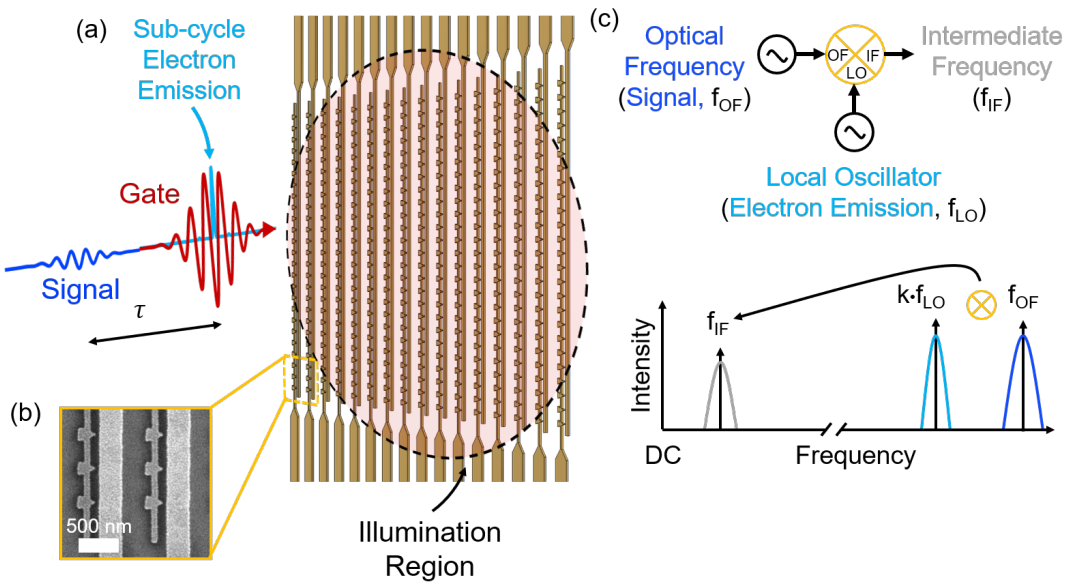

Figure 5-1: **Experiment Overview.** (a) A gate pulse illuminates the nanoantenna network and drives sub-optical cycle electron emission. A small signal is introduced over a variable delay. This small signal modulates the electron emission from the nanoantennas leading to the optical-frequency mixing process. (b) A representative scanning electron microscope image showing the nanoantennas. (c) The devices can be conceptualized as electronic harmonic frequency mixers (top schematic) with the sub-cycle electron emission serving as the local oscillator (LO, with central frequency f_{LO}), and the signal as the optical frequency input (OF, with central frequency f_{OF}). The mixing process (bottom schematic) provides a current signal at baseband (intermediate frequency, IF) for detection of harmonics of the local oscillator kf_{LO} (right plot). Here the baseband response for field-resolved sampling of the signal is measured as a function of delay τ.

ing techniques to mid-infrared frequencies (up to 88 THz) using metal point-contact diodes [106]. However, progress stagnated until recent advancements in optical and nanofabrication technologies. Recent work has shown that nanoscale needle tips and plasmonic antennas having nanoscale vacuum channels act as nonlinear electronic diode elements similar to the earlier point-contact diodes [106], [107]. Through their carrier-envelope-phase sensitivity [11], [14], [15], [43], [44], [48], use in field sampling [17], [45], and measurements of their photoemission response [9], [12], [13], [41], [80], researchers have demonstrated that their electronic response can extend up to 1 PHz and beyond.

We show that the highly nonlinear, broadband electronic response of plasmonic

nanoantennas enables the extension of electronic harmonic frequency mixing into the petahertz regime for optical signal processing. In our proof-of-concept measurement, we use electrically-connected nanoantenna devices for accurate amplitude and phase-resolved readout of both the fundamental (0.177 PHz, 1690 nm) and second harmonic (0.353 PHz, 850 nm) fields of an optical waveform using only the fundamental waveform as the local oscillator (see Fig. 5-1 for an overview). Our measurements demonstrate how under multicycle operation, petahertz-electronic nanoantennas can be conceptualized and used as frequency mixers to greatly extend the bandwidth of time-domain, field-resolved optical detection beyond one octave of spectral coverage without the need for prior nonlinear conversion in crystals, spectral phase retrieval, single-cycle waveform generation, or carrier-envelope-phase stabilization. Our study highlights a crucial connection between light-based electronics and traditional nonlinear electronics. This connection serves to unite the electronics and optical physics communities, filling a gap in existing literature predominantly focused on strong-field and optical physics. By clarifying this link, this work acts as a bridge between these two fields.

The increased bandwidth obtained through harmonic mixing enables seamless amplitude- and phase-resolved characterization of nonlinear processes of interest, such as solid-state harmonic generation [63], [108]–[116], coherent Raman scattering [117], [118], and multiphoton processes [119]–[122], without the need for nonlinear frequency conversion, spectral phase retrieval, or a spectrally-overlapped local oscillator reference. In the far term, we anticipate lightwave-electronic harmonic mixer devices will provide basic building blocks for field-resolved electromagnetic signal detection and processing at optical frequencies.

5.2 PHz Harmonic Mixing for Optical Waveform Analysis

Recent work has shown that cross-correlation using the nonlinear photoemission from gases and nanostructures as the electronic readout enables field-resolved optical waveform characterization with sub-cycle resolution [17]–[22], [45], [46], [81], [83], [123], [124]. Each technique starts with a strong gate waveform that drives sub-cycle photoelectron emission (red curve in Fig. 5-1a). A weak signal (blue curve in Fig. 5-1a) is then either polarized along the gate and perturbs the photoemission response (perturbative method, see for *e.g.* Refs. [17], [21], [125], [126]) or is cross-polarized and shifts the electron momentum (streaking-like method, see for *e.g.* Refs. [83], [123], [127], [128]) as a function of delay τ. The streaking-like method results in a time-integrated interaction over the signal field, resulting in a delay-dependent photocurrent that is proportional to the signal's vector potential. For the perturbative method, however, the delay-dependent current relates directly to the signal's electric field through an instantaneous coupling between the signal and gate waveforms analogous to the coupling of voltage waveforms in nonlinear electronic frequency mixers. Here we focus on the perturbative method.

In this section, we first briefly introduce how these perturbative, nonlinear cross-correlation measurements provide amplitude and phase information of the signal. Our treatment focuses on the field-driven photoemission response from asymmetric nanoantenna structures like those used in our experiment but could be extended to other systems. Following this introduction, we show how these perturbative cross-correlation measurements can be viewed through the lens of nonlinear electronic frequency mixing. This framing allows us to better understand how nonlinear, field-driven photoelectron emission devices provide field-resolved readout across spectral harmonics using only a single local oscillator without the need for carrier-envelope-phase stabilization. It also provides a framework for understanding how we might translate technologies used now at lower frequencies (*e.g.* RF or microwave) into the petahertz regime.

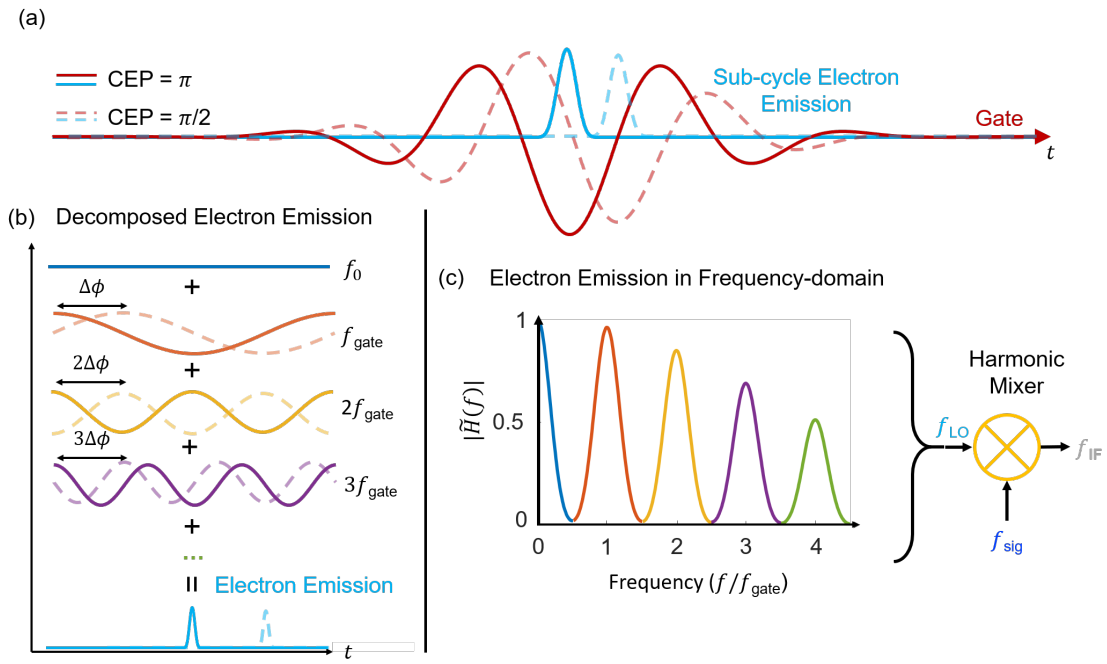

Figure 5-2: **How sub-cycle emission enables harmonic mixing.** (a) Depiction of sub-cycle electron emission calculated using the FN tunneling rate (teal) driven by a single-cycle pulse for a CEP $= \pi$ and CEP $= \pi/2$ (dashed). (b) The sub-cycle electron emission comprises integer harmonic frequencies of the gate frequency f_{gate}, collectively contributing to the sub-cycle electron emission. At each of these frequencies, a phase shift occurs when the CEP of f_{gate} is altered by $\Delta\phi$ (here $\pi/2$). Specifically, for the fundamental frequency f_{gate}, the phase shift corresponds to $\Delta\phi$, while the second harmonic corresponds to $2 \times \Delta\phi$, the third harmonic to $3 \times \Delta\phi$, and subsequent higher harmonics to $k \times \Delta\phi$, k is the harmonic order. (c) The calculated transfer function amplitude $|\tilde{H}(f)|$ for a 4-cycle Gaussian pulse with a center frequency of 0.177 PHz.

When driven by intense, few-cycle waveforms, sub-optical-cycle tunneling current [11], [15] can be emitted from a nanoantenna (connected triangle features in Fig. 5-1a,b) to a collector (adjacent wires in Fig. 5-1a,b). This configuration leads to a half-wave rectified current response relative to the driving field at the antenna apex. In Fig. 5-2a we show a calculation of the sub-cycle electron emission (blue) as a function of a few-cycle gate field (red) for two different values of carrier-envelope phase (solid versus dashed lines). Note that we have used shorter gate pulse durations in Fig. 5-2 for illustration purposes. The current emission was modeled using the Fowler-Nordheim (FN) rate equation as described in Refs. [14], [17], [43]–[45], [77]

A nonlinear cross-correlation measurement similar to that discussed in Refs. [17], [20], [21] can be modeled by using a strong gate waveform which in addition to a weak signal waveform (to be measured). When the signal and gate are superimposed with the same polarization and the relative delay τ between the two is varied, the time-averaged charge transferred across the nanoantenna gap can be modeled as

$$I(\tau) = q \int_{-T_{\text{rep}}/2}^{T_{\text{rep}}/2} \Gamma[E_{\text{gate}}(t-\tau) + E_{\text{signal}}(t)]\, dt \tag{5.1}$$

where Γ is the FN equation. Provided that E_{signal} is sufficiently small, such that the electric field perturbation seen by the nanoantenna can be assumed to be linear and E_{gate} can be Taylor-expanded to the first order. The resulting expression is given by

$$I(\tau) \approx q \int_{-T_{\text{rep}}/2}^{T_{\text{rep}}/2} \Gamma[E_{\text{gate}}(t-\tau)] + [\frac{d\Gamma}{dE}|_{E_{\text{gate}}(t-\tau)} \cdot E_{\text{signal}}(t)]\, dt \tag{5.2}$$

In this equation, the integral of the second term corresponds to the measured electric field waveform. This integral represents the small-signal cross-correlation between $\frac{d\Gamma}{dE}|_{E_{\text{gate}}(t-\tau)}$ and $E_{\text{signal}}(t)$ which we denote as $I_{cc}(\tau)$. Since this expression represents a cross-correlation, in general, the Fourier-transformed expression can be written as $\tilde{I}_{cc}(\omega) \approx \mathcal{F}[\frac{d\Gamma}{dE}|_{E_{\text{gate}}}]^* \cdot \tilde{E}_{\text{signal}}(\omega)$ where $\tilde{H}(\omega) = \tilde{I}_{\text{cc}}(\omega)/\tilde{E}_{\text{signal}}(\omega) = \mathcal{F}[\frac{d\Gamma}{dE}|_{E_{\text{gate}}}]^*$ is the full complex frequency response of the output relative to the signal field, which is plotted as a function of in Fig. 5-2c.

Note that in Fig. 5-2c we see that the detector frequency response contains frequency components at harmonic orders both higher and lower than that of the central frequency of the gate. The operating principle behind this is identical to that of a nonlinear electronic harmonic frequency mixer where the gate generates the local oscillator with $f_{\mathrm{LO}} = f_{\mathrm{gate}}$, f_{LO} being the local oscillator frequency and f_{gate} the central frequency of the gate waveform. Due to the high nonlinearity of the FN tunneling rate Γ and half-wave rectification, the current response contains frequencies outside of the optical local oscillator centered at every integer harmonic [45]. This is visualized in Fig. 5-2b where we show how the sub-cycle burst in charge over one period can be expressed as a sum of harmonic frequency components. These electronic frequency components effectively serve as frequency-distributed local oscillators that mix with the small signal. The difference frequency components then provide the baseband response for amplitude and phase-resolved readout.

Conceptualizing the devices as electronic optical frequency mixers aids in describing important properties of the devices. First, it becomes apparent that carrier-envelope phase (CEP) locking of the gate and signal pulse is not a requirement for amplitude and phase-resolved waveform readout even for the case of signals comprised of higher-order harmonics provided that the gate and signal exhibit relative phase locking. Consider the case of a perfectly sinusoidal gate (*i.e.* local oscillator) and signal functions, where the signal is a harmonic of the gate. Let the signal then be a harmonic of the gate frequency $f_{\mathrm{sig}} = k f_{\mathrm{gate}}$ as represented in Fig. 5-1c. We can then represent $\frac{d\Gamma}{dE}|_{E_{\mathrm{gate}}(t-\tau)}$ as an expanded series of harmonics of the gate frequency

$$\frac{d\Gamma}{dE}|_{E_{\mathrm{gate}}(t-\tau)} = h_0 + \frac{1}{2}\left(\sum_{n=1}^{\infty} \tilde{h}_n e^{in\varphi} e^{i2\pi n f_{\mathrm{gate}}(t-\tau)} + \mathrm{c.c.}\right) \tag{5.3}$$

where φ represents the absolute phase shift of the gate, analogous to the CEP for the case of a pulsed gate. Likewise, the signal is represented by

$$E_{\mathrm{signal}}(t) = \frac{1}{2}\tilde{a}_k e^{ik\varphi + \Delta\varphi} e^{i2\pi k f_{\mathrm{gate}} t} + \mathrm{c.c.} \tag{5.4}$$

where $\Delta\varphi$ represents any remaining phase difference in addition to $k\varphi$. The DC output response is then formed by the multiplication of conjugate and non-conjugate coefficients of $\tilde{h}_k$ and $\tilde{a}_k$ and is found to be

$$I_{\mathrm{cc}}(\tau) = \frac{1}{4}\tilde{h}_k^* \tilde{a}_k e^{i2\pi k f_{\mathrm{gate}}\tau} e^{i\Delta\varphi} + \mathrm{c.c.} \tag{5.5}$$

Note that since the signal and current responses are both phase-locked to the local oscillator (gate), the absolute phase terms φ always cancel and the harmonic mixing response is not sensitive to any fluctuations of the absolute phase φ.

These behaviors translate directly to the case of pulsed gate and signal inputs. A finite envelope of the gate pulse leads to a broadening of the harmonic pass bands as shown in Fig. 5-2c. These shifts are equal and opposite to those of optically-generated harmonic pulses meaning that so long as the source of harmonics and the nonlinear optical radiation exhibit relative phase locking, the measured response does not depend on the absolute carrier-envelope phase. We note here that absolute CEP information is effectively lost for a multi-cycle gate and a CEP-unstable laser. However, using a near single-cycle gate with a CEP-stable laser would allow one to extend this field-resolved measurement to a sampling measurement where the true electric field is measured, rather than a measurement of an ensemble of CEP values.

In addition to highlighting the role of CEP dependence on the readout, we see the importance of high nonlinearities and rectification in extending device bandwidth across harmonics. While one can certainly obtain a mixing response via conventional heterodyning and homodyning using an E^2 detector (*e.g.* a photodiode) [129], we see from this analysis that an E^2 current response without rectification would not yield higher harmonic components in the electronic response. But higher harmonic terms appear at every integer harmonic for higher-order nonlinearities and half-wave rectification. For the plasmonic detectors in this work, these nonlinearities can exceed E^{10}.

To further illustrate this absolute phase cancellation for the case of a pulsed gate and signal, time-domain simulations were performed using a 10-cycle Gaussian pulse

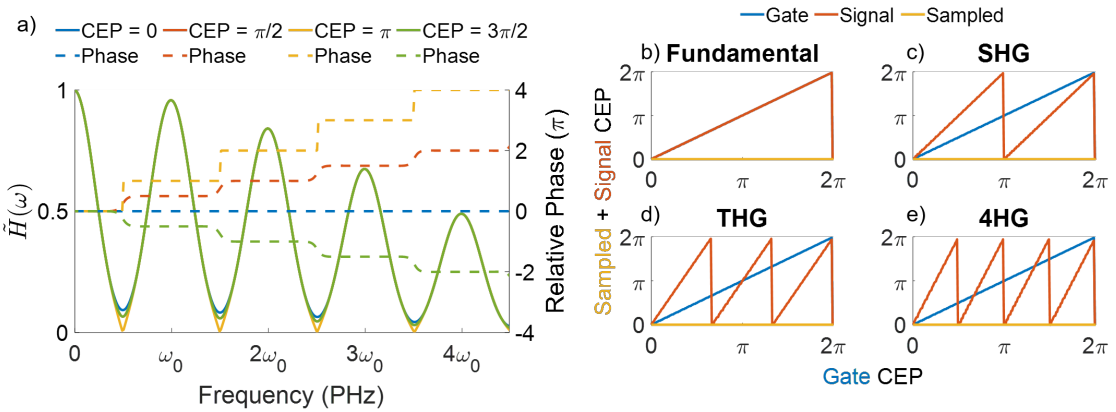

Figure 5-3: **Simulations of the electron emission and how CEP affects sampling of higher order harmonics.** (a) CEP-dependent frequency response and the corresponding relative phase using a 4-cycle Gaussian pulse with a center frequency of 0.177 PHz. (b) CEP of the measured field using a 10-cycle gate and 2-cycle signal that are both 0.177 PHz where the CEP of both pulses are linearly ramped from 0 to 2π. The blue, orange, and yellow lines correspond to the CEP of the gate, signal, and measured electric field waveform, respectively. (c) The CEP of the measured field when the 10-cycle gate is 0.177 PHz and the 2-cycle signal is the second harmonic of the gate at 0.353 PHz. (d) The CEP of the measured field when the 10-cycle gate is 0.177 PHz and the 2-cycle signal is the third harmonic of the gate at 0.528 PHz. (e) The CEP of the measured field when the 10-cycle gate is 0.177 PHz and the 2-cycle signal is the fourth harmonic of the gate pulse at 0.704 PHz.

at 0.177 PHz as the gate and a 2-cycle signal at frequencies of various integer harmonic orders (described in further detail in 3.6.2 and 5.2). For the sampling simulations, we generate a 10-cycle transform-limited Gaussian pulse for E_{gate} (0.177 PHz) and various 2-cycle E_{signal}. We use the Fowler-Nordheim equation (Γ) and numerically calculate the current cross-correlation by

$$I_{cc}(\tau) \propto \int_{-T_{\text{rep}}/2}^{T_{\text{rep}}/2} \Gamma(E_{\text{gate}}(t) + E_{signal}(t))\, dt$$

using a ratio of signal to the gate of 0.001.

To investigate the effect of CEP on the measured electric field waveform, we simultaneously increased the CEP of both the gate and signal pulses linearly from 0 to 2π in individual simulations. We tracked the resulting sampling response for each simulation and found that, regardless of the CEP of the gate and signal pulses, the measured electric field always had a CEP of 0, as shown in Fig. 5-3b. Next, we kept

the same gate conditions (10-cycle Gaussian at 0.177 PHz) and changed the signal pulse to a two-cycle SHG, THG, and 4HG pulse, with the signal CEP being 2, 3, and 4 times the gate CEP, respectively. This resulted in a measured electric field with a CEP of 0, as illustrated in Fig. 5-3c, d, e. These results can also be seen in the group delay in the frequency domain in Fig. 5-3a, where the group delay is constant.

5.2.1 Phase information from harmonic mixing

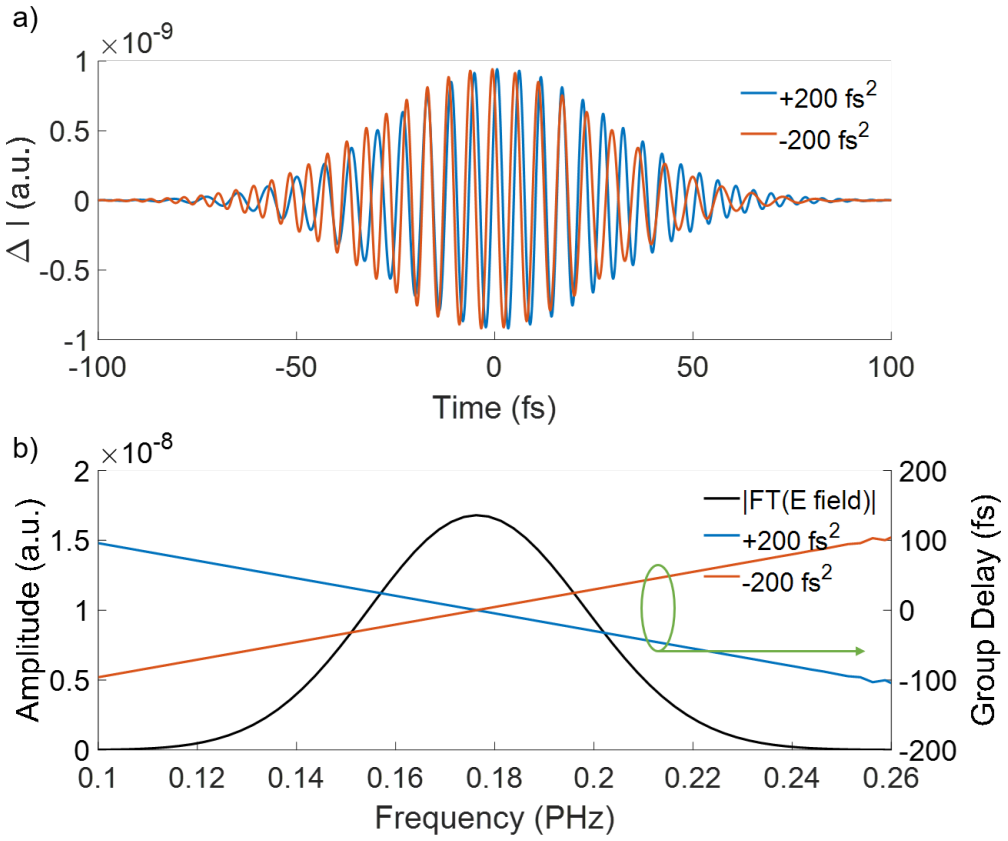

Figure 5-4: **Simulated sampling with a non-zero GDD signal pulse.** (a) 2-cycle 0.177 PHz signal pulse with + 200 fs^2 (blue) and - 200 fs^2 (orange) GDD measured using a 2-cycle 0.177 PHz gate pulse. (b) The corresponding Fourier-transformed measured fields in (a) are shown as the black line while the group delays are shown in blue and orange.

In phase retrieval techniques like FROG, the sign of the phase is not determined due to the integral being proportional intensity, meaning that the sign of the phase

is lost.

$$I_{\text{FROG}} = \left| \int E_{sig}(t,\tau)\exp(-i\omega t)dt \right|^2 \tag{5.6}$$

where E_{sig} is proportional to $E(t)|E(t-\tau)|^2$. With harmonic frequency mixing, we have relative phase information. When we measure our time-domain trace, we directly take our data and FFT into the frequency domain and take the derivative of the phase. To demonstrate that we have the sign of the phase, we perform sampling simulations using a 1690 nm 2-cycle pulse as the signal and gate. The gate pulse has 0 fs^2 GDD and we chirp the signal pulse with + and - 200 fs^2 GDD. The corresponding field we measure in time is different depending on the GDD in the pulse Fig. 5-4a. In the frequency domain, the sign of the GD is resolved as shown in Fig. 5-4b.

5.3 Design of Nanoantenna

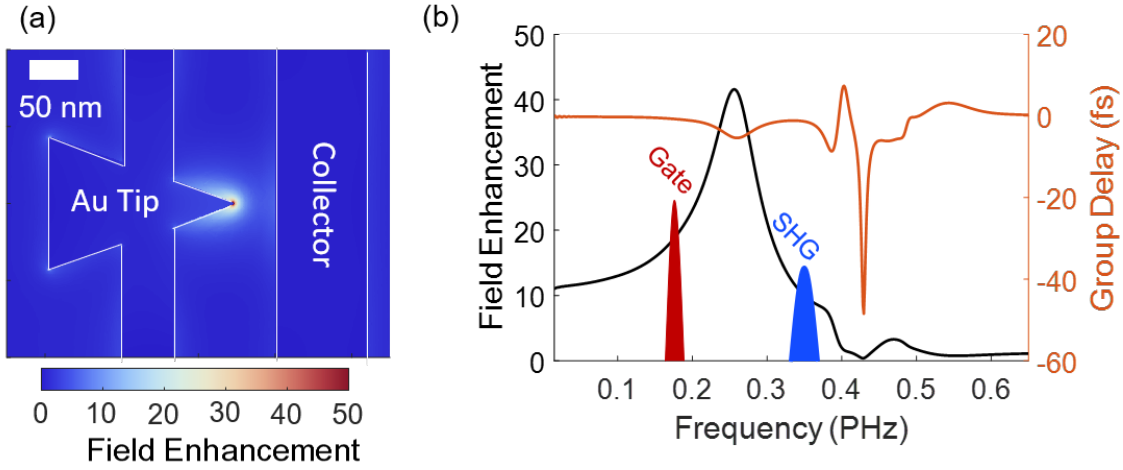

Figure 5-5: **Nanoantenna design.** (a) Finite-difference-time-domain (FDTD) simulation of the electric field enhancement at the tip of a gold nanoantenna. (b) FDTD simulation of the field enhancement and group delay imparted by the antenna response as a function of frequency. Within the spectrum, we highlight the experimental frequencies used with the gate at frequency 0.177 PHz and a higher frequency signal at 0.353 PHz, which corresponds to the second harmonic of the gate (SHG).

In our measurements, we used an asymmetric nanoantenna design as shown in Fig. 5-5a as this naturally breaks inversion symmetry and enables frequency response ($\tilde{H}(\omega)$) to have both even and odd integer harmonics [130]. Gold was chosen as

the antenna material and fused silica as the substrate. In Fig. 5-5b we plot the frequency-dependent field enhancement (black curve) and group delay (red curve) at the antenna apex relative to the incident light for our chosen design. The spectral regions covered by the fundamental (shaded red) and its second harmonic (shaded blue) are also shown for reference. The nominal nanoantenna geometry was chosen to have a resonant frequency between that of the fundamental and second harmonic, corresponding to a triangle base width of 180 nm and a height of 240 nm. This choice was for two reasons. First, it results in a compromise where the fundamental and second harmonic both have maximal field enhancement ($\approx 15\times$ and $\approx 10\times$, respectively). Second, since the fundamental and second harmonic both excite the antennas off-resonance, they experience a negligible amount of intensity reshaping and group delay dispersion (less than 2.5 fs change in group delay over the bandwidth of the fundamental and second harmonic), meaning that the excited field waveforms at the antenna apex are not significantly reshaped in time relative to the incident field waveforms.

For the operation of the harmonic mixer, there are two crucial elements one can control, the gate pulse and the design of the nanoantenna. In our measurements, we carefully chose the gate and signal frequencies such that they are not resonant with the nanoantenna to demonstrate that the large field enhancements due to the plasmonic resonance are not necessary. In our design, we chose an asymmetric design as shown in Fig. 5-5a as this naturally breaks inversion symmetry and enables frequency response ($\tilde{H}(\omega)$) to have both even and odd integer harmonics [130]. Next, we carefully designed the gold nanoantenna with a base of 180 nm and a height of 240 nm such that the higher frequencies of the field enhancement would have field enhancements ≈ 10 which can be achieved with other metals without plasmonic resonances (e.g. platinum, see Chapter 3). With gold, there is a fundamental limit to how high of a frequency the electrons can respond and this is due to the interband transitions happening at ≈ 2.5 eV. In Fig. 5-5b, the field enhancement localized at the tip apex is shown with the gate pulse, and the corresponding second harmonic signal is shown in red and blue, respectively. For these gate and signal pulses, there

is <5 fs of group delay imparted, leading to negligible changes in the measured fields.

5.4 Experimental Setup

5.4.1 Methods

Nanofabrication

We started with 1 cm × 1 cm fused silica pieces (MTI Corp.) and cleaned them using piranha for 10 minutes before use. For the nanoantenna network fabrication, we spin-coated polymethyl methacrylate A2 (Microchem) at 2,750 revolutions per minute and baked at 180 °C for 2 minutes. Afterward, DisCharge H2O X2 (DisChem Inc.) was spun at 3,000 revolutions per minute so that charging did not occur during the electron beam lithography write. The electron beam lithography was performed at 125 keV with a dose ranging from 4000-6000 μC/cm^2 with proximity effect correction. Various doses are assigned to each fabricated chip to account for process variation, ensuring a diverse array of nanoantenna networks for testing purposes. See the appendix for further details. Development of the exposed polymethyl methacrylate samples was done at 0 °C in a solution of 3:1 2-propanol to methyl isobutyl ketone for 50 seconds. Electron beam evaporation was performed at 2×10^{-6} Torr where we first deposited a 2 nm titanium adhesion layer, then 20 nm of gold. Lift-off was performed by submerging the samples in a 65 °C solution of N-methyl pyrrolidone (Microchem) for one hour.

Contacts were made to the nanoantenna using photolithography. We spin coat nLOF 2035 at 3,000 revolutions per minute, then bake the resist at 110 °C for 90 seconds. The exposure was performed using a maskless aligner with a wavelength of 375 nm and at a dose of 300 300 mJ/cm^2. After exposure, we do a post-exposure bake at 110 °C for 90 seconds, then develop for 90 seconds in AZ726. We then use electron beam evaporation to deposit 10 nm of a titanium adhesion layer and 50 nm of gold. Liftoff was performed at room temperature in a solution of acetone for at least 6 hours. The samples were ashed for 30 seconds, then mounted on a printed

circuit board (PCB), and wire bonded.

Measurement setup and methods

The samples on the PCB were used as-is in ambient conditions and the output was connected to a trans-impedance amplifier with a gain of 1 V/nA (FEMTO). We measured the signal pulse-induced current (I_{cc}) through a lock-in measurement referenced by chopping the signal arm at $\sim$ 277 Hz. The x- and y-channels of the lock-in are output to an oscilloscope (Keysight) with a sampling rate of at least 25-50 kSa/s. Before the measurements, we illuminated the device with the gate pulse and ensured that the photocurrent remained constant for at least several minutes. To temporally control the delay between the signal and gate pulse, we placed the gate pulse on a closed-loop piezo stage (Piezosystem Jena) with $\pm$ 14 nm (0.05 fs) repeatability. The scan time for each trace was set to 20 seconds and averaged accordingly. We continuously scan the delay stage in a certain direction with constant velocity to reduce measurement variation.

In every measurement, we used neutral density (ND) filters to control the power of the signal and gate pulses. After recombining the two pulses, we placed a linear film polarizer with an extinction ratio of $\geq 10^5$ (across all wavelengths) to ensure the two beams were horizontally polarized. Once collinearity was ensured between the gate and signal arm, both the signal and gate pulses were focused onto the nanoantenna chip through a reflective objective (Ealing). See the next section for the optics layout.

For frequency doubling, we used a type 1, 1.5 mm thick beta-barium borate (β-BaB_2O_4, BBO) crystal with $\theta = 24$ $\phi = 90$ to generate the second harmonic (SHG) of $f_{\text{gate}} = 0.177$ PHz. The SHG (0.353 PHz) is filtered using a 0.207 PHz (1450 nm) high-frequency pass filter with ND 2 at 0.177 PHz along with a broadband achromatic half waveplate used to rotate the SHG polarization from vertical to horizontal, to match the gate pulse. Note that the integration time was crucial for accurate measurement of the higher frequencies.

We padded the retrieved waveforms with zeros before taking an FFT to improve spectral resolution. This was justified as the spacing between consecutive pulses in

time in the experiment is much larger (one microsecond) than the time window of the retrieved waveforms.

To calculate the bare field strengths, we took the pulse energy and converted it to field strength using the corresponding intensity and a Gaussian beam approximation in time/space.

In our sampling simulations, the Fowler-Nordheim equation, expressed as $\Gamma = \alpha\phi^{-1}E^2\exp\left(-\beta\phi^{3/2}/E\right)$, was utilized. Here, α is 1.54×10^{-6} A eV V^{-2}, β is 6.83 $eV^{-3/2}V$ nm^{-1}, ϕ represents the work function (taken as 5.1 eV), and E denotes the electric field. With this equation, we numerically calculated the current cross-correlation by

$$I_{CC}(\tau) \propto \int \Gamma(E_{\text{gate}}(t-\tau) + E_{\text{signal}}(t))\,dt$$

using a ratio of signal to the gate of 0.03.

5.4.2 Laser source characterization and optics layout

We used a LightConversion optical parametric amplifier pumped by a Yb:KGW laser pulse picked to 1 MHz (Cronus 3P) for our experiments. The idler output was compressed using a prism pair.

We performed frequency-resolved optical gating (FROG) measurements of the pulses in time to provide a reference to compare against the measured fields. For frequency-resolved optical gating (FROG) retrieval, we used the RANA approach (see Ref. [131]) as a robust retrieval algorithm. The MATLAB code is available on the Trebino Group website. The error for the reconstruction shown is 5.510^{-3}. In Fig. 5-7a, b we show the measured and retrieved spectrograms of the 10-cycle 1690 nm pulse used in the measurements. The degenerately measured fields in Fig. 5-7c show relatively good agreement in the time domain with the FROG result. In both traces a small side lobe is present in time near 65 fs. The retrieved pulse duration was 58 fs FWHM and the measured pulse duration was 57 fs FWHM. Lastly, the frequency domain comparison between the measured intensity, retrieved intensity, and the grating-based spectrometer is shown in Fig. 5-7d. The measured group delay

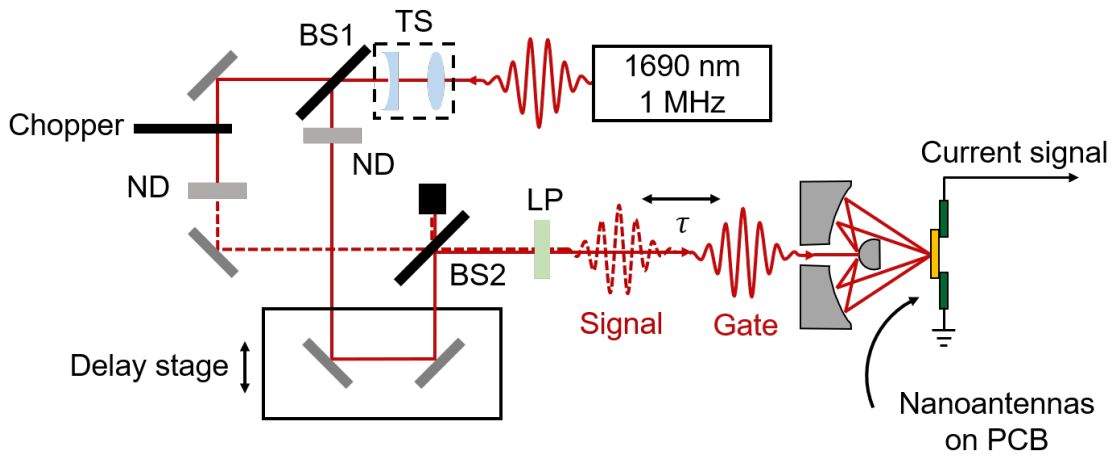

Figure 5-6: **Schematic of the experimental setup for the degenerate measurement of $f = 0.177$ PHz.** The laser light was split using a beamsplitter (BS). One arm has a delay stage and was used as the gate pulse, while the signal arm was chopped and neutral density filters were used to attenuate the signal. Eventually, the two pulses are recombined using an identical beamsplitter before being sent to a reflective objective where they are focused onto the nanoantenna devices.

and retrieved group delay show very good agreement.

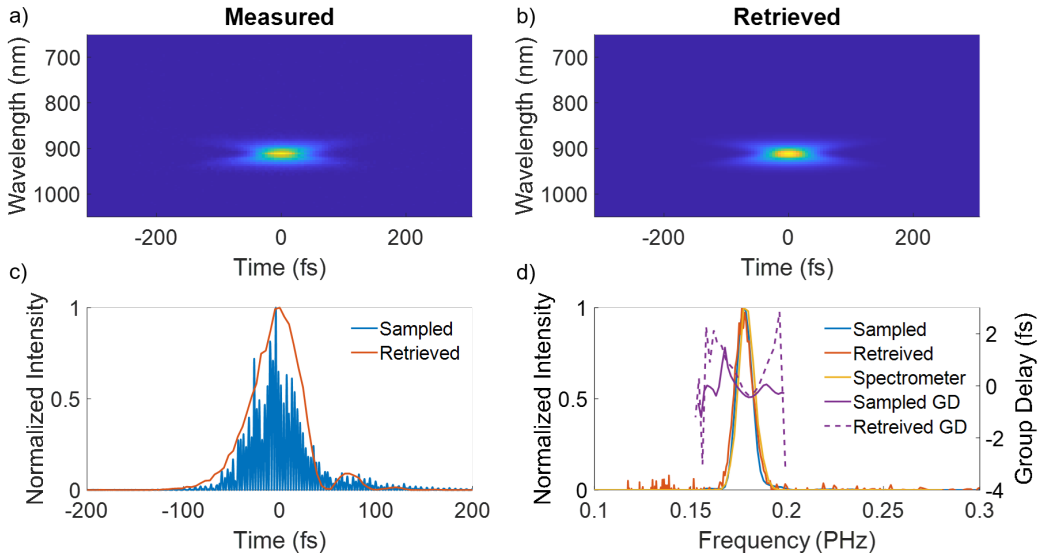

Figure 5-7: **Frequency-resolved optical gating (FROG) of the $f = 0.177$ PHz pulse.** The frequency-resolved optical gating (FROG) (a) measured and (b) retrieved spectrograms. (c) A comparison of the squared modulus of measured optical fields and the retrieved pulse versus time. (d) A comparison of the squared modulus of the Fourier transformed measured fields, retrieved pulse versus frequency, a spectrometer reference, group delay from the measured optical fields, and the retrieved group delay.

In Fig. 5-7a, b we show the measured and retrieved spectrograms of the 10-cycle 1690 nm pulse used in the measurements. The degenerately measured fields in Fig. 5-7c show relatively good agreement in the time domain with the FROG result. In both traces a small side lobe is present in time near 65 fs. The retrieved pulse duration was 58 fs FWHM and the measured pulse duration was 57 fs FWHM. Lastly, the frequency domain comparison between the measured intensity, retrieved intensity, and the grating-based spectrometer is shown in Fig. 5-7d. The measured group delay and retrieved group delay show very good agreement.

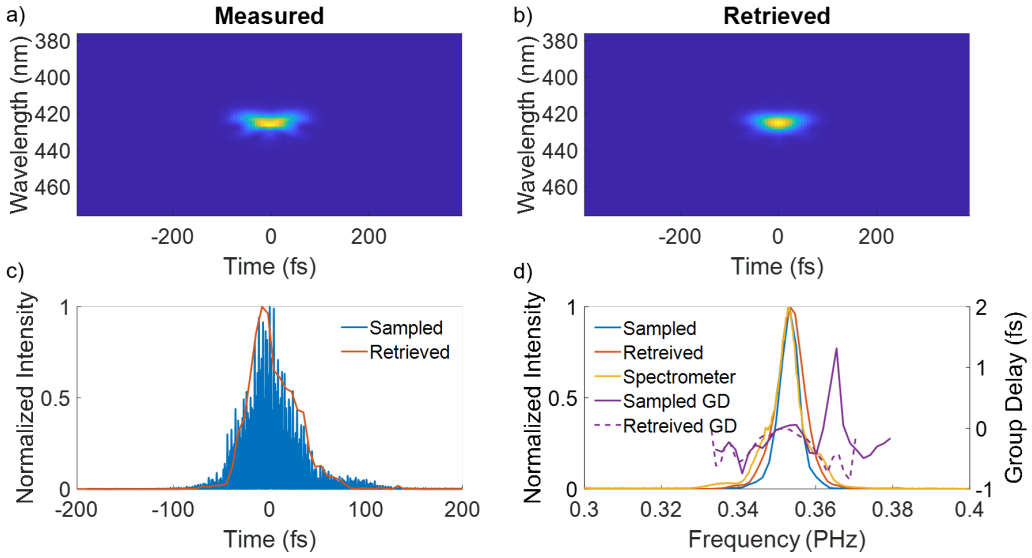

Figure 5-8: **Frequency-resolved optical gating (FROG) of the $f = 0.353$ PHz pulse.** The frequency-resolved optical gating (FROG) (a) measured and (b) retrieved spectrograms. (c) A comparison of the squared modulus of measured optical fields and the retrieved pulse versus time. (d) A comparison of the squared modulus of the Fourier transformed measured fields, retrieved pulse versus frequency, a spectrometer reference, group delay from the measured optical fields, and the retrieved group delay.

We performed FROG measurements on the SHG, and the measured and retrieved spectrograms of the SHG of the 10-cycle 1690 nm pulse used in the measurements are shown in Fig. 5-8a, b. The non-degenerately measured fields in Fig. 5-8c show relatively good agreement in the time domain with the FROG result. The retrieved pulse duration was 49 fs FWHM and the measured pulse duration was 48 fs FWHM. Lastly, shown in Fig. 5-8d is the frequency domain comparison between the measured intensity, retrieved intensity, and the grating-based spectrometer. The measured

group delay and retrieved group delay also show very good agreement.

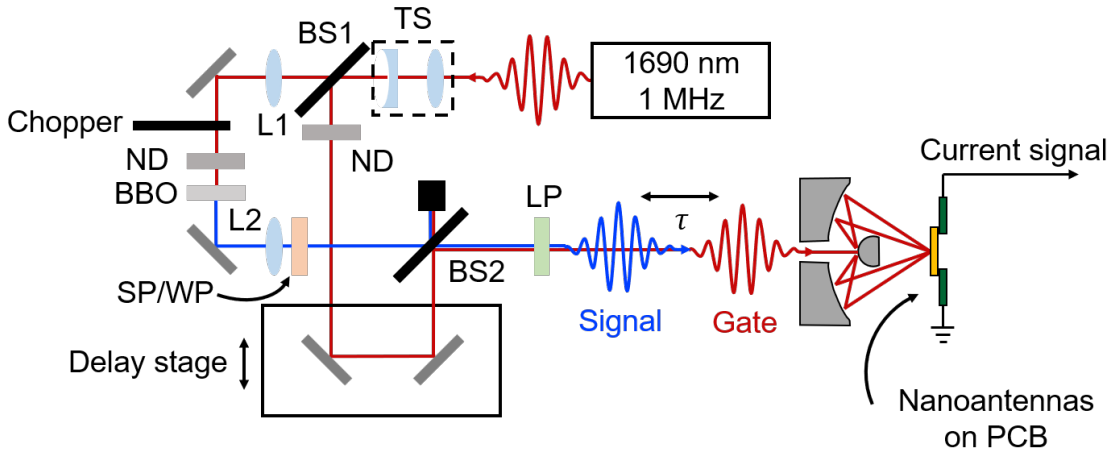

Figure 5-9: **Schematic of the experimental setup for the measurement of the $f_{\text{gate}} = 0.177$ PHz and $f_{\text{signal}} = 0.353$ PHz (SHG of 0.177 PHz).** The laser light first passes through a telescope and is split using a broadband beamsplitter (BS). One arm has a delay stage and was used as the gate pulse, while the chopped signal arm has a lens to focus onto the nonlinear crystal used to double the frequency and another lens was used to collimate the SHG. To control the SHG power, an ND filter was placed before the BBO and a 0.207 PHz (1450 nm) high-frequency pass filter (ND 2 at 0.177 PHz) was used to attenuate the residual $f = 0.177$ PHz and a broadband achromatic waveplate (WP) was used to rotate the SHG polarization from vertical to horizontal. The two pulses are recombined using an identical broadband beamsplitter before being sent to a reflective objective where they are focused onto the nanoantenna devices

For the non-degenerate measurement of 0.353 PHz (850 nm) using a 0.177 PHz (1690 nm) gate, we modified the previously shown setup by adding a telescope for the 1690 nm gate to control the beam spot size before focusing on the nanoantennas. This modification was performed since when the SHG was generated and collimated using the type-1 1.5 mm thick BBO the beam spot was smaller in size before entering the objective. We also used a shortpass filter which was ND2 at wavelengths longer than 1450 nm as well as an achromatic half waveplate to rotate the SHG such that its polarization matched the gate pulse polarization. After the second beamsplitter, the pulse pair passed through a linear polarizer which had an extinction ratio that is $> 10^5$ at 1690 nm and $> 10^6$ at 850 nm.

5.5 Results and Discussion

In this section, we present experimental results demonstrating PHz harmonic mixing through field-resolved optical waveform characterization. First, we characterize our device by measuring the current as a function of peak field strength. Ensuring that we are operating in the optical tunneling regime, we performed degenerate waveform characterization where we used a 10-cycle near-infrared gate and signal waveforms both having a central frequency of 0.177 PHz, corresponding to when $k = 1$ in Eqn. 5.4. This measurement illustrates the capability of multicycle field-resolved waveform analysis without the need for CEP stabilization. We next present the characterization of the second harmonic waveform (0.353 PHz) using the fundamental (10-cycle 0.177 PHz) as the gate to demonstrate harmonic frequency mixing, corresponding to $k = 2$ in Eqn. 5.4. The results are shown in Fig. 5-11.

5.5.1 Device characterization

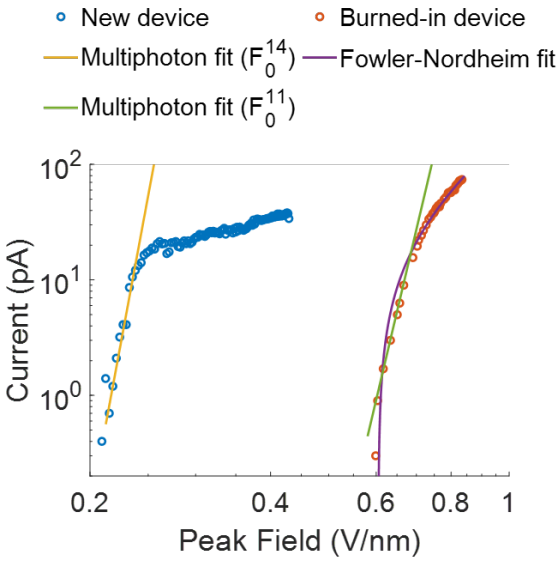

Figure 5-10: **Current as a function of peak field.** Current output of the gold nanoantenna network as a function of peak field with a new device and with a device after performing measurements for >4 hours using the 10-cycle $f = 0.177$ PHz.

There are numerous papers demonstrating that such nanoantenna devices operate in the optical field emission regime using 10s to 100s of pJ pulse energies with few-

cycle pulses [11], [14], [15], [43], [45]. To confirm our devices are operating in the Fowler-Nordheim regime with the 10-cycle $f_{LO} = 0.177$ PHz gate pulse, we measured the current output versus peak field shown in Fig. 5-10 with a typical device that has never been used for waveform measurements, denoted as "New Device", and a device which we used for more than 4 hours of illumination (denoted as "Burned-in device"). We fit the low-pulse-energy section of the new device current vs peak field curve to the conventional multiphoton photoemission form, $I_{MP} \propto |F_0|^{2N}$, where F_0 is the incident peak field, finding a fit of N = 7. However, we note that there is a sharp turnover of the emission which is not fully understood.

While space charge might cause such a sharp turn over in the emission rate, we ruled this out after considering the emitted charge densities. Considering the close to 100 pA currents and the repetition rate of 1 MHz distributed over 306 antennas, we were generating 2 electrons per pulse per antenna. Given the length of the optical pulse of approximately 10 cycles, the electrons were very unlikely to interact within the same optical half-cycle. Furthermore, from Coulomb's law, we can calculate typical forces that would result in an electron 5 nm away from the tip in an electric field strength of $\approx 0.06\,\mathrm{V\,nm^{-1}}$, substantially lower than local fields of around $14\,\mathrm{V\,nm^{-1}}$.

An alternative explanation is that this is emission from a surface state due to an adsorbed molecule. This is consistent with our observation that after some time of operation, we observe that the needed energy for similar emission rates increases indicated by the shift to the right of the "Burned-in Device" (red dots in Fig. 5-10). Our interpretation is that during the process of using the devices, surface adsorbates are removed, and the emission approaches that is expected from Fowler-Nordheim tunneling from gold as noted in past works. In studying similar devices using field-emission from the application of DC biases, it was shown that similar behavior is due largely to water adsorption on the surface that is removed through UV radiation [99]. Here we feel this removal is due to the optical illumination and interaction at the tip from the gate.

We fitted the Fowler-Nordheim curve to the "Burned-in Device" data (green curve in Fig. 5-10) to demonstrate that the emission is indeed well-described by quasi-static

tunneling. We used the initial field of the optical waveform before enhancement in comparison with the field from this fit to determine the enhancement factor. The measured photocurrent and nonlinearity after long-term operation were sufficient to continue using the device for harmonic mixing and waveform detection. Our measurements presented in the main text operated at $\geq$0.8 V/nm, which corresponds to a Keldysh parameter of $\gamma \leq$0.6, indicating that we were operating in the tunneling regime.

Regarding device degradation, we note that previous work from Yang *et al.* ([44]) observed that modifying the antenna tips shifts its resonance and reduces peak field enhancement. This was attributed to reshaping due to heating from time-averaged power. In this study, we operated off-resonance and at lower repetition rates, significantly reducing average power density (by more than one order of magnitude). Consequently, we did not observe significant signal degradation over time after device "burn-in," as mentioned earlier.

5.5.2 Degenerate waveform analysis

Before performing the cross-correlation measurements, we first confirmed that the devices were operated in the optical-field emission regime through the analysis of current scaling with intensity by measuring the output current as a function of the incident gate pulse energy and verifying that the emission could be well-described through a quasi-static Fowler-Nordheim tunneling rate (see previous section and Fig. 5-10). Having confirmed operation in the optical-field emission regime, we then illuminated the antennas with a gate pulse with an energy of 5.4 nJ (0.85 V/nm) and a small signal with an energy of 4.4 pJ (24 V/μm) to obtain $I_{cc}(\tau)$ (red curve in Fig. 5-11). In the experiment, the signal arm was chopped and measured using lock-in detection to isolate $I_{cc}(\tau)$ from the constant background current. The small signal gain from the high nonlinearity of the optical-field emission response enabled the optical waveform analysis of signal pulse energies on the order of 1000$\times$ smaller than those of the gate. The measured optical period was 5.6 fs which matched the expected value for a frequency of 0.177 PHz. The pulse of the measured field was 57 fs full-width at

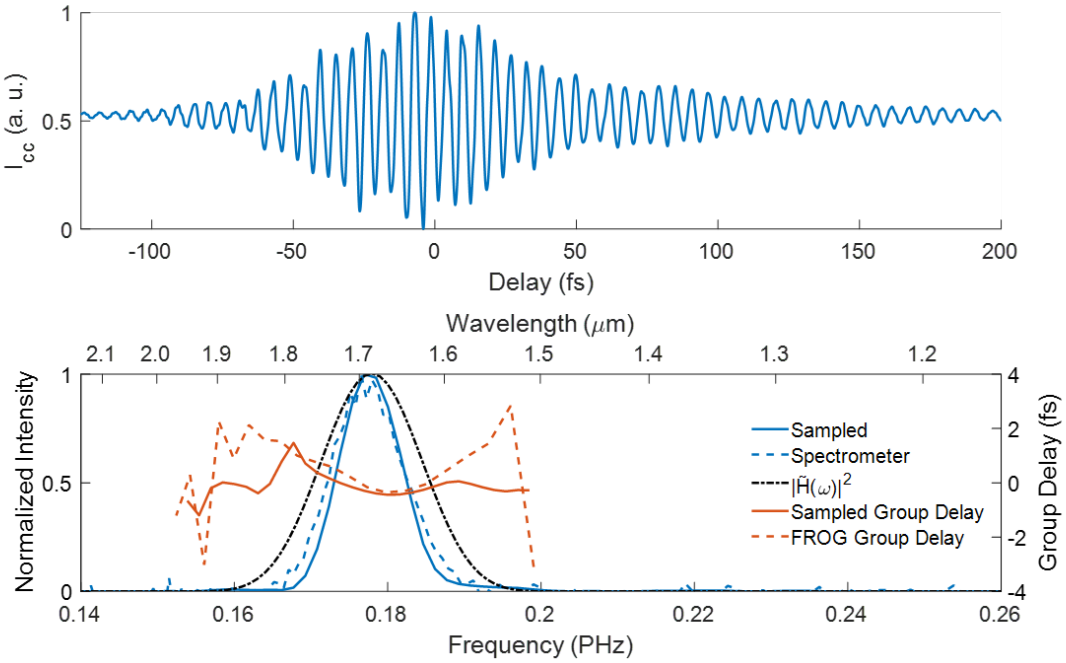

Figure 5-11: **Degenerate field-resolved waveform analysis of a 10-cycle 0.177 PHz pulse.** (a) The measured electric field and (b) the corresponding frequency-domain intensity of the measured electric field compared to a commercial spectrometer and the simulated frequency response. The extracted group delay from the measured optical field is compared to the group delay retrieved from FROG.

half maximum (FWHM), in close agreement with the 58 fs FWHM pulse duration retrieved FROG measurement (see Fig. 5-7c).

Spectral intensity and group delay analysis are shown in Fig. 5-11b. We find good agreement between $|\tilde{I}_{cc}(\omega)|^2$ (solid red line) and the spectral intensity as measured using a commercial grating-based indium gallium arsenide spectrometer (solid black line) after normalization. Also, the extracted group delay of $\tilde{I}_{cc}(\omega)$ (dashed red line) is shown to be concave up and agrees well with the group delay retrieved from the FROG measurement (dashed black line). These results further confirm that I_{cc} accurately represents the signal field of the fundamental to within a constant phase offset.

We note that in these comparisons, we have ignored the impact of the antenna response. To justify this, we simulated the electromagnetic response of the nanoantenna based on the experimentally fabricated geometry. The field enhancement and phase are plotted as a function of frequency in Fig. 5-1c, d. The results of the sim-

ulation show a nearly constant amplitude and group delay from 0.168 PHz to 0.191 PHz (1570 nm to 1784 nm), corresponding to the spectral extent of the signal pulse. The simulated field enhancement factor ranges from 17 to 22, and the group delay from -0.6 to -1.0 fs within this range, leading to negligible reshaping of the pulse.

5.5.3 Non-degenerate waveform analysis

We then performed the non-degenerate waveform characterization of the second harmonic signal waveform via harmonic mixing using the same 10-cycle gate as before ($f_{\mathrm{gate}} = 0.177\,\mathrm{PHz}$) with the signal being the second harmonic of the gate waveform ($f_{\mathrm{sig}} = 0.353\,\mathrm{PHz}$). We note that this measurement is different from other studies using both the first and second harmonic ($\omega - 2\omega$). The work of Arai et al. [32] utilizes $\omega - 2\omega$ for optical phase measurements, whereas Dienstbier et al. [80] use the $\omega - 2\omega$ to break symmetry for the application of ultrafast switching. In this measurement, we use a sufficiently weak second harmonic waveform to demonstrate field-resolved waveform characterization.

The second harmonic was generated by adding lenses and a type 1 beta-barium borate (β-BaB2O4, BBO) crystal to the signal arm of the MZI (see Fig. 5-9 for measurement schematic). We illuminated the antennas on the device using a pulse energy of 4.9 nJ (0.80 V/nm) for the gate and a pulse energy of 23 pJ (49 V/μm) for the second harmonic signal (after removal of the residual fundamental through filtering). The measurement of $I_{\mathrm{cc}}(\tau)$ using the second harmonic signal is shown in Fig. 5-11a (blue curve). The measured optical period was 2.8 fs matching the expected optical period for a center frequency of 0.353 PHz.

To verify the accuracy of the measured field, we again performed FROG and used a commercial grating-based silicon spectrometer as a reference in the same way as in the degenerate case. The pulse duration from our FROG measurement was found to be 49 fs FWHM which matches almost perfectly with the duration of $I_{\mathrm{cc}}(\tau)$, being 48 fs FWHM (see Fig. 5-8 for a comparison of FROG and $I_{\mathrm{cc}}(\tau)$). In Fig. 5-11c we find that $|\tilde{I}_{\mathrm{cc}}(\omega)|^2$ (solid blue line) is in general agreement with the spectral intensity measured using the silicon spectrometer (solid black line) after normalization. There

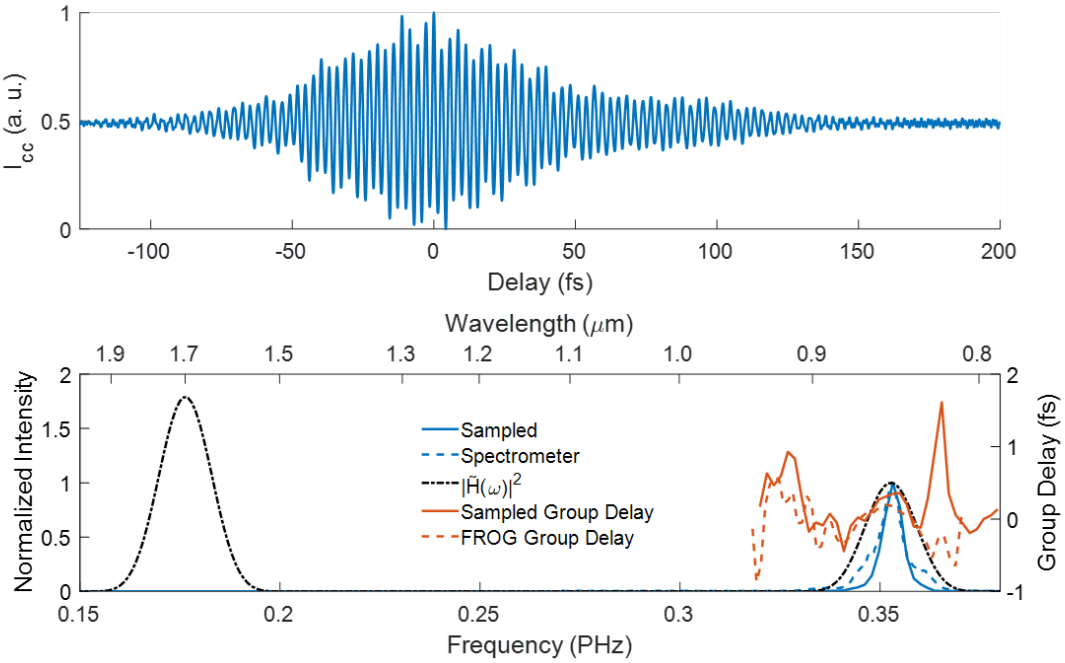

Figure 5-12: **Non-degenerate waveform analysis.** (a) Non-degenerate field-resolved waveform analysis of a $\omega_{\text{signal}} = 0.353$ PHz signal using a lower-frequency gate, $\omega_{\text{gate}} = 0.177$ PHz. (b) The corresponding frequency-domain intensity of the measured electric field compared to a commercial spectrometer and the simulated frequency response (at 0.353 PHz, the relative intensity is 2.3 × lower than 0.177 PHz). The extracted group delay from the measured optical field (orange solid curve) is compared to the group delay retrieved from FROG (dashed orange curve).

is only a discrepancy in the intensity of the spectral wings. However, the group delay of the $\tilde{I}_{\text{cc}}(\omega)$ (solid orange curve) is concave down and matches relatively well with the FROG-retrieved group delay (dashed orange curve). Together, these results lead us to conclude that $I_{\text{cc}}(\tau)$ accurately represents the second harmonic signal's field waveform within a constant phase offset.

As before, we ignored the amplitude and phase response of the nanoantenna. Again looking at the spectral field enhancement and group delay of the antenna response as shown in Fig. 5-1d, we see that over the spectral range of the signal from 0.333 PHz and 0.370 PHz (810 nm and 900 nm), the field enhancement amplitude and group delay were relatively constant, ranging from 8 to 12 and from -1.1 fs to -3.3 fs, respectively. As for the degenerate case, this leads to negligible pulse reshaping in the time domain.

Several aspects of this measurement are important to emphasize. First, given that the second harmonic generation used to generate the signal was phase-locked to the second harmonic of the field-resolved response as noted in Section 1, there was no need for CEP stabilization of the gate. Second, the nonlinearity of the mixing process enabled the phase-resolved, interferometric pulse readout without the need for nonlinear optical generation of a spectrally-overlapped local oscillator as would typically be required for all-optical homodyning or heterodyning techniques using a standard E^2 detector [129], [132]–[135]. Third is that the direct cross-correlation outputs accurately represented the fundamental and signal waveforms as confirmed using FROG without the need for any post-analysis, such as phase retrieval, or any change in the detector setup aside from the change in the signal waveform. Finally, we emphasize that for the case of the second harmonic measurement, the signal pulse was appreciably shorter than the gate (48 fs FWHM signal duration versus 60 fs FWHM gate pulse duration), and of a significantly higher carrier frequency. While techniques such as electro-optic sampling can also provide field information from non-spectrally overlapped signals, the signal frequency must be lower than that of the gate, with gate pulse envelopes shorter than the cycle time of the signal [70], [136]–[138].

5.6 Sampling Outside of the Optical Field Emission Regime

While the previous measurements demonstrate field-resolved waveform analysis using optical field emission, multiphoton processes can also be used for sampling based on the theoretical description described in Chapter 3.

We also performed degenerate waveform analysis using a 63-cycle pulse with a center frequency of 0.291 PHz (1030 nm) using an air-cooled 6 W LightConversion Carbide after characterizing the pulse using SHG FROG. To begin our measurement, we employed the built-in pulse picker to reduce the repetition rate down to 500 kHz from 1 MHz. We then directed the output of the laser through the MZI with

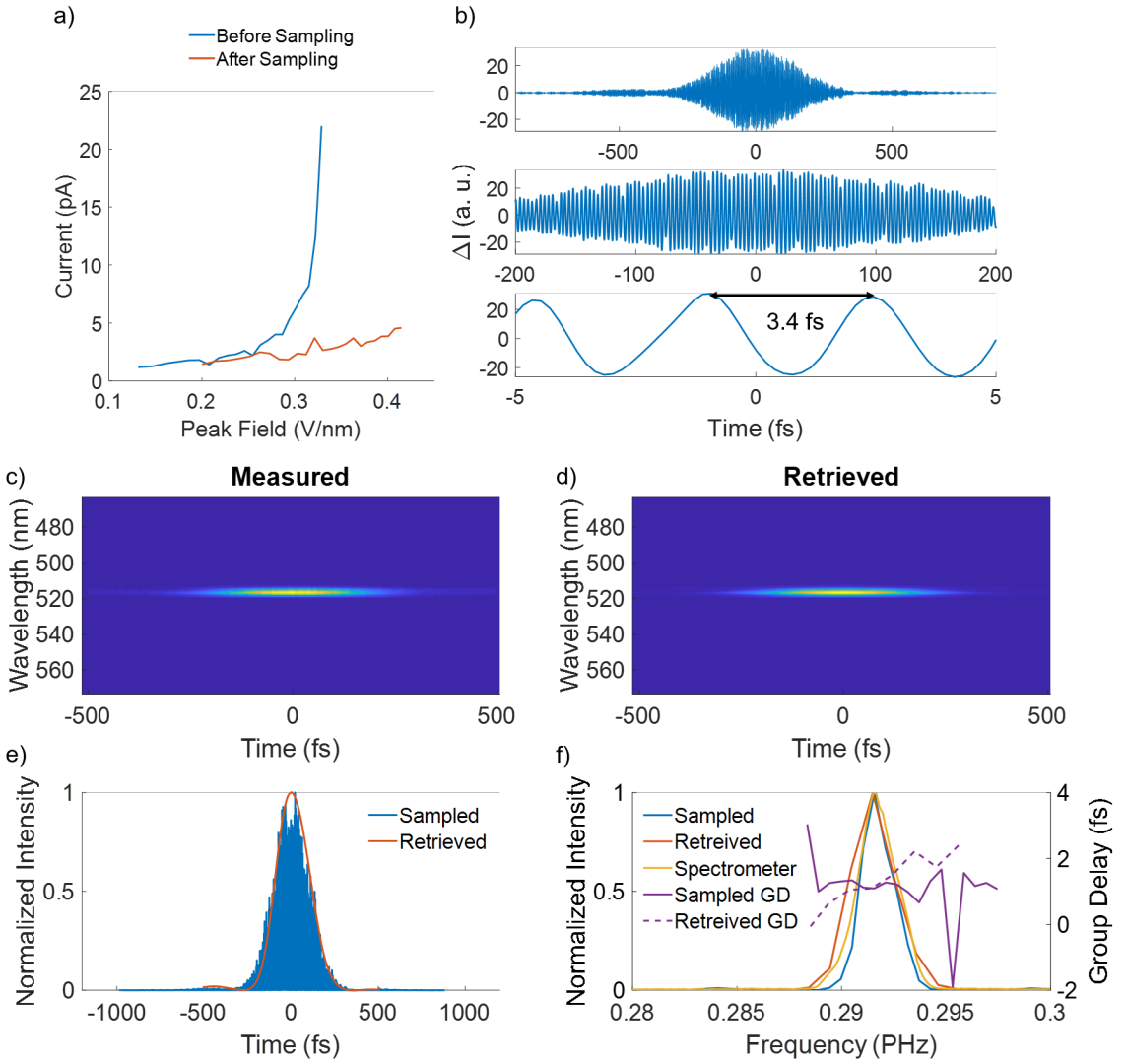

Figure 5-13: **Degenerate field-resolved waveform analysis of a 63-cycle (218 fs) 0.291 PHz (1030 mm) pulse.** (a) The corresponding current vs peak field before and after measurement. (b) The degenerately measured field with varying x-axis limits of 1760 fs, 400 fs, and 10 fs. The frequency-resolved optical gating (FROG) (c) measured and (d) retrieved spectrograms. (e) A comparison of the squared modulus of measured optical fields and the retrieved pulse versus time. (f) A comparison of the squared modulus of the Fourier transformed measured fields, retrieved pulse versus frequency, a spectrometer reference, group delay from the measured optical fields, and the retrieved group delay.

a closed-loop linear piezo stage delay line (Smaract SLC2445-S with MCS2) with ± 40 nm (± 0.13 fs) repeatability. Utilizing a pristine device, we measured the current as a function of the gate pulse energy. We proceeded with measurements

once the total photocurrent reached approximately 20 pA (blue line in Fig. 5-13a), which is equivalent to 1.4 nJ (0.328 V/nm) for this specific device measured. After measurements, we remeasured the current as a function of the gate pulse energy and observed degradation (orange curve Fig. 5-13a) associated with long pulse durations and highly localized fields at the nanoantenna tips. We tried to obtain 20 pA of current after measuring, however, this specific device rapidly degraded at 2.3 nJ. Using a signal pulse energy of 0.02 nJ (38.6 V/um), we degenerately measured the pulse as shown in Fig. 5-13b.

In the top panel (1.76 ps x-axis range) of Fig. 5-13b, at ± 500 fs, small side lobes are seen. As we continue zooming in until the 10 fs x-axis range, the measured optical period is 3.4 fs and the expected optical period for a center frequency of 291 PHz is 3.4 fs. The technique can be generalized beyond 10-cycle pulses, however, since the devices were not operating in the tunneling regime for these measurements, they require future studies to better understand the mechanism.

To verify the measured field, we compared our measured results with SHG FROG. As seen in Fig. 5-13c, d is the measured and retrieved spectrograms of the 63-cycle 1030 nm pulse used in the measurements. The degenerate measured fields in Fig. 5-13e show relatively good agreement in the time domain with the FROG result demonstrating that there is a small side lobe in time at ±500 fs. The retrieved pulse duration is 218 fs and the measured pulse duration is 216 fs. Lastly, shown in Fig. 5-13f is the frequency domain comparison between the measured intensity, retrieved intensity, and the grating-based spectrometer. The measured group delay and retrieved group delay are also shown and show reasonable agreement.

5.7 Conclusion and Outlook

In this study, we used nanoantenna networks to demonstrate a broadband, on-chip electronic optical frequency harmonic mixer using optical-field-driven tunneling. We showed how the harmonic frequency mixing process enables accurate field-resolved readout of optical signal waveforms spanning more than one octave of bandwidth

using a commercial laser without the need for single-cycle pulse generation or carrier-envelope phase locking.

In comparison to wave mixing in crystals, the optical-field-driven tunneling mechanism provides access to higher-order nonlinearities, and thus larger mixing bandwidths, while eliminating the need for phase-matching or a separate photodetection element [132], [139]. Furthermore, unlike FROG and other spectral characterization methods, the measurements provided direct amplitude and phase information in the time domain and did not require broadband spectral measurements or phase-retrieval algorithms. While techniques such as electro-optic sampling can provide similar time-domain information, they require CEP-stabilization and gate pulse envelopes shorter than the cycle time of the signal [136].

We believe similar devices will be used to create compact and sensitive optical oscilloscopes with bandwidths spanning multiple octaves. We anticipate that such optical field oscilloscopes will provide needed time-domain detection tools that will help accelerate the development of ultrafast source technologies (e.g. compact frequency combs and optical waveform synthesizers), and enable new approaches to the field-resolved investigation of ultrafast light-matter interactions. Beyond time-domain, field-resolved detection, petahertz-electronic mixers could also be incorporated as fundamental components within future lightwave electronic systems for PHz-scale communication and computation. Aside from conversion to baseband, they could be used to generate new sum and difference frequency signals to be routed to other nearby on-chip devices.

Chapter 6

Investigation of the Field Sampling Bandwidth using Supercontinuum Generation in Photonic Crystal Fibers

The work presented in this chapter was done in collaboration with Dr. Lu-Ting Chou who helped set up the supercontinuum used in the measurements. This studies the sampling bandwidth from Section 3.6.2 using asymmetric half-wave rectifying antennas shown in Fig. 3-3i-l. Code and data can be found in the following repository: https://github.com/qnngroup/manu-HarmonicMixer

Abstract

Driven by the need for faster technologies, lightwave electronics offer a promising avenue to overcome traditional electronics stemming from the limitations of conventional semiconductors. Metallic nanoantennas have emerged as a key candidate for PHz electronics due to their ability to control light field-driven responses through rectification, resonance control (leading to lower peak fields required to operate), and polarization control, all without the need for phase-matching. Recent work has

demonstrated that nonlinear electron emission from nanoantennas driven by a commercial multi-cycle carrier-envelope-phase (CEP) unstable laser can enable perturbative optical waveform analysis well outside that of the local oscillator. However, the influence of the local oscillator pulse duration on nonlinear electron emission remains uncertain regarding its impact on the detection bandwidth. Here, we investigate the small-signal bandwidth of optical tunneling in nanoantennas using the combination of a CEP-unstabilized 1.5-cycle and 10-cycle pulse, shedding light on electron emission dynamics and highlighting the importance of pulse duration in field-resolved studies. This work contributes to a deeper understanding of electron emission dynamics and underscores the significance of pulse duration in shaping sampling bandwidth, which is crucial for advancing lightwave electronics.

6.1 Introduction

Semiconductor technology, once the bedrock of transistor development, has encountered barriers that veer from the trajectory outlined by Moore's law. Despite the pursuit of alternative pathways, leveraging light as an information carrier emerges as an enticing solution, driven by its inherent advantages such as expansive bandwidth, reduced latency, and potential for heightened energy efficiency. While integrated photonics steadily gains ground, the domain of lightwave electronics garners significant attention, offering the exciting prospect of electronic systems responding to the oscillations of light. This paradigm shift bears profound implications, with the potential to transcend the limitations imposed by traditional semiconductor frameworks, thus indicating the advent of ultrafast electronics crucial for the future landscape of high-speed electronics.

In the realm of ultrafast science, where observations occur on the femto-to-attosecond timescale, there is a concerted effort to directly measure these interactions in the time domain of the electric field. Despite strides in this direction, tools capable of consistently covering the PHz remain elusive. While techniques like electro-optic sampling (EOS) have achieved success up to the near-infrared, they are hindered by limita-

tions such as gate pulse duration and phase-matching constraints. Other methods, including those based on nonlinear optical conversions or nonlinear electron emission (or ionization) gating, show promise for their attosecond response and potential bandwidth coverage. These emission-based (or ionization-based) techniques resemble harmonic mixing in radio frequency electronics, where mixers are employed to analyze unknown signals by combining them with a known reference, thereby generating higher harmonics.

Metallic nanoantennas emerge as particularly promising candidates, enabling operation at petahertz (PHz) bandwidths while necessitating minimal pulse energies. However, much of the extant research on nanoantennas leans heavily on sophisticated few-cycle lasers with carrier-envelope-phase (CEP) stabilization. The previous chapter on harmonic frequency mixing challenged this reliance on CEP, showing that CEP stabilization is not necessary when employing optical tunneling using multi-cycle pulses. This chapter investigates the generation of sub-cycle electrons with frequency bandwidths surpassing those of the input lightwave, thereby enabling the sampling of broadband optical fields, paving the way for studying light-matter interactions with an optical oscilloscope-like detector.

6.2 Limits of Sampling

In this section, we delve into the scenario of measuring a single-cycle pulse at the second harmonic using different gate pulse cycle counts at the fundamental frequency. We conduct time-domain sampling simulations to unravel the dynamics at play, as mathematically described in 3.6.2 and 5.2.

We do this by generating a transform-limited Gaussian pulse for E_{gate} and E_{signal}. We use the Fowler-Nordheim equation (Γ) and numerically calculate the current cross-correlation by

$$I_{cc}(\tau) \propto \int_{-T_{\text{rep}}/2}^{T_{\text{rep}}/2} \Gamma(E_{\text{gate}}(t) + E_{\text{signal}}(t))\, dt$$

using a ratio of signal to the gate of 0.001.

Illuminating the nanoantennas with a gate pulse generates sub-optical-cycle cur-

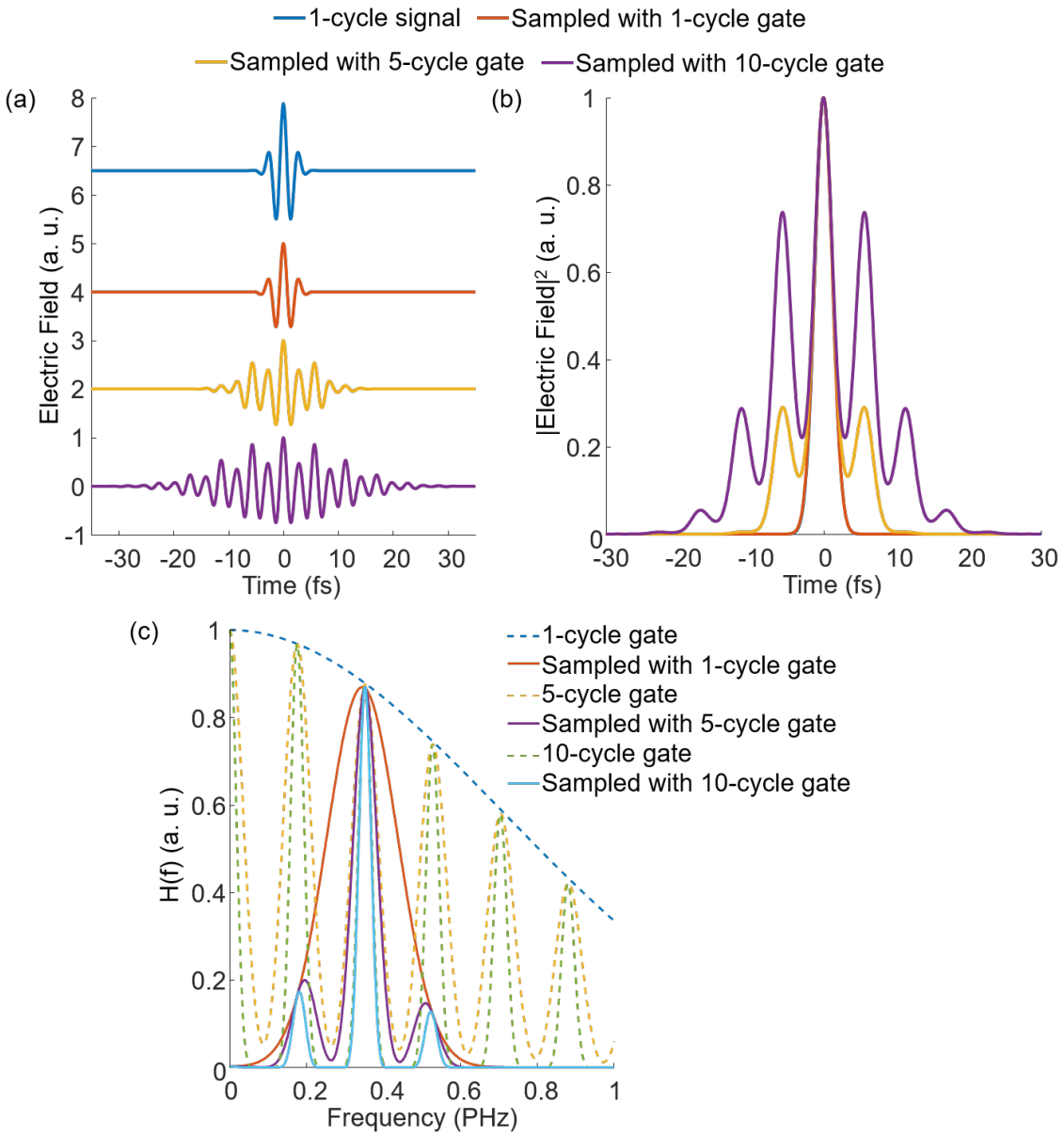

Figure 6-1: **Limits of sampling with varied gate pulse duration.** (a) Blue represents a 1-cycle electric field set for sampling. The orange curve depicts the sampled field utilizing a 1-cycle gate pulse. Yellow illustrates the scenario where the 1-cycle signal is sampled with a 5-cycle gate pulse. Purple showcases the measurement outcome when employing a 10-cycle pulse. (b) Demonstrates the pulse intensity corresponding to the sampled fields depicted in (a). (c) Presents the frequency domain information of the electric fields shown in (a).

rent bursts, creating a comb-like frequency response with peaks centered at higher harmonics of the fundamental, with the bandwidth of these harmonics being dependent on the cycle count of the input gate pulse as seen in Fig. 5-2. The limitations

of sampling the sampling bandwidth are determined by the gate frequency and cycle count, with both being directly related to time resolution due to the emission burst's dependence on the optical period. To illustrate this, the following simulations using a Gaussian 1-, 5-, and 10-cycle $f_{\text{gate}} = 0.177$ PHz (1690 nm) and a single cycle $f_{\text{signal}} = 0.353$ PHz (845 nm). Shown in Fig. 6-1a from top to bottom is a 1-cycle signal (2.9 fs) as a reference and the corresponding sampled field using a 1-, 5- and 10-cycle gate. The corresponding pulse intensity (the absolute squared sampled field) is shown in Fig. 6-1b. When sampling is performed, the CEP of the signal does not change due to the harmonic mixing process as described in Chapter 5.

When a 1-cycle gate is used to measure a 1-cycle frequency-doubled signal, the sampled pulse duration is 2.9 fs, identical to the pulse duration of the signal. The corresponding Fourier-transformed amplitude is also shown in Fig. 6-1c and has a frequency bandwidth of $\Delta f = 0.125$ PHz. As the cycle count of the gate pulse is increased to 5 cycles, it is seen that some of the sampled fields are distorted in the time domain, resulting in a peculiarly shaped optical waveform with side lobes as shown in Fig. 6-1a, b. The sampled pulse duration is nearly the same but has two side lobes at $\pm$ 5.5 fs which have a normalized intensity of 0.29. From the corresponding Fourier-transformed amplitude shown in Fig. 6-1c, we observe the expected frequency response from a 5-cycle gate, which has a bandwidth of 0.08 PHz, and the sampled spectrum is attenuated at the valleys centered at 0.263 PHz and 0.441 PHz. Finally, when the gate consists of 10 cycles, the non-symmetric field becomes even more distorted, resulting in a sampled pulse duration of 13.4 fs. Several additional side lobes appear at $\pm$ 5.5 fs, $\pm$ 11.4 fs, and $\pm$ 17.2 fs with normalized intensities of 0.73, 0.29, and 0.05, respectively. The frequency response with a 10-cycle gate has a bandwidth of 0.04 PHz and causes the previous valleys, which were observed with a 5-cycle gate, to approach 0, resulting in a further broadening of the sampled field.

6.3 Experimental Setup

6.3.1 Nanofabrication and measurement methods

The same measurement setup and devices in Chapter 5 were used for the work presented in this chapter.

6.3.2 Generation of 1.5-cycle supercontinuum

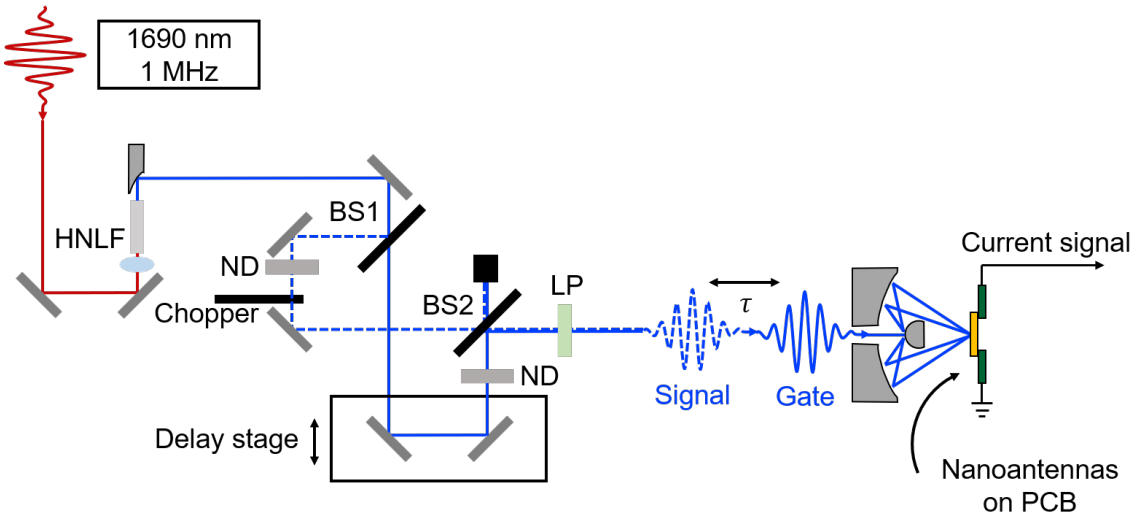

Figure 6-2: **Schematic of the experimental setup for the degenerate measurement of the supercontinuum generated using the 10-cycle $f = 0.177$ PHz pulse.** The laser light was split using a beamsplitter (BS1). One arm had a delay stage and was used as the gate pulse, while the signal arm was chopped and neutral density filters were used to attenuate the signal. Eventually, the two pulses were recombined using an identical beamsplitter before passing the linear polarizer (LP) and sent to a reflective objective where they were focused onto the nanoantenna devices.

To start we utilized a LightConversion Cronus-3P operating at 1 MHz and an endlessly single mode, large mode area photonic crystal fiber (ESM12, NKT Photonics) to self-compress 100 nJ of a 10-cycle (57 fs) pulse with a center frequency of 0.177 PHz using soliton self-compression. The 0.177 PHz fundamental is identical to that in Chapter 5. Due to the balance between the dispersion and self-phase modulation, we were able to generate a 1.5-cycle (8.5 fs) supercontinuum with a

center frequency near 0.17 PHz with continuous spectral coverage from 0.13 to 0.35 PHz. The self-compression process significantly influences the direct output duration, which was predicted to be 6 fs based on generalized nonlinear Schrödinger (NLSE) simulation results. To validate this, we measured this nearly transform-limited pulse through frequency-resolved optical gating, interferometric autocorrelation (IAC), and the nanoantenna harmonic mixer as demonstrated in the previous chapter. This supercontinuum was then split and recombined using an identical pair of beamsplitters. Each arm had an ND filter with the same thickness of glass to control the pulse energy focused onto the nanoantennas. After the pulses were recombined, the pulse pair was passed through a linear polarizer as shown in 6-2.

6.4 Results and Discussion

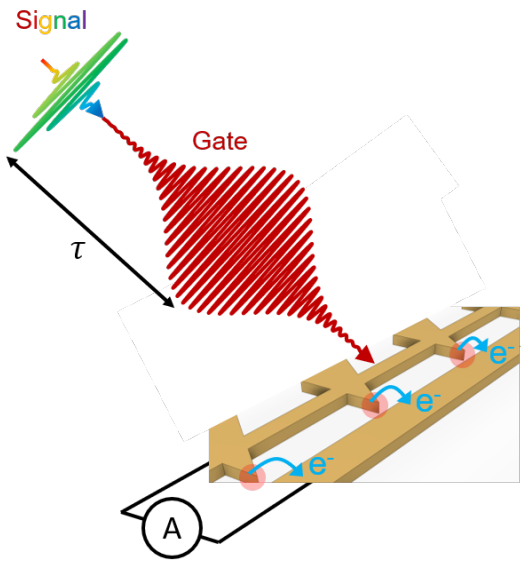

Figure 6-3: **Experimental schematic.** An overview of the field-resolved measurement of a 1.5-cycle supercontinuum using a 10-cycle pulse.

We measured the sampling bandwidth using a non-CEP-stable 1.5-cycle pulse as the gate and signal to demonstrate that CEP-stabilization is not required even in the few-cycle limit (Fig. 6-3). To further explore the spectral and temporal properties of the sampling response (and thus the electronic emission response), and investigate

how the choice of gate pulse influences these properties, we then measured the sampling response using the 10-cycle pulse as the gate while keeping the 1.5-cycle pulse as the signal.

We used the supercontinuum to measure itself (herein referred to as short-gate-measured SCG) as shown in Fig. 6-2. The measured trace with its spectrum is shown in Fig. 6-4c (blue curves). A gate pulse energy of 0.6 nJ (1.1 V/nm) was used for the gate pulse and a pulse energy of 80 fJ (37 V/μm) was used for the signal (see Fig. 6-2 for measurement schematic). The temporal shape of the short-gate-measured trace is in good agreement with the retrieved FROG trace as shown in Fig. 6-4b (for more details see Fig. 6-10), with a central pulse duration of 8.5 fs FWHM (compared to 9 fs and 8.4 fs for the FROG and IAC results, respectively). Moreover, the measurement of the short-gate measured trace using a non-CEP-stable laser highlights the mixing effect discussed in our earlier work shown in Chapter 5. Since the CEP undergoes stochastic drift, one would anticipate substantial variations in the emitted current and resultant sampling response from pulse-to-pulse. However, these variations are averaged away as each sampling trace corresponds to integration over 1.8 $\times 10^7$ pulses, and the signal waveform is reproduced containing only the relative CEP difference as discussed in Chapter 5. Our results demonstrate that the measurement is insensitive to shifts in the absolute CEP of the driving waveform in the few-cycle limit so long as the gate and signal exhibit relative CEP stability.

To study the impact of the gate pulse on the sampling response, we next compare the case of the few-cycle gate to that using the 10-cycle pulse with a central frequency of 0.177 PHz as the gate while leaving the signal pulse fixed. As touched on in Section 6.2, the bandwidth of the integer harmonic peaks in $\tilde{H}(\omega)$ can be adjusted by varying the cycle count of the gate pulse. When the cycle count decreases (*i.e.* the pulse duration is shorter), the frequency bandwidth of the pulse expands, leading to a wider bandwidth of the integer harmonic peaks in $\tilde{H}(\omega)$. Conversely, increasing the cycle count narrows the bandwidth of the integer harmonic peaks. The field enhancement, nonlinearity of the emission response, and gate pulse waveform all contribute to impacting the precise shape of $\tilde{H}(\omega)$. By maintaining the same broadband signal

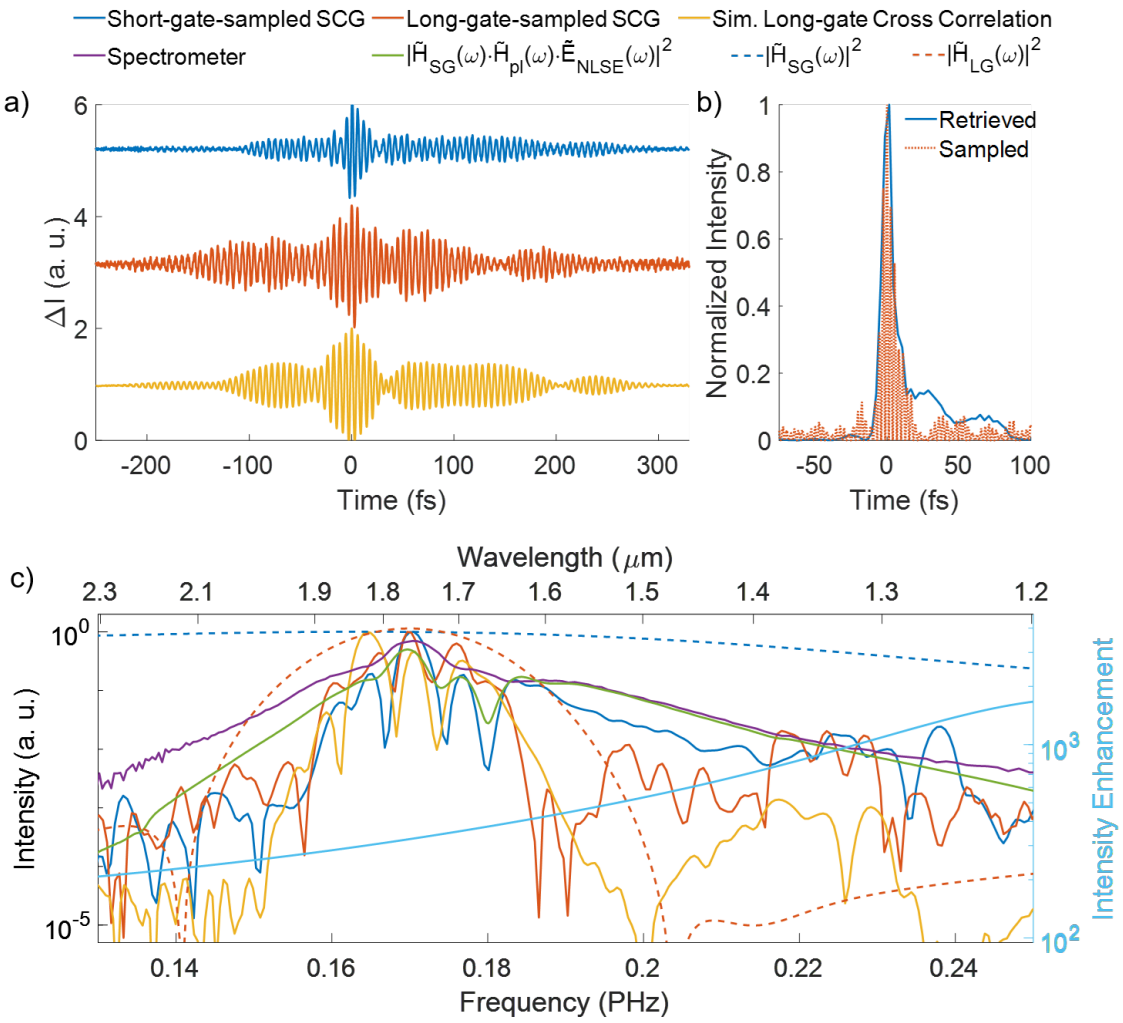

Figure 6-4: **Sampling measurements of the 1.5-cycle supercontinuum.** (a) Using the short-pulse gate (blue curve) and long-pulse gate (orange curve), the 1.5-cycle supercontinuum was measured along with a simulation of $I_{cc}(\tau)$ using the experimentally measured 1.5-cycle signal and 10-cycle gate as inputs (yellow curve). (b) Comparison between the short-gate-measured supercontinuum and the FROG retrieved pulse envelope. (c) Normalized intensity spectra of the supercontinuum when measured using the short-pulse gate (solid blue curve); through a commercial spectrometer (solid green curve); a full simulation of the sampling spectrum (solid purple curve) incorporating the simulated supercontinuum spectrum, the calculated short-gate sampling response $|\tilde{H}_{SG}(\omega)|^2$ (dashed blue curve), and the intensity enhancement from the nanoantenna (solid light blue curve); the measured long-gate-measured spectrum (solid orange curve); the calculation of the long-gate sampling response $|\tilde{H}_{LG}(\omega)|^2$ (dashed orange curve); and the simulated long-gate-measured cross-correlation response (solid yellow curve).

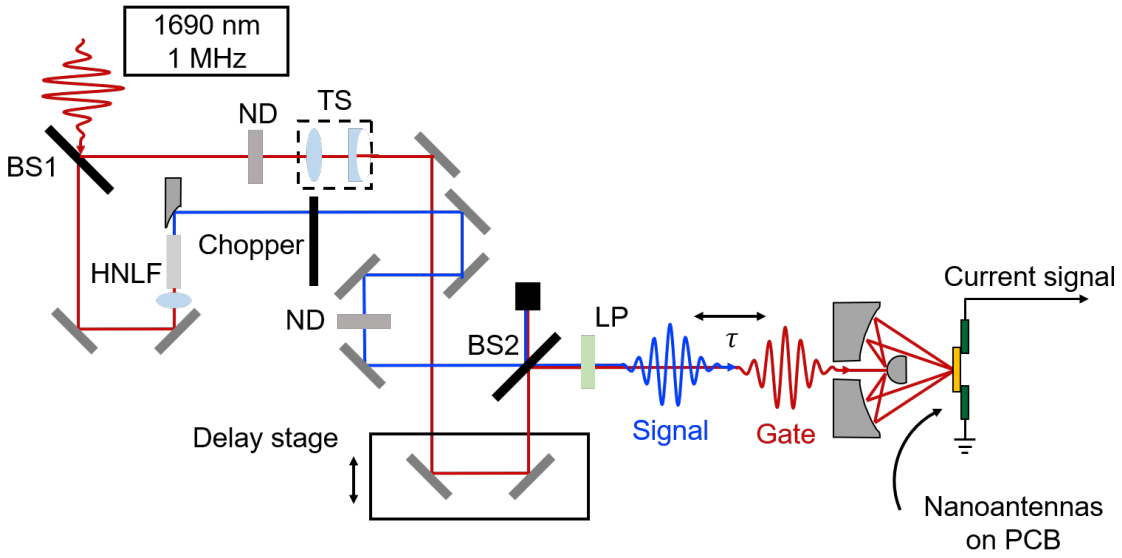

Figure 6-5: **A schematic of the experimental setup for the measurement of the supercontinuum generated and measured using the 10-cycle $f = 0.177$ PHz pulse.** The laser light was split using a beamsplitter (BS), such that one path is for the gate and the other path is for the supercontinuum signal pulse. The gate pulse was directed through a delay stage to enable temporal control of the two pulses. Eventually, the 10-cycle gate and supercontinuum signal were recombined and passed through a linear polarizer before being focused onto the nanoantennas.

while altering the gate pulse waveforms, we can examine precisely how $\tilde{H}(\omega)$ impacts the resultant time and frequency content of the underlying electronic response, and how well our emission model captures this electronic response.

A schematic of the long-gate-measured SCG is shown in Fig. 6-5. We split the gate pulse into two arms such that one can be used to generate the exact continuum used for the short-gate-measured SCG. We add a telescope on the gate arm to control the beam spot size difference before being focused on the nanoantennas. We kept the same ND filter and transmitted the beam through the same beamsplitter to ensure the pulses accumulated nearly the same phase as the degenerate supercontinuum measurement. After the two pulses recombined at BS2, they passed through the same linear polarizer as used before.

The long-gate-measured trace is shown in Fig. 6-4a with its spectrum in Fig. 6-4c (solid orange curves). For the measurements shown, we used a 6.6 nJ (0.94 V/nm) gate and a 2 pJ (52 V/μm) signal pulse. Note that the peak field strengths of the gate

and signal are comparable to those of the short-gate-measured case when accounting for the increased pulse duration.

Due to the longer gate pulse, a longer train of sub-cycle current bursts were generated causing the long-gate-measured trace to have an increased pulse duration. Along with the increased electron pulse duration, we also see the expected bandwidth reduction in the spectral response shown in Fig. 6-4c. While the central frequencies are faithfully retrieved, with a similar structure to the short-gate-measured result, NLSE, and measured spectrum, there is a sharp dropoff moving towards higher and lower frequencies. We observe dips at 0.156, 0.186, and 0.190 PHz in the spectrum which is due to a combination of the gate pulse shape and localized fields at the tip. The dashed orange curve shows the sampling response $|\tilde{H}_{\mathrm{LG}}(\omega)|^2$ of the long gate with a peak field of 30 V/nm and field enhancement of 32. Through the simulation, we estimate the window of emitted current from the 10-cycle gate pulse to be roughly 32 fs under the conditions in the measurement, still significantly shorter than the original pulse duration of roughly 57 fs. We emphasize that operating at lower peak field values or with materials having higher workfunction could further shorten this duration and increase the bandwidth response due to larger nonlinearities, at the cost of lower current yields and thus lower signal-to-noise ratios.

Lastly, to test the validity of our measurements and accuracy of our sampling response simulations, we took our experimentally measured 10-cycle gate pulse from Fig. 5-11a and the short-gate-measured supercontinuum from Fig. 6-4a and used these to calculate the current cross-correlation $I_{\mathrm{cc}}(\tau)$ using Eqn. 5.1. We accounted for a peak gate field strength of 30 V/nm for the 10-cycle gate pulse and a signal-to-gate peak field ratio of 0.03. The simulated $I_{\mathrm{cc}}(\tau)$ is shown in Fig. 6-4a, and its corresponding spectral intensity is shown in Fig. 6-4c (solid yellow curves). While certain details of the temporal tails of the calculated result are different in comparison to the long-gate-measured measurement, the central lobe is faithfully reproduced. The calculated response has a central lobe centered around t = 0 fs of duration 20 fs FWHM, whereas the measured long-gate-measured supercontinuum has a central lobe duration of 18 fs FWHM. The calculated spectral response also reproduces the

bandwidth limits and key features observed in the measurement, indicating that our simplified Fowler-Nordheim model provides a reasonable estimate of the underlying current response.

In Fig. 6-4c, we see that the spectrum of the short-gate-measured trace spans from just below 0.16 PHz to roughly 0.24 PHz. Near the central spectral peak, the structure is observed with several peaks and more prominent dips at 0.167, 0.175, and 0.180 PHz. To understand the response, we compare the spectrum to the supercontinuum spectrum measured with a spectrometer (green curve), as well as a full simulation of the spectral response (purple curve) that incorporates our NLSE simulation result $\tilde{E}_{\mathrm{NLSE}}(\omega)$, the sampling response $\tilde{H}_{\mathrm{SG}}(\omega)$ (dashed blue curve) and the calculated antenna response $\tilde{H}_{\mathrm{pl}}(\omega) = \tilde{E}_{\mathrm{tip}}(\omega)/\tilde{E}_{\mathrm{inc}}(\omega)$, where $\tilde{E}_{\mathrm{tip}}$ is the excited field at the tip and $\tilde{E}_{\mathrm{inc}}$ the field incident on the antenna. The intensity enhancement at the antenna tip $|\tilde{H}_{\mathrm{pl}}(\omega)|^2$ is shown as the solid light blue curve for reference. We note that the NLSE simulation describes the details of the measured supercontinuum spectrum very accurately, with the only major difference being that the spectral structure near the center of the pulse is more pronounced as in our sampling result (for direct comparison, see Fig. 6-8).

It should be noted that for the simulated frequency responses $\tilde{H}(\omega)$ shown in Fig. 6-4c, we used a sech centered at 0.17 PHz with a pulse duration of 8.5 fs with the same center frequency as the measured SCG and with a field enhancement of 30× for the short-gate-measured SCG. For the long-gate-measured SCG we used a 0.17 PHz Gaussian with a pulse duration of 60 fs and a field enhancement of 32×.

The spectral response of the short-gate-measured trace generally agrees well with the full simulation. While the spectral dips near 0.17 PHz are more pronounced in the measured trace spectrum, their frequency locations align well with the NLSE simulation result. Here $\tilde{H}_{\mathrm{SG}}(\omega)$ was calculated assuming a perfect sech pulse with a peak field of 28 V/nm, corresponding to a field enhancement of 30. We recognize that for the measured short-gate-measured trace, the spectral cutoff at lower frequencies is a bit sharper than expected. We attribute this discrepancy to two possible causes: (1) our limited scan range resulting in an underestimation of long-wavelength spectral

components; and (2) weaker focusing of the long-wavelength components onto the nanoantenna detectors.

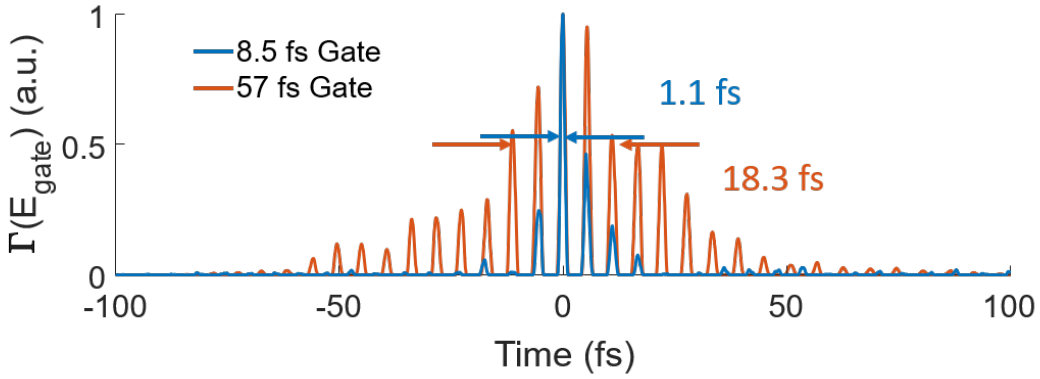

Figure 6-6: **Electron gate dependence on time resolution.** In blue is the electron gate when the short-gate pulse is used and orange is when the long-gate pulse is used. The FWHM corresponds to 1.1 fs and 18.3 fs, respectively.

To understand what is occurring to the temporal electron gate when using the short-gate and long-gate, we took the experimentally measured long-gate pulse from Chapter 5 and the short-gate pulse as shown earlier, then input this into the Fowler-Nordheim emission model. As seen in Fig. 6-6, the electron gate using the short-gate pulse results in a FWHM of 1.1 fs, whereas the long-gate pulse results in a FWHM of 18.3 fs. The FWHM of the electron gate dictates the time resolution for actual field sampling measurements which can be seen in Fig. 6-4a.

To demonstrate non-degenerate waveform analysis of a lower frequency using a higher frequency and to show that lower frequencies that are not integer harmonics can still be measured, we used a separate few-cycle supercontinuum source with details that can be found in [140]. After supercontinuum generation, an SF10 prism pair was used to spatially disperse the beam. After the prism pair, the Er pump was spatially filtered, and the soliton and dispersive wave contributions were spatially separated. The higher-frequency dispersive wave portion of the supercontinuum was returned through the prism pair for compression and the removal of spatial chirp and was used as the gate. We note that the lower-frequency soliton, which was used as the signal, was not returned through the prism pair leaving some residual spatial chirp.

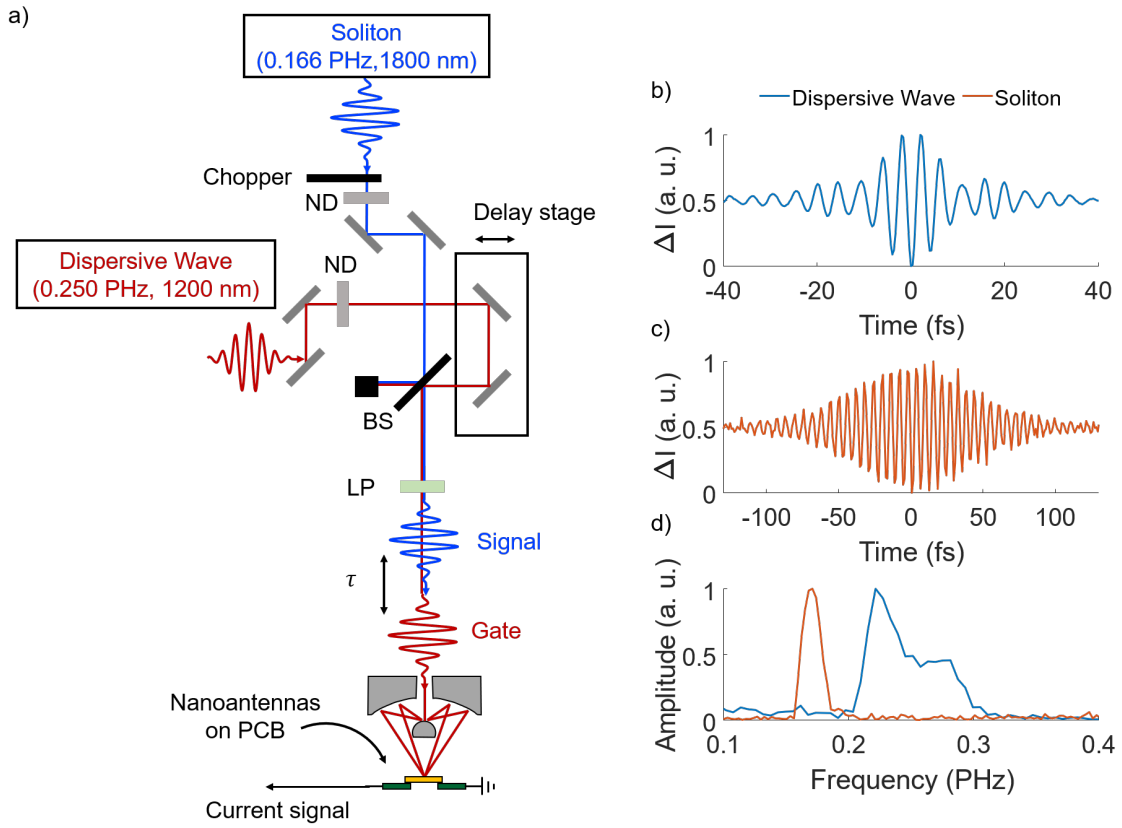

Figure 6-7: **Lower frequency waveform analysis using a 2.5-cycle supercontinuum pumped by a 78.4 MHz Er fiber laser.** (a) The experimental schematic for the measurement. (b) Degenerate measurements of the dispersive wave. (c) The non-degenerate measurement of the soliton using the dispersive wave. (d) The corresponding Fourier transformed measured fields.

For the gate pulse, 19 pJ (0.21 V/nm at focus) of the 3-cycle (12 fs) dispersive wave (0.250 PHz, 1200 nm) was used. For the signal, 30 pJ (0.15 V/nm at focus) of the 11-cycle (65 fs) soliton (0.166 PHz, 1600 nm) was used. The measurement configuration is shown in detail in Fig. 6-7a. Degenerate waveform analysis of the dispersive wave was performed and is shown in Fig. 6-7b. Next, we performed non-degenerate waveform analysis measurement of the soliton and measured an optical period of approximately 6.0 fs as expected as Fig. 6-7c. Lastly, the normalized Fourier-transformed time-domain measured waveforms are shown in Fig. 6-7d. This emphasizes the ability of the nonlinear mixing process to also sample lower frequency contributions at non-integer harmonics in the few-cycle regime without CEP locking.

6.5 Modeling the Influence of Nanoantenna on Sampling

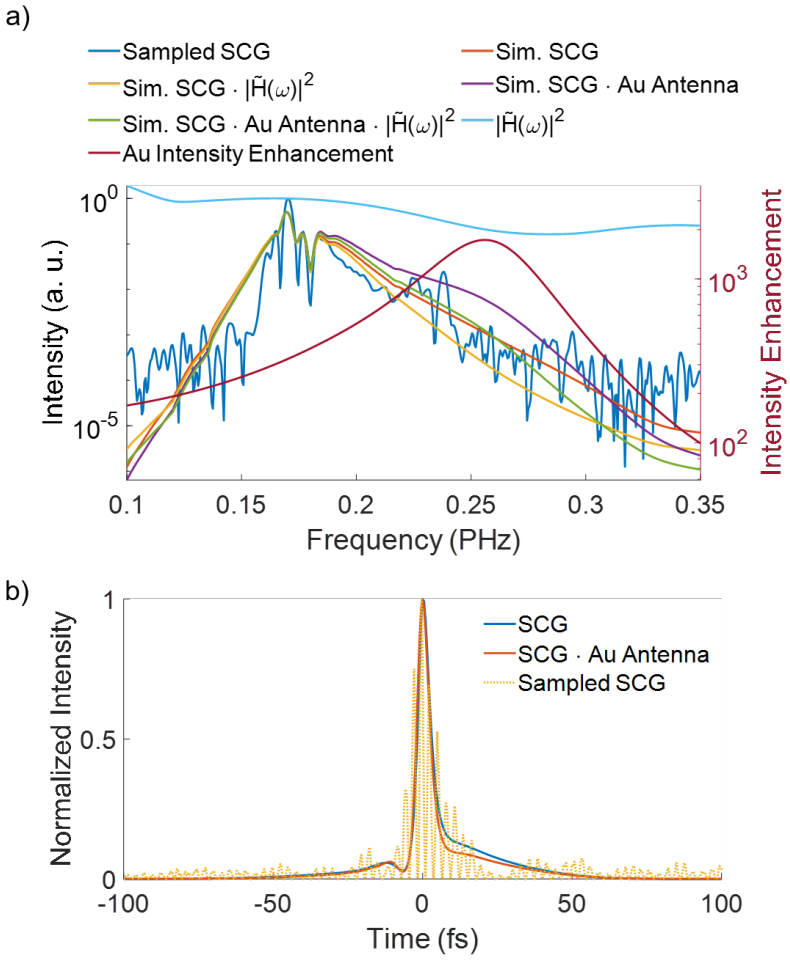

Figure 6-8: **Breakdown of phase imparted by electron emission and gold antenna.** (a) Simulated supercontinuum in frequency with the simulated frequency response, and gold antenna intensity enhancement (right y-axis). (b) The corresponding time-domain SCG with and without interacting with the gold nanoantenna.

We then used the simulated supercontinuum electric fields and added the electromagnetically simulated gold field enhancement amplitude and phase to understand how the gold nanoantenna modified the supercontinuum. We add the gold field enhancement amplitude and phase into the frequency spectrum and normalized the squared modulus of the corresponding frequency spectrum which is shown in Fig. 6-8a. After incorporating the gold antenna response, we also looked at how the sim-

ulated frequency response plays a role in the simulated frequency spectrum. We observed that there is a reduction of intensity which is mainly attributed to the gate-dependent frequency response. Also, it can be seen that where the measured (blue) and gold antenna intensity enhancement (teal) curves intersect at 0.217 PHz, the measured field starts to increase and is related to the intensity enhancement from the nanoantenna. Afterward, we took the inverse Fourier transform of the simulated frequency spectrum and normalized the squared modulus of the time-domain spectrum to understand how the gold nanoantenna affects the pulse duration which is shown in Fig. 6-8b. We observe that the gold nanoantenna does not significantly modify the supercontinuum in frequency or time since the devices are being operated away from their resonant wavelength.

6.6 Measurement Comparison

We then compare our field-resolved measurements to interferometric autocorrelation (IAC) and frequency-resolved optical gating (FROG). Harmonic frequency mixing, with its high nonlinearity, enables time-domain pulse characterization over many octaves. This capability is far from trivial and cannot be replicated with standard techniques.

We performed interferometric autocorrelation measurements (IAC) on the supercontinuum (Fig. 6-9) by focusing the supercontinuum into a 40 μm thick BBO and detected the IAC using a silicon photodiode after passing through a linear polarizer. We measured a duration of 13 fs FWHM, which corresponds to an 8.4-fs pulse width considering a deconvolution factor of 1.54 assuming a sech^2 pulse shape. To validate the field-resolved measurements, we compared the measured IAC trace to the reconstructed IAC trace obtained using the measured field shown in Fig. 6-4. The two traces share comparable features, both having a sub-two-cycle component in the center part of the IAC trace along with pronounced side lobes. The second-order dispersion-induced chirp was not observed to be significant in either trace. The IAC traces both show significant side lobes, which are explained by the long tails observed

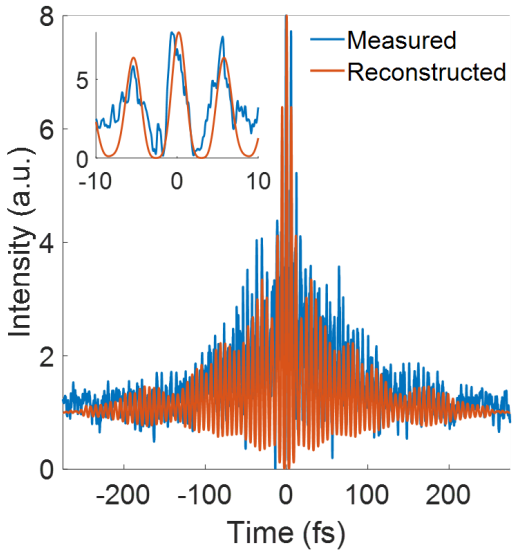

Figure 6-9: **Interferometric autocorrelation of the 1.5-cycle supercontinuum.** The measured (blue) and reconstructed (orange) interferometric autocorrelation of the supercontinuum source. Both show the 8 to 1 ratio expected from an IAC.

in the time domain of the measured waveform. These time-domain tails were also observed in the simulation of the nonlinear pulse propagation. They are primarily induced by higher-order dispersion accumulated during spectral broadening between normal and abnormal dispersion regimes as well as complex higher-order dispersion during nonlinear compression [141], [142].

We then performed Frequency-resolved optical gating (FROG) measurements on the SCG as shown in Fig. 6-10 using the same setup as shown in Fig. 6-2. Fig. 6-10a and b are the measured and retrieved spectrograms of the supercontinuum pulse used in the measurements. For the reconstruction, we utilized a grid size of 256 $\times$ 256 and obtained a reconstruction error of 1.910^{-2}. The degenerately measured fields in Fig. 6-10c show relatively good agreement with the pulses retrieved from the FROG measurements in the time domain. The retrieved pulse duration was 9 fs FWHM and the measured pulse duration was 8.5 fs FWHM. Lastly, shown in Fig. 6-10d is the frequency domain comparison between the measured intensity, retrieved intensity, simulated intensity spectrum, and the grating-based spectrometer. The measured pulse intensity and retrieved pulse intensity are also shown and show good agreement considering that the SCG spans more than an octave of bandwidth.

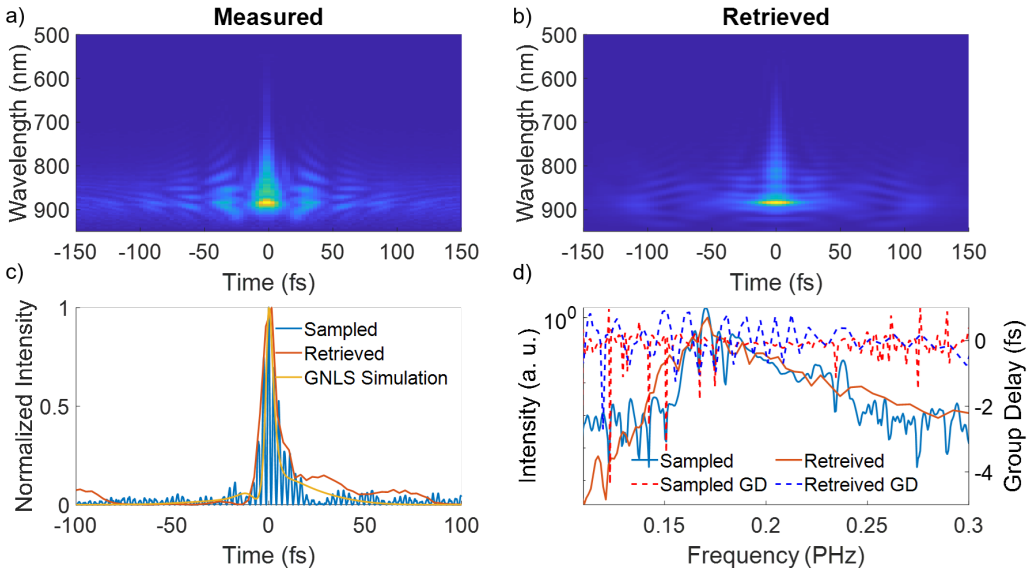

Figure 6-10: **Frequency-resolved optical gating (FROG) of the 1.5-cyle supercontinuum.** The (a) measured and (b) retrieved spectrograms. (c) A comparison of the squared modulus of measured optical fields and the retrieved pulse versus time. (d) A comparison of the squared modulus of the Fourier transformed measured fields, retrieved pulse versus frequency, a spectrometer reference, group delay from the measured optical fields, and the retrieved group delay.

6.7 Conclusion

Our previous work on harmonic frequency mixing experimentally and mathematically demonstrated that optical field-resolved waveform analysis does not require few-cycle pulses or CEP stabilization using multi-cycle pulses. Here, we have demonstrated that field-resolved waveform analysis can be performed with a few-cycle pulse on an unstabilized CEP laser system and that the bandwidth dependence of optical tunneling is dependent on the optical pulse used. While using a longer pulse results in loss of continuous bandwidth, the bandwidth due to the high nonlinearity is broader than the bandwidth of the optical pulse itself. This work studies the bandwidth of optical field emission from nanoantennas, achieving measurement bandwidths outside of the input multicycle local oscillator through the measurement of a 1.5-cycle pulse (8.5 fs) using a 10-cycle pulse (57 fs), resulting in a measurement of a 20 fs pulse.

Chapter 7

Leveraging the Inherent Polarization Sensitivity of Optical Field Emission

The work presented in this chapter builds upon asymmetric half-wave rectifying antennas shown in Fig. 3-3i-l by leveraging the inherent polarization sensitivity of the electron emission process. Just like in conventional RF electronics which use the shape antennas to be sensitive to specific polarizations, we do the same at PHz frequencies using the nanoantenna platform. The work was done in collaboration with Drs. Lu-Ting Chou, Marco Turchetti, and Mina Bionta. They provided help on the circular polarized measurements, fabrication, and writing, respectively. Code and data can be found in the following repository: https://github.com/qnngroup/manu-polarization-and-phase-sensitive-sampling.git

Abstract

Polarization plays a crucial role in high-speed, high-bandwidth RF electronics, often observed in antennas for RF applications such as communication. Beyond its significance in RF electronics, polarization serves as a valuable tool in optical science, particularly in the study of matter with specific optical selection rules and dynamics [143]–[148] or to determine the onset of cancer growth [149]–[151]. Although myriad techniques exist to resolve the polarization states of light in the frequency domain, a

complete vectorial mapping of the temporal polarization state of optical waveforms remains challenging to measure. The lack of vectorial field-resolved polarization dynamics limits the straightforward studies involving circular or elliptical polarization such as studying material properties [143], [146] or biomedical imaging [149]. In this work, we demonstrate a compact detector for vectorial field mapping of few-cycle optical waveforms directly in the time domain. Our results demonstrate a monolithic nanoantenna network design that enables polarization-sensitive field sampling over a broad range of wavelengths spanning from the near- to the mid-infrared. This work has direct implications for the study of sub- to few-femtosecond, polarization-resolved light-matter interaction dynamics. Furthermore, the newfound access to sub-femtosecond polarization dynamics that our devices provide could benefit a wide range of applications including bioimaging, remote sensing, and optical communications.

7.1 Introduction

It has been demonstrated in the THz and mid-infrared that time-domain spectroscopy can provide insightful information such as the dynamics of the contracting or stretching of specific chemical bonds[35], [70]–[73]. This has led to the development and widespread adoption of commercial systems for time-domain THz spectroscopy systems. Such a technique has been extended for polarization-resolved measurements and has enabled studies of polarization-dependent properties of materials [143], [152], [153], molecules [154], and devices[155]. The development of compact polarization detectors is crucial for a wide range of applications [156].

The importance of time-domain spectroscopy in the THz spectral region has spurred the more recent development of similar techniques for field-resolved detection in the visible to infrared spectral regions. Example techniques include Tunneling Ionization with a Perturbation for the Time-Domain Observation of an Electric field (TIPTOE) [21], [123], on-chip multiphoton excitation [126], nonlinear photoconductive sampling (NPS) [22], [81], or on-chip nanoantenna-based Fowler-Nordheim

tunneling devices[45]. All of the previous optical field sampling techniques mentioned typically focus on single-polarization optical field sampling but some are able to do polarization-resolved detection [17] with the caveat of requiring vacuum, large pulse energies, or low-repetition rate lasers. The open challenge of an integrated polarization-resolved detector applicable for bioimaging [121] or low-pulse energy measurements remains.

Here, we focus on on-chip nanoantenna-based Fowler-Nordheim tunneling electric field sampling devices. These devices are compact, can operate at room temperature, and in ambient conditions as it has been shown that the electron mean free capture path is longer than the 20-50 nm gap sizes used in these devices in these conditions [14], [43], [45], [157]. Furthermore, the requirement for large pulse energies which is typical for other cold field emission based devices is alleviated by the combination of geometrical and plasmonic field enhancement, which can peak at $\geq$ 30x (900x intensity enhancement) for gold nanoantennas. This leads to a sensitivity that is 6 orders of magnitude better than alternative approaches [21], [45], [81], [123], [134].

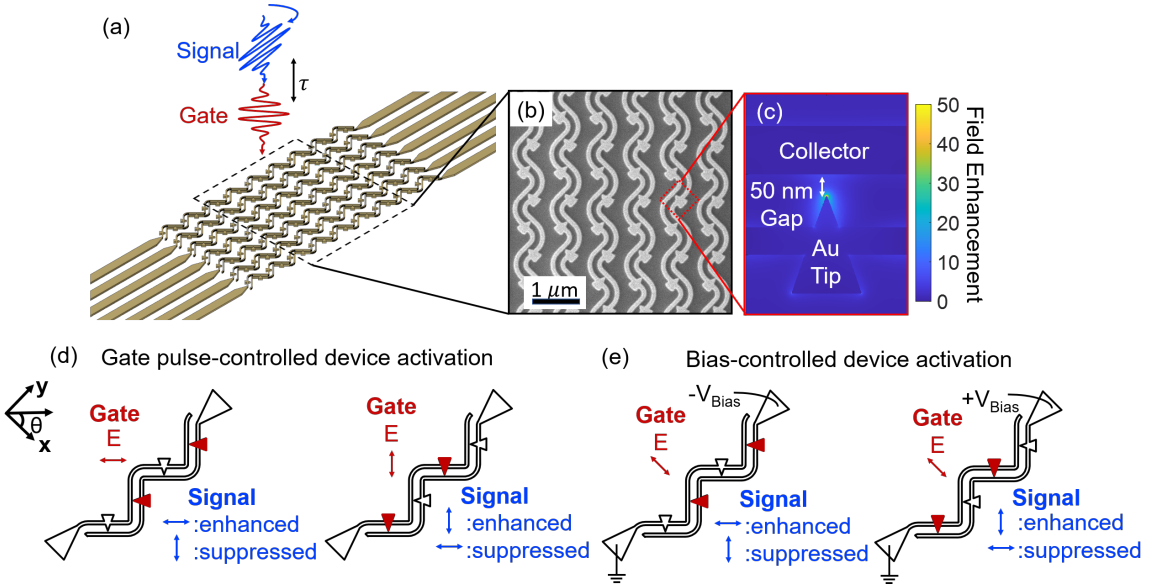

Figure 7-1: **Experimental schematic.** (a) An overview of the polarization-sensitive sampling. (b) A representative scanning electron microscope image of one nanoantenna network. (c) Finite-difference time-domain simulated field enhancement of one nanoantenna. (d) The notional schematic shows gate pulse-controlled device activation. (e) The notional schematic shows bias-controlled device activation.

7.2 Experimental Methods

7.2.1 Nanofabrication and antenna design

The same nanofabrication procedures used in Chapter 5 were used for the work presented in this chapter and are further detailed in the appendix.

However, in these measurements, the devices were operating resonantly such that the field enhancements are ≥ 30. This is necessary to obtain the peak field strengths required for optical field sampling using a high-repetition-rate laser system (described in the next section).

7.2.2 Measurement setup and methods

A homebuilt Erbium-doped fiber laser operating at 78.4 MHz is used to generate a supercontinuum source through a bulk germano-silica fiber [140], [158]. We first split the laser into two arms using a beamsplitter. In the gate and signal arm, we place a broadband waveplate to change the polarization and recombine them using a beamsplitter made for p-polarized light. Splitting the two pulses enables temporal control between the gate and signal pulse by using a closed-loop linear piezo stage delay line (Smaract SLC2445-S with MCS2) with $\pm$ 40 nm ($\pm$ 0.13 fs) repeatability. Once collinearity is ensured between the gate and signal arm, the gate and signal pulse are focused on the nanoantenna device through an objective. The time delay between the pulses is scanned, allowing us to measure the signal pulse current-induced change, which is amplified using a transimpedance amplifier (TIA) with a gain of 1 V/nA. The output of the TIA was fed into a lock-in amplifier. The lock-in reference was obtained by chopping the signal arm operating at $\sim$ 277 Hz. The lock-in x- and y-channel are sent into an oscilloscope which has a maximum sampling rate of 5 GSa/s. We auto-phased the lock-in before measurements. In the measurements, the sampling rate was set to 25 kSa/s. We ensured that we were in the linear sampling regime as when the pulse energy was too high, we observed the sampled waveforms appeared more like an interferometric autocorrelation [10], [12], [14]. As a result, the

small signal model used in Ref. [[45]] was no longer valid.

A motorized rotation stage was used to control the waveplate for the measurements. The circularly polarized light was generated by passing the signal pulse through a linear polarizer fixed at 45°, then passing a quarter waveplate. The ratio of the projected horizontal and vertical polarization was measured using another linear polarizer and the ratio was set to 1. Note that the beamsplitter does not transmit the horizontal and vertical polarization equally. To apply a bias to the nanoantennas, a sourcemeter was used to remotely control the adjustable bias voltage on the transimpedance amplifier input. The measurements were averaged 5-30 times depending on the signal-to-noise ratio. The time axis for the measurements was determined using linear interference from a photodiode.

7.3 Results and Discussion

In this work, we leverage the inherent polarization sensitivity of on-chip nanoantenna-based Fowler-Nordheim tunneling electric field sampling devices to make a broadband field-resolved polarization-sensitive detector. Our device architecture is shown in Fig. 7-1. The experimental schematic and an image of a representative device are shown in Fig. 7-1a, b. Networks of triangular nanoantennas were fabricated on a fused silica substrate with various gap sizes ranging from 10 to 50 nm in a meandering structure using electron beam lithography. The networks were illuminated using a broadband supercontinuum which spans 950 nm to 1450 nm with pulse durations of 12 fs [140], [158]. An example of the measurement layout is shown in Fig. 7-2a where the laser source was split into two arms, which will be referred to as the gate and signal, respectively. The two arms were recombined with adjustable time delay, after which both pulses were focused on the nanoantennas mounted on a printed circuit board (PCB).

In the following sections, we demonstrate two schemes for which polarization-sensitivity can be selected: (1) gate pulse-polarization-controlled device activation; and (2) bias-controlled device activation. In gate pulse-controlled device activation

shown in Fig. 7-1d, the gate pulse enhances the polarization that is sampled. In bias-controlled device activation shown in Fig. 7-1e, the gate pulse is distributed between the two types of nanoantennas, and the polarization selection is done by biasing the device. Through these two schemes, we demonstrate the ability to sample linearly polarized light, circularly polarized light, and elliptically polarized light with relative phases between the projected vertical and horizontal linear polarizations.

7.3.1 Gate pulse-polarization-controlled device activation

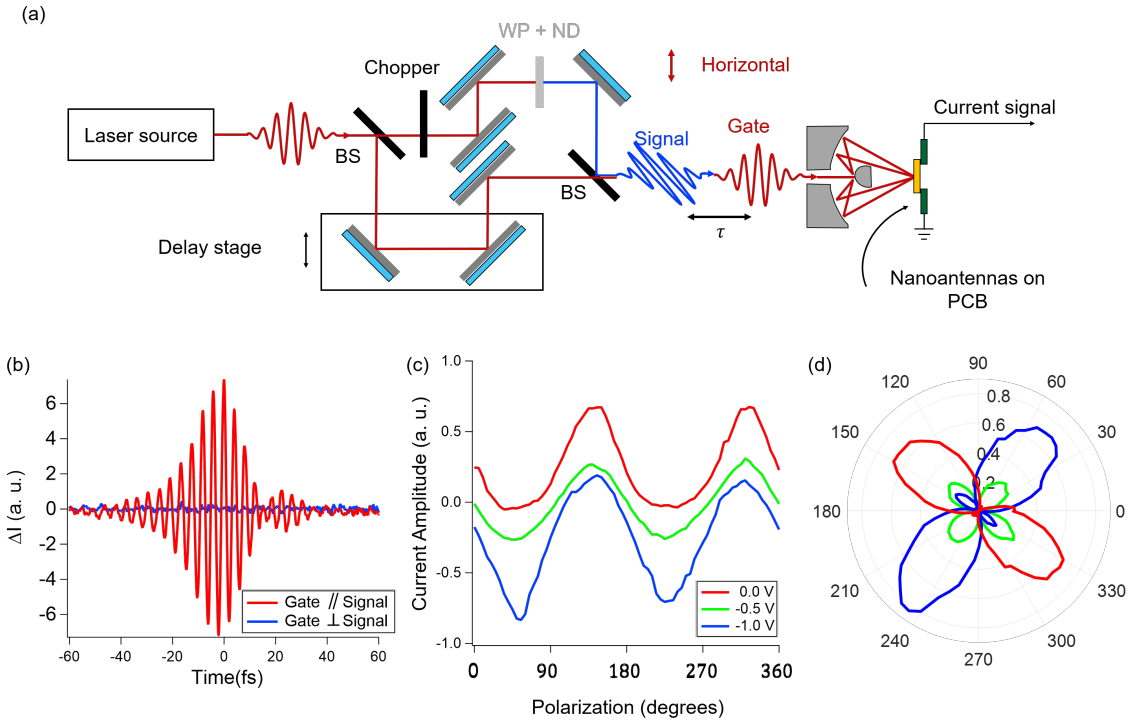

Figure 7-2: **Linear polarization measurements.** (a) A schematic of the experimental setup. The laser light is split using a group-delay-dispersion (GDD)-controlled beamsplitter (BS). One arm has a delay stage and was used as the gate pulse. The signal arm was chopped, including a waveplate (WP) to change the polarization, and neutral density filters to attenuate the signal. Eventually, the two pulses are recombined using an identical GDD-controlled beamsplitter before being sent to an objective where they are focused onto the nanoantenna devices. (b) A typical sampled electric field trace when the gate and signal pulses are parallel (red) and perpendicular (blue) with respect to each other. (c) Polarization-dependent current from an network of antennas with varying sensitivity tuned by applied bias. (d) The corresponding polar coordinate plot (in degrees) of the polarization-dependent current.

In gate pulse-polarized-controlled device activation, which is shown in Fig. 7-1d, the gate pulse optically selects the sampled polarization by activating antennas with the tip axis parallel to the gate pulse polarization. The polarization of the gate pulse enhances the optical-field emission from the tip having its axis aligned with the polarization of the gate (e.g. $\theta = +45^\circ$ or -45°). When the polarization of the signal pulse is parallel with the gate pulse polarization, the signal is enhanced. However, when the signal polarization is orthogonal to the gate polarization, the optical-field emission is unchanged. This was experimentally demonstrated and shown in Fig. 7-2a by adding a half-wave plate into the signal arm which allows us to tune the polarization. In Fig. 7-2b the red trace demonstrates the electric field sampling when both the gate and signal pulse polarization is parallel to the nanoantenna tip axis. The sampled electric field is relatively symmetric, except for some dephasing components around 20 fs, which is attributed to the electron dynamics due to the plasmonic response of the nanoantenna [159]. When the half waveplate was rotated by 45° such that the signal pulse was perpendicular with respect to the gate pulse, only noise was observed as seen in Fig. 7-2b.

To further test the polarization sensitivity, the device was biased while continuously rotating the half-waveplate. Corresponding traces are shown in 7-2c. As the magnitude of the applied bias was larger, the polarization sensitivity was enhanced. This can be seen clearly through the amplitude of the peaks and valleys of the red and blue traces in 7-2c. In the red trace, the two valleys between 0° and 90° and between 180° and 270° (highlighted) can be seen to be broadband, and as the device was biased more, and the valley becomes more pronounced and more sawtooth-like. Shown in Fig. 7-2d is the corresponding polar coordinate plot of the differential current with varied bias. At 0 V, the polar plot shows mirror symmetry since there are two large lobes. At -0.5 V, the corresponding polar plot shows that the detector is balanced and has four-fold symmetry, meaning that it can measure 45° , 135° , 225° , and 315° equally. At -1 V, the corresponding polar plot shows the same four-fold symmetry, but the two lobes at 135° and 315° are less pronounced. This demonstrates that the bias can be adjusted to measure polarization equally. This can also be used to

compensate for non-idealities in the fabrication that can generate unbalance between nanoantennas. For the gate pulse-polarization-controlled device activation measurements, the pulse energy focused onto the tips for the gate pulse was $\sim$ 18 pJ, and the energy for the signal pulse was 0.16 pJ.

7.3.2 Bias-controlled device activation

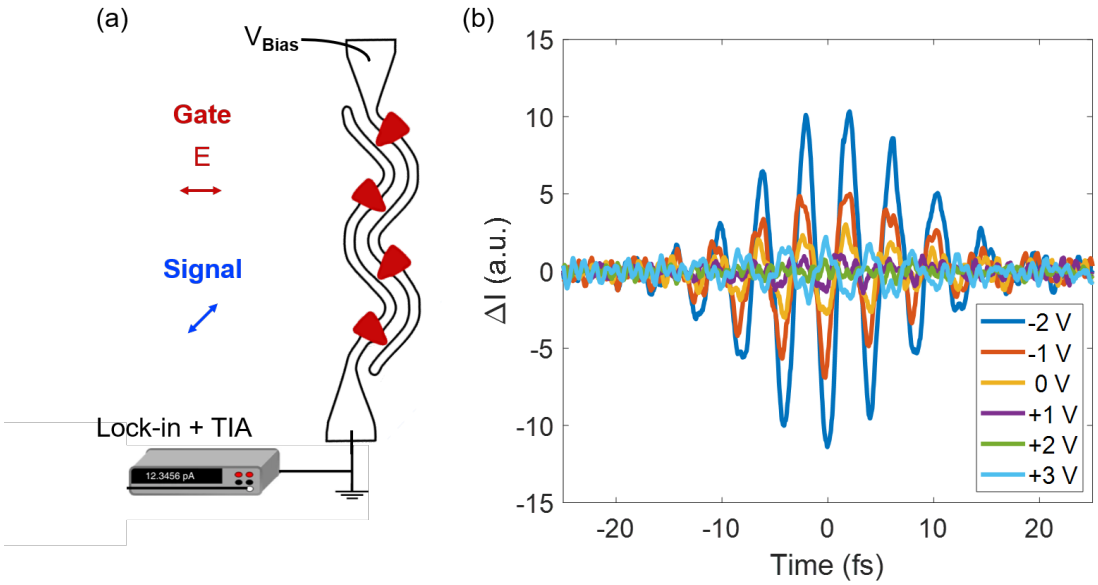

Figure 7-3: **Voltage sweep with linear polarized light.** (a) Schematic of the bias voltage sweep with a linear polarized gate set to 0 ° and a signal which was set to 45 °. (b) The experimentally measured voltage sweep starts from -2 V and increases to + 3 V.

In bias-controlled device activation, the gate pulse polarization is rotated to $\theta = 0^\circ$ such that an equal component of the electric field vector is projected onto the two different tip orientations. This equal projection results in the equivalent activation of each antenna as shown in Fig. 7-1e. First, we performed measurements where the polarization of the gate pulse was set to 0° such that both types of nanoantennas are activated while the signal was set to 45° linear polarized light as shown schematically in Fig. 7-3a. The measurement results are shown in Fig. 7-3b. We start by using the largest negative bias possible before background shot noise due to the bias dominating the current output (-2 V) then sweep the voltage in increments of 1 V until the

biasing dominates the current output. Taking the peak amplitude of the waveforms also reveals that the charge neutral point (the point where the signal is nulled) resides at +2 V. At negative voltages, the antennas facing 45° are activated. At -2 V, the strongest response was observed and quickly decreased as the bias voltage was set to 0. Afterward, a positive bias was applied, and due to light not being exactly 45° with respect to the sample, there was a weak finite response that is $\lambda/2$ phase shifted from the electric field waveforms obtained with a negative bias. This demonstrates that the bias can be used to select the antennas of interest.

Circularly Polarized Light

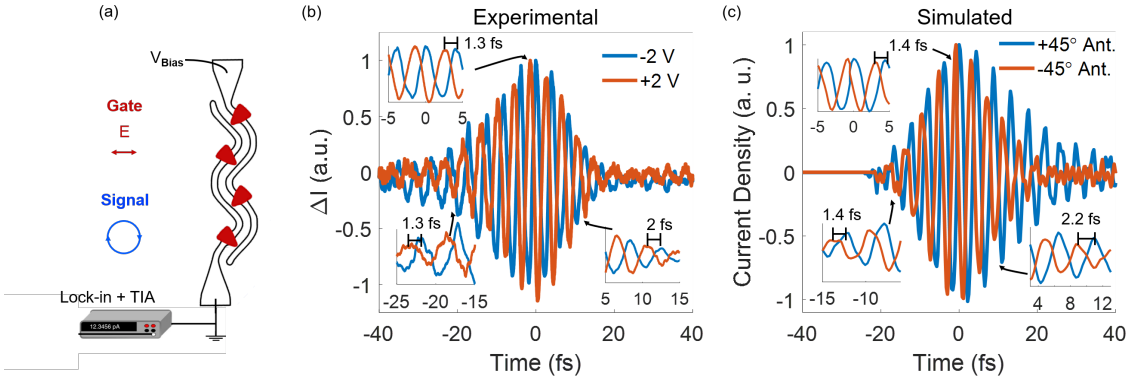

Figure 7-4: **Sampling with a signal pulse rotated by a quarter waveplate (QWP).** (a) Schematic for the sampling of circularly polarized light. The insets show the zoomed-in differential current showing the measured phase shift between the two types of antennas (b) An experimentally sampled electric field trace when the input gate pulse was linearly polarized at 0° and the signal pulse was made into circular polarization. The polarization sensitivity was selected by biasing the nanoantennas. The positive voltage (orange) and negative (blue) correspond to the -45° axis and +45° axis, respectively. The insets are the zoomed-in simulated results showing similar phase shifts as seen in experimental results. (c) The simulated sampling response with the corresponding antenna pairs.

To study the cross-polarization field and phase sensitivity of the device, we performed sampling of circularly polarized light both experimentally and through simulations. The setup for the experiments and simulation is shown in 7-4a. The gate is distributed among the two types of antennas, and then a bias voltage is used to select the sampled polarization while the signal pulse is made to be circular. The magnitude

of the voltage applied was different since the gap between antennas may be slightly different due to variations in the nanofabrication (e.g., slightly different gap sizes). A corresponding bias voltage was chosen such that either the +45° or -45° antennas are chosen. As seen in Fig. 7-4b is the sampled circularly polarized fields. There is a shift of 1.3 fs, which is approximately $\lambda/4$, between the two sampled electric fields that were constant from -40 fs until 0 fs. Afterward, at times after 5 fs, dephasing occurs which is attributed to a coupling of the two resonant plasmonic modes through the connecting wires [159]. The shift observed is $\sim$ 2 fs, which corresponds to a $\lambda/2$ shift between the two sampled traces. Post-measurement, such as plasmonic dephasing from the system response can be removed provided that the phase response through electromagnetic simulations is accurate.

We also perform simulations to model the response observed in the experiments. As the simulation starts, the phase shift is approximately $\lambda/4$ and persists until t = 0 where it shifts to $\lambda/2$, following the exact same trend observed in the experimental measurements. This characteristic of a $\lambda/4$ shift seen at the beginning of the sampling is predicted by a coupled oscillator model where two modes exist [160]. Here, the two types of nanoantennas are the two modes and the wire connecting the two tips can be seen as a spring coupling the two modes. In any coupled oscillator system, the system starts off with the same driven response and starts to change due to the coupling of the two modes. This means that if we excite the coupled oscillator system with a $\lambda/4$ phase, we would expect to see a $\lambda/4$ phase shift in the beginning, then the system would relax to its natural phase. We note that the field sampling detector is very sensitive to geometric effects (e.g., the width of the wire connecting the triangular nanoantennas together), we further systematically performed FDTD simulations to understand the sensitivity of the actual electron beam lithography process when compared to the computer-aided designed layout. Due to device fabrication, not all devices result in a $\lambda/4$ phase shift before t = 0 when expected.

Based on these results measuring a circularly polarized signal, it is expected that arbitrary polarizations (e.g. elliptical) can be measured. In this proposed experiment, we would systematically perform bias-controlled device activation measurements us-

ing the same device and conditions as the circularly polarized experiments except we would rotate the quarter waveplate while measuring the corresponding electric field waveforms sequentially (*i.e.* measured one right after another, averaging for each condition). First, this would be done using electromagnetic simulations and then tested in the lab. We could then verify our results between the electromagnetic simulations and experimental results against the expected phase shifts calculated using Jones matrices for the various quarter waveplate conditions.

7.3.3 Comparison of spectral measurements

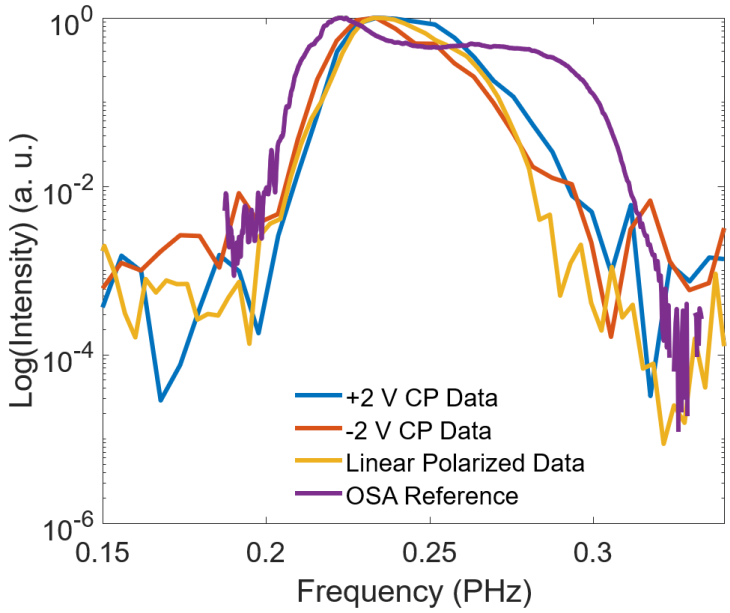

Figure 7-5: **Comparison of the spectral measurements with a reference.** The experimentally measured linearly polarized and circularly polarized squared Fourier-transformed spectra compared against a commercial optical spectrum analyzer.

Finally, we compare the intensity spectra from the field-resolved measurements obtained from linearly polarized and circularly polarized configurations, as illustrated in Figures 7-2 and 7-4, respectively, with those acquired using a commercial optical spectrum analyzer. We Fourier transformed the sampled fields into the frequency domain and squared the result to obtain their intensity. As depicted in Figure 7-5, the spectral characteristics of the sampled fields exhibit remarkable similarity, albeit

with minor discrepancies observed around 0.275 PHz. These differences primarily stem from slight variations in antenna resonance due to fabrication tolerances. Upon closer examination, it becomes evident that the intensity disparities, particularly on the higher frequency end, are attributable to antenna resonance roll-off or reduction of nonlinearity due to biasing. Despite these differences, discernible intensity profiles persist across the spectrum, albeit at differing ratios compared to the optical spectrum analyzer reference.

7.4 Sensitivity Simulations on Fabrication Tolerance

We performed simulations to understand how the sampled waveforms and phase shifts between the two polarizations occur as a function of geometric shifts. This provides insight into what happens in a measurement when the fabrication of the devices is not perfect.

7.4.1 Methodology

The optical response of the polarization-sensitive nanoantennas was simulated using finite-difference time-domain solver Lumerical and MEEP [69]. For Lumerical simulations, we used the data from the Lumerical library for Au (Palik) and SiO_2 (Palik). We define the wavelength minimum and maximum to be the same as our supercontinuum spectrum from an optical spectrum analyzer (see section 7.3.3). For the circular polarization simulations, two sources of the same amplitudes are used except one has a phase of 0° and another with 90°, and the source polarizations are offset by 90°.

For the sampling simulations, we directly take the local electric fields from Lumerical for E_{gate} and E_{signal} which are separately simulated for the gate and signal. We use the Fowler-Nordheim equation (Γ) and numerically calculate the current cross-correlation by

$$I_{cc}(\tau) \propto \int_{-T_{\text{rep}}/2}^{T_{\text{rep}}/2} \Gamma(E_{\text{gate}}(t) + E_{\text{signal}}(t))\, dt$$

using a ratio of signal to the gate of 0.001.

7.4.2 Simulation results

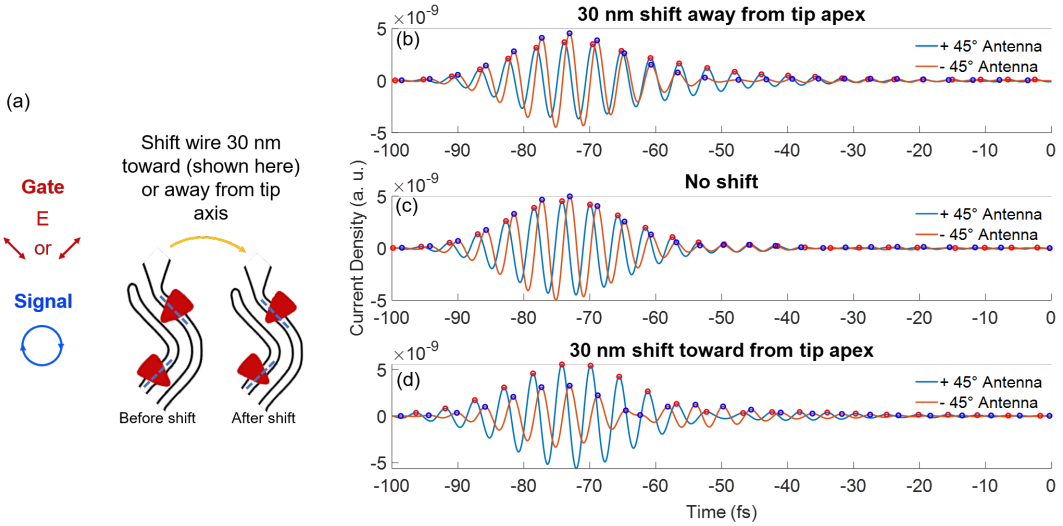

Figure 7-6: **Simulated sampling response of nanoantennas with a length of 0.8 μm between the tips with the wire shifted toward or away from the tip axis by 30 nm.** (a) Schematic of simulation and the parameter that was changed. (b) The simulated sampling response from the two types of antennas with a 30 nm shift away from the tip axis when the antennas are activated with a linear 45° or -45° gate. (c) The simulated sampling response with the wire lying at the center of the triangle (d) The simulated sampling response with the wire shifted 30 nm toward the tip axis.

Shown in the simulations are the simulated sampling waveform for the circularly polarized light. For the circular polarization simulations, two sources of the same amplitudes are used except one has a phase of 0° and another with 90° , and the source polarization is offset by 90° with respect to each other. The gate was simulated by using a single source that is parallel to the tip axis of the two antennas.

The schematic is shown in Fig. 7-6a. The gate is either +45° or -45° with the signal being circularly polarized. In Fig. 7-6b, one curve looks at the response with gate exciting one pair of antennas and inputting circularly polarized light. There is a 30 nm shift away from the tip axis and at the beginning at -60 fs, the two waveforms start off as $\lambda/4$ and evolve into being out of phase starting at -40 fs. In Fig. 7-6c, there is no shift and this is what is intentionally written in the electron beam lithography. We targeted the wire to be at the center of the antenna since it disturbs

the plasmonic mode of the antenna the least [44]. The two waveforms start off as nearly $\lambda/4$ shifted with respect to each other and at -50 fs, they are nearly in phase and then later evolve back to $\lambda/4$. Lastly, in Fig. 7-6d when the wire is shifted 30 nm towards the tip axis, the two waveforms start off as nearly $\lambda/4$ shifted and are again nearly in phase at -50 fs. It can also be seen at -45 fs that there are some dynamics that occur in this situation that are not seen in Fig. 7-6bc. It is attributed to the coupling between the two antennas. What is occurring can be modeled as a coupled oscillator where there are two modes that exist [160]. As the wire connecting the two tips is changed, the response of the coupled oscillator changes and is the superposition of the two modes that exist. At later times beyond -35 fs, the waveforms are in phase. The wire placement plays a large role in the phase shift of the sampled waveforms, especially at later times.

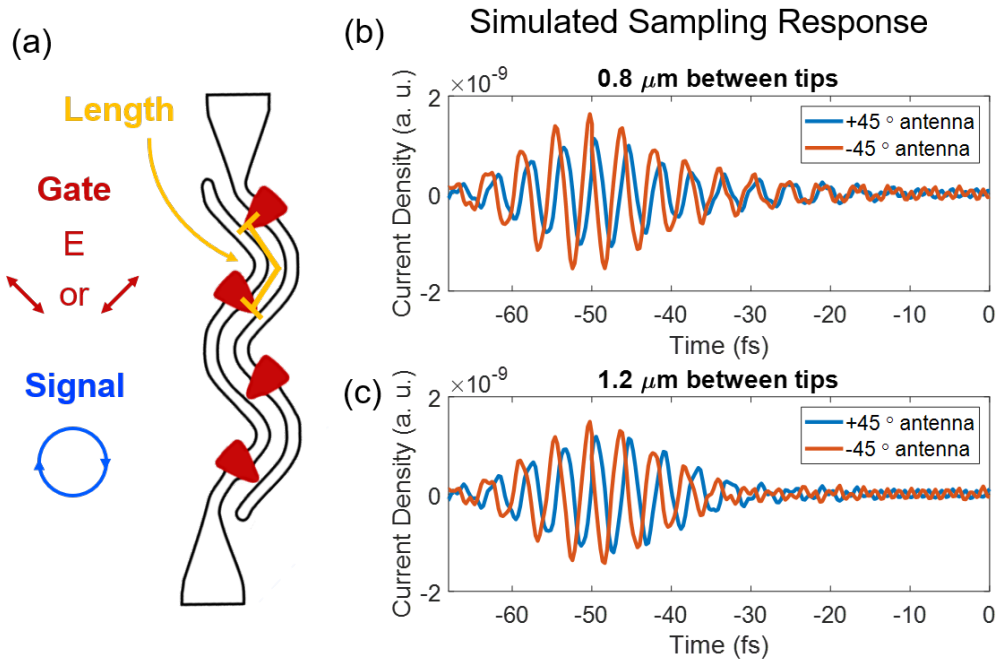

Figure 7-7: **Simulated sampling response with varied distance between the tips.** (a) The schematic of the distance between the tips. (b) The simulated sampling response when the antennas are activated with a linear 45° or -45° gate from the two types of antennas keeping a 0.8 μm length between the tips. (c) The simulated sampling response with the length between the tips set to 1.2 μm

Shown in Fig. 7-7 is the effect of the length between the two tips and the length

is defined as shown in the schematic in Fig. 7-7a. In Fig. 7-7 b, when the distance between the two tips is set to 0.8 μm, it can be seen that the phase shift between the two antennas starts off as $\lambda/4$ and by -50 fs, the shift becomes smaller and at later times, it is in phase with respect to each other. However, in Fig. 7-7c, it can be seen that the $\lambda/4$ stays consistent between the two waveforms. The distance between the two triangular nanoantennas can also play a role in the phase shift observed in the sampled traces.

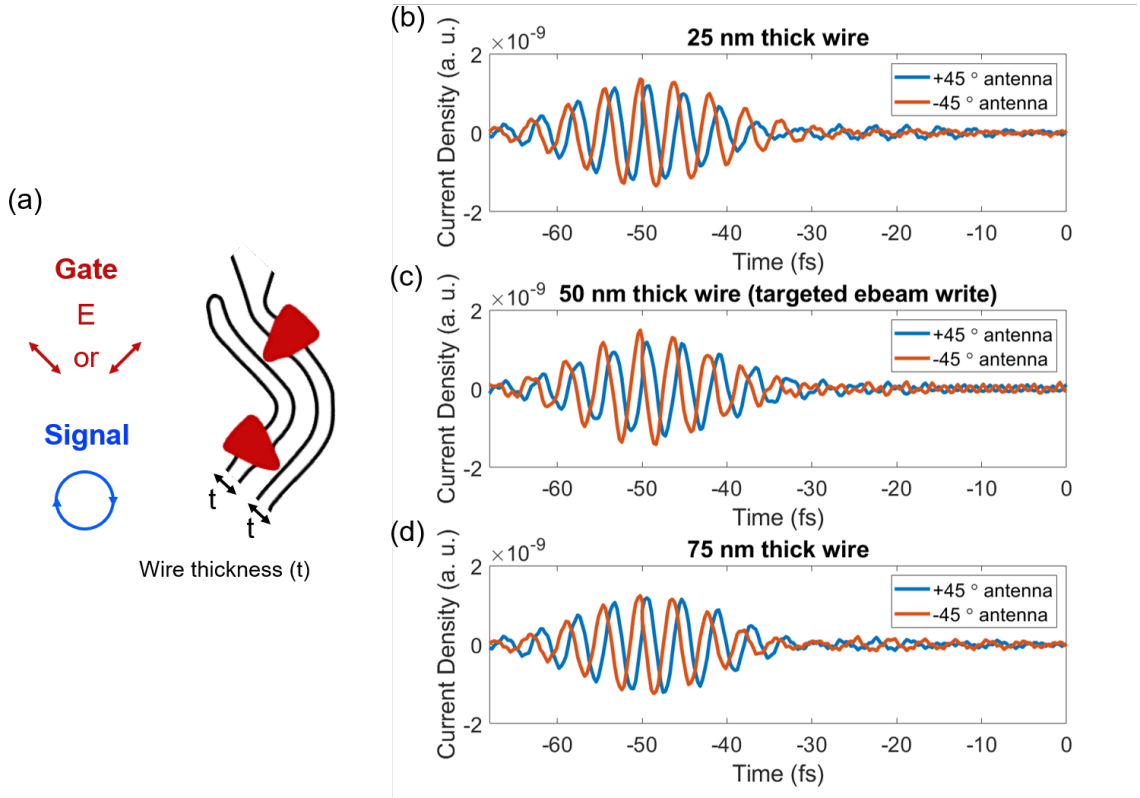

Figure 7-8: **Simulated sampling response with varied wire thickness.** (a-c) The response of antennas with a circularly polarized source with a varied length between the two types of tips. (d-f) The response of antennas with linear polarized light with a varied length between the two types of tips.

Next, the wire connecting the triangular nanoantennas together is varied in thickness as shown in Fig. 7-9a. As seen from Fig 7-9b-d, the thickness has a negligible effect on the phase shift between the two waveforms and the amplitude of the current density.

Lastly, the simulations shown above were using either 45° or -45° polarized light,

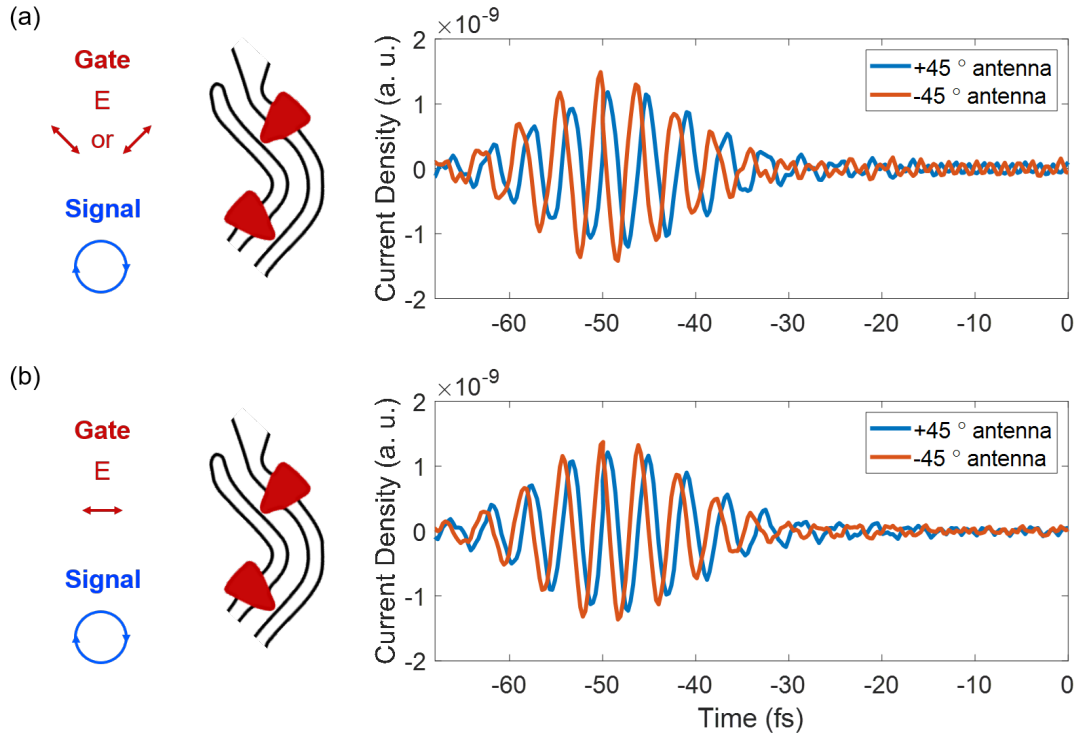

Figure 7-9: **Simulated sampling response with the experimental target design.** (a) Simulated sampling response of the 50 nm thick wire, 0.8 μm between the tips, and no shift of the wire when a linear 45° or -45° gate is used with a circularly polarized signal. (b) Simulated sampling response when a linear horizontal gate is used with circularly polarized signal

selectively activating a pair of tips. We utilized the parameters that are targeted in the electron beam lithography, specifically, a 50 nm thick wire, 0.8 μm between the tips, and no shift of the wire placement. There is a slight change in the phase shift between -60 fs and -50 fs where the shift is 1.6 fs when the gate is set to be parallel to the tip axis and the shift is 0.8 fs when the gate is split among the two antenna types.

7.5 Conclusion and Outlook

We report a new device architecture for polarization-sensitive nanoantenna-based on-chip time-domain spectroscopy. Our experimental results, using a pJ-scale 78.4 MHz laser along with simulations, show that light with different polarizations can be

sampled such that the full field response can be retrieved in terms of relative amplitude and phase. We also emphasize that device degradation was observed throughout tens of minutes of constant illumination. In the future, further investigations of the phase sensitivity and measurements at lower repetition rates should be performed to understand the device degradation mechanisms of gold devices. Other more robust metals, such as platinum or tungsten, could be used, but may not offer as large field enhancements seen in plasmonic metals. A device such as this can be used for low pulse energy polarization-resolved optical field sampling. We also show through a combination of experimental results and simulations that the device geometry of the triangular nanoantenna network can play a role in the ability to sample the phase shift between two polarizations of light.

Chapter 8

Conclusion and Future Work

Revolutionary scientific and technological developments in lasers have opened the door to the development of ultrafast optoelectronics. Demonstrating practical and scalable all-optical switching with attosecond speed through optical transistors with petahertz speed (a billion times faster than the clock cycle of commercial computers) could revolutionize electronics. Thus, this thesis demonstrates the potential impact of metallic nanoantennas as a platform for light field-driven electronics. Here, a summary of the main results and future directions are presented.

8.1 Conclusion and Follow-up Experiments

The ability to control which oscillations of light contribute to a measurable current has been demonstrated to be crucial in electronics found in daily life. Thus, rectification control is also crucial in lightwave-driven electronics. A framework for understanding how rectification, what order of nonlinearities are required for lightwave-driven electronics, and how the input lightwave affects the output characteristics of a lightwave device is presented in Chapter 3. The power of nanoantennas is further illustrated through the tunability in geometry and material choices.

Based on the nanoantenna platform, numerous experiments and applications can be envisioned, leveraging both single nanoantennas and larger network structures. Singular antennas hold promise for delving into PHz-bandwidth logic gates and mem-

ory cells [47], [82]. Conversely, network structures offer unique advantages, with their device size similar to the pixel dimensions found in contemporary Si-based CMOS detectors. Coupled with reduced pulse energy requisites, this enables seamless integration of multiple nanoantenna networks within expansive pixel matrices. More broadly, pushing the boundaries in PHz electronics will require future investigations of new device classes such as transistors and logic circuits and also new material platforms. With our results, we illustrate a path towards scalable and directly applicable PHz electronics.

First, a nanoantenna device without rectification is demonstrated for the shot-to-shot measurement of optical phase. More than 2000 CEP-sensitive electrons are generated and read out on a shot-to-shot basis. Given the exceptional current densities generated in these nanometer-sized devices, further studies will be necessary to elucidate the role of electron-electron interaction during the sub-cycle emission process [16].

This demonstration allows for a CEP-sensitive camera with further improved noise performance (e.g. [161] but for CEP instead). Absolute single-shot CEP tagging can also be implemented by adapting I/Q detection with two separate networks recording $\pi/2$ phase-shifted currents. The previously demonstrated techniques of attosecond-resolved field sampling can be extended to single-shot readout, by making large line arrays of individual networks [45], [126].

The next experimental demonstration is a nanoantenna-based frequency mixer that enables the mixing of PHz frequencies beyond the input light bandwidth using a commercial CEP-unstable laser. This is showcased through the field-resolved measurement of the second harmonic of an optical waveform using the first harmonic. Similar devices could be used to create compact and sensitive sampling optical oscilloscopes with bandwidths spanning multiple octaves. It is anticipated that such optical field oscilloscopes will provide needed time-domain detection tools that will help accelerate the development of ultrafast source technologies (e.g. compact frequency combs and optical waveform synthesizers), and enable new approaches to the investigation of nonlinear light-matter interactions. Given a single-cycle gate pulse,

one can have continuous sampling bandwidth ranging from the sub-THz to the PHz. Beyond field sampling, electronic optical-frequency harmonic mixers could also be incorporated as fundamental components within future lightwave electronic systems for PHz-scale communication and computation.

Lastly, polarization rectification is demonstrated for vectorial field measurements by developing a new architecture that leverages the polarization sensitivity of the optical field-driven process. Scaling up this approach to create a multi-channel imager with multiple nanoantenna networks could enable spatial polarization-sensitive electric-field detection with attosecond time resolution. It also opens opportunities for polarization-resolved attosecond holography, allowing one to reconstruct optical fields with amplitude and phase information. In regards to pulse characterization, one unique demonstration of this platform would be to measure a single-femtosecond pulse, something that is non-trivial for simple pulse characterization techniques [162]. Beyond ultrafast pulse characterization, such a detector will enable optical oscilloscope experiments that can have a profound impact on understanding dynamical processes in chemistry, physics, and microscopy.

8.2 Future Work

In conventional electronics frequency mixers and phase detectors are pivotal in radio and cellular technologies. Likewise, these devices are expected to be instrumental in broadening the applications of lightwave devices. However, to realize the full potential of universal optical frequency electronics, the development of an optical transistor is imperative. While the planar structures demonstrated in this thesis provide a promising foundation, it is conceivable that they may impose limitations in the long run. Thus, new fabrication techniques may be necessary to create intricate 3D nanoantenna networks, thereby advancing the field toward its ultimate goal.

The demonstrations of a carrier-envelope phase detector and a harmonic frequency mixer using gold nanoantennas in this thesis mark significant strides toward practical lightwave electronics and can be extended to integrated lightwave electronics. Build-

ing upon this work by understanding how the workfunction/electron affinity plays a practical role in lightwave electronics (e.g. noise characteristics, emission regimes) or how other nonlinearities can be utilized for on-chip lightwave electronics will be fruitful. In principle, based on Fig. 3-2 and [21], [126], one can explore the work performed in this thesis through the use of multiphoton absorption, offering an alternative to relying solely on optical tunneling.

While speed often takes precedence in discussions about lightwave electronics' applications [4], [103], [163], practical challenges in guiding information persist. Waveguides or striplines, akin to those utilized for Auston switches [27], [28], [164]–[168] or integrated photonics, offer one solution. However, electron dispersion during propagation necessitates meticulous engineering of the waveguide or stripline to mitigate pulse stretching while ensuring large bandwidths. Using the idea of apodized gratings or double-chirped mirrors could potentially overcome this problem.

Although gold nanoantennas are employed for their fabrication simplicity in this work, transitioning to a fully CMOS-compatible platform is imperative for practical device realization and making the experimental demonstrations in this thesis commercial. This transition may entail the adoption of alternative nanoantenna materials, such as plasmonic or refractory metals capable of optical tunneling, as discussed in Figure 3-5. Achieving bandwidths exceeding 1 PHz demands materials responsive to such frequencies, while lower frequencies ($\sim$THz) are already within reach of numerous metals. Additionally, understanding the role of vacuum, encapsulation, or tunneling through a thin dielectric is crucial for the longevity of devices.

Advancing on-chip sources, like THz generation photoconductive antennas, could involve mid-infrared light generation, waveguiding, and amplification, coupled off-chip for compact mid-infrared sources where parametric amplifiers could enhance output power, offering a compact alternative to quantum cascade lasers.

Beyond on-chip electronics, the nanoantenna platform can be utilized as a tunable bandwidth detector that can be integrated on any dielectric as seen in Fig. 3-4. This platform translates the traditional materials problem into a geometric problem, which is much more straightforward to tune. However, as a regular intensity detector,

the emission mechanism will be very different than the optical tunneling/field-driven emission mechanism used throughout this thesis. This idea was demonstrated in Piltan et al [169] and requires further studies into the physical mechanism. Based on the analysis of the data presented by Piltan et al, the main mechanism is Schottky rather than pure field emission.

In the domain of fundamental science, as mentioned earlier, the nanoantenna devices showcased in this thesis offer a direct avenue for exploring dynamics with polarization sensitivity. Due to their field-sensitive nature, these detectors have the capacity to measure phenomena inaccessible to traditional intensity detectors. Consequently, envisioning experiments to investigate electromagnetic fluctuations (or correlations) and collective excitations at quantum critical points or vacuum is now possible (assuming that the noise characteristics are below that of the fluctuations or correlations). This can lead to innovative approaches to actively manipulate fluctuations in matter via nonlinear and non-thermal pathways.

While nanoantennas hold promise for various light-related applications, practical lightwave electronics for everyday use remain distant. Nevertheless, niche applications may emerge with time, reminiscent of microwave frequencies finding unexpected utility in heating food, suggesting a bright future for lightwave technologies.

Appendix A

Modeling

A.1 Fourier Transform of a Cross-correlation

For Chapters 5-7, a cross-correlation is often used to analyze experimental data and modeling. Here, the cross-correlation is derived

The cross-correlation of two functions $A(t)$ and $B(t)$ can be written as

$$(A \star B)(\tau) = \int_{-\infty}^{\infty} \mathrm{d}t A(t-\tau)B(t). \tag{A.1}$$

If we then take some function $C(t) = A(-t)$, we find that

$$(A \star B)(\tau) = (C * B)(\tau), \tag{A.2}$$

where $*$ denotes a convolution. It is a well-understood property that the Fourier transform of a convolution of two functions in the time domain is expressed as the multiplication of the Fourier transform of each function individually in the frequency-domain, *i.e.* that

$$\mathcal{F}\{(C * B)(\tau)\} = \tilde{C}(\omega)\tilde{B}(\omega). \tag{A.3}$$

Finally, we use the property that $\mathcal{F}\{f(-t)\} = \tilde{f}(-\omega)$ to conclude that

$$\mathcal{F}\{(A \star B)(\tau)\} = \tilde{A}(-\omega)\tilde{B}(\omega). \tag{A.4}$$

This is the most general solution for the Fourier transform of a cross-correlation. However, in the special case that $A(t)$ is purely real, we have that $\tilde{A}(-\omega) = \tilde{A}(\omega)^*$. Putting this all together, for a purely real $A(t)$ we have that

$$\mathcal{F}\{(A \star B)(\tau)\} = \tilde{A}(\omega)^* \tilde{B}(\omega). \tag{A.5}$$

A.2 Modeling tools

The optical response of the nanoantennas used in Chapters 5-7 was simulated using FDTD solver Lumerical and MEEP [69]. For Lumerical simulations, we used the data from the Lumerical library for Au (Palik) and SiO_2 (Palik).

For field enhancement simulations, we used the standard materials library included in the MEEP Python package. We use periodic boundary conditions in the nanoantenna on a silicon oxide plane with perfectly matched layers in the direction of propagation of the plane-wave source to prevent multi-reflections affecting the simulation. We also ensured the nanoantenna tips had a 10 nm radius of curvature, which corresponds to the measured radius of curvature of the as-fabricated antenna network.

For the work described in Chapter 7, we define the wavelength minimum and maximum to be the same as our supercontinuum spectrum from an optical spectrum analyzer. For the circular polarization simulations, two sources of the same amplitudes are used except one has a phase of 0° and another with 90° , and the source polarizations are offset by 90 degrees.

Appendix B

Sample Fabrication

B.1 Device Layout

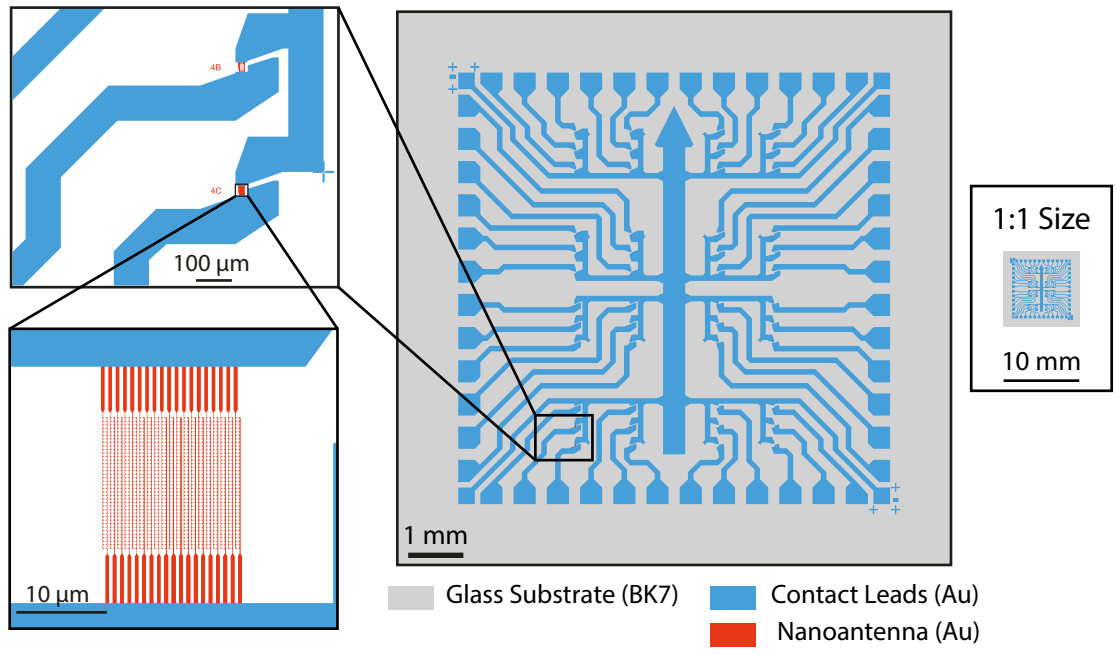

Figure B-1: **Circuit layout.** Layout of the microchip with various nanoantenna networks used in Chapters 5-7. Progression of sizes from a 1:1 scale down to 1:1000. Blue areas mark the contact leads fabricated through photolithography in gold (Au). Red areas mark the nanoantenna network fabricated through electron-beam lithography in gold (Au). The grey area marks the substrate.

Fig. B-1 shows the complete layout of the tested chip that contains the nanoan-

tenna networks. The chip layout is shown on a 1:1 scale with zoom-in on the relevant network tested in the main text. The device is fabricated through a two-step process which is discussed in detail in the appendix. The example shown here is for gold nanoantenna networks which are fabricated on a dielectric substrate through electron-beam lithography in gold. The second step, performed for all devices tested, is the fabrication of larger-scale contact through photolithography in gold. The role of the contact leads is to make electrical contact with the nanoantenna networks and to provide large pads at the outer edge of the chip for wire bonding. After visual analysis in a scanning electron microscope, 24 of the 48 networks are selected for wire bonding to a printed circuit board.

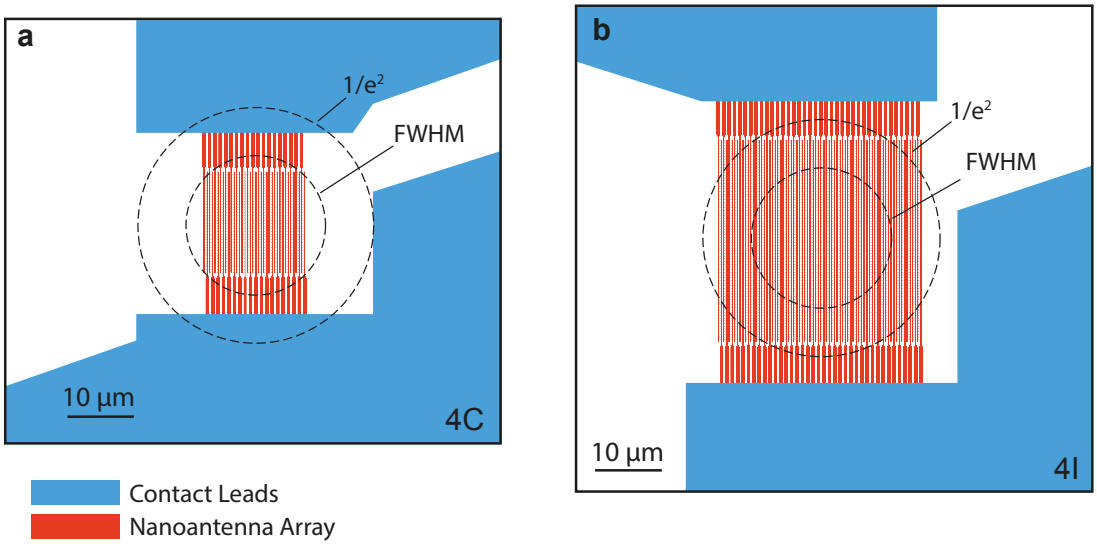

Figure B-2: **Device layout.** The blue area shows the contact leads fabricated by photolithography used in Chapters 5-7. The red areas show the nanoantennas made by electron-beam lithography. The dashed circles mark the approximate spatial distribution of the laser focus (Chapter 4, FWHM: 21 µm, $1/e^2$: 35.5 µm). (a) A schematic of the small area network used in Chapter 4. The nanoantenna network area of the device measures 15 µm × 15 µm. (b) The large area nanoantenna network used in Chapter 4 with an area of 30 µm × 30 µm.

The layout of the device presented in Chapter 4 is shown in Fig. B-1a. The nanoantenna network, produced by electron beam lithography, is marked by the red-shaded structure. The nanotenna network measures 15 µm × 15 µm. For comparison,

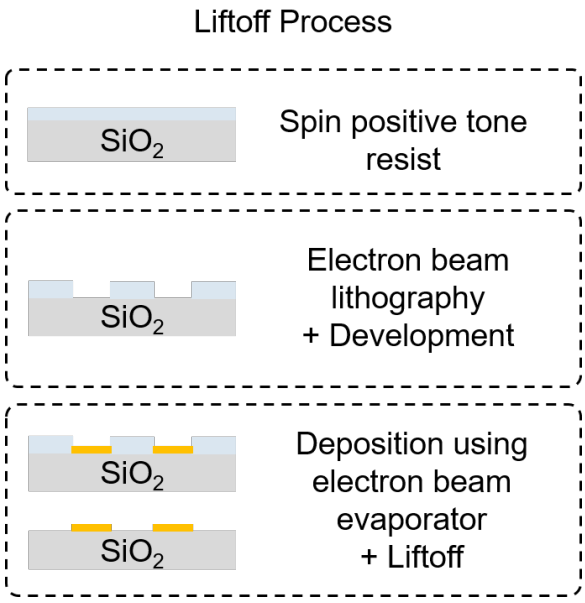

Figure B-3: **Liftoff process.** Initially, positive tone resist is spun onto a dielectric substrate (illustrated here using SiO_2). Subsequently, the nanoantenna pattern is written and developed, then the nanoantenna metal is deposited on top of the developed resist. Following this, liftoff is performed to remove the undesired region with resist remaining.

the spatial dimension of the optical focus (FWHM and $1/e^2$) is shown as dashed circles. An additional device with an area of 30 µm × 30 µm is shown in Fig. B-2b. The two devices show the case of a network smaller than the laser focus and larger than the laser focus.

B.2 Gold Antennas

BK7 or Fused Silica (MTI Corp.) was cleaned by sonicating in acetone and isopropyl alcohol for five minutes in each solvent. Afterward, the substrates are dried using nitrogen and cleaned further using piranha. Before use, the substrates were ashed with an oxygen plasma. For all electron beam lithography, various doses are assigned to each fabricated chip to account for process variation, ensuring a diverse array of nanoantennas with various characteristics for testing purposes.

B.2.1 Electron beam lithography

125 keV

PMMA 950 A2 (Microchem) was spun onto the substrates and baked at 180° C for two minutes. As these substrates are insulating, DisCharge H2O (DisChem Inc.) was spun on top of the PMMA layer. Electron beam lithography with proximity effect correction was then performed using an Elionix F125 with a write current of 2 nA and a dose ranging from 4000 - 6000 μC/cm^2. After the exposure, the DisCharge H2O was removed by rinsing the sample in deionized water and then the exposed PMMA was cold-developed in a 3:1 ratio of isopropyl alcohol to 4-Methyl-2-pentanone at 0° C.

50 keV

ZEP 530A (Zeon) was diluted with a 1 to 1 ratio (volume/volume) using anisole, then spun onto the substrates and baked at 180° C for two minutes. As these substrates are insulating, DisCharge H2O (DisChem Inc.) was spun on top of the ZEP layer. Electron beam lithography with proximity effect correction was then performed using an Elionix HS50 with a write current of 1 nA and a dose ranging from 250-325 μC/cm^2. After the exposure, the DisCharge H2O was removed by rinsing the sample in deionized water and then the exposed PMMA was cold-developed in ortho-xylene (o-xylene) at 0° C for 30 seconds, then rinsed in a bath of isopropyl alcohol for another 30 seconds.

B.2.2 Antenna deposition and liftoff

For nanoantennas, electron beam evaporation was used to deposit a 2 nm Ti adhesion layer followed by 20 nm of Au using a Temescal FC2000. The base pressure before evaporation is 2×10$^-$6 Torr. The target deposition rate is 1 Å/second. Subsequently, liftoff was performed at 65° C of n-methyl-2-pyrrolidone (Microchem).

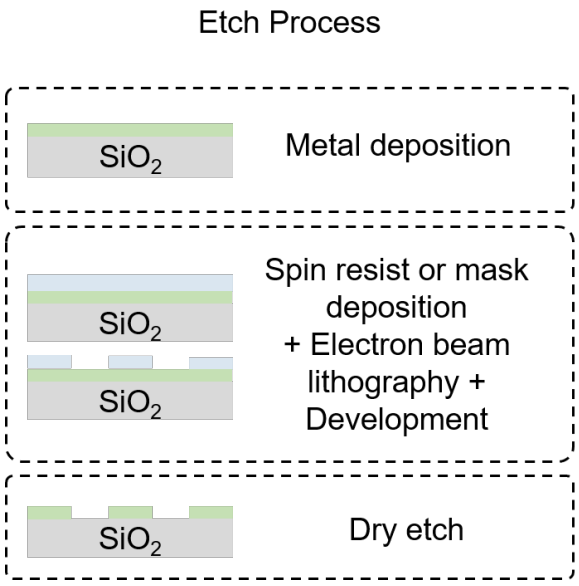

Figure B-4: **Etch process.** Initially, the nanoantenna metal is deposited onto a dielectric substrate (illustrated here using SiO_2). Subsequently, either a negative tone resist is applied, written, and developed, or a hard mask with the desired pattern is deposited on top of the metal film. Following this, etching removes the undesired regions.

B.2.3 Contacts

To make contact with the nanoantenna networks, photolithography was performed using nLOF 2035 (MicroChemicals GmbH) with a $\lambda = 375$ nm maskless aligner with the dose set to 300 mJ/cm^2. For development, the samples are immersed in AZ 726 MIF (MicroChemicals GmbH) at room temperature. Electron beam evaporation was then used to deposit 10-40 nm Cr and 20-160 nm Au. The liftoff was performed in n-methyl-2-pyrrolidone or acetone. Afterward, the antenna networks were checked using a scanning electron microscope, then mounted onto a printed circuit board and wire-bonded, which was used to connect the nanoantenna networks to an external voltage source.

B.3 Titanium Nitride Antennas

B.3.1 Deposition

Reactive sputtering was used to deposit a 50 nm TiN film on a 4-inch fused silica wafer using an AJA sputtering tool. A pre-sputtering process is run with 3 mTorr, 20 sccm of argon, 15 sccm of nitrogen, and 300 W of RF power. The low deposition rate of 0.3 Å/second ensures that the titanium has sufficient time to react with nitrogen.

B.3.2 Electron beam lithography

A die saw (DISCO DAD3230) was used to cut 1 cm × 1 cm dies of the PMMA 950 A8 (spun at 3000 rpm) on 50 nm TiN on fused silica. After the dies were cleaned by sonicating in acetone and isopropyl alcohol for five minutes in each solvent. Afterward, the substrates are dried using nitrogen, and hydrogen silsesquioxane (HSQ) is spun.

HSQ, often referred to as FOx (flowable oxide), is a widely used negative-tone electron beam resist known for its exceptional resolution capabilities, achieving sub-nanometer resolutions in single-digit nanometers. Unlike conventional organic polymer resists, HSQ is a spin-on-glass material that, upon development, leaves behind a SiO_2-like layer in exposed regions. Despite its remarkable performance, HSQ presents certain challenges, notably in storage and shelf-life, requiring refrigeration at temperatures as low as -60°C. The thickness of the spun layer can vary significantly depending on its concentration, typically dissolved in methyl isobutyl ketone (MIBK). Cleanroom facilities, such as MIT.nano, offer pre-diluted HSQ vials with concentrations ranging from 2% to 16%, enabling the fabrication of layers spanning from 40 nm to 600 nm.

HSQ Hardmask using a 50 keV system

2% or 4% HSQ is spun ensuring that the spin conditions accelerate as fast as possible to 3000 rpm. If this is not done, then HSQ may not spin uniformly. Lithography was performed using an Elionix HS50 with doses ranging from 1800-2100 $\mu C/cm^2$. After

the exposure, the exposed HSQ was developed using 25% tetramethylammonium hydroxide (TMAH) for 3 minutes. The film cannot be overdeveloped as HSQ becomes an SiO_2-like layer. After, the developed chip is rinsed in water for 30 seconds and dried using nitrogen.

Metallic Hard mask

An alternative to HSQ is by depositing a metallic hard mask. Two choices are Cr/Al [170] or nickel. First, positive tone resist such as ZEP or PMMA is spun and exposed as previously mentioned for the gold nanoantenna fabrication section. Then the metallic hard mask is deposited using ebeam evaporation and lifted off in heated NMP. Subsequently, a dry etch can be used to remove the unwanted regions.

B.3.3 Dry Etch

Fluorine etches can be utilized for etching of the metallic hard mask, however, in MIT.nano the problem of using Cr/Al is that it requires TMAH sonication [170]. A chlorine etch was developed using a Samco RIE-200. Before etching, the chamber is conditioned. A plasma spark step with 12 sccm of chlorine and 20 sccm of boron trichloride with 120 W for the ICP source at 15 mTorr is run for 5 seconds, then the etch is run using the same conditions with an RF bias of 40 W for 10 minutes. Once the conditioning is completed, the developed HSQ on 50 nm TiN is etched for 105 seconds. Subsequently, the samples are rinsed with deionized water for 30 seconds. Afterward, the samples are dipped into a 7:1 buffered oxide etch for 10 seconds. As the oxide density is so low, the etch rate is relatively high when compared to denser oxides [171]. Afterward, contacts can be made using gold as mentioned in the gold nanoantenna fabrication procedure above.

B.3.4 Contacts

To make contact with the nanoantenna networks, photolithography was performed using nLOF 2035 (MicroChemicals GmbH) with a $\lambda = 375$ nm maskless aligner with

the dose set to 300 mJ/cm^2. For development, the samples are immersed in AZ 726 MIF (MicroChemicals GmbH) at room temperature. Electron beam evaporation was then used to deposit 10-40 nm Cr and 50-160 nm Au. The liftoff was performed in n-methyl-2-pyrrolidone or acetone. Afterward, the antenna networks were checked using a scanning electron microscope, then mounted onto a printed circuit board and wire-bonded, which was used to connect the nanoantenna networks to an external voltage source.

Bibliography

[1] P. B. Corkum, N. H. Burnett, and M. Y. Ivanov, "Subfemtosecond pulses," *Optics Letters*, vol. 19, no. 22, pp. 1870–1872, Nov. 1994. DOI: 10.1364/OL.19.001870.

[2] M. Hentschel, R. Kienberger, C. Spielmann, *et al.*, "Attosecond metrology," *Nature*, vol. 414, no. 6863, pp. 509–513, Nov. 2001. DOI: 10.1038/35107000.

[3] G. Sansone, E. Benedetti, F. Calegari, *et al.*, "Isolated Single-Cycle Attosecond Pulses," *Science*, vol. 314, no. 5798, pp. 443–446, Oct. 2006. DOI: 10.1126/science.1132838.

[4] F. Krausz and M. I. Stockman, "Attosecond metrology: From electron capture to future signal processing," *Nature Photonics*, vol. 8, no. 3, pp. 205–213, Mar. 2014. DOI: 10.1038/nphoton.2014.28.

[5] M. Ferray, A. L'Huillier, X. F. Li, L. A. Lompre, G. Mainfray, and C. Manus, "Multiple-harmonic conversion of 1064 nm radiation in rare gases," *Journal of Physics B: Atomic, Molecular and Optical Physics*, vol. 21, no. 3, p. L31, Feb. 1988. DOI: 10.1088/0953-4075/21/3/001.

[6] M. Lewenstein, P. Balcou, M. Y. Ivanov, A. L'Huillier, and P. B. Corkum, "Theory of high-harmonic generation by low-frequency laser fields," *Physical Review A*, vol. 49, no. 3, pp. 2117–2132, Mar. 1994. DOI: 10.1103/PhysRevA.49.2117.

[7] P. M. Paul, E. S. Toma, P. Breger, *et al.*, "Observation of a Train of Attosecond Pulses from High Harmonic Generation," *Science*, vol. 292, no. 5522, pp. 1689–1692, Jun. 2001. DOI: 10.1126/science.1059413.

[8] M. Krüger, M. Schenk, and P. Hommelhoff, "Attosecond control of electrons emitted from a nanoscale metal tip," *Nature*, vol. 475, no. 7354, pp. 78–81, Jul. 2011. DOI: 10.1038/nature10196.

[9] H. Y. Kim, M. Garg, S. Mandal, L. Seiffert, T. Fennel, and E. Goulielmakis, "Attosecond field emission," *Nature*, vol. 613, no. 7945, pp. 662–666, Jan. 2023. DOI: 10.1038/s41586-022-05577-1.

[10] G. Herink, D. R. Solli, M. Gulde, and C. Ropers, "Field-driven photoemission from nanostructures quenches the quiver motion," *Nature*, vol. 483, no. 7388, pp. 190–193, Mar. 2012. DOI: 10.1038/nature10878.

[11] T. Rybka, M. Ludwig, M. F. Schmalz, V. Knittel, D. Brida, and A. Leitenstorfer, "Sub-cycle optical phase control of nanotunnelling in the single-electron regime," *Nature Photonics*, vol. 10, no. 10, pp. 667–670, Oct. 2016. DOI: 10.1038/nphoton.2016.174.

[12] C. Ropers, D. R. Solli, C. P. Schulz, C. Lienau, and T. Elsaesser, "Localized Multiphoton Emission of Femtosecond Electron Pulses from Metal Nanotips," *Physical Review Letters*, vol. 98, no. 4, p. 043 907, Jan. 2007. DOI: 10.1103/PhysRevLett.98.043907.

[13] L. Wimmer, G. Herink, D. R. Solli, S. V. Yalunin, K. E. Echternkamp, and C. Ropers, "Terahertz control of nanotip photoemission," *Nature Physics*, vol. 10, no. 6, pp. 432–436, Jun. 2014. DOI: 10.1038/nphys2974.

[14] W. P. Putnam, R. G. Hobbs, P. D. Keathley, K. K. Berggren, and F. X. Kärtner, "Optical-field-controlled photoemission from plasmonic nanoparticles," *Nature Physics*, vol. 13, no. 4, pp. 335–339, Apr. 2017. DOI: 10.1038/nphys3978.

[15] M. Ludwig, G. Aguirregabiria, F. Ritzkowsky, *et al.*, "Sub-femtosecond electron transport in a nanoscale gap," *Nature Physics*, vol. 16, no. 3, pp. 341–345, Mar. 2020. DOI: 10.1038/s41567-019-0745-8.

[16] J. Schötz, L. Seiffert, A. Maliakkal, *et al.*, "Onset of charge interaction in strong-field photoemission from nanometric needle tips," *Nanophotonics*, vol. 10, no. 14, pp. 3769–3775, Oct. 2021. DOI: 10.1515/nanoph-2021-0276.

[17] J. Blöchl, J. Schötz, A. Maliakkal, *et al.*, "Spatiotemporal sampling of near-petahertz vortex fields," *Optica*, vol. 9, no. 7, pp. 755–761, Jul. 2022. DOI: 10.1364/OPTICA.459612.

[18] A. Schiffrin, T. Paasch-Colberg, N. Karpowicz, *et al.*, "Optical-field-induced current in dielectrics," *Nature*, vol. 493, no. 7430, pp. 70–74, Jan. 2013. DOI: 10.1038/nature11567.

[19] M. Schultze, E. M. Bothschafter, A. Sommer, *et al.*, "Controlling dielectrics with the electric field of light," *Nature*, vol. 493, no. 7430, pp. 75–78, Jan. 2013. DOI: 10.1038/nature11720.

[20] N. Altwaijry, M. Qasim, M. Mamaikin, *et al.*, "Broadband Photoconductive Sampling in Gallium Phosphide," *Advanced Optical Materials*, vol. 11, no. 9, p. 2 202 994, 2023. DOI: 10.1002/adom.202202994.

[21] S. B. Park, K. Kim, W. Cho, *et al.*, "Direct sampling of a light wave in air," *Optica*, vol. 5, no. 4, pp. 402–408, Apr. 2018. DOI: 10.1364/OPTICA.5.000402.

[22] D. Zimin, M. Weidman, J. Schötz, *et al.*, "Petahertz-scale nonlinear photoconductive sampling in air," *Optica*, vol. 8, no. 5, pp. 586–590, May 2021. DOI: 10.1364/OPTICA.411434.

[23] F. Braun, "Ueber die Stromleitung durch Schwefelmetalle," *Annalen der Physik*, vol. 229, no. 12, pp. 556–563, 1875. DOI: 10.1002/andp.18752291207.

[24] W. Schottky, "Halbleitertheorie der Sperrschicht," *Naturwissenschaften*, vol. 26, no. 52, pp. 843–843, Dec. 1938. DOI: 10.1007/BF01774216.

[25] J. A. Fleming, "On the conversion of electric oscillations into continuous currents by means of a vacuum valve.," *Proceedings of the Royal Society of London*, vol. 74, no. 497-506, pp. 476–487, Apr. 1905. DOI: 10.1098/rspl.1904.0143.

[26] M. Bass, P. A. Franken, J. F. Ward, and G. Weinreich, "Optical Rectification," *Physical Review Letters*, vol. 9, no. 11, pp. 446–448, Dec. 1962. DOI: 10.1103/PhysRevLett.9.446.

[27] D. H. Auston, "Picosecond optoelectronic switching and gating in silicon," *Applied Physics Letters*, vol. 26, no. 3, pp. 101–103, Feb. 1975. DOI: 10.1063/1.88079.

[28] D. H. Auston, A. M. Johnson, P. R. Smith, and J. C. Bean, "Picosecond optoelectronic detection, sampling, and correlation measurements in amorphous semiconductors," *Applied Physics Letters*, vol. 37, no. 4, pp. 371–373, Sep. 1980. DOI: 10.1063/1.91947.

[29] J. A. Valdmanis, G. Mourou, and C. W. Gabel, "Picosecond electro-optic sampling system," *Applied Physics Letters*, vol. 41, no. 3, pp. 211–212, Aug. 1982. DOI: 10.1063/1.93485.

[30] P. B. Corkum, "Plasma perspective on strong field multiphoton ionization," *Physical Review Letters*, vol. 71, no. 13, pp. 1994–1997, Sep. 1993. DOI: 10.1103/PhysRevLett.71.1994.

[31] P. Hommelhoff, Y. Sortais, A. Aghajani-Talesh, and M. A. Kasevich, "Field Emission Tip as a Nanometer Source of Free Electron Femtosecond Pulses," *Physical Review Letters*, vol. 96, no. 7, p. 077 401, Feb. 2006. DOI: 10.1103/PhysRevLett.96.077401.

[32] K. Arai, D. Okazaki, I. Morichika, and S. Ashihara, "All-Solid-State Optical-Field-Sensitive Detector for Sub-Nanojoule Pulses Using Metal–Insulator Hybrid Nanostructure," *ACS Photonics*, vol. 10, no. 6, pp. 1702–1707, Jun. 2023. DOI: 10.1021/acsphotonics.2c01855.

[33] L. Keldysh, "Ionization in the field of a strong electromagnetic wave," *Journal of Experimental and Theoretical Physics*, vol. 20, no. 5, pp. 1307–1314, May 1965.

[34] P. Hommelhoff, C. Kealhofer, and M. A. Kasevich, "Ultrafast Electron Pulses from a Tungsten Tip Triggered by Low-Power Femtosecond Laser Pulses," *Physical Review Letters*, vol. 97, no. 24, p. 247 402, Dec. 2006. DOI: 10.1103/PhysRevLett.97.247402.

[35] T. L. Cocker, D. Peller, P. Yu, J. Repp, and R. Huber, "Tracking the ultrafast motion of a single molecule by femtosecond orbital imaging," *Nature*, vol. 539, no. 7628, pp. 263–267, Nov. 2016. DOI: 10.1038/nature19816.

[36] T. L. Cocker, V. Jelic, M. Gupta, *et al.*, "An ultrafast terahertz scanning tunnelling microscope," *Nature Photonics*, vol. 7, no. 8, pp. 620–625, Aug. 2013. DOI: 10.1038/nphoton.2013.151.

[37] J. Vogelsang, G. Hergert, D. Wang, P. Groß, and C. Lienau, "Observing charge separation in nanoantennas via ultrafast point-projection electron microscopy," *Light: Science & Applications*, vol. 7, no. 1, p. 55, Aug. 2018. DOI: 10.1038/s41377-018-0054-5.

[38] B. Ahn, J. Schötz, M. Kang, *et al.*, "Attosecond-controlled photoemission from metal nanowire tips in the few-electron regime," *APL Photonics*, vol. 2, no. 3, p. 036 104, Feb. 2017. DOI: 10.1063/1.4974529.

[39] K. E. Echternkamp, G. Herink, S. V. Yalunin, K. Rademann, S. Schäfer, and C. Ropers, "Strong-field photoemission in nanotip near-fields: From quiver to sub-cycle electron dynamics," *Applied Physics B*, vol. 122, no. 4, p. 80, Mar. 2016. DOI: 10.1007/s00340-016-6351-x.

[40] B. Piglosiewicz, S. Schmidt, D. J. Park, *et al.*, "Carrier-envelope phase effects on the strong-field photoemission of electrons from metallic nanostructures," *Nature Photonics*, vol. 8, no. 1, pp. 37–42, Jan. 2014. DOI: 10.1038/nphoton.2013.288.

[41] P. Dombi, A. Hörl, P. Rácz, *et al.*, "Ultrafast Strong-Field Photoemission from Plasmonic Nanoparticles," *Nano Letters*, vol. 13, no. 2, pp. 674–678, Feb. 2013. DOI: 10.1021/nl304365e.

[42] C. Karnetzky, P. Zimmermann, C. Trummer, *et al.*, "Towards femtosecond on-chip electronics based on plasmonic hot electron nano-emitters," *Nature Communications*, vol. 9, no. 1, p. 2471, Jun. 2018. DOI: 10.1038/s41467-018-04666-y.

[43] P. D. Keathley, W. P. Putnam, P. Vasireddy, *et al.*, "Vanishing carrier-envelope-phase-sensitive response in optical-field photoemission from plasmonic nanoantennas," *Nature Physics*, vol. 15, no. 11, pp. 1128–1133, Nov. 2019. DOI: 10.1038/s41567-019-0613-6.

[44] Y. Yang, M. Turchetti, P. Vasireddy, *et al.*, "Light phase detection with on-chip petahertz electronic networks," *Nature Communications*, vol. 11, no. 1, p. 3407, Jul. 2020. DOI: 10.1038/s41467-020-17250-0.

[45] M. R. Bionta, F. Ritzkowsky, M. Turchetti, *et al.*, "On-chip sampling of optical fields with attosecond resolution," *Nature Photonics*, vol. 15, no. 6, pp. 456–460, Jun. 2021. DOI: 10.1038/s41566-021-00792-0.

[46] T. Higuchi, C. Heide, K. Ullmann, H. B. Weber, and P. Hommelhoff, "Light-field-driven currents in graphene," *Nature*, vol. 550, no. 7675, pp. 224–228, Oct. 2017. DOI: 10.1038/nature23900.

[47] T. Boolakee, C. Heide, A. Garzón-Ramírez, H. B. Weber, I. Franco, and P. Hommelhoff, "Light-field control of real and virtual charge carriers," *Nature*, vol. 605, no. 7909, pp. 251–255, May 2022. DOI: 10.1038/s41586-022-04565-9.

[48] V. Hanus, B. Fehér, V. Csajbók, *et al.*, "Carrier-envelope phase on-chip scanner and control of laser beams," *Nature Communications*, vol. 14, no. 1, p. 5068, Aug. 2023. DOI: 10.1038/s41467-023-40802-z.

[49] A. M. Weiner, *Ultrafast Optics* (Wiley Series in Pure and Applied Optics). Hoboken, N.J: Wiley, 2009.

[50] U. Keller, *Ultrafast Lasers: A Comprehensive Introduction to Fundamental Principles with Practical Applications* (Graduate Texts in Physics). Cham: Springer International Publishing, 2021. DOI: 10.1007/978-3-030-82532-4.

[51] Shen, Yuen-Ron, *The Principles of Nonlinear Optics | Wiley.*

[52] G. Rosen and F. C. Whitmore, "Experiment for Observing the Vacuum Scattering of Light by Light," *Physical Review*, vol. 137, no. 5B, B1357–B1359, Mar. 1965. DOI: 10.1103/PhysRev.137.B1357.

[53] P. A. Franken, A. E. Hill, C. W. Peters, and G. Weinreich, "Generation of Optical Harmonics," *Physical Review Letters*, vol. 7, no. 4, pp. 118–119, Aug. 1961. DOI: 10.1103/PhysRevLett.7.118.

[54] Boyd, Robert W., *Nonlinear Optics*. Elsevier, 2020. DOI: 10.1016/C2015-0-05510-1.

[55] F. Shimizu, "Frequency Broadening in Liquids by a Short Light Pulse," *Physical Review Letters*, vol. 19, no. 19, pp. 1097–1100, Nov. 1967. DOI: 10.1103/PhysRevLett.19.1097.

[56] Argawal, Govind, *Nonlinear Fiber Optics*. Elsevier, 2013. DOI: 10.1016/C2011-0-00045-5.

[57] J. M. Dudley and J. R. Taylor, Eds., *Supercontinuum Generation in Optical Fibers*. Cambridge: Cambridge University Press, 2010. DOI: 10.1017/CBO9780511750465.

[58] T. Okamoto, Y. Kunihashi, Y. Shinohara, H. Sanada, M.-C. Chen, and K. Oguri, "Operation at 1 MHz of 1.7-cycle multiple plate compression at 35-W average output power," *Optics Letters*, vol. 48, no. 10, pp. 2579–2582, May 2023. DOI: 10.1364/OL.477372.

[59] A.-L. Viotti, M. Seidel, E. Escoto, *et al.*, "Multi-pass cells for post-compression of ultrashort laser pulses," *Optica*, vol. 9, no. 2, pp. 197–216, Feb. 2022. DOI: 10.1364/OPTICA.449225.

[60] P. Lenard, "Ueber die lichtelektrische Wirkung," *Annalen der Physik*, vol. 313, no. 5, pp. 149–198, Jan. 1902. DOI: 10.1002/andp.19023130510.

[61] A. Einstein, "Über einen die Erzeugung und Verwandlung des Lichtes betreffenden heuristischen Gesichtspunkt," *Annalen der Physik*, vol. 322, no. 6, pp. 132–148, 1905. DOI: 10.1002/andp.19053220607.

[62] I. Orfanos, I. Makos, I. Liontos, *et al.*, "Attosecond pulse metrology," *APL Photonics*, vol. 4, no. 8, p. 080 901, Aug. 2019. DOI: 10.1063/1.5086773.

[63] S. Ito, M. Schüler, M. Meierhofer, *et al.*, "Build-up and dephasing of Floquet–Bloch bands on subcycle timescales," *Nature*, vol. 616, no. 7958, pp. 696–701, Apr. 2023. DOI: 10.1038/s41586-023-05850-x.

[64] Folwer, Ralph Howard and Nordheim, Lothar Wolfgang, "Electron emission in intense electric fields," *Proceedings of the Royal Society of London. Series A, Containing Papers of a Mathematical and Physical Character*, vol. 119, no. 781, pp. 173–181, May 1928. DOI: 10.1098/rspa.1928.0091.

[65] Bunkin, F V and Fedorov, M V, "Cold emission of electrons from the surface of a metal in a strong radiation field," *Journal of Experimental and Theoretical Physics*, vol. 21, no. 5, pp. 1341–1346, Oct. 1964.

[66] M. Krüger, C. Lemell, G. Wachter, J. Burgdörfer, and P. Hommelhoff, "Attosecond physics phenomena at nanometric tips," *Journal of Physics B: Atomic, Molecular and Optical Physics*, vol. 51, no. 17, p. 172 001, Aug. 2018. DOI: 10.1088/1361-6455/aac6ac.

[67] D. R. Lide, Ed., *CRC Handbook of Chemistry and Physics: A Ready-Reference Book of Chemical and Physical Data*, 88. ed. Boca Raton, Fla.: CRC Press, 2008.

[68] M. W. Knight, N. S. King, L. Liu, H. O. Everitt, P. Nordlander, and N. J. Halas, "Aluminum for Plasmonics," *ACS Nano*, vol. 8, no. 1, pp. 834–840, Jan. 2014. DOI: 10.1021/nn405495q.

[69] A. F. Oskooi, D. Roundy, M. Ibanescu, P. Bermel, J. D. Joannopoulos, and S. G. Johnson, "Meep: A flexible free-software package for electromagnetic simulations by the FDTD method," *Computer Physics Communications*, vol. 181, no. 3, pp. 687–702, Mar. 2010. DOI: 10.1016/j.cpc.2009.11.008.

[70] I. Pupeza, M. Huber, M. Trubetskov, *et al.*, "Field-resolved infrared spectroscopy of biological systems," *Nature*, vol. 577, no. 7788, pp. 52–59, Jan. 2020. DOI: 10.1038/s41586-019-1850-7.

[71] M. Naftaly and R. E. Miles, "Terahertz Time-Domain Spectroscopy for Material Characterization," *Proceedings of the IEEE*, vol. 95, no. 8, pp. 1658–1665, Aug. 2007. DOI: 10.1109/JPROC.2007.898835.

[72] M. Neuhaus, J. Schötz, M. Aulich, *et al.*, "Transient field-resolved reflectometry at 50–100 THz," *Optica*, vol. 9, no. 1, pp. 42–49, Jan. 2022. DOI: 10.1364/OPTICA.440533.

[73] P. Gallagher, C.-S. Yang, T. Lyu, *et al.*, "Quantum-critical conductivity of the Dirac fluid in graphene," *Science*, vol. 364, no. 6436, pp. 158–162, Apr. 2019. DOI: 10.1126/science.aat8687.

[74] P. Fellgett, "Conclusions on Multiplex Methods," *Le Journal de Physique Colloques*, vol. 28, no. C2, pp. C2-165-C2–171, Mar. 1967. DOI: 10.1051/jphyscol:1967230.

[75] S. Markmann, M. Franckié, M. Bertrand, *et al.*, "Frequency chirped Fourier-Transform spectroscopy," *Communications Physics*, vol. 6, no. 1, pp. 1–12, Mar. 2023. DOI: 10.1038/s42005-023-01157-5.

[76] P. Jacquiont, "Interferometry and Grating Spectroscopy: An Introductory Survey," *Applied Optics*, vol. 8, no. 3, p. 497, Mar. 1969. DOI: 10.1364/AO.8.000497.

[77] F. Ritzkowsky, M. Yeung, E. Bebeti, *et al.*, *Large Area Optical Frequency Detectors for Single-Shot Phase Readout*, https://arxiv.org/abs/2306.01621v1, Jun. 2023.

[78] D. Hoff, F. J. Furch, T. Witting, *et al.*, "Continuous every-single-shot carrier-envelope phase measurement and control at 100 kHz," *Optics Letters*, vol. 43, no. 16, pp. 3850–3853, Aug. 2018. DOI: 10.1364/OL.43.003850.

[79] C. Guo, M. Miranda, A.-K. Raab, *et al.*, "Single-shot, high-repetition rate carrier-envelope-phase detection of ultrashort laser pulses," *Optics Letters*, vol. 48, no. 20, pp. 5431–5434, Oct. 2023. DOI: 10.1364/OL.498664.

[80] P. Dienstbier, L. Seiffert, T. Paschen, *et al.*, "Tracing attosecond electron emission from a nanometric metal tip," *Nature*, vol. 616, no. 7958, pp. 702–706, Apr. 2023. DOI: 10.1038/s41586-023-05839-6.

[81] S. Sederberg, D. Zimin, S. Keiber, *et al.*, "Attosecond optoelectronic field measurement in solids," *Nature Communications*, vol. 11, no. 1, p. 430, Jan. 2020. DOI: 10.1038/s41467-019-14268-x.

[82] J. D. Lee, Y. Kim, and C.-M. Kim, "Model for petahertz optical memory based on a manipulation of the optical-field-induced current in dielectrics," *New Journal of Physics*, vol. 20, no. 9, p. 093 029, Sep. 2018. DOI: 10.1088/1367-2630/aae100.

[83] D. Hui, H. Alqattan, S. Yamada, V. Pervak, K. Yabana, and M. T. Hassan, "Attosecond electron motion control in dielectric," *Nature Photonics*, vol. 16, no. 1, pp. 33–37, Jan. 2022. DOI: 10.1038/s41566-021-00918-4.

[84] M. Kubullek, Z. Wang, K. von der Brelje, *et al.*, "Single-shot carrier–envelope-phase measurement in ambient air," *Optica*, vol. 7, no. 1, pp. 35–39, Jan. 2020. DOI: 10.1364/OPTICA.7.000035.

[85] F. Ritzkowsky, E. Bebeti, G. M. Rossi, *et al.*, "Passively CEP stable sub-2-cycle source in the mid-infrared by adiabatic difference frequency generation," *Optics Letters*, vol. 48, no. 7, pp. 1870–1873, Apr. 2023. DOI: 10.1364/OL.485610.

[86] I. J. Sola, E. Mével, L. Elouga, *et al.*, "Controlling attosecond electron dynamics by phase-stabilized polarization gating," *Nature Physics*, vol. 2, no. 5, pp. 319–322, May 2006. DOI: 10.1038/nphys281.

[87] G. M. Rossi, R. E. Mainz, Y. Yang, *et al.*, "Sub-cycle millijoule-level parametric waveform synthesizer for attosecond science," *Nature Photonics*, vol. 14, no. 10, pp. 629–635, Oct. 2020. DOI: 10.1038/s41566-020-0659-0.

[88] S. V. Yalunin, M. Gulde, and C. Ropers, "Strong-field photoemission from surfaces: Theoretical approaches," *Physical Review B*, vol. 84, no. 19, p. 195 426, Nov. 2011. DOI: 10.1103/PhysRevB.84.195426.

[89] G. L. Yudin and M. Y. Ivanov, "Nonadiabatic tunnel ionization: Looking inside a laser cycle," *Physical Review A*, vol. 64, no. 1, p. 013 409, Jun. 2001. DOI: 10.1103/PhysRevA.64.013409.

[90] D. Buckley, Y. Yang, Y. Yang-Keathley, K. K. Berggren, and P. D. Keathley, "Nanoantenna design for enhanced carrier–envelope-phase sensitivity," *JOSA B*, vol. 38, no. 9, pp. C11–C21, Sep. 2021. DOI: 10.1364/JOSAB.424549.

[91] R. G. Forbes, "Description of field emission current/voltage characteristics in terms of scaled barrier field values (f-values)," *Journal of Vacuum Science & Technology B: Microelectronics and Nanometer Structures Processing, Measurement, and Phenomena*, vol. 26, no. 1, pp. 209–213, Jan. 2008. DOI: 10.1116/1.2834563.

[92] A. D. Rakić, "Algorithm for the determination of intrinsic optical constants of metal films: Application to aluminum," *Applied Optics*, vol. 34, no. 22, pp. 4755–4767, Aug. 1995. DOI: 10.1364/AO.34.004755.

[93] J. R. Birge, H. M. Crespo, and F. X. Kärtner, "Theory and design of two-dimensional spectral shearing interferometry for few-cycle pulse measurement," *JOSA B*, vol. 27, no. 6, pp. 1165–1173, Jun. 2010. DOI: 10.1364/JOSAB.27.001165.

[94] J. R. Birge, R. Ell, and F. X. Kärtner, "Two-dimensional spectral shearing interferometry for few-cycle pulse characterization," *Optics Letters*, vol. 31, no. 13, pp. 2063–2065, Jul. 2006. DOI: 10.1364/OL.31.002063.

[95] I. E. Gordon, L. S. Rothman, R. J. Hargreaves, *et al.*, "The HITRAN2020 molecular spectroscopic database," *Journal of Quantitative Spectroscopy and Radiative Transfer*, vol. 277, p. 107 949, Jan. 2022. DOI: 10.1016/j.jqsrt.2021.107949.

[96] O. Oliaei, "Noise analysis of correlated double sampling SC integrators with a hold capacitor," *IEEE Transactions on Circuits and Systems I: Fundamental Theory and Applications*, vol. 50, no. 9, pp. 1198–1202, Sep. 2003. DOI: 10.1109/TCSI.2003.816314.

[97] H. Wey and W. Guggenbuhl, "Noise transfer characteristics of a correlated double sampling circuit," *IEEE Transactions on Circuits and Systems*, vol. 33, no. 10, pp. 1028–1030, Oct. 1986. DOI: 10.1109/TCS.1986.1085840.

[98] G. Timm and A. Van Der Ziel, "Noise in field emission diodes," *Physica*, vol. 32, no. 7, pp. 1333–1344, Jul. 1966. DOI: 10.1016/0031-8914(66)90125-X.

[99] R. Bhattacharya, M. Turchetti, M. Yeung, P. Donald Keathley, K. K. Berggren, and J. Browning, "Effect of ultraviolet light on field emission performance and lifetime of lateral field emitter devices," *Journal of Vacuum Science & Technology B*, vol. 41, no. 6, p. 063 202, Dec. 2023. DOI: 10.1116/6.0003142.

[100] L. Shi, I. Babushkin, A. Husakou, *et al.*, "Femtosecond Field-Driven On-Chip Unidirectional Electronic Currents in Nonadiabatic Tunneling Regime," *Laser & Photonics Reviews*, vol. 15, no. 8, p. 2 000 475, 2021. DOI: 10.1002/lpor.202000475.

[101] T. Wittmann, B. Horvath, W. Helml, *et al.*, "Single-shot carrier–envelope phase measurement of few-cycle laser pulses," *Nature Physics*, vol. 5, no. 5, pp. 357–362, May 2009. DOI: 10.1038/nphys1250.

[102] M. Andrä, R. Barten, A. Bergamaschi, *et al.*, "Towards MYTHEN III - prototype characterisation of MYTHEN III.0.2," *Journal of Instrumentation*, vol. 14, no. 11, p. C11028, Nov. 2019. DOI: 10.1088/1748-0221/14/11/C11028.

[103] M. Borsch, M. Meierhofer, R. Huber, and M. Kira, "Lightwave electronics in condensed matter," *Nature Reviews Materials*, vol. 8, no. 10, pp. 668–687, Oct. 2023. DOI: 10.1038/s41578-023-00592-8.

[104] J. Schoetz, Z. Wang, E. Pisanty, M. Lewenstein, M. F. Kling, and M. F. Ciappina, "Perspective on Petahertz Electronics and Attosecond Nanoscopy," *ACS Photonics*, vol. 6, no. 12, pp. 3057–3069, Dec. 2019. DOI: 10.1021/acsphotonics.9b01188.

[105] M. F. Ciappina, J. A. Pérez-Hernández, A. S. Landsman, *et al.*, "Attosecond physics at the nanoscale," *Reports on Progress in Physics*, vol. 80, no. 5, p. 054 401, Mar. 2017. DOI: 10.1088/1361-6633/aa574e.

[106] K. M. Evenson, G. W. Day, J. S. Wells, and L. O. Mullen, "Extension of Absolute Frequency Measurements to the cw He–Ne Laser at 88 THz (3.39 μ)," *Applied Physics Letters*, vol. 20, no. 3, pp. 133–134, Feb. 1972. DOI: 10.1063/1.1654077.

[107] J. G. Small, G. M. Elchinger, A. Javan, A. Sanchez, F. J. Bachner, and D. L. Smythe, "Ac electron tunneling at infrared frequencies: Thin-film M-O-M diode structure with broad-band characteristics," *Applied Physics Letters*, vol. 24, no. 6, pp. 275–279, Mar. 1974. DOI: 10.1063/1.1655181.

[108] Z. Wang, H. Park, Y. H. Lai, *et al.*, "The roles of photo-carrier doping and driving wavelength in high harmonic generation from a semiconductor," *Nature Communications*, vol. 8, no. 1, p. 1686, Nov. 2017. DOI: 10.1038/s41467-017-01899-1.

[109] F. Langer, M. Hohenleutner, U. Huttner, S. W. Koch, M. Kira, and R. Huber, "Symmetry-controlled temporal structure of high-harmonic carrier fields from a bulk crystal," *Nature Photonics*, vol. 11, no. 4, pp. 227–231, Apr. 2017. DOI: 10.1038/nphoton.2017.29.

[110] P. D. Keathley, S. V. B. Jensen, M. Yeung, M. R. Bionta, and L. B. Madsen, "Uncovering extreme nonlinear dynamics in solids through time-domain field

analysis," *Physical Review B*, vol. 107, no. 5, p. 054 302, Feb. 2023. DOI: 10.1103/PhysRevB.107.054302.

[111] P.-C. Huang, C. Hernández-García, J.-T. Huang, *et al.*, "Polarization control of isolated high-harmonic pulses," *Nature Photonics*, vol. 12, no. 6, pp. 349–354, Jun. 2018. DOI: 10.1038/s41566-018-0145-0.

[112] O. Schubert, M. Hohenleutner, F. Langer, *et al.*, "Sub-cycle control of terahertz high-harmonic generation by dynamical Bloch oscillations," *Nature Photonics*, vol. 8, no. 2, pp. 119–123, Feb. 2014. DOI: 10.1038/nphoton.2013.349.

[113] M. Hohenleutner, F. Langer, O. Schubert, *et al.*, "Real-time observation of interfering crystal electrons in high-harmonic generation," *Nature*, vol. 523, no. 7562, pp. 572–575, Jul. 2015. DOI: 10.1038/nature14652.

[114] C. Jin, E. Y. Ma, O. Karni, E. C. Regan, F. Wang, and T. F. Heinz, "Ultrafast dynamics in van der Waals heterostructures," *Nature Nanotechnology*, vol. 13, no. 11, pp. 994–1003, Nov. 2018. DOI: 10.1038/s41565-018-0298-5.

[115] J. Reimann, S. Schlauderer, C. P. Schmid, *et al.*, "Subcycle observation of lightwave-driven Dirac currents in a topological surface band," *Nature*, vol. 562, no. 7727, pp. 396–400, Oct. 2018. DOI: 10.1038/s41586-018-0544-x.

[116] C. P. Schmid, L. Weigl, P. Grössing, *et al.*, "Tunable non-integer high-harmonic generation in a topological insulator," *Nature*, vol. 593, no. 7859, pp. 385–390, May 2021. DOI: 10.1038/s41586-021-03466-7.

[117] D. L. Marks and S. A. Boppart, "Nonlinear Interferometric Vibrational Imaging," *Physical Review Letters*, vol. 92, no. 12, p. 123 905, Mar. 2004. DOI: 10.1103/PhysRevLett.92.123905.

[118] V. Kumar, A. De la Cadena, A. Perri, *et al.*, "Invited Article: Complex vibrational susceptibility by interferometric Fourier transform stimulated Raman scattering," *APL Photonics*, vol. 3, no. 9, p. 092 403, Jul. 2018. DOI: 10.1063/1.5034114.

[119] J. Alves, J. Feng, L. Nienhaus, and T. W. Schmidt, "Challenges, progress and prospects in solid state triplet fusion upconversion," *Journal of Materials Chemistry C*, vol. 10, no. 20, pp. 7783–7798, May 2022. DOI: 10.1039/D1TC05659J.

[120] S. Wen, J. Zhou, P. J. Schuck, Y. D. Suh, T. W. Schmidt, and D. Jin, "Future and challenges for hybrid upconversion nanosystems," *Nature Photonics*, vol. 13, no. 12, pp. 828–838, Dec. 2019. DOI: 10.1038/s41566-019-0528-x.

[121] T. Wang and C. Xu, "Three-photon neuronal imaging in deep mouse brain," *Optica*, vol. 7, no. 8, pp. 947–960, Aug. 2020. DOI: 10.1364/OPTICA.395825.

[122] C. L. Evans and X. S. Xie, "Coherent Anti-Stokes Raman Scattering Microscopy: Chemical Imaging for Biology and Medicine," *Annual Review of Analytical Chemistry*, vol. 1, no. 1, pp. 883–909, 2008. DOI: 10.1146/annurev.anchem.1.031207.112754.

[123] K. T. Kim, C. Zhang, A. D. Shiner, *et al.*, "Petahertz optical oscilloscope," *Nature Photonics*, vol. 7, no. 12, pp. 958–962, Dec. 2013. DOI: 10.1038/nphoton.2013.286.

[124] A. Herbst, K. Scheffter, M. M. Bidhendi, M. Kieker, A. Srivastava, and H. Fattahi, "Recent advances in petahertz electric field sampling," *Journal of Physics B: Atomic, Molecular and Optical Physics*, vol. 55, no. 17, p. 172 001, Aug. 2022. DOI: 10.1088/1361-6455/ac8032.

[125] W. Cho, S. I. Hwang, C. H. Nam, *et al.*, "Temporal characterization of femtosecond laser pulses using tunneling ionization in the UV, visible, and mid-IR ranges," *Scientific Reports*, vol. 9, no. 1, p. 16 067, Nov. 2019. DOI: 10.1038/s41598-019-52237-y.

[126] Y. Liu, J. E. Beetar, J. Nesper, S. Gholam-Mirzaei, and M. Chini, "Single-shot measurement of few-cycle optical waveforms on a chip," *Nature Photonics*, vol. 16, no. 2, pp. 109–112, Feb. 2022. DOI: 10.1038/s41566-021-00924-6.

[127] A. Wirth, M. T. Hassan, I. Grguraš, *et al.*, "Synthesized Light Transients," *Science*, vol. 334, no. 6053, pp. 195–200, Oct. 2011. DOI: 10.1126/science.1210268.

[128] R. Borrego-Varillas, M. Lucchini, and M. Nisoli, "Attosecond spectroscopy for the investigation of ultrafast dynamics in atomic, molecular and solid-state physics," *Reports on Progress in Physics*, vol. 85, no. 6, p. 066 401, May 2022. DOI: 10.1088/1361-6633/ac5e7f.

[129] F. Ferdous, D. E. Leaird, C.-B. Huang, and A. M. Weiner, "Dual-comb electric-field cross-correlation technique for optical arbitrary waveform characterization," *Optics Letters*, vol. 34, no. 24, pp. 3875–3877, Dec. 2009. DOI: 10.1364/OL.34.003875.

[130] F. Ritzkowsky, M. R. Bionta, M. Turchetti, K. K. Berggren, F. X. Kärtner, and P. D. Keathley, "Engineering the Frequency Response of Petahertz-Electronic Nanoantenna Field-Sampling Devices," in *Conference on Lasers and Electro-Optics (2022), Paper JW3A.56*, San Jose, CA, USA: Optica Publishing Group, May 2022, JW3A.56. DOI: 10.1364/CLEO_AT.2022.JW3A.56.

[131] R. Jafari, T. Jones, and R. Trebino, "100% reliable algorithm for second-harmonic-generation frequency-resolved optical gating," *Optics Express*, vol. 27, no. 3, pp. 2112–2124, Feb. 2019. DOI: 10.1364/OE.27.002112.

[132] D. A. Zimin, V. S. Yakovlev, and N. Karpowicz, "Ultra-broadband all-optical sampling of optical waveforms," *Science Advances*, vol. 8, no. 51, eade1029, Dec. 2022. DOI: 10.1126/sciadv.ade1029.

[133] M. Mamaikin, Y.-L. Li, E. Ridente, *et al.*, "Electric-field-resolved near-infrared microscopy," *Optica*, vol. 9, no. 6, pp. 616–622, Jun. 2022. DOI: 10.1364/OPTICA.454562.

[134] E. Ridente, M. Mamaikin, N. Altwaijry, *et al.*, "Electro-optic characterization of synthesized infrared-visible light fields," *Nature Communications*, vol. 13, no. 1, p. 1111, Mar. 2022. DOI: 10.1038/s41467-022-28699-6.

[135] S. Keiber, S. Sederberg, A. Schwarz, *et al.*, "Electro-optic sampling of near-infrared waveforms," *Nature Photonics*, vol. 10, no. 3, pp. 159–162, Mar. 2016. DOI: 10.1038/nphoton.2015.269.

[136] P. Sulzer, K. Oguchi, J. Huster, *et al.*, "Determination of the electric field and its Hilbert transform in femtosecond electro-optic sampling," *Physical Review A*, vol. 101, no. 3, p. 033 821, Mar. 2020. DOI: 10.1103/PhysRevA.101.033821.

[137] P. Steinleitner, N. Nagl, M. Kowalczyk, *et al.*, "Single-cycle infrared waveform control," *Nature Photonics*, vol. 16, no. 7, pp. 512–518, Jul. 2022. DOI: 10.1038/s41566-022-01001-2.

[138] D. M. B. Lesko, H. Timmers, S. Xing, A. Kowligy, A. J. Lind, and S. A. Diddams, "A six-octave optical frequency comb from a scalable few-cycle erbium fibre laser," *Nature Photonics*, vol. 15, no. 4, pp. 281–286, Apr. 2021. DOI: 10.1038/s41566-021-00778-y.

[139] E. Fresch, F. V. A. Camargo, Q. Shen, *et al.*, "Two-dimensional electronic spectroscopy," *Nature Reviews Methods Primers*, vol. 3, no. 1, pp. 1–16, Nov. 2023. DOI: 10.1038/s43586-023-00267-2.

[140] W. P. Putnam, P. D. Keathley, J. A. Cox, A. Liehl, A. Leitenstorfer, and F. X. Kärtner, "Few-cycle, carrier–envelope-phase-stable laser pulses from a compact supercontinuum source," *JOSA B*, vol. 36, no. 2, A93–A97, Feb. 2019. DOI: 10.1364/JOSAB.36.000A93.

[141] D. Schade, F. Köttig, J. R. Koehler, M. H. Frosz, P. S. J. Russell, and F. Tani, "Scaling rules for high quality soliton self-compression in hollow-core fibers," *Optics Express*, vol. 29, no. 12, pp. 19 147–19 158, Jun. 2021. DOI: 10.1364/OE.426307.

[142] T. Balciunas, C. Fourcade-Dutin, G. Fan, *et al.*, "A strong-field driver in the single-cycle regime based on self-compression in a kagome fibre," *Nature Communications*, vol. 6, no. 1, p. 6117, Jan. 2015. DOI: 10.1038/ncomms7117.

[143] C. Heide, Y. Kobayashi, D. R. Baykusheva, *et al.*, "Probing topological phase transitions using high-harmonic generation," *Nature Photonics*, vol. 16, no. 9, pp. 620–624, Sep. 2022. DOI: 10.1038/s41566-022-01050-7.

[144] S. G. Drapcho, J. Kim, X. Hong, *et al.*, "Apparent breakdown of Raman selection rule at valley exciton resonances in monolayer $\mathrm{Mo}{\mathrm{S}}_{2}$," *Physical Review B*, vol. 95, no. 16, p. 165 417, Apr. 2017. DOI: 10.1103/PhysRevB.95.165417.

[145] J. Kim, X. Hong, C. Jin, *et al.*, "Ultrafast generation of pseudo-magnetic field for valley excitons in WSe2 monolayers," *Science*, vol. 346, no. 6214, pp. 1205–1208, Dec. 2014. DOI: 10.1126/science.1258122.

[146] D. Baykusheva, A. Chacón, J. Lu, *et al.*, "All-Optical Probe of Three-Dimensional Topological Insulators Based on High-Harmonic Generation by Circularly Polarized Laser Fields," *Nano Letters*, vol. 21, no. 21, pp. 8970–8978, Nov. 2021. DOI: 10.1021/acs.nanolett.1c02145.

[147] D. Baykusheva, A. Chacón, D. Kim, D. E. Kim, D. A. Reis, and S. Ghimire, "Strong-field physics in three-dimensional topological insulators," *Physical Review A*, vol. 103, no. 2, p. 023 101, Feb. 2021. DOI: 10.1103/PhysRevA.103.023101.

[148] O. Neufeld, D. Podolsky, and O. Cohen, "Floquet group theory and its application to selection rules in harmonic generation," *Nature Communications*, vol. 10, no. 1, p. 405, Jan. 2019. DOI: 10.1038/s41467-018-07935-y.

[149] C. He, H. He, J. Chang, B. Chen, H. Ma, and M. J. Booth, "Polarisation optics for biomedical and clinical applications: A review," *Light: Science & Applications*, vol. 10, no. 1, p. 194, Sep. 2021. DOI: 10.1038/s41377-021-00639-x.

[150] R. Patel, A. Khan, R. Quinlan, and A. N. Yaroslavsky, "Polarization-Sensitive Multimodal Imaging for Detecting Breast Cancer," *Cancer Research*, vol. 74, no. 17, pp. 4685–4693, Sep. 2014. DOI: 10.1158/0008-5472.CAN-13-2411.

[151] R. Cisek, A. Joseph, M. Harvey, and D. Tokarz, "Polarization-Sensitive Second Harmonic Generation Microscopy for Investigations of Diseased Collagenous Tissues," *Frontiers in Physics*, vol. 9, p. 726 996, Aug. 2021. DOI: 10.3389/fphy.2021.726996.

[152] S. Spielman, B. Parks, J. Orenstein, *et al.*, "Observation of the Quasiparticle Hall Effect in Superconducting Y Ba 2 Cu 3 O 7 - δ," *Physical Review Letters*, vol. 73, no. 11, pp. 1537–1540, Sep. 1994. DOI: 10.1103/PhysRevLett.73.1537.

[153] R. Shimano, Y. Ino, Y. P. Svirko, and M. Kuwata-Gonokami, "Terahertz frequency Hall measurement by magneto-optical Kerr spectroscopy in InAs," *Applied Physics Letters*, vol. 81, no. 2, pp. 199–201, Jul. 2002. DOI: 10.1063/1.1492319.

[154] J. Xu, J. Galan, G. Ramian, *et al.*, "Terahertz circular dichroism spectroscopy of biomolecules," in *Chemical and Biological Standoff Detection*, vol. 5268, SPIE, Feb. 2004, pp. 19–26. DOI: 10.1117/12.518533.

[155] N. Kanda, K. Konishi, and M. Kuwata-Gonokami, "Terahertz wave polarization rotation with double layered metal grating of complimentary chiral patterns," *Optics Express*, vol. 15, no. 18, pp. 11 117–11 125, Sep. 2007. DOI: 10.1364/OE.15.011117.

[156] K. Peng, D. Jevtics, F. Zhang, *et al.*, "Three-dimensional cross-nanowire networks recover full terahertz state," *Science*, vol. 368, no. 6490, pp. 510–513, May 2020. DOI: 10.1126/science.abb0924.

[157] W. P. Putnam, P. D. Keathley, R. G. Hobbs, K. K. Berggren, and F. X. Kärtner, "Probing the Femtosecond Response of Plasmonic Nanoparticles with Strong-field Photoemission," in *Conference on Lasers and Electro-Optics (2017), Paper FM3H.1*, Optica Publishing Group, May 2017, FM3H.1. DOI: 10.1364/CLEO_QELS.2017.FM3H.1.

[158] A. Sell, G. Krauss, R. Scheu, R. Huber, and A. Leitenstorfer, "8-fs pulses from a compact Er:fiber system: Quantitative modeling and experimental implementation," *Optics Express*, vol. 17, no. 2, pp. 1070–1077, Jan. 2009. DOI: 10.1364/OE.17.001070.

[159] A. Anderson, K. S. Deryckx, X. G. Xu, G. Steinmeyer, and M. B. Raschke, "Few-Femtosecond Plasmon Dephasing of a Single Metallic Nanostructure from Optical Response Function Reconstruction by Interferometric Frequency Resolved Optical Gating," *Nano Letters*, vol. 10, no. 7, pp. 2519–2524, Jul. 2010. DOI: 10.1021/nl101090s.

[160] B. Metzger, M. Hentschel, M. Nesterov, T. Schumacher, M. Lippitz, and H. Giessen, "Nonlinear optics of complex plasmonic structures: Linear and third-order optical response of orthogonally coupled metallic nanoantennas," *Applied Physics B*, vol. 122, no. 4, p. 77, Mar. 2016. DOI: 10.1007/s00340-016-6348-5.

[161] J. Ma, S. Masoodian, D. A. Starkey, and E. R. Fossum, "Photon-number-resolving megapixel image sensor at room temperature without avalanche gain," *Optica*, vol. 4, no. 12, pp. 1474–1481, Dec. 2017. DOI: 10.1364/OPTICA.4.001474.

[162] J. C. Travers, T. F. Grigorova, C. Brahms, and F. Belli, "High-energy pulse self-compression and ultraviolet generation through soliton dynamics in hollow capillary fibres," *Nature Photonics*, vol. 13, no. 8, pp. 547–554, Aug. 2019. DOI: 10.1038/s41566-019-0416-4.

[163] M. T. Hassan, "Lightwave Electronics: Attosecond Optical Switching," *ACS Photonics*, vol. 11, no. 2, pp. 334–338, Feb. 2024. DOI: 10.1021/acsphotonics.3c01584.

[164] D. H. Auston, A. M. Glass, and A. A. Ballman, "Optical Rectification by Impurities in Polar Crystals," *Physical Review Letters*, vol. 28, no. 14, pp. 897–900, Apr. 1972. DOI: 10.1103/PhysRevLett.28.897.

[165] D. H. Auston, "Subpicosecond electro-optic shock waves," *Applied Physics Letters*, vol. 43, no. 8, pp. 713–715, Oct. 1983. DOI: 10.1063/1.94486.

[166] D. H. Auston, K. P. Cheung, J. A. Valdmanis, and D. A. Kleinman, "Cherenkov Radiation from Femtosecond Optical Pulses in Electro-Optic Media," *Physical Review Letters*, vol. 53, no. 16, pp. 1555–1558, Oct. 1984. DOI: 10.1103/PhysRevLett.53.1555.

[167] D. H. Auston and A. M. Glass, "Optical Generation of Intense Picosecond Electrical Pulses," *Applied Physics Letters*, vol. 20, no. 10, pp. 398–399, Oct. 2003. DOI: 10.1063/1.1653991.

[168] D. H. Auston, P. Lavallard, N. Sol, and D. Kaplan, "An amorphous silicon photodetector for picosecond pulses," *Applied Physics Letters*, vol. 36, no. 1, pp. 66–68, Jul. 2008. DOI: 10.1063/1.91276.

[169] S. Piltan and D. Sievenpiper, "Plasmonic nano-arrays for enhanced photoemission and photodetection," *JOSA B*, vol. 35, no. 2, pp. 208–213, Feb. 2018. DOI: 10.1364/JOSAB.35.000208.

[170] A. Nardi, M. Turchetti, W. A. Britton, *et al.*, "Nanoscale refractory doped titanium nitride field emitters," *Nanotechnology*, vol. 32, no. 31, p. 315 208, May 2021. DOI: 10.1088/1361-6528/abf8de.

[171] F. C. M. J. M. van Delft, F. J. H. van der Kruis, P. P. J. van Eerd, H. A. van Esch, and H. W. J. J. van de Laar, "Reversing the hydrogen silsesquioxane image by silicon nitride and silicon oxide chemical mechanical polishing," *Journal of Vacuum Science & Technology B: Microelectronics and Nanometer Structures Processing, Measurement, and Phenomena*, vol. 24, no. 6, pp. 3125–3127, Dec. 2006. DOI: 10.1116/1.2357969.